



DISSERTATION

# Which-Way Experiments with a Three-Path Quantum Cheshire Cat & Simultaneous Weak-Path Measurements in Neutron Interferometry

Ausgeführt zum Zwecke der Erlangung des akademischen Grades  
eines Doktors der Naturwissenschaften  
unter der Leitung von

Assoz. Prof. Dipl.-Ing. Dr. Yuji Hasegawa  
141 Atominstitut

eingereicht an der Technischen Universität Wien  
Fakultät für Physik

durch  
Armin Danner  
0727146





to my friends



# Abstract

Weak values are defined for a procedure with a pre-selected and a post-selected state. Weak values in its standard form are the result of weak measurements, where a weak interaction is applied in between pre- and post-selection. The interaction entangles a system observable with a meter. Measurement of the meter gives information about the system. Weak values are an extension of expectation values. While the expectation value is the arithmetic mean of the possible results to a measurement, the meaning of the weak value is debated. In this thesis, two experiments in neutron interferometry are presented which use weak values to describe the measurement results. The meaning of weak values in context of the experiments is discussed. The theory of weak values and weak measurements is recapitulated. The neutron optical devices used are explained.

The first experiment presented realises a three-path quantum Cheshire Cat where three properties, i.e. particle, spin, and energy of the neutron, seem to be spatially separated in three paths of the interferometer. In contrast, the properties of a physical entity as the neutron are considered to be integral parts and therefore inseparable. For the experiment, different weak interactions are implemented one at a time in a path in the intermediate region between pre- and post-selection to locate the properties of the pre- and postselected quantum state. The interactions are absorption, a spin manipulation, and a coupled spin-energy manipulation. Each weak interaction is supposed to be sensitive to a single property of the neutron. The response in the detected signal after the post-selection is a qualitative measure of the location of the property. For the chosen pre- and post-selection, a specific weak interaction causes a significant response only when applied in a specific path. This behaviour is quantified by weak values such that no response is equivalent to a weak value of zero and the maximally expected response to an absolute value of the weak value of 1.

While the results allow for the interpretation of separated properties, a more conventional explanation is developed. The significance of the cross-term between different paths in the interference effect is pointed out such that the quantum Cheshire Cat can be described without spatial separation of the properties.

In the second experiment, simultaneous path weak-measurements are performed. The weak values of two path operators are measured at the same time with the same ensemble. Former experiments quantified the weak value of each path operators with a separate ensemble. To retrieve multiple weak values, as many ensembles had to be used.

Through interaction with oscillating magnetic fields of different frequencies,

the resulting weak energy manipulations uniquely mark each path with a time-dependent phase. The phase difference is observed at the output of the interferometer as a beating in the time-resolved intensity. Weak values are extracted from the fit parameters of a double-sine fit. Because there is no limitation on the frequencies of the magnetic fields, the procedure is expandable to the weak values' simultaneous measurement of an arbitrary number of path observables.

Both presented experiments involve which-way measurements. The applied procedures do not strictly follow the original weak measurement scheme in a strict sense. However, the procedures can be regarded as generalised weak measurements. The retrieved weak values quantify the behaviour of the system with regards to different paths of the interferometer. The changes in intensity can be backtracked to manipulations in specific paths. Because weak values are only retractable with an ensemble, no individual neutron is regarded as localised in a specific path. The interference effect is preserved while characterising different interferometer paths.

The presented experiments can potentially be expanded or adapted to meet the original criteria of weak measurements. Beyond the quantification of the results through weak values, the meaning of weak values is still an issue of interpretation. Further studies are necessary to solve the quantum measurement problem.

# Kurzfassung

Schwache Werte sind für Prozeduren mit Prä- und Postselektion definiert. Schwache Werte in ihrer Ursprungsform sind das Ergebnis von schwachen Messungen, in denen eine schwache Wechselwirkung zwischen Prä- und Postselektion angewandt wird. Die Wechselwirkung verschränkt eine Systemobservable mit einem Messgerät. Auswertung des Messgerätes gibt Information über das Ursprungssystem. Schwache Werte sind eine Erweiterung von Erwartungswerten. Während Erwartungswerte das arithmetische Mittel der möglichen Messwerte bilden, steht die Bedeutung von schwachen Werten zur Debatte. In dieser Arbeit werden zwei Experimente in der Neutroneninterferometrie vorgestellt, deren Ergebnisse mit schwachen Werten beschrieben sind. Die Bedeutung von schwachen Werten wird anhand der Experimente besprochen. Die Theory von schwachen Werten und schwachen Messungen wird wiederholt. Die verwendeten neutronenoptischen Geräte werden erklärt.

Das erste vorgestellte Experiment verwirklicht eine drei-Pfad Quantengrinsekatz, in der drei Eigenschaften — hier Teilchen, Spin und Energy des Neutrons — räumlich in die drei Pfade des Interferometers getrennt erscheinen. Im Gegensatz dazu werden die Eigenschaften eines physikalischen Gebildes als unveräußerlich und damit untrennbar erachtet. Für das Experiment werden verschiedene schwache Wechselwirkungen angewendet, eine nach der anderen in einem Pfad des Raums zwischen Prä- und Postselektion, um die Eigenschaften des prä- und postselektierten Quantenzustands zu verorten. Die Wechselwirkungen sind Absorption, Spinmanipulation und gekoppelte Spin-Energiemanipulation. Jede schwache Wechselwirkung wird als auf eine einzige Neutroneneigenschaft empfindlich angenommen. Die Auswirkung auf das detektierte Signal nach der Postselektion ist ein qualitatives Maß für den Ort der Eigenschaft. Für die gewählte Prä- und Postselektion verursacht jede schwache Wechselwirkung nur eine auffällige Auswirkung bei Anwendung in einem bestimmten Pfad. Dieses Verhalten ist durch schwache Werte quantifiziert, sodass keine Auswirkung durch einen schwachen Wert von null und die größtmöglich erwartete Auswirkung durch einen Absolutwert des schwachen Werts von eins ausgedrückt ist.

Während die Ergebnisse die Interpretation von getrennten Eigenschaften erlauben, wird eine herkömmlichere Erklärung entwickelt. Die Bedeutung der Kreuzterme zwischen verschiedenen Pfaden im Interferenzeffekt wird betont, sodass die Quantengrinsekatz ohne räumliche Trennung der Eigenschaften erklärt ist.

Im zweiten Experiment werden gleichzeitige Messungen von schwachen Werten des Pfads durchgeführt. Die schwachen Werte von zwei Pfadoperatoren werden gleichzeitig gemessen mit dem gleichen Ensemble. Frühere Experimente quantifizierten

schwache Werte von Pfadoperatoren mit eigenen Ensembles. Um mehrere schwache Werte auszulesen, wurden gleichviele Ensembles benötigt.

Durch Wechselwirkung mit schwingenden Magnetfeldern mit unterschiedlicher Frequenz markieren die ergebnen schwachen Energiemanipulationen jeden Pfad eindeutig mit einer zeitabhängigen Phase. Die Phasendifferenz wird am Ausgang des Interferometers als Schwebung der zeitaufgelösten Intensität beobachtet. Schwache Werte werden von den Fitparametern eines Doppelsinusfits ausgelesen. Weil keine Einschränkung der verwendeten Frequenzen gibt, kann die Prozedur auf beliebig viele gleichzeitige Messungen von schwachen Werten ausgeweitet werden.

Beide vorgestellten Experimente beinhalten Welcher-Weg-Messungen. Die angewandten Prozeduren folgen nicht strikt dem ursprünglichen Schema von schwachen Messungen. Nichtsdestotrotz können die Prozeduren als verallgemeinerte schwache Messungen betrachtet werden. Die erhaltenen schwachen Werte quantifizieren das Verhalten des Systems in Beziehung zu verschiedenen Pfaden des Interferometers. Die Änderungen der Intensität können zu Manipulationen in bestimmten Pfaden zurückgeführt werden. Weil schwache Werte nur für ein Ensemble erhalten werden können, wird kein einziges Neutron als in einem bestimmten Pfad lokalisiert angesehen. Der Interferenzeffekt bleibt erhalten, während verschiedene Interferometerpfade charakterisiert werden.

Die vorgestellten Experimente können potenziell erweitert werden oder angepasst, um die ursprünglichen Kriterien von schwachen Messungen zu erfüllen. Über die Quantifizierung der Resultate bleibt die Bedeutung von schwachen Werten weiter eine Frage der Interpretation. Weitere Studien sind nötig, um das Problem von quantenmechanischen Messungen zu lösen.

# Acknowledgments

I am in gratitude towards my supervisor Yuji Hasegawa for supporting me time and again during this thesis. His thoughtful guidance and insight into physics were principal for the success of the presented experiments. My hope is that many more students will experience his open-mindedness in complex discussions.

Many thanks go to my dear colleagues Bülent Demirel, Hermann Geppert-Kleinrath, Hartmut Lemmel, Richard Wagner, Wenzel Kersten, Martin Suda, Andreas Dvorak, and Ismaele Vincent Masiello, who all supported me whenever they could.

Parts of this thesis are published and reproduced with permission from Springer Nature.

# Contents

<b>1</b>	<b>Introduction</b>	<b>13</b>
<b>2</b>	<b>Theory</b>	<b>17</b>
2.1	Weak Values and Weak Measurements	17
2.1.1	Weak Values	17
2.1.2	Weak Measurements	19
2.2	Properties of the Neutron	22
2.2.1	Spin of the Neutron	22
2.2.2	Neutron scattering	25
<b>3</b>	<b>Neutron Optics</b>	<b>27</b>
3.1	Neutron Optical Ansatz	27
3.2	Neutron Sources	28
3.2.1	Spallation Sources	28
3.2.2	Nuclear Reactors	28
3.3	Manipulation of and Interaction with Neutrons	36
3.3.1	Monochromator	36
3.3.2	Spin Polarisers	39
3.3.3	Single Crystal Neutron Interferometer	48
3.3.4	Phase Shifter	50
3.3.5	Absorbers	51
3.3.6	Spin Manipulations via Magnetic Fields	52
3.3.7	Detectors	56
<b>4</b>	<b>Three-Path Quantum Cheshire Cat</b>	<b>61</b>
4.1	Introduction	61
4.2	Schematic and Theory	63
4.3	Experimental Data	68
4.3.1	Orienting the interferometer	68
4.3.2	Interferograms with Empty Interferometer	70
4.3.3	Coil Adjustment	76
4.3.4	Interferograms with Applied Preparation	77
4.3.5	Interferograms with Applied Preparation and Weak Interaction	78
4.3.6	Extraction of Weak Values	79
4.3.7	Second Order Behaviour	85
4.4	Discussion	86
4.4.1	Experimental Resources	86
4.4.2	Comparison with Standard Weak Measurements	88

4.4.3	Comparison with Proposal by Pan . . . . .	88
4.4.4	Comparison with Realistic Interpretation . . . . .	91
4.4.5	Subjective Remarks . . . . .	93
4.5	Conclusion . . . . .	95
<b>5</b>	<b>Simultaneous Path Weak-Measurements</b>	<b>97</b>
5.1	Introduction . . . . .	97
5.2	Theory and Schematic . . . . .	99
5.3	Setup . . . . .	100
5.4	Experimental Data . . . . .	103
5.4.1	Orienting the Interferometer . . . . .	103
5.4.2	Time-Resolved Measurements . . . . .	106
5.4.3	Data Correction . . . . .	110
5.4.4	Conversion to Weak Values . . . . .	112
5.5	Discussion . . . . .	115
5.5.1	Comparison with Standard Weak Measurements . . . . .	115
5.5.2	Emergence and Properties of the Results . . . . .	117
5.5.3	Complementarity Principle . . . . .	119
5.5.4	Subjective Remarks . . . . .	119
5.6	Conclusion . . . . .	120
<b>6</b>	<b>Conclusion and outlook</b>	<b>123</b>
<b>A</b>	<b>Detailed Calculations</b>	<b>125</b>
A.1	Three-Path Quantum Cheshire Cat . . . . .	125
A.2	Simultaneous Weak-Path Measurements . . . . .	129
A.2.1	Calculation of Intensity . . . . .	129
A.2.2	Data Correction . . . . .	131



# Chapter 1

## Introduction

The duality between wave and particle properties of physical systems goes back to the times of Isaac Newton when the question of the nature of light in form of waves or particles was highly contested. While Newton favoured the particle picture, Young's double-slit experiment with light [1] and the works on electrodynamics cumulating in the Maxwell equations gave strong evidence for the wave properties of light in classical physics.

Quantum theory was introduced with the explanations of the quantised transition of energy in black-body radiation [2] and of the photo-electric effect [3] which both indicate a particle behaviour of light. On the flip side, massive particles were postulated by de Broglie [4] to exhibit wave properties by de Broglie which was confirmed beginning with electron diffraction [5, 6]. In the context of nuclear reactors, neutron diffraction [7, 8] and Mach-Zehnder neutron interferometers with silicon single-crystals [9] and spin-echo instruments [10] were implemented. Devices for ever larger and more complicated systems were developed such that interference has been established for atoms [11, 12], ions [13], molecules [14], and positrons [15].

The mathematical description of massive quantum system in the non-relativistic case is given by the Schrödinger equation which acts as the equation of motion [16]. The Schrödinger equation is a wave equation for quantum mechanical systems and its solutions are wave functions. While the time evolution is based on wave mechanics, the detection of the quantum system happens not in continuous but discrete numbers, which is strongly associated with the particle aspect. Many peculiarities appear from the fact that the evolution of a wave function follows the Schrödinger equation. However, in the Copenhagen interpretation of quantum mechanics, measurement results are considered to involve the collapse of the wave function. The quantum state after collapse is predicted probabilistically. One counter-intuitive effect involved in this thesis is the complementarity of wave and particle in an interferometer.

Quantum mechanics has revealed an abundance of effects which defy our classical understanding of nature. Examples are entanglement as studied in the Einstein-Podolsky-Rosen [17] paradox and subject to Bell tests [18], the superposition principle as illustrated by the Schrödinger Cat [19], uncertainty relations as introduced by Heisenberg [20], the quantum Zeno effect [21], and the quantum Cheshire Cat [22, 23]. Investigating and understanding these effects is detrimental for fields from philosophy to industrial application.

In an interferometer, a wave is split into sub-beams, propagates, and is recom-

bined according to the phase relation between the sub-beams. The detection events after the interferometer are discrete, while the distribution of events follows the wave description. For definitive statements about the traversed path of a physical system through an interferometer, projective measurements have to be used. Projective measurements entail a large disturbance on the system such that the interference effect is lost.

To investigate the undisturbed quantum state inside an interferometer, weak measurements [24] can be used. They are realised as the measurement of an observable in combination with a pre- and post-selected state. Between pre- and post-selection, a weak interaction is applied. Weak values quantify the change of the output intensity in the limit of applying the quantum operator with vanishing interaction strength. Weak measurements are a means to investigate a quantum state with minimal disturbance to the wavefunction.

Weak values are an extension of expectation values and in general complex. In the vicinity of orthogonality between the two states, the weak value can exhibit anomalous properties, i.e. exceed the eigenvalue range of the respective operator. The first realisation of a weak measurement was implemented with photons [25]. With neutrons, the path DOF was used as a pointer system to retrieve spin weak values [26] and, vice versa, the spin degree of freedom to retrieve path weak values [27, 28]. For atoms, the weak measurements of the polarisation and spin were reported [29, 30].

The meaning of weak values is not conclusively resolved. The weak value's real part is considered to characterise the respective operator in the limit of minimal disturbance [31]. The imaginary part is considered to quantify the disturbance on the quantum system [32]. Weak values can be related to many fundamental phenomena such as uncertainty relations [33, 34], quantum paradoxes [35, 36], and negative quasi-probability distributions [37, 38]. Among the wide spectrum of applications, weak measurements were exploited, e.g. for signal amplification [39, 40], wave-function tomography [41], and proposals for quantum smoothing [42, 43].

In this thesis, two experiments in neutron interferometry are presented which use weak values to describe the measurement results. Their analysis provides some insight about the meaning of weak values in the context of wave-particle duality. [24]

Single-crystal neutron interferometry is a powerful tool to investigate fundamental effects of quantum theory. The technique exploits the phase dependence of the intensity at the output of the interferometer. The count rate is such that the observed phenomena can be strictly related to self-interference. Although the matter waves in neutron optics have microscopic wavelengths, many devices used have macroscopic dimensions. The beam separation in a neutron interferometer of several centimetres was exceeded by atom interferometers a decade ago [44]. Neutron interferometry can be conducted at atmospheric pressure and at room temperature. Neutrons are subject to all four known forces of nature. For certain experiments, the low electrical polarisability is advantageous.

Early achievements in neutron interferometry were to establish the neutron as a wave [9], demonstrating the  $4\pi$  symmetry of fermions [45], and the observation of gravitationally induced phase shifts on a quantum system [46]. In addition to the

path degree of freedom, the neutron's spin with spin quantum number  $S = 1/2$  was manipulated to demonstrate spinor superposition [47]. The developed techniques of manipulation were used more recently to demonstrate the coupling between the neutron's degrees of freedom, i.e. intra-particle entanglement. Their study revealed the violation of a Bell-like inequality with the degrees of freedom of path and spin for single neutrons [48]. With further energy manipulations, studies with entanglement between three degrees of freedom followed [49]. Counter-intuitive and fundamental aspects of quantum mechanics have been investigated.

The quantum Cheshire Cat [22] is a quantum paradox where distinct properties of a physical system in an interferometer appear to be separated in different paths. The phenomenon necessitates a pre- and post-selection procedure as in weak measurements. A experimental realisation [23] was implemented with neutrons. The quantum Cheshire Cat is a controversial topic. Its realisations are often found to be non-genuine realisations of an ideal Gedankenexperiment. The imperfections regard the interaction strength, lacking distinct meter systems. Even if all formal requirements were fulfilled, some interpret the effect as sheer interference effect.



# Chapter 2

## Theory

### 2.1 Weak Values and Weak Measurements

#### 2.1.1 Weak Values

An observable  $\hat{O}$  can be written in spectral representation as

$$\hat{O} = \sum_a a |a\rangle \langle a|. \quad (2.1)$$

For the Hermitian observables considered henceforth, the eigenvectors  $|a\rangle$  are pairwise orthonormal and the eigenvalues  $a$  are real. In quantum mechanics, the eigenvalues are identified with measurement outcomes for the respective eigenvector. For a given state vector  $|\psi\rangle$ , the probabilities  $p(a)$  for measuring the outcome  $a$  are calculated as

$$p(a) = \frac{|\langle a|\psi\rangle|^2}{\langle \psi|\psi\rangle}. \quad (2.2)$$

The expectation value  $\langle \hat{O} \rangle$  is defined for a quantum state  $|\psi\rangle$  as

$$\langle \hat{O} \rangle = \frac{\langle \psi|\hat{O}|\psi\rangle}{\langle \psi|\psi\rangle} = \sum_a \frac{\langle \psi|a\rangle \langle a|\psi\rangle}{\langle \psi|\psi\rangle} = \sum_a a \frac{|\langle \psi|a\rangle|^2}{\langle \psi|\psi\rangle} = \sum_a a p(a) \in \mathbb{R}. \quad (2.3)$$

The expectation value is equal to the weighted arithmetic mean of the eigenvalues and is therefore within the eigenvalue range, i.e.  $\min(a) \leq \langle \hat{O} \rangle \leq \max(a)$ .

The weak value  $\langle \hat{O} \rangle_w$  is defined as

$$\langle \hat{O} \rangle_w = \frac{\langle f|\hat{O}|i\rangle}{\langle f|i\rangle} \in \mathbb{C}, \quad (2.4)$$

with a pre-selected state  $|i\rangle$  and a post-selected state  $|f\rangle$ . The concept of weak values and weak measurements is based on a time-symmetric formulation of quantum mechanics [50–52]. In this framework, it is argued that a complete description of an ensemble necessitates both an initial (i) and final (f) state.

The probability of post-selection given the pre-selection is written as

$$p(f|i) = |\langle f|i\rangle|^2. \quad (2.5)$$

For  $\langle f|i \rangle = 0$ , the weak value is in general undefined. However, in the specific case that in addition either the pre- or post-selected state is an eigenvector of the operator  $\hat{O}$  with eigenvalue  $a$ , the weak value is defined. The weak value then calculates as

$$\langle \hat{O} \rangle_w = \frac{\langle f|\hat{O}|i \rangle}{\langle f|i \rangle} = \frac{\langle f|a|i \rangle}{\langle f|i \rangle} = a \in \mathbb{R}. \quad (2.6)$$

In contrast to the expectation value, the weak value can diverge in the proximity of orthogonal pre- and post-selected states if the denominator  $\langle f|i \rangle$  approaches zero faster than the numerator  $\langle f|\hat{O}|i \rangle$  or if the numerator is finite, e.g. in case  $\hat{O}|i \rangle = |f \rangle$ . Close to the orthogonality, the weak value can exceed the eigenvalue range, in which case one speaks of anomalous weak values [53–58]. This behaviour begs the question: what is the meaning of anomalous and weak values in general?

If we consider a normalised initial state  $|i \rangle$ , we can write the expectation value in terms of weak values as [24]

$$\begin{aligned} \langle \hat{O} \rangle &= \langle i|\hat{O}|i \rangle = \langle i|\mathbb{1}\hat{O}|i \rangle \\ &= \sum_f \langle i|f \rangle \langle f|\hat{O}|i \rangle = \sum_f \frac{|\langle i|f \rangle|^2 \langle f|\hat{O}|i \rangle}{\langle f|i \rangle} \\ &= \sum_f \langle \hat{O} \rangle_{w,f} |\langle i|f \rangle|^2 = \sum_f \langle \hat{O} \rangle_{w,f} p(f|i) \in \mathbb{R}, \end{aligned} \quad (2.7)$$

where we used the completeness and identity relation  $\mathbb{1} = \sum_f |f \rangle \langle f|$ . The weak value  $\langle \hat{O} \rangle_{w,f}$  is relative to the post-selected state  $|f \rangle$ . In the comparison of the calculations of the expectation value in Eqs. (2.3) and (2.7), the eigenvalues and the probability of its measurement are replaced, respectively, by the weak values and the probability of post-selection of a pre-selected state. It can be seen in Eq. (2.7), that the real expectation value is the weighted arithmetic mean of the weak values which are complex scalars. Therefore, the weighted imaginary parts,  $\text{Im} \{ \cdot \}$ , sum up to zero,

$$\text{Im} \left\{ \sum_f \langle \hat{O} \rangle_{w,f} p(f|i) \right\} = \sum_f \text{Im} \left\{ \langle \hat{O} \rangle_{w,f} \right\} p(f|i) = 0, \quad (2.8)$$

the weighted real parts,  $\text{Re} \{ \cdot \}$ , sum up to the expectation value,

$$\text{Re} \left\{ \sum_f \langle \hat{O} \rangle_{w,f} p(f|i) \right\} = \sum_f \text{Re} \left\{ \langle \hat{O} \rangle_{w,f} \right\} p(f|i) = \langle \hat{O} \rangle. \quad (2.9)$$

The representation of the expectation value via weak values begs the question which properties weak values share with eigenvalues. Are both representations of physical reality? Lev Vaidman argues in this sense that the outcome of weak measurements should be considered valid [59] in the same sense that eigenvalues are valid quantitative characterisations of physical systems. Everyone agrees that weak values only characterise a pre- and post-selected ensemble. Both pre- and post-selection filter certain properties. The anomalous properties of weak values become only apparent when the filtering separates the vast majority of elements of the initial ensemble.

## 2.1 Weak Values and Weak Measurements

Weak values were introduced in 1988 [24] with the finding that it is possible to measure values outside the eigenvalue range of an operator. In the earliest publications, the weak value is treated as a synonym for the results of weak measurements. with their small interaction strength. The measurement results are compared between the results with and without the weak interaction applied. In those kind of weak measurements, the weak values are extracted by normalising the differences with the interaction strength.

However, weak values are not constrained to the description of weak measurements. As a matter of fact, any measurement can be described through weak values.

### 2.1.2 Weak Measurements

Weak measurements are introduced in [24]. Recapitulations of the theory [60, 61] are used as a source for this section. The basis for weak measurements are von Neumann measurements [62]. A von Neumann measurement assumes an observable  $\hat{O}$  of a quantum system with state  $|\psi_s\rangle$ . The quantum system is coupled to a continuous meter with canonical variables  $\hat{q}$ ,  $\hat{p}$  of the state

$$|\phi_m\rangle = \int dq \phi_m(q) |q\rangle = \int dp \tilde{\phi}_m(p) |p\rangle. \quad (2.10)$$

The coupling is described by the interaction Hamiltonian

$$\hat{H}_{\text{int}} = -g(t)\hat{p} \otimes \hat{O}, \quad (2.11)$$

where  $g(t)$  describes the coupling rate over the time  $t$  and the coupling strength is

$$G = \int_{t_i}^{t_f} g(t) dt. \quad (2.12)$$

Time evolution is given via the operator

$$\hat{U} = \exp\left(-\frac{i}{\hbar} \int_{t_i}^{t_f} \hat{H}_{\text{int}} dt\right). \quad (2.13)$$

The composite state is written as  $|\Psi\rangle = |\psi_s\rangle \otimes |\phi_m\rangle$ . Due to the interaction, the meter evolves as

$$|\Psi'\rangle = \hat{U} |\Psi\rangle = \exp\left(-\frac{i}{\hbar} \int_{t_i}^{t_f} \hat{H}_{\text{int}} dt\right) |\Psi\rangle. \quad (2.14)$$

The measurement of the meter is written as  $(\mathbb{1} \otimes \langle q|) |\Psi\rangle = \mathbb{1} |\psi\rangle \otimes \langle q|\phi\rangle$  (further tensor product signs will be omitted). Performing this measurement after the interaction is written as

$$\begin{aligned} \langle q|\Psi'\rangle &= \langle q| \exp\left(-\frac{i}{\hbar} \int_{t_i}^{t_f} \hat{H}_{\text{int}} dt\right) |\Psi\rangle \\ &= \langle q| \exp\left(\frac{i}{\hbar} \int_{t_i}^{t_f} g(t)\hat{p}\hat{O} dt\right) |\psi_s\rangle |\phi_m\rangle \\ &= \langle q| \exp\left(iG\hat{p}\hat{O}/\hbar\right) |\psi_s\rangle |\phi_m\rangle. \end{aligned} \quad (2.15)$$

## 2 Theory

We now assume the coupling strength to satisfy  $G = 1$  such that

$$\begin{aligned}
 \langle q|\Psi'\rangle &= \langle q| e^{i\hat{p}\hat{O}/\hbar} \mathbb{1} |\psi_s\rangle |\phi_m\rangle \\
 &= \langle q| \sum_a e^{i\hat{p}\hat{O}/\hbar} |a\rangle \langle a|\psi_s\rangle |\phi_m\rangle \\
 &= \langle q| \sum_a e^{i\hat{p}a/\hbar} |\phi_m\rangle |a\rangle \langle a|\psi_s\rangle \\
 &= \sum_a \phi_m(q - a) |a\rangle \langle a|\psi_s\rangle.
 \end{aligned} \tag{2.16}$$

In the latter equation, we used the property of the displacement operator

$$e^{i\hat{p}a/\hbar} \phi(q) = \phi(q - a). \tag{2.17}$$

So far, the distribution  $\phi_m(q)$  is unspecified. For eigenvalues  $a$  and a distribution  $\phi_m(q)$  such that the shifts  $\phi(q - \frac{a}{\hbar})$  do not overlap for any pair of eigenvalues, the obtained meter value unambiguously implies the measurement of a specific observable. This is considered as the regime of a strong measurement. This can also hold for a more realistic situation, when assuming a Gaussian distribution of the classical meter system, written as a function of either canonical observable as

$$\begin{aligned}
 \phi_m(q) &= \langle q|\phi_m\rangle = \exp\left(-\frac{q^2}{4\Delta_q^2}\right) \\
 \tilde{\phi}_m(p) &= \langle p|\phi_m\rangle = \exp\left(-\frac{p^2}{4\Delta_p^2}\right) = \exp(-\Delta_q^2 p^2).
 \end{aligned} \tag{2.18}$$

with the spreads in the distribution  $\Delta_q$  and  $\Delta_p$ , respectively. If the system is in the state  $|a\rangle$ , the distribution of the meter system is shifted by the respective eigenvalue  $a$ . If the spread in the initial distribution  $\Delta_q$  is small compared to the eigenvalues, the shift and the corresponding eigenstate can be retrieved with confidence from a single measurement.

However, the coupling strength can also satisfy  $G \ll 1$ . Instead of Eq. (2.16), the result of the measurement gives

$$\begin{aligned}
 \langle q|\Psi'\rangle &= \langle q| e^{iG\hat{p}\hat{O}/\hbar} \mathbb{1} |\psi_s\rangle |\phi_m\rangle \\
 &= \sum_a \phi_m(q - Ga) |a\rangle \langle a|\psi_s\rangle,
 \end{aligned} \tag{2.19}$$

where the the separation between the distributions is small compared to the spreads. The sum of the distributions is a broadened Gaussian. With a single measurement, one cannot distinguish between the eigenstates any more. If we add a post-selection  $|f\rangle$  to Eq. (2.19) and write the initial state of the system  $|\psi_s\rangle = |i\rangle$ , the result is

adjusted to

$$\begin{aligned}
 \langle f | \langle q | \Psi' \rangle &= \langle f | \langle q | \exp \left( -\frac{i}{\hbar} \int_{t_i}^{t_f} \hat{H}_{\text{int}} dt \right) | \Psi \rangle \\
 &= \langle q | \langle f | e^{iG\hat{p}\hat{O}/\hbar} | i \rangle | \phi_m \rangle \\
 &\approx \langle q | \langle f | (1 + iG\hat{p}\hat{O}/\hbar) | i \rangle | \phi_m \rangle \\
 &= \langle q | \left[ \langle f | i \rangle + iG\hat{p}/\hbar \langle f | \hat{O} | i \rangle \right] | \phi_m \rangle \\
 &= \langle q | \left[ \langle f | i \rangle + iG\hat{p}/\hbar \frac{\langle f | i \rangle}{\langle f | i \rangle} \langle f | \hat{O} | i \rangle \right] | \phi_m \rangle \\
 &= \langle q | \left[ \langle f | i \rangle \left( 1 + iG\hat{p}/\hbar \langle \hat{O} \rangle_w \right) \right] | \phi_m \rangle \\
 &\approx \langle q | \left[ \langle f | i \rangle e^{iG\hat{p}\langle \hat{O} \rangle_w/\hbar} \right] | \phi_m \rangle \\
 &= \langle f | i \rangle \phi_m \left( q - G \langle \hat{O} \rangle_w \right).
 \end{aligned} \tag{2.20}$$

The latter procedure with a small coupling strength to a meter and a post-selection of the system is regarded as a standard weak measurement. The shift in the meter distribution is proportional to the weak value  $\langle \hat{O} \rangle_w \in \mathbb{C}$ . The displacement operator can be split up as

$$\exp \left( iG\hat{p} \langle \hat{O} \rangle_w / \hbar \right) = \exp \left( iG\hat{p} \text{Re}\{\langle \hat{O} \rangle_w\} / \hbar \right) \exp \left( -G\hat{p} \text{Im}\{\langle \hat{O} \rangle_w\} / \hbar \right) \tag{2.21}$$

such that the imaginary part causes a non-unitary operation. The meter  $q$  is shifted proportionally to  $\text{Re}\{\langle \hat{O} \rangle_w\}$  and the canonical conjugate variable  $p$  is shifted proportionally to  $\text{Im}\{\langle \hat{O} \rangle_w\} \Delta_p$  [24, 63, 64]. Although the coupling strength is assumed as small, the real part can be extracted to arbitrary precision by repeating the procedure for an ensemble of systems. In case of almost orthogonal pre- and post-selection,  $\langle f | i \rangle \ll 1$ , the weak values are in general anomalous (see Sec. 2.1.1) and the shift in the meter is amplified.

Weak values appear also in measurements which are not regarded as standard weak measurements. As an example, we consider the time evolution

$$\hat{U} = \exp \left( -iG\hat{O}/\hbar \right) \tag{2.22}$$

without coupling to a separate meter system and  $G \ll 1$ . The intensity after post-selection calculates as

$$\begin{aligned}
 |\langle f | \hat{U} | i \rangle|^2 &= |\langle f | \exp \left( -iG\hat{O}/\hbar \right) | i \rangle|^2 \\
 &= |\langle f | (1 + iG\hat{O} + \mathcal{O}(G^2)) | i \rangle|^2 \\
 &= |\langle f | i \rangle|^2 + 2G \text{Im}\{\langle i | f \rangle \langle f | \hat{O} | i \rangle\} + \mathcal{O}(G^2) \\
 &= |\langle f | i \rangle|^2 + 2G \text{Im}\{\langle i | f \rangle \frac{\langle f | i \rangle}{\langle f | i \rangle} \langle f | \hat{O} | i \rangle\} + \mathcal{O}(G^2) \\
 &= |\langle f | i \rangle|^2 \left( 1 + 2G \text{Im}\{\langle \hat{O} \rangle_w\} \right) + \mathcal{O}(G^2),
 \end{aligned} \tag{2.23}$$

where the intensity is described through the weak value. In analogy to the representation of the expectation value through weak values in Eq. (2.7), weak values can describe measurements outside the context of standard weak measurements.

## 2.2 Properties of the Neutron

The neutron was discovered as nuclear radiation in 1934 by Chadwick [65]. It was named after its electrical neutrality and has a mass  $m_n = 1.67 \times 10^{-34}$  kg. Through high-energy experiments at particle accelerators, the composition of the neutron is described by quarks. One up quark with electrical charge  $q_u = +(2/3)e$  and two down quarks with electrical charge  $q_d = -(1/3)e$  compose the neutron, where  $e = 1.602 \times 10^{-19}$  C is the charge of the positron. Besides the quarks' rest masses, the majority of the neutron's mass is due to the interactions between the quarks, described in quantum chromodynamics primarily through the mediating gluons.

### 2.2.1 Spin of the Neutron

The total angular momentum is written as  $\vec{J} = \vec{L} + \vec{S}$ . It is divided in contributions from the orbital angular momentum  $\vec{L}$  of the motion around an external centre of rotation and the intrinsic angular momentum, or spin,  $\vec{S}$ . Each kind of particle or quasi-particle has a certain spin value. All angular momenta are quantised in units of  $\hbar = h/(2\pi)$ , with the Planck constant  $h = 6.626 \times 10^{-34}$  J/K. All particles studied so far can be classified either as Bosons or Fermions, i.e. particles of integer or half-integer spin, respectively. The wave function of multiple bosons is symmetrical under particle exchange whereas the wave function is anti-symmetric for fermions. This property describes the Fermi exclusion principle which states that a number of fermions can exist only if each one is characterised by a unique set of quantum numbers which differs from every other set. We will consider the neutron as an idealised Dirac fermion without internal structure with a spin quantum number  $S_n = 1/2$  and a magnetic spin quantum number  $m_S \in \{-S, -S + 1, \dots, S\} = \{-1/2, +1/2\}$ . The neutron's spin system constitutes a two-level system and the neutron is a fermion. Therefore, if all other quantum numbers are the same, two neutrons can coexist with different values of  $m_S$ , i.e. their spin orientations are in opposite directions.

The spin of the neutron is written as

$$\vec{S} = \frac{\hbar}{2} \vec{\sigma} = \frac{\hbar}{2} \begin{pmatrix} \hat{\sigma}_x \\ \hat{\sigma}_y \\ \hat{\sigma}_z \end{pmatrix} \quad (2.24)$$

with the Pauli matrices

$$\hat{\sigma}_x = \begin{pmatrix} 0 & 1 \\ 1 & 0 \end{pmatrix}, \quad \hat{\sigma}_y = \begin{pmatrix} 0 & -i \\ i & 0 \end{pmatrix}, \quad \hat{\sigma}_z = \begin{pmatrix} 1 & 0 \\ 0 & -1 \end{pmatrix} \quad (2.25)$$

in the  $z$ -spin eigenbasis.

The polarisation vector is the expectation value of the spin operators, written as

$$\vec{P} = \langle \psi | \vec{\sigma} | \psi \rangle. \quad (2.26)$$

The polarisation vector can be represented on the Bloch sphere which has similarities with the Poincaré sphere representing light polarisation. Both spheres describe two level systems with opposing poles representing the states composing a complete

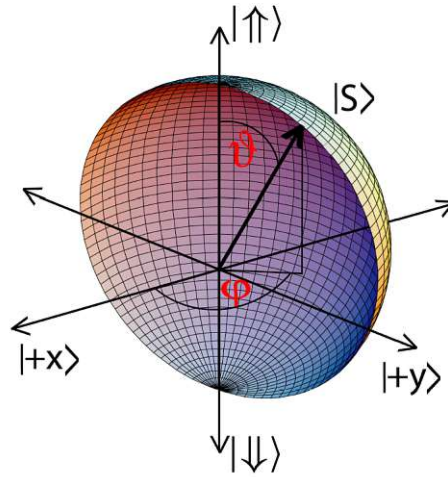


Figure 2.1: Representation of the polarisation vector on the Bloch sphere with the angles  $\vartheta$  and  $\varphi$  as in Equation 2.27.

orthonormal basis in spin space. The two eigenstates of the Pauli spin matrix  $\sigma_z$ , called up- and down-state, are written as  $|\uparrow\rangle$  and  $|\downarrow\rangle$ . When a different basis is used in this thesis, the according spatial coordinate is added as an index to the spin states. Possible bases for the Poincaré sphere for photons are horizontal and vertical polarisations or left and right-handed circular polarisation. A sphere is most easily described in polar coordinates. The points on a unit sphere are parametrised with two angles of polar coordinates. Any polarised spin state  $|\eta\rangle$  of the neutron can be written in the form

$$|\eta\rangle = \left( \cos \frac{\theta}{2} |\uparrow\rangle + e^{i\phi} \sin \frac{\theta}{2} |\downarrow\rangle \right), \quad (2.27)$$

with the polar angle  $\theta$ , the azimuthal angle  $\phi$ . The sinusoidal terms dependent on the angle  $\theta$  in Eq. (2.27) give the components relative to the basis vectors, while the angle  $\phi$  gives the relative phase between the basis states. If the degree of polarisation is reduced from its maximum possible value of 1, the length of the polarisation vector is reduced accordingly. A possible cause for this is partial incoherence between the components of the spin state. A single wave function can then not describe all physical properties of a system. In the limit of a totally mixed state, no prediction about the orientation of the neutron spin is possible. This lack of information is represented as a zero vector with  $P = 0$ . The experiments presented provide initial degrees of polarisation  $P > 0.99$ , such that all descriptions will assume a maximal degree of polarisation  $P = 1$ .

Given the spin state of Eq. (2.27), the probabilities of measuring the z-spin components are written as

$$p_{\uparrow} = |\langle \uparrow | \eta \rangle|^2 = \cos^2(\vartheta/2), \quad (2.28)$$

$$p_{\downarrow} = |\langle \downarrow | \eta \rangle|^2 = \sin^2(\vartheta/2), \quad (2.29)$$

$$p_{\uparrow} + p_{\downarrow} = 1. \quad (2.30)$$

The azimuthal angle  $\varphi$  affects measurements of spin components in other directions  $p_{\pm x}$ ,  $p_{\pm y}$ .

## 2 Theory

The spin  $\vec{S}$  and the magnetic moment  $\vec{\mu}$  of a particle are closely related properties. Their proportional magnitudes are connected via the relation

$$\vec{\mu} = \mu\vec{\sigma} = \frac{2\mu}{\hbar}\vec{S} = \gamma\vec{S} = g\frac{\mu_p}{\hbar}\vec{S} = g\frac{e}{2m_p}\vec{S}, \quad (2.31)$$

with the neutron's magnetic moment  $\mu = -9.6623653(23)$  J/T, the gyromagnetic ratio  $\gamma$ , the proton's magnetic moment  $\mu_p$ , and the g-factor for the neutron  $g \approx -3.826085$ .

In a classical attempt to describe the emergence of a magnetic moment, one can assume the quarks with their charges to rotate around some axis, giving a current around an area. Although only a handwaving argument, this illustrates the relation between rotation and magnetism for the neutron spin. The equation of motion of the polarisation vector on the Bloch sphere is now derived:

$$\begin{aligned} \frac{d\vec{P}}{dt} &= \frac{d}{dt} (\langle \eta(t) | \vec{\sigma} | \eta(t) \rangle) \\ &= \left( \frac{d}{dt} \langle \eta(t) | \right) \vec{\sigma} | \eta(t) \rangle + \langle \eta(t) | \left( \frac{d\vec{\sigma}}{dt} \right) | \eta(t) \rangle + \langle \eta(t) | \vec{\sigma} \left( \frac{d}{dt} | \eta(t) \rangle \right) + \langle \eta(t) | \left[ \frac{d}{dt}, \vec{\sigma} \right] | \eta(t) \rangle \\ &= \left\langle \frac{d\vec{\sigma}}{dt} \right\rangle - \frac{i}{\hbar} \langle [\vec{\sigma}, \hat{H}] \rangle. \end{aligned} \quad (2.32)$$

In Schrödinger notation, the operators are constant and the first term vanishes. For a system in a magnetic field  $\vec{B}$ , where  $\hat{H} = -\vec{\mu} \cdot \vec{B}$ , it follows that

$$\frac{d\vec{P}}{dt} = \frac{i\mu}{\hbar} [\vec{\sigma}, \vec{\sigma} \cdot \vec{B}] \quad (2.33)$$

The commutation relations for angular momenta

$$[\hat{\sigma}_i, \hat{\sigma}_j] = 2i\epsilon_{ijk}\hat{\sigma}_k \quad (2.34)$$

lead to

$$\frac{d\vec{P}}{dt} = \frac{d}{dt} \gamma \vec{B} \times \vec{P}. \quad (2.35)$$

The equation of motion describes Larmor precession of the neutron spin around an external magnetic field. The magnitude of the effect is proportional to the magnetic moment  $\mu = \hbar\gamma/2$ .

The Pauli-Schrödinger equation for a neutron in an external magnetic field is written as

$$\hat{H} |\psi\rangle = \hat{E} |\psi\rangle \quad (2.36)$$

with the Hamiltonian  $\hat{H} = -\hbar^2 \vec{\nabla}^2 / (2m) - \vec{\mu} \cdot \vec{B}$ . This eigenvalue problem is discussed further for the example of a specific time-dependent magnetic field in Sec. 3.3.6. The Pauli-Schrödinger equation does not only describe the orientation of the polarisation vector as Eq. (2.32) but also phase information which becomes relevant in an interferometer.

### 2.2.2 Neutron scattering

Free neutrons are scattered by nuclei. In a simplified model, each nucleus is regarded as a solid sphere with a radius characteristic for the specific isotope. If and only if the neutron's centre of mass touches the sphere, scattering takes place through elastic collisions. When using this model, the radii are referred to as scattering lengths  $b$ .

There are the coherent and the spin-dependent incoherent contribution to the scattering length  $b$  such that [66]

$$b = b_{\text{coh}} + \frac{2b_{\text{inc}}}{\sqrt{I(I+1)}} \vec{S} \cdot \vec{I}, \quad (2.37)$$

with the neutron spin  $\vec{S}$  and the nuclear spin  $\vec{I}$ . For a macroscopic body, the nuclear spins are in general randomly oriented such that the average of the incoherent contribution becomes zero. Each incoherent scattering event occurs anyway and causes an isotropic background in scattering experiments, which is the reason for its name [67]. Only in ferromagnets, a long-range magnetic parallel alignment of the nuclear spins emerges, such that the average of the scattering length has an incoherent contribution. If we consider the total angular momentum  $J = I \pm S = I \pm 1/2$ , and substitute the relation [68]

$$\vec{S} \cdot \vec{I} = \frac{1}{2} \sqrt{J(J+1) - I(I+1) - S(S+1)}, \quad (2.38)$$

two results emerge:

$$b_+ = b_{\text{coh}} + b_{\text{inc}} \sqrt{\frac{I}{I+1}} \quad (2.39)$$

$$b_- = b_{\text{coh}} - b_{\text{inc}} \sqrt{\frac{I+1}{I}}. \quad (2.40)$$

Therefore, the magnitude of the incoherent contribution also depends on the relative orientation between the neutron and the nuclear spin.

The scattering and absorption cross-sections,  $\sigma$  and  $\sigma_{\text{abs}}$ , listed in Tab. 2.1 are given by

$$\sigma = \sigma_{\text{coh}} + \sigma_{\text{inc}}, \quad \sigma_{\text{abs}} = \frac{4\pi}{k} \langle \text{Im}\{b\} \rangle, \quad (2.41)$$

with

$$\sigma_{\text{coh}} = 4\pi \langle |b_{\text{coh}}|^2 \rangle \quad \sigma_{\text{inc}} = 4\pi \langle |b_{\text{inc}}|^2 \rangle, \quad (2.42)$$

where  $\langle \cdot \rangle$  is the average over all orientations of neutron and the nuclei.

High absorption cross-sections indicate materials which are suited as absorbers but are unsuited for other purposes; carbohydrates with their  $^1\text{H}$  are to be avoided in a neutron beam especially in a neutron interferometer because of its high incoherent scattering length which causes spin-dependent phase shifts, see Sec. 3.3.4. Air on the other hand with its compounds  $\text{O}_2$ ,  $\text{N}_2$ , and  $\text{Ar}$  only weakly attenuate the neutron beam. Because all beam paths in a perfect crystal neutron interferometer (see Se. 3.3.3) are equally long, the intensity ratios between the paths are unaffected.

## 2 Theory

Table 2.1: Coherent and incoherent scattering lengths  $b_{\text{coh}}$  and  $b_{\text{inc}}$ , coherent, incoherent, and overall scattering cross sections  $\sigma_{\text{coh}}$ ,  $\sigma_{\text{inc}}$ , and  $\sigma$ , respectively, and absorption cross sections  $\sigma_{\text{abs}}$  for thermal neutrons of elements and isotopes relevant in neutron optics, excerpt from [66]. Lengths are given in femtometre (fm), cross-sections in barn, 1 barn = 100 fm<sup>2</sup>. If not specified, the values are valid for the natural isotope ratio. The incoherent measures refer to the spin-dependent contributions. Imaginary parts describe absorption of the neutronic wave in the material. The relations between the measures are given in Eqs. (2.37), (2.41), and (2.42). The scattering lengths and cross-section are roughly constant for thermal neutrons (see Tab. 3.1). The absorption cross-sections follow a  $1/v$  law with the velocity  $v$  and are listed by convention for neutrons with a wavelength  $\lambda = 1.798 \text{ \AA}$ .

element/isotope	$b_{\text{coh}}$	$b_{\text{inc}}$	$\sigma_{\text{coh}}$	$\sigma_{\text{inc}}$	$\sigma$	$\sigma_{\text{abs}}$
<sup>1</sup> H	3.7406	25.274	1.7583	80.27	82.03	0.3326
<sup>2</sup> H	6.671	4.04	5.592	2.05	7.64	0.000519
He	3.26	—	1.34	0	1.34	0.00747
<sup>3</sup> He	5.74–1.483i	–2.5+2.568i	4.42	1.6	6	5333
Li	–1.90	—	0.454	0.92	1.37	70.5
<sup>6</sup> Li	2.00–0.261i	–1.89+0.26i	0.51	0.46	0.97	940
B	5.30–0.213i	—	3.54	1.7	5.24	767
<sup>10</sup> B	–0.1–1.066i	–4.7+1.231i	0.144	3.0	3.1	3835
C	6.6460	—	5.551	0.001	5.551	0.0035
N	9.36	—	11.01	0.50	11.51	1.90
O	5.803	—	4.232	O	4.232	0.00019
Al	3.449	0.256	1.495	0.0082	1.503	0.231
Si	4.1491	—	2.163	0.004	2.167	0.171
Ar	1.909(6)	—	0.458	0.225	0.683	0.675
Ti	–3.438	—	1.485	2.87	4.35	6.09
Fe	9.45	—	11.22	0.4	11.62	2.56
Co	2.49	–6.2	0.779	4.8	5.6	37.18
Ni	10.3	—	13.3	5.2	18.5	4.49
Cu	7.718	—	7.485	0.55	8.03	3.78
Cd	4.87–0.70i	—	3.04	3.46	6.5	2520
In	4.065–0.0539i	—	2.08	0.54	2.62	193.8
Gd	6.5–13.82i	—	29.3	151	180	49700
<sup>235</sup> U	10.47	(+/-)1.3	13.78	0.2	14	680.9
<sup>238</sup> U	8.402	0	8.871	0	8.871	2.68

# Chapter 3

## Neutron Optics

The descriptions of neutron optical devices in this section broadly follow the author's diploma thesis [69], shortened, amended, and extended by additional information.

### 3.1 Neutron Optical Ansatz

The manipulation of light developed as the field of optics. Despite the fundamental differences between light and neutrons, optical principles apply to both of them based on their common wave nature. The duality between wave and particle for massive systems such as the neutron is described by de Broglie's relation [4]

$$\lambda = h/p, \quad (3.1)$$

with the wavelength  $\lambda$  characterising the wave, Planck's constant  $h = 6.626 \times 10^{-34}$  Js/K, and the particle momentum  $p$ . With increased energy or momentum, the wavelength is reduced which pronounces more localised effects such as collisions or absorptions, typically identified with the particle nature.

On the other hand, for interactions with periodic structures, the wavelength of the studied neutrons must be of the same magnitude as the characteristic distance  $a$  between the objects comprising the structure, i.e.

$$\lambda \sim a. \quad (3.2)$$

In the limit of large wavelengths, i.e.

$$\lambda \gg a, \quad (3.3)$$

the structure becomes quasi-continuous in relation to the extent of the wave. A basic example with the latter assumptions is refraction of a wave at an interlayer between two homogeneous media. This condition holds for lenses in light optics. Although lenses are used in neutron optics [70], they are less effective than for light because the respective refraction indices of most materials differ only minutely from 1. Therefore, divergences of the neutron sources are often handled with less effective or more complex [71] means, such as apertures and mirrors. Due to divergences, higher relative losses in intensity occur in neutron optics compared to light optics. Consequently, light optics has a significant statistical advantage in experiments.

For most neutron optical elements presented in this chapter, it holds that

$$\lambda \gtrsim a, \quad (3.4)$$

such that the wave nature of the neutron is pronounced. The detectors, explained at the end of this chapter, work on the exhibited particle nature of neutrons.

The order of neutron optical elements for the presented experiments is: source, aperture, neutron guide, monochromator, spin polariser, interferometer, spin polarisation manipulators, spin analyser, and detector. Their functions and names are, respectively, analogies and copies of their light optical counter-parts such that the term neutron optics is warranted.

## 3.2 Neutron Sources

### 3.2.1 Spallation Sources

Large neutron sources for scientific purposes are working on either nuclear fission or spallation. For the latter spallation, hydrogen is ionised to produce protons. The protons are accelerated and targeted on matter which prompts spallation of the target nuclei into several smaller parts, comprising up to dozens of free neutrons per target nucleus. There are linear accelerators (LinAc) and cyclic accelerators, where cyclic accelerators can in turn be either cyclotrons with spiraling trajectories or synchrotrons with trajectories of fixed radii. The proton beam can be pulsed which makes the following neutron beam pulsed, too. Some experiments have periodic intervals of the order of milliseconds where no neutrons are counted. These experiments can benefit from a pulsed source in their statistics because these intervals do not affect the neutron count as for a continuous source.

Spallation sources can be found at, e.g.: ISIS, United Kingdom, with a combination of a linear accelerator and a synchrotron (LinAc + synchrotron); Spallation Neutron Source (SNS), USA, (LinAc); Japan Proton Accelerator Research Complex (J-PARC), Japan, (LinAc + 2 synchrotrons); and the European Spallation Source (ESS), Sweden, (LinAc), which is presently under construction.

### 3.2.2 Nuclear Reactors

#### Basics in Reactor Physics

For a fission reactor, fuel elements are tightly ordered in a core where some lower initial neutron flux is increased in a chain reaction to a stable higher neutron flux. The reactor type used as a source for this thesis is based on uranium-235 as fuel. Natural uranium has relative abundances of uranium-235 (subsequently U-235 or  $^{235}\text{U}$ ) of 0.72% and of uranium-238 (subsequently U-238 or  $^{238}\text{U}$ ) of 99.275%. The abundances of the isotopes  $^{233}\text{U}$ ,  $^{234}\text{U}$ , and  $^{236}\text{U}$  are negligible for our purposes. The natural abundances can be explained roughly by considering the time evolved from the last supernova in our astronomical region about 4 billion years ago. We consider this to also be the age of our solar system. We assume that for the nucleosynthesis during the supernova all uranium isotopes have the same abundance, which is plausible for large nuclei. No uranium is assumed to be formed after the

## 3.2 Neutron Sources

Table 3.1: Classification of neutrons according to their energy, excerpt from [72].

energy (eV)		velocity (m/s)		neutrons' name
$< 2 \cdot 10^{-5}$		$< 40$		ultra cold
$10^{-5}$	– $5 \cdot 10^{-3}$	40	– $10^3$	cold
$5 \cdot 10^{-3}$	– $5 \cdot 10^{-1}$	$10^3$	– $10^4$	thermal
$5 \cdot 10^{-1}$	– $10^3$	$10^4$	– $4 \cdot 10^5$	epithermal
$10^3$	– $10^5$	$4 \cdot 10^5$	– $4 \cdot 10^6$	intermediate
$10^5$	– $2 \cdot 10^7$	$4 \cdot 10^6$	– $4 \cdot 10^7$	fast
$> 2 \cdot 10^7$		$> 4 \cdot 10^7$		relativistic

supernova. Only the two mentioned isotopes have a half-life  $\tau$  comparable to the age of our solar system, i.e.  $\tau_{\text{U-235}} = 0.7 \times 10^9$  a and  $\tau_{\text{U-238}} = 4.5 \times 10^9$  a. Until now,  $^{238}\text{U}$  underwent less than one half-life while  $^{235}\text{U}$  underwent about 6 half-lives. Therefore,  $^{235}\text{U}$  underwent 5 more half-lives which reduces its absolute abundance to  $1/2^5 = 1/32 \approx 3\%$  of its initial absolute abundance. This reasoning yields an expected relative abundance of  $^{235}\text{U}$  of  $\approx 6\%$  of the total number of uranium nuclei. This model correctly estimates the observed relative abundance of 0.72% today at least within one order of magnitude.

Chemically,  $^{235}\text{U}$  and  $^{238}\text{U}$  are indistinguishable. To enrich  $^{235}\text{U}$  for the presented reactor type, centrifuges are filled with gaseous natural uranium. After fast rotation of the centrifuges, the heavier  $^{238}\text{U}$  is concentrated via the centrifugal force at the outsides and depleted at the axes of the centrifuges. At the same time, the lighter  $^{235}\text{U}$  is depleted outside but enriched at the axes. This process can be repeated with more enriched  $^{235}\text{U}$  and larger centrifugal forces to reach enrichments  $> 90\%$  to fuel high-flux neutron sources such as research reactors and nuclear weapons. Some  $^{238}\text{U}$  will always remain in the compounds enriched with  $^{235}\text{U}$ . When speaking about enriched and depleted uranium without further context, it is meant with regards to  $^{235}\text{U}$ .

Neutrons are referred to according to their kinetic energy and velocity as listed in Tab. 3.1. The isotope  $^{235}\text{U}$  is fissioned by thermal neutrons with a mean kinetic energy  $\bar{E}_{\text{kin}}$  of about  $\bar{E}_{\text{kin, th}} = \frac{3}{2}k_{\text{B}}T_{\text{room}} \approx 25$  meV, with the index “th” for thermalised, the Boltzmann constant  $k_{\text{B}} \approx 8.62 \times 10^{-5}$  eV/K and standard room temperature  $T_{\text{room}} = 295$  K. The fission produces two daughter nuclei of roughly the same size, with a preferred slight asymmetry of the nuclei mass [73]. A mean of  $>2$  free neutrons are produced in each fission. They have a kinetic energy  $E_{\text{kin}}$  of the order of MeV and need to be slowed down to induce further fissions at other  $^{235}\text{U}$  nuclei. The slowing down procedure is called moderation. Moderation is achieved by scattering at other nuclei. Classically, the maximum momentum transfer happens during a frontal or collinear collision which reduces the problem to one dimension. While a residual thermal kinetic energy must remain to induce fission at a  $^{235}\text{U}$  nucleus, the reduction of kinetic energy over 8 orders of magnitude from MeV to 10 meV is close to the case of transferring the entire kinetic energy. The energy transfer  $\Delta E_{\text{kin}}$  during an ideal elastic collision in one dimension, normalised over

### 3 Neutron Optics

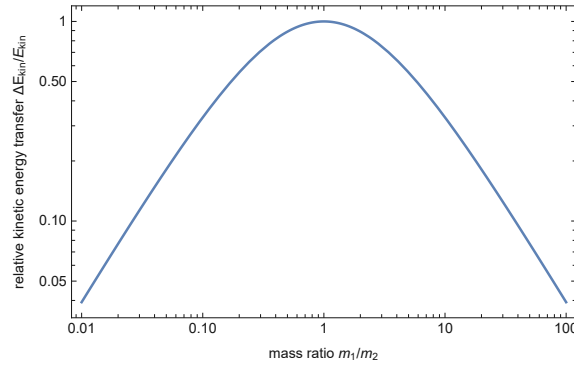


Figure 3.1: Double logarithmic plot of the relative energy transfer in a collinear, ideal elastic collision between two bodies with masses  $m_1$  and  $m_2$ , as given by Eq. (3.5). For equal masses  $m_1 = m_2$  the total kinetic energy is transferred whereas less energy is transferred the more the masses differ.

the initial kinetic energy  $E_{\text{kin}}$ , is written as [74]

$$\frac{\Delta E_{\text{kin}}}{E_{\text{kin}}} = \frac{4m_1m_2}{(m_1 + m_2)^2}, \quad (3.5)$$

with the masses  $m_1$  and  $m_2$  of the two particles scattered at each other. A graph of Eq. (3.5) dependent on the ratio between the masses  $m_1$  and  $m_2$  is plotted in Fig. 3.1. The maximum energy is transferred by scattering at a particle with the same mass. Due to the low density of free neutrons in a reactor, amassing  $^1\text{H}$  nuclei with a relative difference in mass of  $< 10^{-3}$  to neutrons is a possible way to facilitate moderation of fast neutrons. Common moderator materials are hydrogen as in water ( $\text{H}_2\text{O}$ ) and zirconium hydride ( $\text{ZrH}_n$ ) [75], Deuterium as in heavy water ( $^2\text{H}_2\text{O}$ ) and carbon, the latter typically in the form of graphite. Water can at the same time serve both as moderator and as cooling agent. (For power reactors, the cooling is the first step to transfer the energy freed through the fissions to a turbine to convert the thermal into electric energy.) With the assumption of same masses,  $^1\text{H}$  can inherit the entire kinetic energy of a neutron. In three spatial dimensions, frontal collisions are rare. The neutrons will still thermalise after enough scattering processes, meaning the mean kinetic energy of the Maxwell-Boltzmann distribution will be at  $\bar{E}_{\text{kin,th}} \approx 25 \text{ meV}$ . Subsequent fission processes can then be induced which produce the next generation of free neutrons. Some unmoderated, fast neutrons will fission  $^{238}\text{U}$  nuclei remaining in the enriched uranium of the reactor fuel. If each generation  $i$  of thermal neutrons takes a time interval  $t_{\text{gen}}$  to multiply its number by  $\tilde{\kappa}$  for the next generation, it is equivalent to producing a multiple  $\kappa = \tilde{\kappa}/t_{\text{gen}}$  per time unit. A chain reaction is started, whose dynamics are described by the differential relation

$$dN(t) = (\kappa - 1) N(t) dt, \quad (3.6)$$

with the number of free neutrons  $N$ . The parameter  $\kappa$  is characterised into three regimes:

$$\begin{aligned} \kappa &> 1, && \text{super - critical;} \\ \kappa &= 1, && \text{critical;} \\ \kappa &< 1, && \text{sub - critical.} \end{aligned} \quad (3.7)$$

## 3.2 Neutron Sources

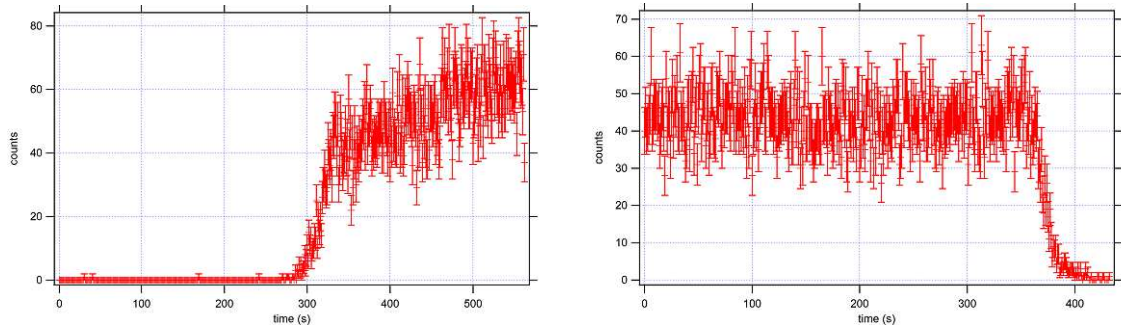


Figure 3.2: Count rate at (a) start-up and (b) shut-down over time. Before the start-up, the mean count rate is close to zero. Electronic noise of the detection system is the dominant reason for the few detection events. During the start-up, an exponential growth of the count rate is observed. This is characterised with a parameter  $\kappa > 1$ . When the count rate is stabilised,  $\kappa = 1$ . The sudden increase by about 10% in the stable neutron count rate at 450 s in sub-figure (a) is explained by the activated guide field (see Sec. 3.3.6). During the shut down, the count rate reduces exponentially with  $\kappa < 1$ . Error bars indicate one standard deviation.

The neutron balance for following generations of neutrons is a crucial parameter for fission processes. After integration of Eq. (3.6), the total number of free neutrons follows as the exponential relation

$$N(t) = N(0) e^{(\kappa-1)t}. \quad (3.8)$$

In a super-critical process, the number of fission processes is increased with each generation which holds during the build-up of a nuclear explosion and while starting up a reactor; in a critical process, the number of fission processes is constant over time, which characterises stable reactor operation. This equilibrium state is called criticality. The time of constant free neutron flux during a reactor shut-down is not critical because the neutron density is dominated by spontaneous neutron emissions outside of chain reactions; in a sub-critical process, the number of fission processes is reduced with each generation. The latter holds during the shut-down of a reactor and after the peak energy discharge in a fission explosion. Examples for the three regimes are depicted in Fig. 3.2 via the neutron count rate at a reactor outlet.

During stable reactor operation, the rate of newly produced neutrons balances all the losses. The balance is regulated by moderators, absorbers and reflectors. Absorbers capture free neutrons without subsequently emitting any neutrons. The latter reflectors are placed around the reactor core composed of materials which are good scatterers and can potentially change the direction of the free neutrons back to the reactor core. The scattering is in principle the same as necessary for moderation because a change in direction is related to a momentum or, indirectly, to an energy transfer. Affordable graphite is widely used for reflectors. Reflectors and moderators are passive elements in a reactor, whereas absorber rods are actively regulated in their position in the reactor. For a start-up, absorbers are withdrawn from the reactor core to allow super-criticality. For the criticality necessary for stable reactor operation, an absorber rod is moved partly into the reactor again. During operation, small fluctuations of the neutron flux are smoothed out by moving an absorber rod

in and out by a few millimeters or centimeters.

At the start-up of a nuclear reactor, a stable neutron flux at a low level is elevated to a stable higher level. In case of a first start-up of a reactor or after a long shut-down, the initial flux of the fuel rods is too low for secure operation of the reactor, due to the large half-lives of both considered uranium isotopes. A sufficient neutron flux is then provided by a secondary neutron source, such as a Sb-Be (antimony-beryllium) photoneutron source. Therein, the unstable isotope  $^{124}\text{Sb}$  emits photons with an energy of 1.69 MeV. The photons can excite  $^9\text{Be}$  with its close enough transition energy of 1.67 MeV. Subsequently, a decay with emission of a free neutron with 14 keV kinetic energy occurs. For activated fuel rods and shut-down periods below 1 year, the activity of the fuel elements suffices for a high enough neutron flux to securely monitor the start-up procedure which is imperative for civil use of the reactor technology.

#### Specific Reactor Properties

Both nuclear reactors used by the author for experiments use  $^{235}\text{U}$  as a fuel and are of the swimming pool type. The latter means that one can see the reactor core from the top through water. The high-flux reactor at the Institute Laue-Langevin in Grenoble, France, was used as a neutron source for the presented experiments [76]. The reactor has a thermal power of  $\approx 60$  MW and a maximum neutron flux of  $1.5 \times 10^{15} \text{ cm}^{-2} \text{ s}^{-1}$  during each operation cycle of several weeks. For each cycle, a new highly enriched fuel element is burnt until the density of  $^{235}\text{U}$  nuclei is too low to maintain criticality. The fuel elements can be recycled in a reprocessing plant such as in La Hague.

The Vienna University of Technology (TU Wien) possesses the TRIGA (Training, Research, Isotopes production, General Atomics) Mark II reactor at the Atom-institut [77]. This reactor has a thermal power of 250 kW and maximum neutron flux of  $10^{13} \text{ cm}^{-2} \text{ s}^{-1}$ . Two specific security features of the TRIGA reactor type are worth mentioning. Firstly, the water between the fuel elements does not provide enough moderation for criticality. The second moderator is hydrogen chemically bound in zirconium hydride mixed to the uranium in the fuel elements. The moderation rate provided by the zirconium compound raises the sub-criticality of the chain reaction to a critical or super-critical level during the start-up of the reactor. Furthermore, the hydrogen atoms in the zirconium compound have a temperature dependent probability of scattering the fast neutrons produced by the uranium fissions. For higher temperatures, the moderation is reduced as described by a negative temperature coefficient of the moderation rate. In effect, if the reactor power is increasing beyond the stipulated power, the heat is not diverted, and the reactor temperature increases such that moderation decreases. Hence, the chain reaction breaks down. This is called an intrinsic reactor security feature because it works on physical principles and without human intervention.

Secondly, the time dynamics of the chain reaction can be roughly split into two contributions. One is based on prompt neutrons which are moderated right after the fission process. The other is due to delayed neutrons. It was stated earlier that the fission produces two daughter nuclei. These are most oftenly unstable themselves and decay in some cases through neutron emission. However, the half-lives can be much larger than the mean moderation time and therefore delay the

next step in the chain reaction. The vast majority of the neutrons in a TRIGA Mark II are prompt neutrons which are moderated by the zirconium compound in the fuel rods. But the prompt neutrons are not enough to elevate the neutron balance per generation above the critical level. Only with the contribution of the delayed neutrons, super-criticality is reached inside the reactor. This lengthens the reactor period during which the reactor power doubles (or rises by a factor of  $e$  with a different definition). The lengthening serves as security feature in that there is a time buffer from a sensor signal which indicates a necessary change in the regulation of the reactor to the result of an adjustment in the position of the absorber rods in the reactor.

The combination of negative temperature coefficient of the moderation and domination of the chain reaction by prompt neutrons can be actively used for reactor pulses as explained in the following. By quickly pushing the absorber rods out of the reactor with pressured air, the neutron balance per generation is suddenly and drastically increased. Because in this case the process is super-critical even without delayed neutrons, each neutron generation can be characterised with a time interval of the order of  $1\mu\text{s}$ . An exponential rise in reactor power up to several MW during a time interval of about 10 ms is then observed until the rising moderator temperature as suddenly reduces the moderation rate and the chain reaction collapses. Because the drastic temperature changes procedure mechanical stress on the fuel elements, such reactor pulses necessitate a cool-down time after each pulse. The resting times after each pulse are such that the use of successive reactor pulses do not increase the mean reactor power compared to a stable operation at 250 kW.

The difference of the two described reactors in power between 60 MW for Grenoble and 250 kW for Vienna is the reason why the presented experiments in polarised neutron interferometry are realised in Grenoble. The power is roughly proportional to the neutron flux at the experiment and therefore the counting statistics. Each experiment necessitates some magnitude in the number of neutrons to achieve a reliable level in the counting statistics. This number of neutrons must undergo the experiment under stable conditions. There are several steps of filtering in the experiment as described in Sec. 3.3. For the neutron interferometer station at the reactor in Grenoble, this time ranges over weeks with single interferograms recorded over single hours. As will be explained in a later section, the temperature stability of the interferometer is aimed to be in the range of  $\Delta T \approx 0.01\text{ K}$ . In Vienna, the time frame for the same counting statistics would be in the range of weeks. Constructing a control system stabilising the temperature over these time frames at a smaller reactor is complex and laborious. This was not done so far.

A peripheral but aesthetically pleasant feature of swimming pool reactors is the Cherenkov radiation. Parts of it are perceived by humans as blue light from the reactor core, see Fig. 3.3. The blue light is produced in the interaction of fast electrically charged particles in the electromagnetic fields of water molecules. Small mass particles are easier accelerated. In the case of Cherenkov radiation in a reactor, the charged particles are typically electrons and positrons from  $\beta$  decays of unstable daughter nuclei of the fissioned  $^{235}\text{U}$  nuclei. Kinetic energy of the charged particles is dissipated in the form of light, one photon after another. The light waves irradiate concentrically around their creation points which are around the approximately

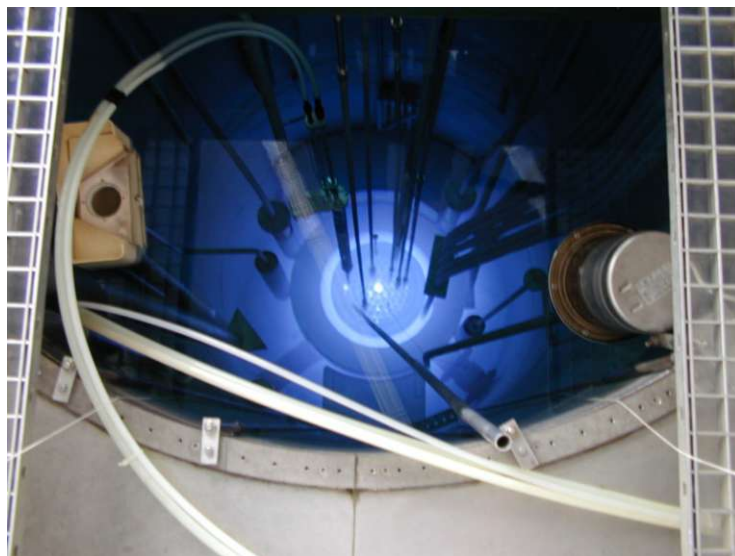


Figure 3.3: The view from top into the TRIGA nuclear reactor of swimming pool type at Atominstitut with the reactor core on the bottom. The fission process produces fast charged particles. In their interaction with water molecules, Cherenkov radiation is emitted. The blue light is the visible part of the spectrum. The directions with highest intensity are those volumes flooded with water in combination with the highest flux of charged particles, which is practically equivalent here to a high neutron flux. The centre of the core is not equipped with a fuel element and has the highest neutrons flux of  $\approx 10^{13} \text{ cm}^{-2} \text{ s}^{-1}$ . Water serves as shielding against the higher energy light. The height of the water column of the swimming pool is calculated such that exposure at the site of the photo conforms with the allowed legal threshold for the dose of ionising radiation.

linear trajectories of the charged particles. If a particle is faster than the speed of light in the medium  $\tilde{c}$ , the excited waves superpose to a conical wavefront with its tip at the present location of the particle as depicted in Fig. 3.4. This is similar to a sonic boom with a Mach cone for supersonic acoustical sources. The angle  $\beta$  of the cone is given by the velocity of a particle  $v$  via  $\sin \beta = v/\tilde{c}$  with  $\tilde{c} < v$ .

### Societal Aspects

Construction of the TRIGA reactor at Atominstitut was supported by the United States of America (USA). Its then president Dwight D. Eisenhower started the “Atoms for Peace” initiative. The initiative also stimulated the “Treaty on the Non-Proliferation of Nuclear Weapons” to control the proliferation of fissionable material with the long term goal of the disarmament of all nuclear weapons [78]. Besides dozens of lowly enriched fuel elements, a few with high enrichments  $> 90\%$  were delivered by the USA. According to contract, the USA took the fuel elements back when they were burnt out, i.e. the density of  $^{235}\text{U}$  became too low. The subsequently delivered fuel elements were enriched to 19.8%. This level is just below the defined threshold to highly enriched uranium of 20%. This is caused by changes in US policy which now prohibit the delivery of highly enriched uranium. The present fuel elements will burn out faster due to the lower enrichment.

### 3.2 Neutron Sources

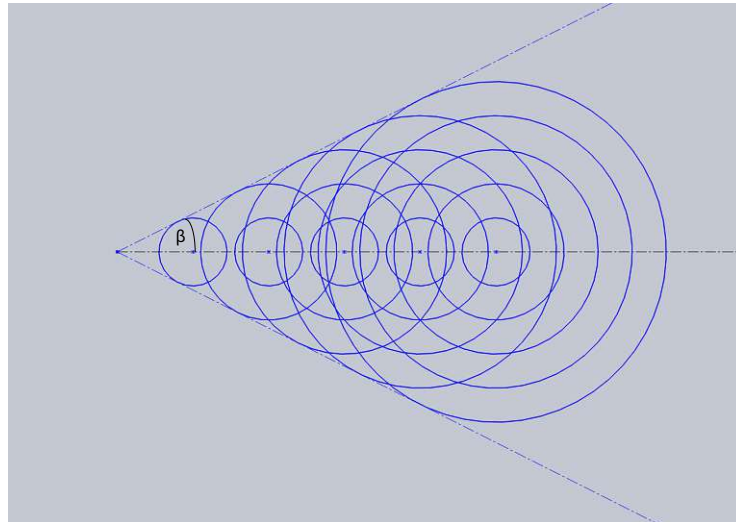


Figure 3.4: Geometrical construction of the Mach cone emerging from a fast charged particle emitting light in a medium such as water. The equidistant point sources can be assumed to excite light at equal intervals if the photon energy is much smaller than the kinetic energy of the charged particle,  $hf \ll E_{\text{kin}}$ . The wavefronts overlap to a cone with angle  $\beta$ , with  $\tan \beta = c/v$  and  $c < v$ .

The supervision of nuclear waste produced in nuclear technology is problematic. The half-lives of uranium and many isotopes produced by nuclear reactors exceed the human lifetime by orders of magnitude. During these time frames, the health of humankind and environmental hazards have to be limited. It can be argued that the effort of supervision outweighs the benefits, that our society will forget about the danger of nuclear waste repositories over time or that our present society could collapse such that accurate handling of nuclear waste is not possible. One approach to circumvent the reliance on permanent human oversight is to use deep geological repositories. However, all candidates for storage deemed safe in the past, such as salt mines and granite formations, have in the meantime revealed other and bigger problems than assumed a couple of decades ago.

For Austria and the TRIGA reactor of TU Wien, the suppliers of the fuel rods are the USA. Austrian law demands that no fuel rods are disposed in the country [79]. Therefore, the USA did and will take back the burnt out fuel elements such that no final nuclear waste management for these excessively demanding fuel rods is necessary in Austria. However, the surroundings of the Austrian reactors and other medical and industrial sources produce nuclear waste. Up until now, more than 350 000 t of nuclear waste are stored in Austria's temporary repository in Seibersdorf, Niederösterreich [80]. While some of the nuclear waste quickly decreases its activity below the stipulated threshold and can be treated as toxic waste, Austria will also have to find a way to handle nuclear waste within its borders longterm.

Reactor technology as a whole is closely intertwined with military purposes. A main motive for political support of the pressurised light water reactor was its military use to propel nuclear submarines with their tight volume restrictions during the cold war [81]. This support disadvantaged alternative reactor types such as those with thorium based fuel. This reactor type is claimed to produce nuclear waste with shorter half-lives while also being able to use waste from uranium based reactors

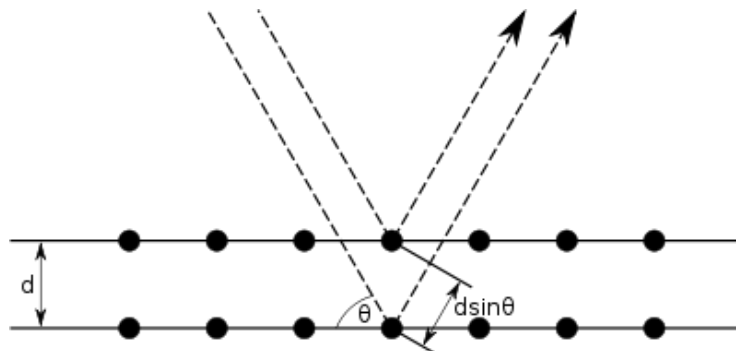


Figure 3.5: Geometric construction of the Bragg condition for reflection of a monochromatic incident wave at a crystal lattice. If all partial waves reflected are displaced by a multiple of the wavelength  $n\lambda$ , they interfere constructively. Constructive interference is conditioned on Bragg's law of Eq. (3.9) which relates the incidence angle  $\theta$ , the wavelength  $\lambda$ , and the lattice distance  $d$ .

as fuel. However, thorium based reactors come with their own waste problems such that a sustainable handling of nuclear technology seems out of reach at the moment [82]. The spallation sources mentioned in Sec. 3.2.1 also produce nuclear waste, albeit lower amounts with lower half-lives. It is therefore questionable if state-of-the-art nuclear technology producing such waste should be applied at all.

On the other hand, one can argue like the physicist David Deutsch [83]: as long as we breed a society in which solving problems is encouraged, humankind will increase its means more than the problems from previous levels of development can require to solve. This resembles the generation contract used figuratively in social security systems such as the pension system. It is debatable, whether the economic and scientific progress through nuclear technology warrants the undetermined burden of nuclear waste over an unknown number of generations. As scientists, we can only hope that the waste produced in our investigations is justified in light of human curiosity.

### 3.3 Manipulation of and Interaction with Neutrons

Each source has some basic characteristics concerning the properties of the emitted neutrons. Dependent on its geometry, every reactor is to some degree isotropic. For the presented reactor type, a thermalised spectrum of the neutron's wavelength distribution is achieved through moderation as described in Sec. 3.2.2. Any further selection and manipulation of properties conducted in the presented experiments is described in the following.

#### 3.3.1 Monochromator

In analogy to light optics, the term monochromatising refers to selecting a wavelength out of a spectrum with a continuous wavelength distribution. Sapphire and bismuth crystals can filter fast neutrons out of the spectrum [84]. Crystals can be

used as monochromators. Their function is based on the regularity of the crystal structure such that an atomic core is assumed to oscillate around each lattice site. The lattice sites can be grouped in sets of parallel and equidistant lattice planes, as indicated in Fig. 3.5. (In the depicted case, the lattice planes are in parallel to the surface of the crystal such that Bragg diffraction occurs. The case of Laue diffraction is regarded in Sec. 3.3.3.) The atomic cores act as scattering centres, which can be treated as a Fermi pseudo-potential as written in Eq. (3.22) in context of the polarising supermirror in Sec. 3.3.2. The difference in optical density  $\Delta n$  between the crystal and the outside medium of air or vacuum is assumed to be small,  $\Delta n \ll 1$ , as is common for neutrons. (This is connected to the magnitude of the scattering lengths as described below.) At incidence of a wave, each scattering centre produces a partial wave of spherical shape. In the reflected direction, the partial wave scattered at the first lattice plane has a longitudinal displacement compared to the partial wave scattered by the second lattice plane. For the third lattice plane, the displacement is doubled and so on. The displacement depends on the incidence angle  $\theta$ , the wavelength  $\lambda$ , and the layer distance  $d_{hkl}$  with the respective Miller indices  $h, k$ , and  $l$  specifying the orientation of the considered lattice plains. If all scattered partial waves are longitudinally displaced by a multiple of the wavelength, constructive interference between the partial waves occurs; a wave front in the reflected direction emerges. This case is conditioned by Bragg's law,

$$n\lambda = 2d_{hkl} \sin \theta, \quad (3.9)$$

with  $n \in \mathbb{N}$ . A geometric construction for this condition is depicted in Fig. 3.5.

In directions of the so-called grazing angle  $\theta$  satisfying the condition, an intense reflection occurs in the direction of the output angle being the same as the incidence angle. The displacement in length of  $n\lambda$  is equivalent to a phase shift by  $2\pi n$ . The Bragg condition is always satisfied by a set of harmonics, given by varying  $n$ . Therefore, a strict separation of a single wavelength is only possible if the initial spectrum from the source emits only one harmonic in the set. This is not the case for the continuous neutron spectrum from a reactor which is a thermal Maxwell-Boltzmann distribution. The first harmonic has the largest wavelength and the higher harmonics have fractions  $1/n$  of this wavelength. The higher harmonics have the same spatial displacements in the reflected direction but multiples of the phase shifts.

In other directions than the grazing angle, the scattered partial wave from a specific scattering centre always has a  $\pi$ -shifted counter-part in the form of another partial wave scattered at some other scattering centre in the crystal. An according second scattering centre is expected if the crystal is large in size such that the number of scattering centres is high. The superposition of both partial waves yields to destructive interference. Therefore, a finite intensity is only observable at exiting angles being the same as the incident angle and if the Bragg condition is fulfilled. The quantisation of the elements in the crystal structure leads to discrete solutions to the Bragg condition.

For the perfect crystal silicon monochromator at the instrument S18, the lattice is cubic face-centred as in diamonds. The lattice parameter is  $a = 5.43 \text{ \AA}$ . The layer distance is calculated as  $d_{(hkl)} = a/\sqrt{h^2 + k^2 + l^2}$ . With the (220) plain used for monochromatising the neutron beam, this results in a layer distance  $d_{(220)} \approx$

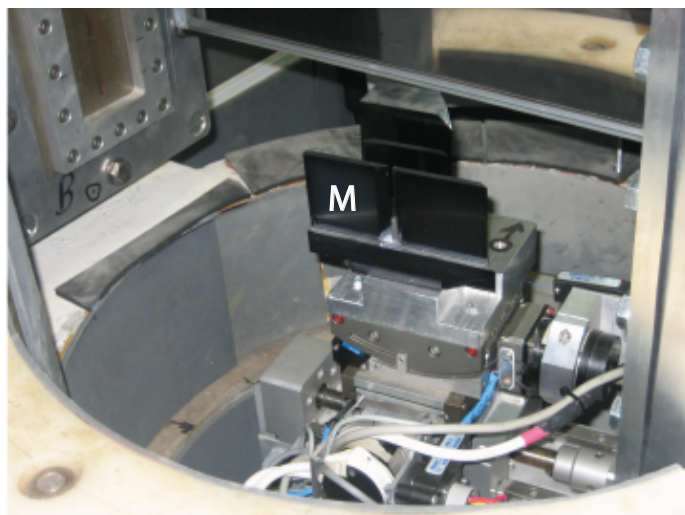


Figure 3.6: Photo of the monochromator used at instrument S18 of the Institut Laue-Langevin in Grenoble, France. A single crystal silicon ingot is cut, etched, and oriented such that incoming neutrons with a wavelength of  $1.92 \text{ \AA}$  are reflected at the (220) lattice planes. Neutrons with the selected wavelength traverse a three-fold reflection; one of the three mirrors is indicated as M. The lattice planes are parallel to the surface of the crystal such that Bragg reflection occurs. Each reflection further sharpens the monochromatised spectrum. The unreflected part of the spectrum propagates to the subsequent instruments D23 and IN22 at the same neutron guide. Those instruments utilise different wavelengths of the remaining neutron spectrum for condensed matter neutron scattering experiments in high magnetic fields with two and three axes, respectively.

$1.92 \text{ \AA}$ , as experimentally confirmed in [85, 86]. The incidence angle is chosen as  $\theta = 30^\circ$ . The first harmonic is thus calculated as  $\lambda \approx 2 \cdot 1.92 \text{ \AA} \cdot \sin 30^\circ = 1.92 \text{ \AA}$ . This is reasonably close to the maximum of the thermal wavelength distribution such that the reflected beam has a high flux. The higher harmonics have a lower probability density in the initial Maxwell-Boltzmann distribution and can often be neglected. Because of the high neutron flux at the ILL, a monochromator with three-fold reflection as depicted in Fig. 3.6 is utilised. For a specific orientation of the crystal to the neutron beam from the reactor, the wave with  $\lambda = 1.92 \text{ \AA}$  is reflected at three different plates before traversing towards the neutron interferometer. At each reflection, the spectrum is multiplied with the reflectivity  $R(\theta, \lambda)$  which has pronounced Gaussian maxima when the Bragg condition is fulfilled. The three reflections further sharpen the maxima in the reflected wavelength distribution. The beam transmitted through the first plate of the monochromator propagates to the subsequent instruments D23 and IN22 which are located downstream at the same neutron guide. Those instruments utilise different wavelengths in the remaining neutron spectrum for condensed matter neutron scattering experiments in high magnetic fields with two and three axes, respectively.

Mosaic monochromators consist of many small grains—each one a perfect crystal with a small variance in orientation between them. Due to the variance, an incident wave not fulfilling the Bragg condition at one crystal grain propagates to the next grain with a different orientation. This implies an additional chance of reflection

towards the experiment dependent on the spread in orientations, called mosaicity [87]. The probability of reflection for the neutrons in the incident divergent beam is increased compared to a single perfect crystal. Because a reflected neutron wave may traverse a high number of grains before reflection towards the experiment, further reflections away from the experiment may occur. Only an odd number of reflections increases the intensity at the experiment. The higher acceptance range in the incident angle for Bragg reflection towards an experiment trades a higher neutron flux off for a broader peak in the neutron spectrum. A trade-off for a higher intensity is often preferred at smaller reactors with their lower neutron fluxes. At the TRIGA reactor of Atomintstitut, graphite mosaic crystals [88] monochromatise the neutron beams.

#### 3.3.2 Spin Polarisers

An unpolarised neutron beam is described as a mixed state with the density operator

$$\hat{\rho} = \sum_i p_i |\psi_i\rangle \langle\psi_i| = \frac{1}{2} (|\uparrow\rangle \langle\uparrow| + |\downarrow\rangle \langle\downarrow|), \quad (3.10)$$

with the probabilities  $p_i$ . Two devices used are presented which select a specific spin state.

#### Magnetic Prism

For light, a dispersive prism is composed of a material with a wavelength-dependent index of refraction. Different colours of an incident beam are separated or dispersed. Analogously, a magnetic field introduces a neutron to a spin-dependent potential which can act as a dispersive prism by separating the two spin components. The potential of the medium will be treated in two ways: through forces applied to the particles in gradient fields and through the refraction of the waves at the interlayers between the media. The magnetic field is assumed to be static and oriented in  $+z$ -direction, perpendicular to the incident direction.

One way of describing the effect is to consider the forces on the single particles produced at the transitions of the potential caused by the magnetic field. The potential of a magnetic moment in a magnetic field is written as  $V(\vec{r}) = -\vec{\mu}(\vec{r}) \cdot \vec{B}(\vec{r})$ . The relation between magnetic moment and spin is described in Sec. 2.2.1. We will assume a constant orientation of the magnetic moment. The latter holds because the magnetic field in  $z$ -direction defines the quantisation axis, such that each spin component is either parallel or anti-parallel to the magnetic field; the magnetic moments are separated without Larmor precession of the spin as introduced in Sec. 2.2.1. Due to the stated assumptions, the force on the particle follows as

$$\vec{F}(\vec{r}) = -\vec{\nabla}V(\vec{r}) = \vec{\nabla} \left( \vec{\mu}(\vec{r}) \cdot \vec{B}(\vec{r}) \right) = \vec{\nabla} \mu_z(\vec{r}) B_z(\vec{r}) = \mu_z \vec{\nabla} B_z(\vec{r}). \quad (3.11)$$

The field direction determines which spin components are separated. The direction of the gradient determines in which direction the spin components are separated. If we further assume constant magnetic fields in and outside the magnetic prism, the gradient of the potential is only non-zero at the transitions. If the transitions

are abrupt, the gradients can be considered to be Dirac delta functions. It follows that the trajectories are linear in the constant fields but bent or diverted when entering and exiting the magnetic prism. The force is oriented in opposite directions dependent on the magnetic spin quantum number  $m_S$  which implies the sign of  $\mu_z$ . The directions of the linear trajectories are spin dependent and a divergence between the spin components is produced. We define the momentary direction of propagation as the  $y$ -direction. The remaining  $x$ -direction is perpendicular to both  $y$ - and  $z$ -direction, composing a right-handed trihedron.

The tangential force  $\vec{F}_{\parallel}$ , changing the velocity, is expressed through the gradient in  $y$ -direction as

$$\vec{F}_{\parallel} = \mu_z \frac{\partial B_z}{\partial y}. \quad (3.12)$$

Spatial integration of the latter force through the transition will always give the same change in momentum, independent of both the incident direction and the suddenness of the transition.

We can attribute the force  $\vec{F}_{\perp}$ , perpendicular to the trajectory, to the field gradient in  $x$ -direction,

$$\vec{F}_{\perp} = \mu_z \frac{\partial B_z}{\partial x}. \quad (3.13)$$

If we assume the potential to be small compared to the initial energy  $E_0$ , i.e.  $E_0 \gg |\vec{\mu} \cdot \vec{B}|$ , the particle will not be reflected but always refracted by the magnetic field. The gradient in Eq. (3.13) is zero for incidence perpendicular to the boundary of the magnetic region. The flatter the incidence is on the boundary, the longer the force is present and the stronger the force is, producing a larger diversion after the interlayer. This is the case for entering as well as exiting the prism. A smaller incidence angle does not necessarily result in a larger divergence angle when leaving the prism, because refraction also occurs when exiting the prism.

A magnetic field can also be regarded as a medium with spin-dependent index of refraction  $n_{\uparrow\downarrow}$ . We derive  $n_{\uparrow\downarrow}$  from the kinetic energy of the neutron in the medium, written as  $E'_{\text{kin},\uparrow\downarrow} = E_0 \mp \mu B$ . The negative sign describes the kinetic energy of the up spin component, the positive sign of the down spin component. The wave number  $k_{\uparrow\downarrow}$  is related to the particle momentum  $p$  by

$$\vec{p}_{\uparrow\downarrow} = \hbar \vec{k}_{\uparrow\downarrow} \Rightarrow k_{\uparrow\downarrow} = |\vec{k}_{\uparrow\downarrow}| = |\vec{p}_{\uparrow\downarrow}/\hbar|. \quad (3.14)$$

(Alternatively, the Schrödinger equation, as applied on the supermirror in the next section, gives the wave number.) With  $E_{\text{kin},\uparrow\downarrow} = p_{\uparrow\downarrow}^2/(2m)$ , Eq. (3.14) results in the index of refraction (the inverse for light)

$$n_{\uparrow\downarrow} = \frac{k_{\uparrow\downarrow}}{k_0} = \frac{\sqrt{2m(E_0 \mp \mu B)}}{\sqrt{2mE_0}} = \sqrt{1 \mp \frac{\mu B}{E_0}}, \quad (3.15)$$

where the field as a medium is denser for the down spin state.

A geometric construction of the polarised beam paths valid for both particle and the following wave picture is depicted in Fig. 3.7. The generated angle of divergence

### 3.3 Manipulation of and Interaction with Neutrons

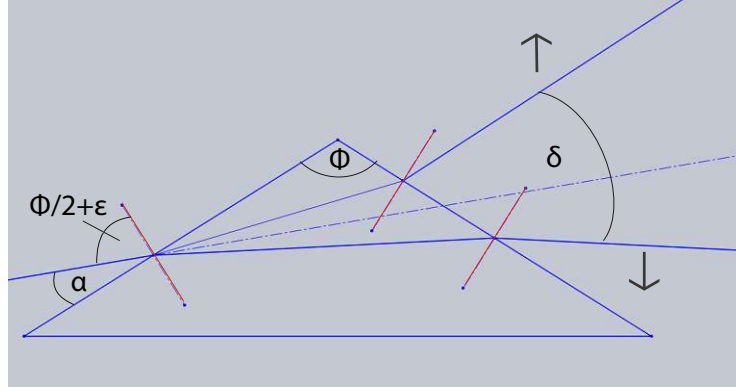


Figure 3.7: Construction of the beam paths of the two spin components of a neutron through a magnetic prism. A magnetic field is present in a volume with a triangular base. The magnetic field causes a spin-dependent potential. The two spin components of the neutrons traversing the field are refracted differently, resulting in a divergence between the polarised sub-beams. The incidence direction is marked by the dashed line. The divergence angle  $\delta$  between two polarised sub-beams is dependent on the apex angle  $\phi$  and the asymmetric angle  $\epsilon$  related to the incidence angle  $\alpha$  as expressed in Eqs. (3.17) and (3.16).

$\delta$  was presented in [89] as

$$\delta = \frac{2\mu B}{E_0} \frac{\sin \phi}{\cos \phi + \cos 2\epsilon}, \quad (3.16)$$

with the apex angle  $\phi$ , the asymmetric angle  $\epsilon$ , the magnetic field strength  $B$  and the initial kinetic energy of the neutron  $E_0$ . With the angle  $\alpha := \pi - (\phi/2 + \epsilon)$  between incident direction and interlayer, Eq. (3.16) is rewritten as

$$\delta = \frac{2\mu B}{E_0} \frac{\sin \phi}{\cos \phi - \cos(\phi + 2\alpha)}. \quad (3.17)$$

The divergence angle  $\delta$  dependent on the angles  $\phi$  and  $\alpha$  is plotted in radians in Fig. 3.8(a). The divergence for the apex angle  $\phi = 118^\circ \hat{=} 2.025$  rad is plotted in Fig. 3.8(b). The plotted region is divided by a pole line at  $\phi + \alpha = \pi$  where  $\delta \rightarrow \pm\infty$ . The assumption of the model assumes refraction at the two interlayers defining the angle  $\phi$ . However, at the pole line, at least one of the polarised sub-beams traverses through the prism without intersecting the second interlayer. The region in Fig. 3.8 given by  $\phi + \alpha \geq \pi$  represents an unphysical solution to Eq. (3.17).

The magnetic prisms installed at instrument S18 are magnetic yokes as depicted in Fig. 3.9. A slit of about 1 cm allows the transmission of the neutron beam through a volume with a strong magnetic field of about 1 T. Significantly higher magnetic fields can only be achieved through superconductors. With the apex angle  $\phi = 116^\circ$  (assumed for Fig. 3.8(b)), an asymmetric angle  $\epsilon = 25^\circ$ , a magnetic field strength  $B = 0.88$  T and a neutron wavelength of  $1.895 \text{ \AA}$  determining the energy, the maximum divergence for two prisms is calculated to  $2.4 \times 10^{-3} \text{ } \hat{=} 4$  mrad. This is the doubled divergence as for one prism and assumes a large distance between the prisms such that the stray fields do not overlap.

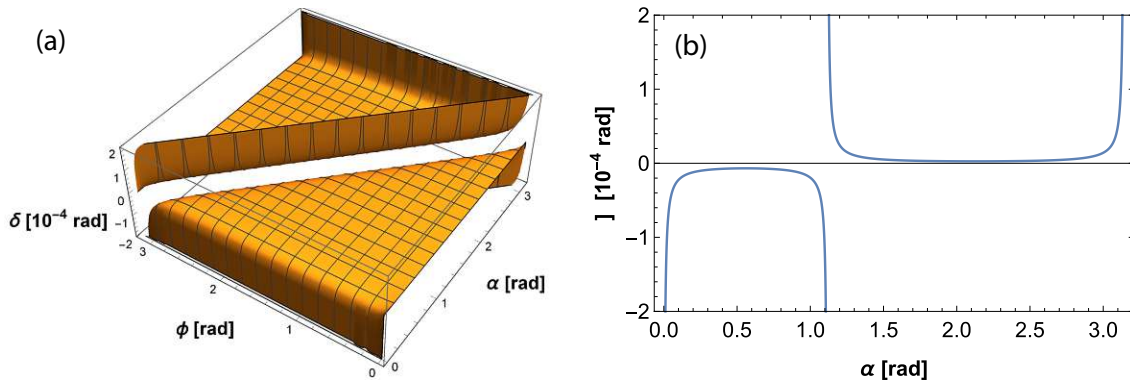


Figure 3.8: The divergence angle  $\delta$  between the polarised sub-beams exiting the magnetic prism (a) dependent on the apex angle  $\phi$  of the prism and the angle  $\alpha$  between incident beam and the first interlayer. The plot is split in two regions by a pole line at  $\phi + \alpha = \pi$ . For higher angles  $\phi$  and  $\alpha$ , at least one of the sub-beams does not intersect the second interlayer; the assumptions of the model brake down, such that Eq. (3.17) does not apply. For the region  $\phi + \alpha \leq \pi$ , the divergence angle  $\delta$  goes  $-\infty$  in the limits of  $\alpha \rightarrow 0_+$  and  $\alpha \rightarrow \phi_-$ . The indices  $\pm$  indicate if the limit is approached from higher (+) or lower (-) values. The first case represents almost parallel incidence relative to the first interlayer of the prism, the second case relative to the second interlayer. For better readability, the depicted range of divergence angles is smaller than the experimental value of 4 mrad. (b) The divergence angle  $\delta$  dependent on  $\alpha$  for  $\phi = 116^\circ \hat{=} 2.02$  rad.

In an experimental adjustment, there are in principle two optimal angles for a high divergence angle  $\delta$ :  $\alpha \rightarrow 0_+$  and  $\alpha \rightarrow \phi_-$ . In practice, the prior is found easier. A recording with two successive prisms of an experimentally large divergence of  $1.2 \times 10^{-3}$  degree is depicted in Fig. 3.10. Although the angle  $\delta$  diverges in the limit  $\alpha \rightarrow 0_+$ , the experimental maximum is much smaller. This can be attributed to a finite beam cross-section which can only fully traverse the prism with a minimum incident angle  $\alpha_{\min}$ . Another reason is the initial divergence which entails a range of incident angles  $\alpha$ .

It is noteworthy that these rather small divergence angles caused by a magnetic prism of the order of mrad are suitable for subsequent perfect crystal neutron interferometer experiments, because the perfect crystal allows the discrimination of such angles due to the even smaller acceptance angle of the Si perfect crystal. This is explained in Sec. 3.3.3.

### Polarising Supermirror

A basic experimental parameter is the neutron flux at a setup. The further an instrument is from the source, the lower the neutron flux will generally be due to the spatial dilution of free neutrons. A neutron guide [90] can channel the neutrons from an outlet to an experiment and maintain the flux. We will follow the historical development from neutron guides to multilayers [91], supermirrors and finally polarising supermirrors [92]. All those devices are based on the processes at incidence of the neutronic wave on an interlayer between two media. The relevant



Figure 3.9: Photo of the two magnetic prisms installed at the neutron interferometer station S18 at the Institut Laue-Langevin in Grenoble, France. The adjustment by hand gives an impression of the sizes. The prisms are magnetic yokes with slits at the height of the neutron beam. The magnetic field inside these slits has a field strength of about 1 T. The two spin components of the neutrons traversing the slits are refracted differently, resulting in a divergence between the polarised sub-beams as depicted in Fig. 3.7.

time-independent Schrödinger equation is written as

$$\begin{aligned}
 \hat{H}\psi(\vec{r}) &= E\psi(\vec{r}) \\
 \left(-\frac{\hbar^2}{2m}\vec{\nabla}^2 + V(\vec{r})\right)\psi(\vec{r}) &= E\psi(\vec{r}) \\
 \Rightarrow 0 &= \left(\vec{\nabla}^2 + \frac{2m}{\hbar^2}(E - V(\vec{r}))\right)\psi(\vec{r}) \\
 0 &= \left(\vec{\nabla}^2 + k^2(\vec{r})\right)\psi(\vec{r}).
 \end{aligned} \tag{3.18}$$

First, we constrain ourselves to the transition from vacuum to some homogeneous medium. The interlayer is assumed to be at  $z = 0$  such that  $V(z \geq 0) = 0$  and  $V(z < 0) = V$ . Because of this geometry, the wavefunction is separable into the parallel and orthogonal components,  $\psi(\vec{r}) = \psi_{\parallel}(x, y)\psi_{\perp}(z)$ . The free wave solution to  $\psi_{\parallel}(x, y)$  is  $\sim e^{-i(k_x x + k_y y)}$ . The remaining function  $\psi_{\perp}(z)$  takes the potential into account and is the solution to the one-dimensional Schrödinger equation

$$0 = \left(\frac{\partial^2}{\partial z^2} + k_{\perp}^2(z)\right)\psi_{\perp}(z). \tag{3.19}$$

The initial wave numbers in vacuum and in the medium with indices 0 and V, respectively, are written as

$$k_{0,\perp} = \frac{\sqrt{2mE_{\perp}}}{\hbar}, \quad k_{V,\perp} = \frac{\sqrt{2m(E_{\perp} - V)}}{\hbar}. \tag{3.20}$$

### 3 Neutron Optics

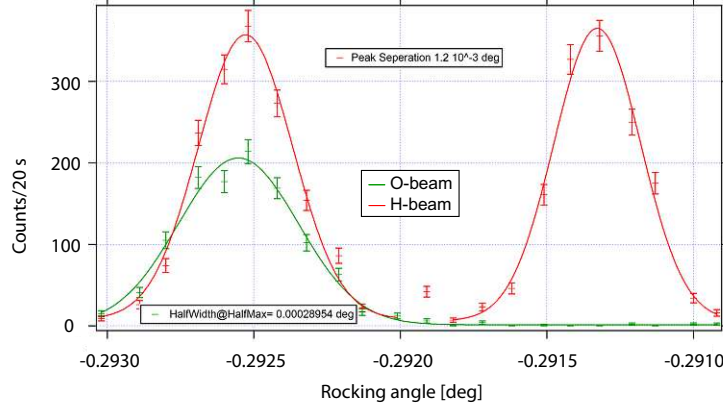


Figure 3.10: Recording of the intensity after the interferometer dependent on the orientation of the interferometer with two properly adjusted polarising magnetic prisms upstream. Because of the small acceptance angle of the interferometer, the divergence between the polarised sub-beams is resolved. The divergence observed as the separation between the two Gaussian peaks in the red fit is  $2.4 \times 10^{-3}$  degree. The green data and fit are recorded for a spin analysis downstream of the interferometer with a polarising supermirror as described at the end of Sec. 3.3.2.

From the case of perpendicular incidence, we calculate the index of refraction  $n$  of the medium as

$$n = \frac{k_{V,\perp}}{k_{0,\perp}} = \sqrt{1 - V/E_{\perp}}, \quad (3.21)$$

which implies a dispersion due to the dependence on the initial kinetic energy of the neutron. Let us model  $V$  as the nuclear Fermi pseudo-potential [93]

$$V_{\text{nuc}} = \sum_i \frac{2\pi\hbar^2}{m} b \delta(\vec{r} - \vec{r}_i), \quad (3.22)$$

with the index  $i$  over all nuclei, their position vectors  $\vec{r}_i$ , the Dirac delta function  $\delta$ , and the scattering length  $b$  as introduced in Sec. 2.2.2. Scattering lengths of materials frequently used in neutron optics are listed in Tab. 2.1. We integrate and average Eq. (3.22) over the three spatial coordinates to derive the mean nuclear potential

$$\bar{V}_{\text{nuc}} = \frac{2\pi\hbar^2 N}{m} b, \quad (3.23)$$

with the density of nuclei  $N$ . By substituting Eq. (3.23) and the relations  $E_{0,\perp} = \hbar^2 k_{0,\perp}^2 / (2m)$  and  $k_{0,\perp} = 2\pi/\lambda$  into Eq. (3.21), the Taylor expansion of the refraction index follows as [94]

$$n = 1 - \frac{\lambda^2 N b}{2\pi} + \mathcal{O}(\lambda^4). \quad (3.24)$$

Coming back to the index of refraction in Eq. (3.21), let us assume  $b_{\text{inc}} = 0$  and  $b_{\text{coh}} \in \mathbb{R} \Rightarrow V \in \mathbb{R}$  for now. The case of  $V/E_{\perp} > 1$  signifies a strong repelling potential in the medium, higher than the kinetic energy. The refraction index becomes imaginary which describes the attenuation in the medium equivalent to a penetration depth. The wave can only pass through the medium by tunnelling.

### 3.3 Manipulation of and Interaction with Neutrons

For  $V/E_{\perp} < 0$ , the attractive potential accelerates a neutron in relation to its propagation in vacuum. The index of refraction follows as  $n > 1$ . This describes an optically denser medium than vacuum. An attractive potential is equivalent to negative coherent scattering lengths such as of lithium and titanium, cf. Tab. 2.1. Snell's law for refraction is written as

$$n' \sin \beta = n \sin \beta', \quad (3.25)$$

with dashed measures for the second medium and the incident angles  $\beta, \beta'$  relative to lead. We assume  $n' = 1$  as in vacuum. For a given  $n$ , the directions of propagation  $\beta$  of the wave in the medium is related to the incident angle  $\beta'$ .

Finally,  $0 \leq V/E_{\perp} < 1$  refers to materials slowing a neutron down. It follows  $1 \geq n > 0$  which is equivalent to an optically thinner medium than vacuum. At the transition from vacuum to a thinner medium, Snell's law cannot be fulfilled for incident angles  $\beta$  close to  $90^{\circ}$ . In this case, total reflection occurs. A material with a respective index of refraction can be used to focus a diverging neutron beam or to divert a collimated neutron beam which increases the neutron flux at subsequent experiments. A pipe around a neutron beam composed of an optically thin medium with this purpose is called a neutron guide. Higher divergences than the angle of total reflection still decrease the neutron flux. As a standard, the angle of total reflection for thermal neutrons of nickel,  $\theta_{\text{crit, Ni}} = 0.1 \text{ deg } \text{\AA}^{-1}$ , is used. This angle is enclosed by incident direction and interlayer like the angle  $\alpha$  in Sec. 3.3.2. Nickel has a comparatively large coherent scattering length as listed in Tab. 2.1 and consequently an incidence on nickel exhibits a relatively large critical angle  $\theta_{\text{crit, Ni}}$ . Any material then possesses a characteristic critical angle  $\theta_{\text{crit, mat}} = m \theta_{\text{crit, Ni}}$ , with the proportionality factor  $m$  for that material. A plot of the reflectivity dependent on the incidence angle is depicted in Fig. 3.11.

When considering a coherent scattering length with both real and imaginary components, the index of refraction has in general both components, too. This means that refraction at the interlayer and absorption in the medium are expected.

The following are developments based on the neutron guide with its regime of total reflection. To prevent losses due to divergences higher than the critical angle, another angle with high reflectivity can be added by building a multilayer structure [95] as depicted in Fig. 3.12. Alternating layers of two materials with different indices of refraction are deposited on a substrate. The layer structure causes another incidence angle with high reflectivity due to partial reflections at the interlayers satisfying the Bragg condition of Eq. (3.9). The thickness of each layer is in the range between  $1 \text{ \AA}$  and hundreds of  $\text{\AA}$  [95]. Between the added angle of reflection and the regime of total reflection, an interval of incidence angles with low reflectivity remains, cf. Fig. 3.11. Further considerations concern the shape of the peak and its resonances, whether the regime of total reflection is upheld, the coating technique, choice of the layer materials, layer depths, layer number, surface roughness, mechanical stress [95] and diffusion [96].

To close the gap in the reflectivity and implement a whole bandwidth of angles with high reflectivity, one can construct a supermirror structure [92]. In a supermirror, the thickness of the layers is steadily increasing with the depth from the

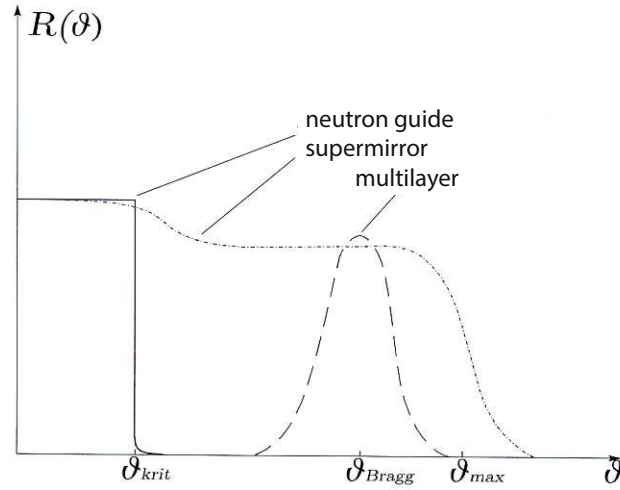


Figure 3.11: Reflectivity of different layer structures dependent on the incident angle [97]. For the neutron guide, the critical angle ends the regime of high reflectivity [97]. For a multilayer, an additional Bragg peak is created. The supermirror practically implements several overlapping Bragg peaks. For the polarising supermirror, the Bragg peaks are only existent for a specific spin component. The increased regime of reflectivity for a given supermirror is quantified through its value  $m$ , such that the reflectivity drastically decreases at an angle  $\theta_{\text{crit, supermirror}} = m \theta_{\text{crit, Ni}}$ .

surface. Each thickness adds another angle with high reflectivity. Depending on the highest layer thickness, the reflectivity of a supermirror is high up to a cut-off angle  $\theta_{\text{crit, supermirror}} = m \theta_{\text{crit, Ni}}$  with  $m$  characterising a given supermirror.

The last step to achieve a polarising supermirror is to choose one of the two materials as ferromagnetic [92]. The scattering length  $b$  is then spin-dependent as described by Eq. (2.37). We will take the example of CoTi polarising supermirrors used for this thesis to understand the mechanisms involved in the polarisation of the neutron beam. The relevant scattering lengths, listed in Tab. 2.1, are  $b_{\text{coh, Co}} = 2.49$  fm,  $b_{\text{inc, Co}} = -6.2$  fm,  $b_{\text{coh, Ti}} = -3.438$  fm, and  $b_{\text{inc, Ti}} = 0$  fm. With magnetised Co at the surface, the sign of the scattering length  $b$  is spin-dependent. For the component of the neutron spin parallel to the magnetisation vector of cobalt, the material possesses a negative scattering length  $b_{\text{Co, par}} = -3.7$  fm. The Co layer is therefore optically denser and total reflection cannot occur. The parallel component is refracted and enters the supermirror. The behaviour of the anti-parallel spin-component is described by  $b_{\text{Co, antipar}} = 8.7$  fm  $\Rightarrow 0 < n_{\text{Co, antipar}} < 1$ . Total reflection occurs for small incident angles.

Above the angle of total reflection, both sub-beams enter the supermirror at different angles of refraction. For the parallel component, the difference in scattering lengths between Co and Ti is rather small, i.e.  $b_{\text{Co, par}} = -4.5 \approx b_{\text{Ti}} = -3.438$ . This has to be compared to the scattering length for the antiparallel component  $b_{\text{Co, antipar}} \approx 8.7$ . It follows that the reflections of the parallel component at the interlayers in the supermirror are of low intensity and the reflectivity is low also above the critical angle. The substrate absorbs the transmitted parallel spin-component. The principle of the supermirror applies however for the anti-parallel component

### 3.3 Manipulation of and Interaction with Neutrons

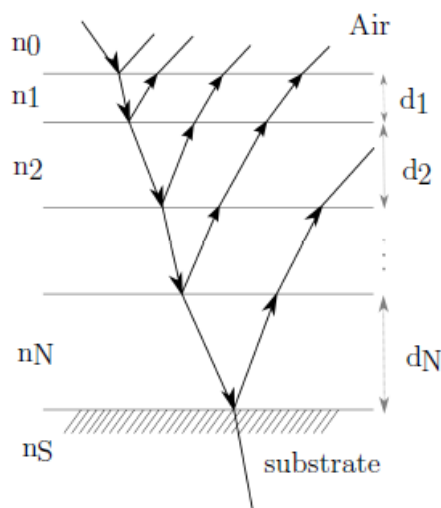


Figure 3.12: Schematic of a general multilayer structure deposited on a substrate [72]. Each layer  $i$  has an index of refraction  $n_i$  and thickness  $d_i$ . For the neutron guide, only one thick layer is considered. For a multilayer, two alternating materials, i.e.  $n_i = n_{i+2}$ , with alternating thicknesses  $d_i = d_{i+2}$  are arranged. The supermirror has decreasing layer thicknesses, i.e.  $d_i < d_{i+1}$ . Finally, a polarising supermirror is constructed by making one index of refraction spin-dependent, i.e.  $n_{2i+1} = n_{\uparrow\downarrow}$ .

such that the reflectivity is high for a large range of incident angles. The polarising supermirror separates the spin components of the neutron according to the orientation of the polarisation vector in the cobalt layers.

The degree of polarisation of a supermirror depends on its quality. This includes the purity of the chemical elements, the degree of magnetisation of the ferromagnetic material and the precision and accuracy of the layer thicknesses. The layers are usually deposited through a sputtering technique. The relative fluctuations of the layer height then decreases with absolute layer height due to the statistics of vapour deposition. In general, there is a vanishing correlation between the deposited atoms such that Poisson statistics apply: with a mean layer thickness of  $N$  atoms, the standard deviation is  $\sqrt{N}$ . For a supermirror, the changing layer thickness affects the longitudinal displacements at recombination between the reflected partial beams. The case of purely constructive interference between all partial beams is not fulfilled any more. In effect, the supermirror gives a high reflectivity over a broader interval of angles than a neutron guide. However, for a specific combination of incident angle and neutron wavelength, the reflectivity is higher for a properly constructed multilayer, see Fig. 3.11.

For an ideal spin polariser or analyser, the transmitted intensity of an unpolarised neutron beam drops to 1/2; all neutrons with one spin state are transmitted and all neutrons of the orthogonal spin state are absorbed or traversing in a discriminable direction. For the CoTi supermirror with its imperfections used, further losses due to absorption occur. The absorption can be either in the CoTi layer structure or in the boron substrate. The magnitude of the absorption effect from low to high orders the three elements as Ti, Co and B, cf.  $\sigma_{\text{abs}}$  in Tab. 2.1. For this thesis, a bender array is used, i.e. multiple bent supermirror structures are arranged with a small displacement perpendicular to the incident beam direction. No neutron can pass the

bender without interacting either with the supermirror or the substrate. Because of the large incident area onto the strongly absorbing substrate, the intensity after the supermirror drops by about one order of magnitude.

### 3.3.3 Single Crystal Neutron Interferometer

The absolute phase of a quantum state is indeterminable and can therefore be considered not to exist. Relative phases, however, are determinable interferometrically. An interferometer separates either the wavefront emitted from a source or the amplitudes of a specific part of said wavefront. There are different neutron interferometers such as gratings [98] (wavefront separation) and spin echo instruments [10, 99] (amplitude separation).

We will describe the central element of the presented experiments: the single crystal silicon neutron interferometer (amplitude separation) [100]. This type of interferometer is built-up by a face-centred cubic crystal structure. The structure and its orientation are the same throughout the length of the interferometer of  $\approx 10$  cm. Similarly as for the neutron monochromator, the wavelength of thermal neutrons  $\lambda \approx 2 \text{ \AA}$  is comparable with the lattice constant  $d_{(220)} = 1.92 \text{ \AA}$  of the (220) crystal planes. The basic Mach-Zehnder single crystal neutron interferometer contains three plates which each serve as a beam splitter. The incident neutron wave is split at the first interferometer plate into two parts: a transmitted and a reflected part. The respective path states are denoted as  $|I\rangle$  and  $|II\rangle$ . The second plate in both sub-beams produces a total of four sub-beams: two sub-beams traversing outward of the experiment and two converging sub-beams. The third plate produces superpositions of the converging sub-beams. The O-beam in incident direction and the diffracted H-beam exit the interferometer. In both O and H-beam, both path states are superposed and interference between the paths is observed. A rendering of a two-path neutron interferometer is depicted in Fig. 4.2.

A single beam splitting in the neutron interferometer is described through the ansatz [101]

$$\begin{pmatrix} a'_1 \\ a'_2 \end{pmatrix} = \begin{pmatrix} t_1 & r_2 \\ r_1 & t_2 \end{pmatrix} \begin{pmatrix} a_1 \\ a_2 \end{pmatrix}, \quad (3.26)$$

with the incident amplitudes  $a_1, a_2$  of a beam splitter and the output amplitudes  $a'_1, a'_2$ . The matrix elements  $r_i$  and  $t_i$ ,  $i \in 1, 2$  represent reflection and transmission by the beam splitter, respectively.

A rigorous description of the beam splitter is given by the dynamical theory of diffraction. It considers that in Laue configuration of neutron beam and crystal, each part of the neutron wave traverses a large number of crystal plains. A myriad of consecutive reflections and transmissions occurs inside each crystal plate, including the case of back and forth scattering between two adjacent crystal planes. We introduce the parameters

$$F = \frac{k}{2 \cos \gamma} \frac{|V(\vec{G})|}{E} D, \quad y = \frac{1}{2} \frac{E}{|V(\vec{G})|} \alpha \quad (3.27)$$

with the angle  $\gamma$  between incident direction and lead, the potential  $V$  for the lattice vector  $\vec{G}$ , the initial kinetic energy  $E$  of the neutron, the thickness  $D$  of the crystal plate, the deviation  $\alpha$  of the incident direction from the ideal Bragg angle  $\theta$ . The

### 3.3 Manipulation of and Interaction with Neutrons

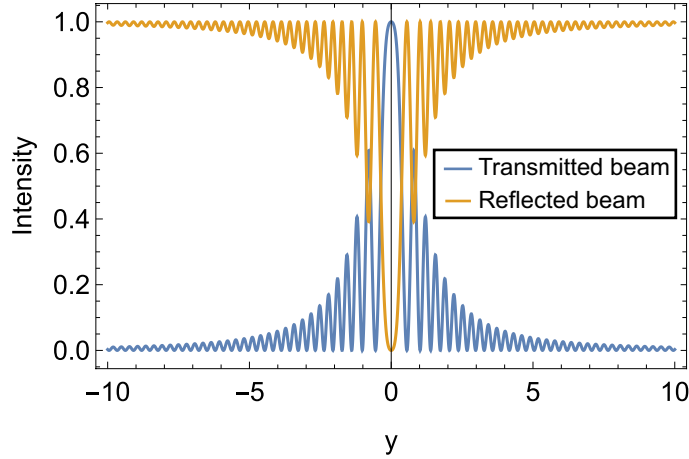


Figure 3.13: Intensities of the transmitted and reflected beam after a single beam splitter of a perfect crystal neutron interferometer according to Eq. (3.30). The parameter  $F$  is chosen as  $7/2\pi$ , is linear in the beam splitter thickness  $D$ , and describes the properties of the incident neutrons as well as the geometry. The intensities sum up to 1 and rapidly oscillate dependent on  $y$ . The period is called “Pendellösungslänge” which is given in Eq. (3.29).

intensities  $I$  of the transmitted (t) and reflected (r) output beams, normalised with the incident (inc) intensity are given by [102]

$$\begin{aligned} \frac{I_t(D)}{I_{\text{inc}}} &= \frac{\sin^2(F\sqrt{1+y^2})}{1+y^2}, \\ \frac{I_r(D)}{I_{\text{inc}}} &= 1 - \frac{\sin^2(F\sqrt{1+y^2})}{1+y^2}. \end{aligned} \quad (3.28)$$

The parameters  $F$  and  $y$  both take the neutron properties and geometry into account and are linearly dependent on  $D$ . A plot of Eq. (3.28) is given in Fig. 3.13. The “Pendellösungslänge” (German for length of the pendulum solution)

$$\delta_0 = \frac{\pi D}{E} \quad (3.29)$$

is the period of the intensity oscillations in Eq. (3.28). The intensity rapidly oscillates back and forth between the outputs of a beam splitter dependent on its thickness and the incident direction of the neutrons. If there is some divergence in the neutron beam, the intensity after the beam splitter is the average over the rapid oscillations.

With three consecutive beam splitters for each sub-beam, a loop is formed. The intensities of the output beams O and H according to the ansatz made in Eq. (3.26) are derived nicely in [101]. This reference considers a single input amplitude, e.g.  $a_1 \neq 0$  and  $a_0 = 0$ . The solution for the intensities is written as

$$\begin{aligned} I_O &= A(1 + \cos \chi), \\ I_H &= B + A \cos \chi, \end{aligned} \quad (3.30)$$

with the mean intensity  $A$  in the O-beam, the mean intensity  $B \geq A$  in the H-beam, and the relative phase shift  $\chi$  between the separated sub-beams. If we consider a

light interferometer with 50:50 beam splitters, it is known that  $A = B$ . However, the beam splitters in a single crystal neutron interferometer are generally not 50:50 beam splitters. That  $B > A$  is plausible because reflection and transmission are different operations such that an asymmetry between the output ports is introduced by the interferometer. Only the amplitude reaching the O-beam is split in halves by the first beam splitter. Therefore, the contrast

$$C = \frac{I_{\max} - I_{\min}}{I_{\max} + I_{\min}}, \quad (3.31)$$

with the maximum and minimum intensities  $I_{\max}$ ,  $I_{\min}$  is larger in the O-beam. Because  $I_O$  exhibits more pronounced characteristics of quantum interference, primarily the O-beam is used for measurements.

The single crystal neutron interferometer produces a beam separation of several centimetres. That allows to use macroscopic devices to manipulate a quantum state. In addition to the two-path neutron interferometer, there is a three-path variation. The use of this kind of interferometer allows the interference of three sub-beams. This may be used for extensions of experiments or as a phase reference.

### 3.3.4 Phase Shifter

A phase shifter spatially moves the wave fronts of a plain wave. As in light optics, this is realised primarily by introducing a parallel surfaced slab of material in the beam path with a different optical density than the surrounding medium. Suitable materials in neutron interferometry ideally have a high difference in the optical density compared to air, such that one can easily induce a phase shift with minimal means of material and space. To reduce the losses, a low absorption cross-section is favourable. A high homogeneity and low roughness of the surfaces allow a homogeneously induced phase shift over the entire cross-section of a neutron beam.

The phase shift to a single neutron beam is written as [100]

$$\Delta\chi = (n - 1)kD_0 \approx -\frac{\lambda^2 Nb}{2\pi} \frac{2\pi}{\lambda} D_0 = -Nb_{\text{coh}}\lambda D_0, \quad (3.32)$$

with the nuclei density  $N$ , the coherent scattering length  $b_{\text{coh}}$ , the neutron's wavelength  $\lambda$ , the thickness of the phase shifter slab  $D_0$ , the optical density of the material  $n$ , and the neutron wave number  $k$ . In Eq. (3.32), we consider only the real part of the coherent scattering length. Incoherent scattering induces dephasing for an unpolarised neutron beam, while producing a distinct phase shift for a polarised neutron beam. The imaginary parts describe absorption. The phase shift is higher for longer wavelengths due to the dependence on the index of refraction  $n \sim \lambda^2$ . The dependence on  $k \sim 1/\lambda$  implies that the same spatial translation of a wave results in a higher phase shift for shorter wavelengths. The effects combined give a dependence of the relative phase shift linear to the wavelength.

In a perfect crystal neutron interferometer, the established method to induce phase shifts is to use a slab of material which extends into two beams. Both partial waves are therefore phase shifted. Because global phases are not possible to measure, only the relative phase shift is of importance. Therefore, the slab is rotated by an angle  $\zeta$  such the one beam traverses a longer distance inside the material while

### 3.3 Manipulation of and Interaction with Neutrons

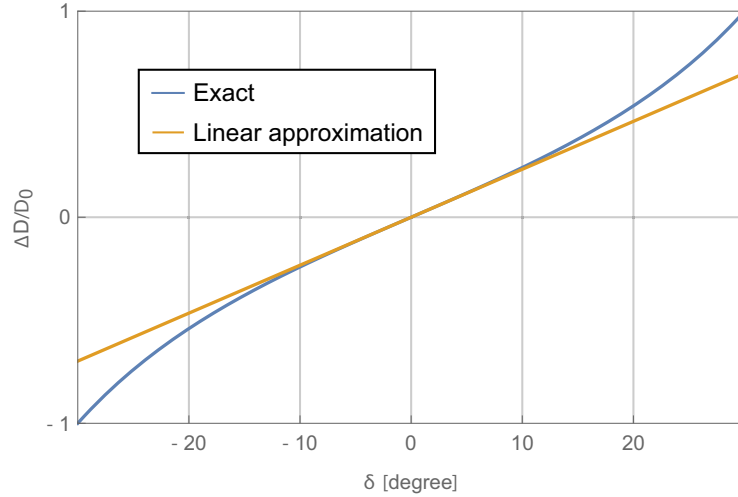


Figure 3.14: Relative difference in traversed distance inside a phase shifter slab with thickness  $D_0$  between the two sub-beams in a two path neutron interferometer dependent on the rotation angle  $\zeta$  of the phase shifter slab. The zero position refers to the symmetrical orientation. The relative length difference is proportional to the relative phase shift. Blue line is the exact result when applying Eq. (3.33). The linear approximation for small rotations of the phase shifter slab is drawn in yellow. Dependent on the experimental requirements, the approximation is suitable for an interval of a few degrees.

the other traverses a shorter distance. Adjustment of the phase shifter orientation necessitates a motor for rotation with accordingly high precision and accuracy. The path difference  $\Delta D$  through the material between two paths dependent on the angle  $\zeta$  is given as

$$\Delta D(\zeta) = \left( \frac{1}{\cos(\theta_B + \zeta)} - \frac{1}{\cos(\theta_B - \zeta)} \right) \cdot D_0, \quad (3.33)$$

with the opening angle between the interferometer paths  $2\theta_B$

In the limit of small rotations of the phase shifter slab, i.e.  $\zeta \ll 1$ , this approximates to a linear relation. Therefore, one can record an interferogram by rotating the phase shifter in (equidistant) steps of the angle  $\zeta$ . The difference between linear approximation and the exact calculation can be seen in Fig. 3.14.

For the presented experiments, aluminium and sapphire ( $\text{AlO}_3$ ) phase shifters were used. As indicated below Eq. (3.32), the incoherent scattering length can influence the properties of a neutron beam. The incoherent scattering length of aluminium is larger than that of oxygen. In the experiment of Sec. 5 with two phase shifters, the aluminium phase shifter is positioned upstream and the sapphire phase shifter downstream. This order increases the phase homogeneity and in turn the contrast of interferograms.

#### 3.3.5 Absorbers

Absorbers have different purposes in neutron optical experiments. Absorption is necessary for radio protection but also to realise experimental concepts. The elements and isotopes  $^3\text{He}$ , B, Cd, In,  $^{235}\text{U}$ , and specifically Gd are notable for high

absorption cross-section  $\sigma_{\text{abs}}$ , as listed in Tab. 2.1. Apart from Gd, all these elements were purposefully used as absorbers for the present thesis:

- $^{235}\text{U}$  in the reactor source, cf. Sec. 3.2.2,
- $^3\text{He}$  as the filling gas in the detecting counting tubes, cf. Sec. 3.3.7,
- B as shielding of the detectors against background and as beam blockers,
- Cd as shielding of the detectors against background, as beam blockers, and as aperture material, and
- In for slight adjustments in the intensity ratios between the sub-beams of the interferometer.

The intensity of a neutron beam transmitted through an absorber dependent on the absorber's thickness  $d$  is written as

$$I(d) = I_0 e^{-\kappa d}, \quad (3.34)$$

with the incident intensity  $I_0$  and the attenuation factor  $\kappa$ . For the experiment presented in Sec. 4, an attenuation of about 10% in intensity is required. For most elements,  $\kappa$  is either too low or too high for such a fine tuning with slabs of thickness in the range of 0.1 mm–1 mm. Indium is suited for this purpose due to its absorption coefficient  $\kappa_{\text{In}} \approx 0.84/\text{mm}$ . For beam shaping of the thermal neutron beam, a strong neutron absorption is accomplished by properly positioning cadmium foils. To induce an interaction of weak absorption, indium foils with a thickness of 0.125 mm and an absorption coefficient  $\mathcal{A} \approx 0.1$  are used.

### 3.3.6 Spin Manipulations via Magnetic Fields

As discussed in context of Larmor precession (Sec. 2.2.1) and spin polarisers (Sec. 3.3.2), the neutron spin and magnetic fields interact. In contrast to spin polarisers, magnetic coils are not used to separate neutrons with different spin states but to induce specific trajectories of the orientation of the polarisation vector of Eq. (2.26) on the Bloch sphere. Electromagnetic coils produce magnetic fields in a confined interval of the neutron beam. The Hamiltonian of the system is written as

$$\hat{H} = -\vec{\mu} \cdot \vec{B}. \quad (3.35)$$

This describes Larmor precession of the neutron spin around the magnetic field.

#### Guide field

Apart from the intended spin manipulations, earth's magnetic field or uncontrolled and unknown stray fields from electrical devices and adjacent experiments perturb the spin state. This can be prevented by mitigating the stray fields through shielding with Mu-metal. Another option is creating a much stronger field than the stray fields which is called a guide field. Its interaction is controlled and predictable as Larmor precession. Typically, the guide field is induced by a Helmholtz coil surrounding the sections where unintended spin manipulations perturb the measurement results.

### Larmor Accelerator

The guide field is typically induced in a large volume, covering entire sections of the experiment with multiple devices. In general, such a “global” implementation does induce global phases. The intensities are unaffected and global phases are in turn unattainable. However, when applying a static field to a parallel polarisation vector in a constrained volume of the experiment, a relative phase shift compared to other beam paths is induced. This can change intensities and is measurable.

### Radio-Frequency Spin Manipulators

Spin manipulations with rotating field (RF) coils are discussed for various specific field configurations in , e.g. [69, 103–105]. We will focus only on the main ansatzs which are necessary to understand the function of the RF flippers in Sec. 5. Let us assume a time-dependent magnetic field which is written for  $t \leq 0$  as  $\vec{B}(t) = 0$  and for  $t > 0$  as

$$\vec{B}(t) = \begin{pmatrix} B_1 \cos(\omega t + \phi) \\ B_1 \sin(\omega t + \phi) \\ B_0 \end{pmatrix}. \quad (3.36)$$

with the angular velocity  $\omega$ , the phase offset  $\phi$ , and the magnetic field strengths  $B_0$  and  $B_1$ , respectively, of the static and rotating field. We will now solve the Pauli-Schrödinger equation for this specific situation, written as

$$\begin{aligned} \hat{H}\psi(\vec{r}, t) &= E\psi(\vec{r}, t) \\ \left( -\frac{\hbar^2}{2m}\nabla^2 - \vec{\mu}(t) \cdot \vec{B}(t) \right) \psi(\vec{r}, t) &= i\hbar \frac{\partial}{\partial t} \psi(\vec{r}, t) \\ \left( -\frac{\hbar^2}{2m}\nabla^2 - \mu\vec{\sigma}(t) \cdot \vec{B}(t) \right) \psi(\vec{r}, t) &= i\hbar \frac{\partial}{\partial t} \psi(\vec{r}, t). \end{aligned} \quad (3.37)$$

At incidence in  $x$ -direction and assuming a linear trajectory without refraction at the interlayer, above equation reduces to one spatial dimension, written as

$$\left( -\frac{\hbar^2}{2m} \frac{\partial^2}{\partial x^2} - \vec{\mu}(t) \cdot \vec{B}(t) \right) \psi(x, t) = i\hbar \frac{\partial}{\partial t} \psi(x, t) \quad (3.38)$$

The separation ansatz

$$\psi(x, t) = \Phi(x)\chi(t) \quad (3.39)$$

into a purely spatially dependent function  $\Phi(x)$  and a purely time-dependent function  $\chi(t)$  is made. Substituting Eq. (3.39) and reordering of terms in Eq. (3.38) leads to

$$-\frac{\hbar^2}{2m} \frac{(\partial_x^2 \Phi(x))}{\Phi(x)} = i\hbar \frac{(\partial_t \chi(t))}{\chi(t)} + \mu\vec{\sigma}(x) \cdot \vec{B}(x) = \kappa, \quad (3.40)$$

Because spatial and time-dependent terms are separated, the parameter  $\kappa$  is constant. On the left side, the operator for the kinetic energy appears such that  $\kappa$  equals the kinetic energy  $E_{\text{kin}} = \frac{\hbar^2 k^2}{2m}$  with the wave number  $k$ . This offers the ansatz for the spatial function

$$\Phi(x) = Ae^{-ikx} + Ce^{ikx}, \quad (3.41)$$

### 3 Neutron Optics

with the amplitudes  $A$  and  $C$  which solves the spatial part of Eq. (3.40). The term proportional to  $A$  is evolving forward in  $x$ -direction, the term proportional to  $C$  backwards. We constrain ourselves to the case of small magnetic field strengths compared to the initial kinetic energy,  $|\mu B_1|, |\mu B_0| \ll \kappa$ . Reflections when penetrating the field can then be neglected and assuming  $C = 0$  is rectified. For the function  $\chi(t)$ , we make the transformation

$$\chi(t) = e^{-i\frac{\hbar k^2}{2m}t} \xi. \quad (3.42)$$

Substituting the latter into the time-dependent relation of Eq. (3.40) leads to

$$[i\hbar\partial_t + \mu(\hat{\sigma}_x B_1 \cos \Omega t + \hat{\sigma}_y B_1 \sin \Omega t + \hat{\sigma}_z B_0 \sin \Omega t)] \xi(t) = 0. \quad (3.43)$$

The transformation into the system rotating with the orientation of the field is written as

$$\hat{U}(t) = e^{-i\omega t \sigma_z / 2}, \quad (3.44)$$

such that  $\xi(t) = \hat{U}(t)\xi_{\text{rot}}(t)$ . We introduce the rotation vector

$$\vec{\alpha}(t) = \begin{pmatrix} \omega_1 t \\ 0 \\ (\omega_0 - \omega) t \end{pmatrix}. \quad (3.45)$$

with the abbreviations  $\omega_0 = \gamma B_0$ ,  $\omega_1 = \gamma B_1$ , and  $\gamma = 2\mu/\hbar = -2|\mu|/\hbar$  as in Eq. (2.31). The absolute of the rotation vector is written as  $\alpha = t\sqrt{\omega_1^2 + (\omega_0 - \omega)^2} = \gamma t B_{\text{eff}}$  with the effective magnetic field  $B_{\text{eff}}$  in the rotating system.

The solution for an initial spin state  $\xi(0) = (1, 0)^T$  is given in [105] as

$$\psi(x, t) = \frac{1}{\sqrt{2\pi}} e^{i(kx - \frac{E_{\text{tot}}}{\hbar}t)} \times \begin{pmatrix} e^{-i\omega t/2} \left( \cos\left(\frac{\alpha(t)}{2}\right) + i\frac{B_0 + \omega/\gamma}{B_{\text{eff}}} \sin\left(\frac{\alpha(t)}{2}\right) \right) \\ i e^{i\omega t/2} \frac{B_1}{B_{\text{eff}}} \sin\left(\frac{\alpha(t)}{2}\right) \end{pmatrix}. \quad (3.46)$$

In the case of resonance, the resonance frequency  $\omega_{\text{res}}$  is written as

$$\omega_{\text{res}} = \omega = \omega_0 = -\gamma B_0, \quad (3.47)$$

and Eq. (3.46) simplifies to

$$\psi(x, t) = \frac{1}{\sqrt{2\pi}} e^{i(kx - \frac{E_{\text{tot}}}{\hbar}t)} \times \begin{pmatrix} e^{-i\omega t/2} \cos\left(\frac{\alpha(t)}{2}\right) \\ i e^{i\omega t/2} \sin\left(\frac{\alpha(t)}{2}\right) \end{pmatrix}. \quad (3.48)$$

This spin state is spiralling on the Bloch sphere in time back and forth from up to down spin state. Analogous results emerge for an initial down-spin state  $\xi(0) = (0, 1)^T$ . When factoring out  $e^{-i\omega t/2}$  and excluding the plane wave solution, the transformation on a general spin state can be written as

$$\hat{U}_{\text{RF}}(t, \alpha, \omega, \delta) = \begin{pmatrix} \cos\left(\frac{\alpha}{2}\right) & i \sin\left(\frac{\alpha}{2}\right) e^{+i(\omega t + \delta)} \\ i \sin\left(\frac{\alpha}{2}\right) e^{-i(\omega t + \delta)} & \cos\left(\frac{\alpha}{2}\right) \end{pmatrix}. \quad (3.49)$$

The time-dependent phase term  $\exp(i\omega t)$  describes the relative phase compared to the initial wave function. The relative phase originates in the shift in total energy due to the time-dependent Hamiltonian.

Experimentally, an oscillating field in a guide field

$$\vec{B}(t) = \begin{pmatrix} B_1 \cos(\omega t + \phi) \\ 0 \\ B_0 \end{pmatrix} \quad (3.50)$$

is more feasible to realise than a rotating field. The latter equation can be re-written in terms of two rotating fields with opposite directions of rotation in a static field as

$$\vec{B}(t) = \begin{pmatrix} B_1/2 \cos(\omega t + \phi) \\ B_1/2 \sin(\omega t + \phi) \\ 0 \end{pmatrix} + \begin{pmatrix} B_1/2 \cos(\omega t + \phi) \\ -B_1/2 \sin(\omega t + \phi) \\ 0 \end{pmatrix} + \begin{pmatrix} 0 \\ 0 \\ B_0 \end{pmatrix}. \quad (3.51)$$

One of the magnetic fields rotates in the same direction as the polarisation vector. The second is rotating in the opposite direction. The counter-rotating field induces the Bloch-Siegert shift [106] which modifies the resonance frequency of Eq. (3.47) to

$$\omega_{\text{res}} = -\gamma B_0 \left( 1 + \frac{B_1^2}{16B_0^2} \right). \quad (3.52)$$

In case of  $B_0 \gg B_1$ , the Bloch-Siegert shift is neglected which is called the rotating wave approximation.

#### Direct Current Spin Manipulator

The special case of the RF flipper is the direct-current (DC) spin manipulator for  $\omega = 0$ . Equation (3.49) further reduces to

$$\hat{U}_{\text{DC}}(t, \alpha) = \begin{pmatrix} \cos(\frac{\alpha}{2}) & ie^{+i\delta} \sin(\frac{\alpha}{2}) \\ ie^{-i\delta} \sin(\frac{\alpha}{2}) & \cos(\frac{\alpha}{2}) \end{pmatrix}, \quad (3.53)$$

where the phase  $\delta$  is equivalent to the static orientation of the field. If the magnetic field is static, the neutron spin follows a circle on the Bloch sphere. In Eq. (3.53), there is no time-dependent phase term as in Eq. (3.49). The static Hamiltonian describing DC spin manipulations conserve the total energy such that no relative phase is induced compared to the initial wave function.

#### Temperature Control System

As described in Sec. 3.3.3, a neutron interferometer functions on the basis of the regularity of its crystal structure. When operating magnetic coils in an electrical circuit, they possess an electrical resistance. Heat is dissipated through radiation, conduction and convection. When the heat reaches the interferometer crystal, the crystal expands and the lattice parameter is increased. If this happens homogeneously over the entire crystal, a slightly increased neutron wavelength may be necessary as an input. The neutron interferometer is more sensitive to local deviations of the lattice parameter, which is equivalent to mechanical stress. This is induced by local temperature fluctuations and mechanical vibrations. If these influences become too strong, the interference effect is not observable.

A mechanical dampening system attenuates external vibrations, specifically in the interval between 1 Hz-10 Hz. The thermal control system entails multiple layers of thermal insulation and temperature control. The outermost layers are the guide hall and the structure in it constructed for instrument S18. The structure has an outer and an inner room which are both air conditioned. In the inner room, the interferometer crystal is encased by acrylic glass. Outside the case, the guide field coils operate. Inside the case, magnetic coils operate close to the crystal. The heat of both guide field and local coils is diverted through a separate water cooling system. Each coil is submerged in water which is constantly pumped to an active cooler in the outer room. Several temperature probes in meaningful positions regulate the air conditioning and water cooling. A schematic of the temperature control system is depicted in Fig. 3.15.

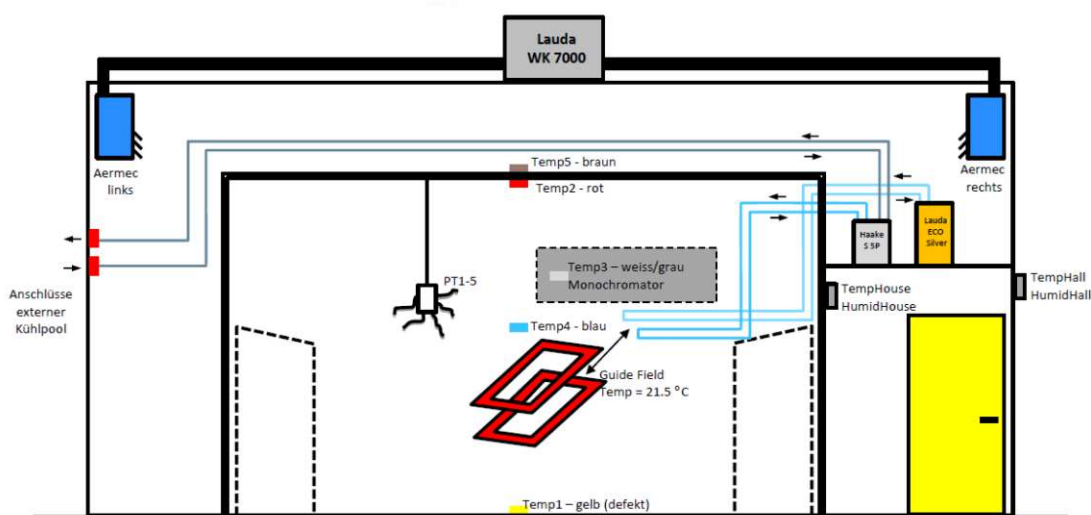
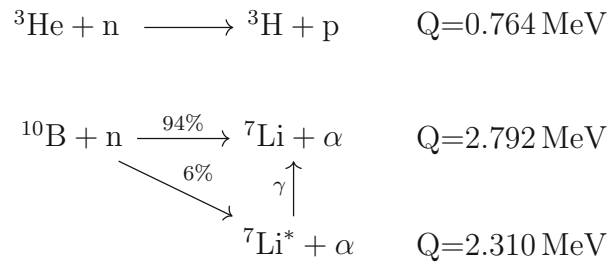


Figure 3.15: Schematic of the temperature control system at instrument S18. Multiple layers of thermal insulation and control regulate the interferometer to a stable and homogeneous temperature. Multiple temperature sensors at key positions regulate the air conditioning and water cooling systems. The interferometer crystal is regulated in its temperature and temperature gradient such that the regularity of the crystal allows to coherently split and recombine the neutron beams.

### 3.3.7 Detectors

Neutrons are chargeless [107, 108] and have a small magnetic moment. Their detection therefore relies on absorption via the strong nuclear force. Solid state detectors [109, 110] and gaseous counting tubes [68] are common where the latter are used in this study. The elements helium and boron have high absorption cross-sections (see Tab. 2.1), such that the nuclear reactions

### 3.3 Manipulation of and Interaction with Neutrons



with the freed energy  $Q$ , can each be used as an initial process for detection.

Before and after above helium reaction, one nucleon is free. A proton in the helium core is replaced by a neutron. Because the nucleons are bound through the strong force and repelled by the electromagnetic force, a rigorous description of the nuclei necessitates an ansatz through quantum chromo and electro dynamics. However, the classical estimate through the Coulomb potential of two protons constrained to 1 fm in a helium nucleus leads to a repulsive potential of

$$V_{\text{Coulomb}} = \frac{1}{4\pi\epsilon_0} \frac{q_1 q_2}{r} = \frac{1}{4\pi\epsilon_0} \frac{e^2}{1 \text{ fm}} \approx 1.45 \text{ MeV}, \quad (3.54)$$

with the charges  $q_1, q_2$  and the dielectric constant  $\epsilon_0$ . This correctly describes at least the order of magnitude in freed binding energy of the helium reactions. The freed binding energy in the helium reaction can be attributed to the decreased electromagnetic potential when separating two protons. The reverse reaction of fusion between two protons to a diproton is the dominant process in stable stars [111] as is currently our sun. Despite being essential to sustaining life on earth, basic parameters of the process are unknown. Specifically, the life-time of a diproton is constrained only roughly to be  $\ll 10^{-9}$  s.

In the boron reaction, the free neutron is absorbed, resulting in an excited boron nucleus. This induces fission into lithium and an  $\alpha$  particle. Fission of nuclei lighter than iron is in general only possible through excitation. Because all nucleons are bound after the reaction, net binding energy is freed. Some of the binding energy of the initially free neutron is compensated by weaker nuclear bonds in the produced lithium core.

The boron reaction sets free significantly more binding energy ( $>2$  MeV) than the helium reaction (0.7 MeV). The difference in binding energy and the masses before and after each reaction define the momenta and kinetic energies of the reaction products through conservation of energy and momentum. The smaller reaction products receive the majority of the kinetic energy. The smaller and faster reaction products comprise less protons and charge such that they escape most of the initial electron cloud; positive ions emerge. The slower, larger and stronger charged reaction products, together with the remainder of the electronic cloud, compose negative ions. In context of the counting tube, both reaction products are called primary ions.

While  ${}^3\text{He}$  is gaseous,  ${}^{10}\text{B}$  can be bound in the gas boron trifluoride  $\text{BF}_3$ . Each gas is separately used to fill gas counting tubes. In counting tubes, the filling gas is stored under high pressure to increase the probability for a reaction. When reacting in a counting tube, the fast reaction products collide with atoms or molecules of the filling gas in their path. The atoms or molecules are ionised by exciting electrons.

### 3 Neutron Optics

Each ionisation reduces the kinetic energy of the primary ions by the ionisation energy. After a certain number of ionisations, the remaining kinetic energy of the primary ions is insufficient to ionise further. In the trajectory of the primary ions, a trail of secondary ions and electrons is produced.

A counting tube is constructed as a cylinder with a wire in the central axis. An electrical voltage is applied between the grounded exterior and the inner wire. The secondary ions are accelerated outwards, the secondary electrons inwards. The charges are accelerated on the characteristic mean free path, which depends on the pressure, until a collision. If the gain in kinetic energy is high enough, further ionisations are induced. Due to the cylindrical geometry, the field is stronger in proximity to the central wire. Most ionisations are induced close to the wire where a charge multiplication takes place through a cascade of ionisations. For a cylindrical geometry, a voltage in the range of kV is sufficient for a proper charge multiplication. In contrast, a parallel plate geometry necessitates tens of kV.

The above assumes multiple ionisations through each free electrons at the wire. With opposite polarisation of the electric circuit, the more massive ions are accelerated towards the wire. A few problems arise from this. e.g. due to the smaller velocities of ions, they have a lower mean free path between collisions. With the same voltage, the volume of charge multiplication is smaller and the signal is lower. Because a strong signal is a priority, the polarisation is chosen the other way round, as described in the previous paragraph.

With decreased diameter of the counting tube, boundary effects become important. A trail of primary ions will tend to reach out of the detector. Some amount of primary ions will not be inside the applied potential to cause a cascade. The output voltage is decreased. It is rare, however, that a nuclear reaction takes place close to the outer wall of the detector and that both trails of ions face tangentially to the wall. Only in this case, a nuclear reaction produces a negligible output signal.

By choosing the proportional regime of the applied voltage, the amount of charges reaching the inner wire is proportional to the kinetic energy of the initial neutron. For higher voltages applied, the avalanche of charges becomes oversaturated as in a Geiger-Müller device; all initial ions have the same large output signal. For lower voltages, the gained energy between two collisions is insufficient to induce ionisations; all initial ions produce a small output signal.

The signal in terms of charge is transformed into a voltage. A pre-amplifier increases the signal. When feeding this voltage signal to a multi-channel analyser, the voltage spectrum depicted in Fig. 3.16 is obtained. The distributions of voltages quantifies the probability of  $\gamma$  signals at low voltages. The peak at high voltages is due to neutrons depositing all their energy within the counting tube. The neutron peak extends into a plateau at lower voltages which are caused by neutrons whose trail of secondary ions extends outside the counting tube. The amplification or gain of the voltage in the pre-amplifier is chosen such that the high neutron peak in the spectrum is located close to the maximal voltage of 5 V but also not cut off. For experiments, the voltage output is not fed to an MCA but a discriminator before the signal is passed on to a user interface. The threshold voltage is chosen at the minimum between  $\gamma$  signals and neutron signals. The discriminator transforms the analogue into a digital signal where each pulse is considered to indicate a detection of a neutron in the counting tube. Electronic noise accounts typically to a count

### 3.3 Manipulation of and Interaction with Neutrons

rate of 0.01 counts/s. The background as given in proximity of a nuclear reactor is reduced through shielding for the presented experiments to  $< 0.01$  counts/s.

Because the single detection events cannot be correlated in time, the count distribution is described by Poisson statistics. Therefore, for a neutron count of  $N$  neutrons, the standard deviation is  $\sqrt{N}$ .

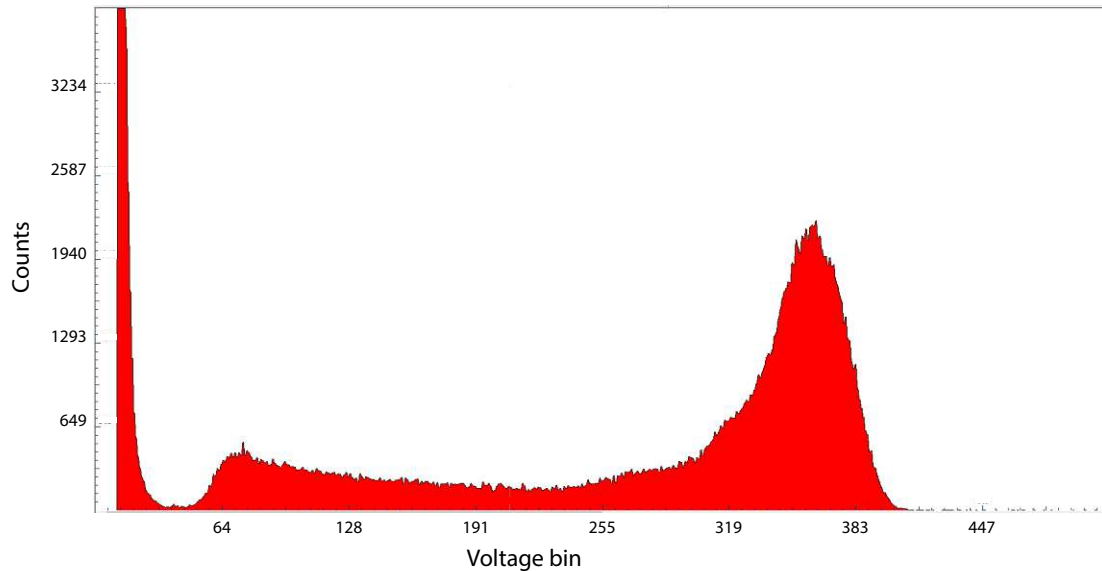


Figure 3.16: Spectrum of output voltages from the detector, recorded with a multi-channel analyser (MCA). In the proportional regime of the input voltage applied to the counting tube, the output voltage is proportional to the initial energy of the neutron. Gamma rays produce the peak at low output voltages. Counts at output voltages higher than the first minimum indicate neutron detection. The rightmost peak indicates neutrons which reacted such that all secondary ions are produced within the counting tube. Lower output voltages are attributed to boundary effects such that the trail of secondary ions reaches out of the counting tube. Output signals between 0 V and 5 V are resolved into voltage bins numbered from 0 to  $\approx 500$ . The gain factor of amplification is chosen such that the spectrum ends before the cut-off at 5 V. The threshold for the discriminator is chosen in the minimum between  $\gamma$  and neutron signals.



# Chapter 4

## Three-Path Quantum Cheshire Cat

This chapter is based on publication [112] which is reproduced with permission from Springer Nature.

Although our every-day experience rejects it, the quantum Cheshire Cat suggests a potential spatial separation between different properties of a single particle in an interferometer. The first published experiment with neutrons confirmed the quantum Cheshire Cat effect by using the path and spin degrees of freedom. The locations of each property are determined qualitatively through reactions to locally applied perturbations. Yet, no consensus on the interpretation has been reached. To clarify the origin of the effect, in the present experiment the energy degree of freedom is used as the third property; three properties of neutrons appear to be separated in different paths in the interferometer. The analysis of the experiment suggests the strong involvement of the selection of the final state. The selection is accomplished through projection between the state vectors, one evolved from the initial state through the perturbation and the other being the final state. The projection results in amplitudes from two sub-beams which contribute to the intensity. The cross-term between amplitudes gives rise to the quantum Cheshire Cat.

### 4.1 Introduction

Since the introduction of quantum mechanics, its theoretical framework has suggested counter-intuitive and paradoxical phenomena: entanglement [17, 18], Schrödinger's cat [113, 114], and wave-particle duality [4] are only three of the most popular ones. Their study provides us with a deeper understanding of nature and opportunities for new technology [115–118]. All the mentioned effects contradict our every-day ideas of physical reality. Although the different interpretations of quantum mechanics are equivalent in predicting measurement outcomes, their conflicting assumptions of the fundamental mechanisms vary greatly.

Another such effect concerns the location of a particle and its properties in an interferometer. Usually, a particle and its properties are considered as inseparable. In contrast, Aharonov *et al.* [22] described intriguing interferometer experiments in which different properties of a physical entity appear to be spatially separated – localised in different paths/sub-beams of an interferometer. Aharonov *et al.* coined

the term quantum Cheshire Cat (qCC) in tribute to similar behaviour of the so-called Cheshire Cat in Lewis Carroll’s “Alice’s Adventures in Wonderland” [119]. In the novel, different parts of the Cheshire Cat can appear independently of each other.

Reference [22] suggests applying an interaction in a particular sub-beam of an interferometer. If this generates conspicuous reactions of the detected intensity, the authors propose that the property associated with the interaction is localised in the manipulated sub-beam. The apparent separation of properties emerges in a pre- and post-selection procedure. In the interpretation of Reference [22], by applying an interaction in a path, a statement about the location of a property is deduced. To combine all deduced statements, the disturbance of the interactions needs to be small. This is achieved by choosing small interaction strengths such that the interactions are weak, only minimally disturbing the quantum state. Due to the small disturbances, the locations of the properties cannot be determined for a single neutron but only with the statistics of an ensemble. From the appearance of conspicuous reactions to each weak interaction when applied in a different path, the separation of properties is concluded.

The first experimental realisation of a qCC was reported by Denkmayr *et al.* [23] in a two-path neutron interferometer with the properties of particle and spin. While a particle is affected by an absorber, a neutron-spin interacts with magnetic fields. Implementing the absorption in one path affected the detected mean intensity and implementing a magnetic field in the other path affected the interference contrast, giving rise to the perception of a spatial separation between particle and spin.

A selection of other implementations of the Cheshire Cat effect and some discussions can be found in [120–129]. Possible experimental improvements were suggested, such as the simultaneous realisation of all weak measurements [22], further consideration of not only the first-order but the second-order reactions to the midway interaction [123], and the implementation of additional degrees of freedom as pointer systems [124]. Critique was expressed, for instance, questioning whether the observed effect is purely quantum mechanical [120] and concerning the midway interaction strength [127].

A generalised form of the qCC with arbitrarily many degrees of freedom and properties was proposed by Pan [130]. This chapter presents a three-path quantum Cheshire Cat in a neutron interferometric experiment [100, 131, 132] by additionally using the energy as third property. The schematic of the three-path qCC is illustrated in Fig. 4.1. Each part of the cat corresponds to a property of the neutron. When directly attributing the location of properties to reactions to local manipulations, the associations are as follows: a direct-current (DC) spin rotation affects the spin, a radio-frequency (RF) rotation the energy, and absorption the particle. The reactions to the weak interactions are observed and weak values are determined to quantify the reactions. By means of this extended version it is demonstrated how the qCC emerges through the projection of the involved state vectors and the cross-term of amplitudes from different interferometer paths. This will make the essence of the qCC evident.

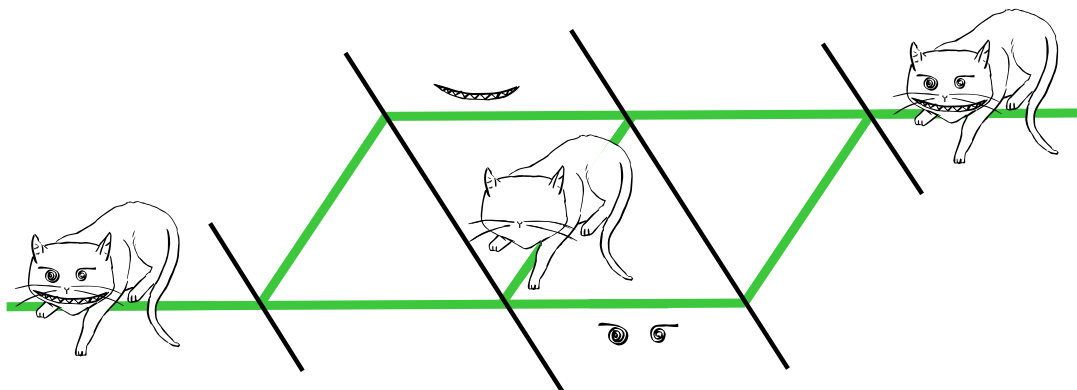


Figure 4.1: **Schematic of the paradoxical effect of the three-path quantum Cheshire Cat.** The cat is separated into three different parts inside the interferometer. This is analogous to how the neutrons and their properties behave in the present experiment. The parts of the cat correspond to the neutron properties of spin (grin), particle (body) and energy (eyes). The reactions to the weak interactions applied during the experiment may lead to the perception that the properties of the neutron are separated.

## 4.2 Schematic and Theory

The experiment was carried out on the neutron interferometry station S18 at the high-flux reactor of the Institut Laue-Langevin (ILL) in Grenoble, France. All neutron optical elements used are described in Sec. 3. The neutrons are monochromatised with a silicon perfect-crystal to a wavelength  $\lambda = 1.9 \text{ \AA}$  and then polarised by magnetic prisms [133] to the upward  $+z$ -direction which defines the quantisation axis. We will use the symbols  $\uparrow$  and  $\downarrow$  to refer to up and down spin states, respectively, which correspond to the  $\pm z$ -directions. The setup downstream of monochromator and polarisers is depicted in Fig. 4.2. The beam is split by the first two of four plates of a silicon perfect-crystal interferometer into the three separated sub-beams indexed by  $j \in \{\text{I, II, III}\}$ . Through recombination of all sub-beams, the O-beam in forward direction and the H-beam in diffracted direction are produced. The H-beam is only used for monitoring. A spin analysis is implemented in the O-beam by a polarising CoTi multilayer array, referred to as a supermirror. The intensities of O- and H-beam are recorded by  $^3\text{He}$  counting tubes. Inside the interferometer, two phase shifters (PS1 and PS2) control the phase relations between the three paths. Furthermore, if necessary, a weak spin or energy manipulation or a weak beam attenuation is applied in the interferometer.

The experimental procedure is divided into the three stages of pre-selection, weak interaction and post-selection. The pre-selection is realised by monochromator, polarising magnetic prisms, the beam splitters of the interferometer and two spin flippers in paths I and III. The spin flipper in path I induces a static DC spin flip and the one in path III an RF spin flip, where the frequency  $f$  of the oscillating field is 60 kHz (see Sec. 4.3 for details of adjustment). The RF spin flip also changes the energy by  $\Delta E = hf \approx 0.25 \text{ neV}$ , shifting the initial kinetic energy  $E_0 \approx 25 \text{ meV}$  of the thermal neutrons to the new energy  $E' = E_0 - \Delta E$ , with  $\Delta E/E_0 \approx 10^{-8}$ . The combined effect of the aforementioned neutron optical components makes the sepa-

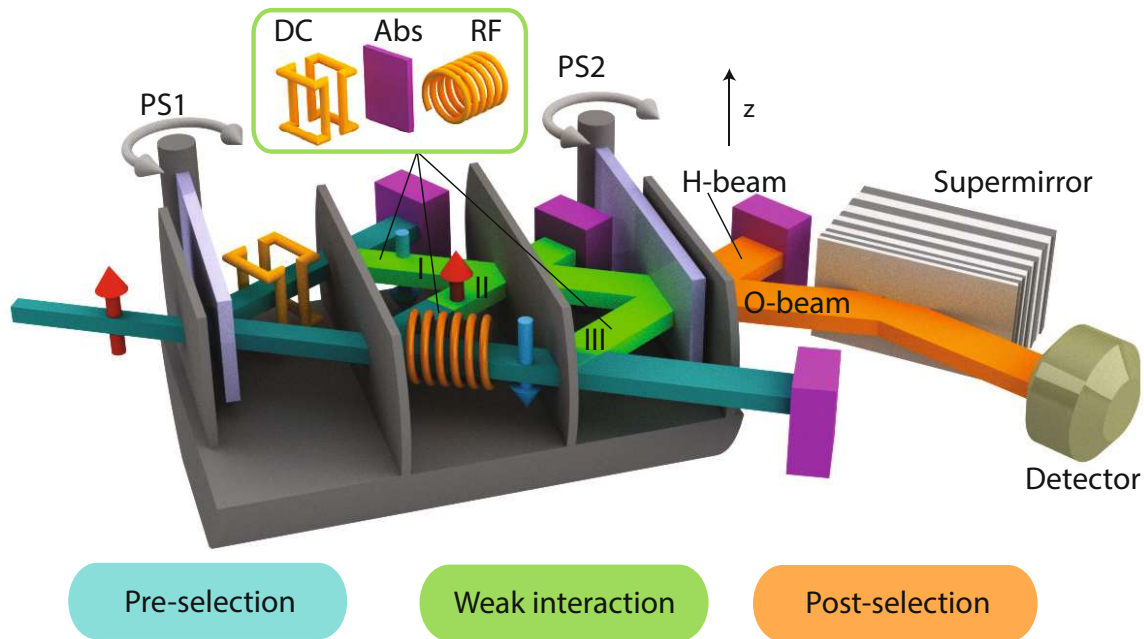


Figure 4.2: **Setup of the neutron interferometer experiment downstream of monochromator and polariser.** An incoming neutron beam which is polarised in  $+z$ -direction (red arrows) is split into three paths inside a perfect-crystal interferometer. All sub-beams are recombined and the neutrons in the outgoing O-beam are detected. The H-beam is only used for monitoring. The experiment consists of three stages: first, the pre-selection or preparation stage (turquoise) where direct-current (DC) and radio-frequency (RF) spin manipulators flip the local spin vectors to the downward orientation (blue arrows) and produce three pairwise orthogonal sub-beams, cf. text and Eq. (4.1). Second, the weak interaction stage (green) where one of three interactions, i.e. beam attenuation/absorption (abs) as well as DC and RF spin rotations, can be applied weakly in one of the three paths. Finally, the analysis or post-selection (orange) where the phase shifters (PS) 1 and 2 determine the phases  $\chi_1$ ,  $\chi_2$ , cf. Eq. (4.2). At the recombination of the sub-beams and at the supermirror, respectively, the post-selection projects the incoming state onto a specific phase relation between the sub-beams in the O-beam and onto the up spin state. Since for the given pre- and post-selection of Eqs. (4.1) and (4.2) only the amplitude through path II is accepted by the post-selection, path II is referred to as the reference beam.

## 4.2 Schematic and Theory

rated sub-beams pairwise orthogonal when recombined: while the spin orientation is up in path II and down in paths I and III, the latter two are in different energy states. The two energy states exhibit time-dependent interference on the microsecond scale [134]. However, the detected counts are time-integrated and the given intensities are regarded as time averaged intensities such that the time-dependent interference is not observable. Our model only needs to describe the observable effects and we assume the two energy states to be orthogonal to each other. Therefore, the two occupied energy levels and their respective two-level system behave like a pseudospin system as applied earlier [49, 135–137]. We will use the bracket notation as an abbreviation to refer to the energy vectors as well as the path and spin vectors. The according triply entangled pre-selected initial state  $|i\rangle$  is then written as

$$|i\rangle = \frac{1}{\sqrt{3}} \left( |I, \downarrow, E_0\rangle + |II, \uparrow, E_0\rangle + |III, \downarrow, E'\rangle \right). \quad (4.1)$$

Therein, all states from different Hilbert spaces associated with a sub-beam are written together in a single ket for each path. The post-selection consists of PS1 and PS2 with their induced relative phases  $\chi_1$  and  $\chi_2$ , the analysing crystal plates and the supermirror in the O-beam. The post-selection is represented by the projector onto the state  $|f\rangle$  given by

$$|f\rangle = |f(\chi_1, \chi_2)\rangle = \frac{1}{\sqrt{3}} |\uparrow\rangle \left( e^{i(\chi_2 - \chi_1)} |I\rangle + e^{i(\chi_1 + \chi_2)} |II\rangle + e^{i(\chi_1 - \chi_2)} |III\rangle \right), \quad (4.2)$$

which does not contain any energy terms, meaning no energy selection is employed in the post-selection. Therefore, all neutrons with up-spins and specific phase relations between the paths and arbitrary energy are selected to propagate towards the detector. We choose to attribute both phase shifts to the post-selection rather than the preparation; both approaches are equivalent. The post-selected intensity  $|\langle f|i\rangle|^2$  only has a single non-zero contribution, coming from path II, while the components from the other paths in the initial state  $|i\rangle$  are orthogonal to  $|f\rangle$  such that their contributions to the post-selected intensity are zero. Consequently, given the pre-selection, only the component of the sub-beam through path II is post-selected. We will therefore refer to path II as the reference beam in our experiment. The other paths I and III can contribute to the post-selected intensity, however, when additional weak interactions are applied as described in the next paragraph. In contrast to the generalised proposal by Pan [130] (see Sec. 4.4), our post-selection is not energy selective. Nonetheless, our setup exhibits the same effects in the limit of small interaction strengths as clarified in Sec. 4.4.

In the weak interaction stage between pre- and post-selection, we apply a weak DC or RF spin rotation, or a beam attenuation. (For the reference measurements, all weak interactions are turned off.) The interaction strengths are tuned by the DC/RF spin rotation angles  $\alpha_{\text{rot}} = \pi/9 \hat{=} 20^\circ$ , and the absorption coefficient  $\mathcal{A} = 0.1$  as realised by an indium foil of 0.125 mm thickness. The absorption differs from the cases of DC/RF spin manipulations as it is not a unitary operation; the conceptual implications will be explained throughout this chapter. We apply only one interaction in one beam at a time. Any of the three interactions can be applied to any of the three paths, obtaining nine different situations. All interactions are weak

and create only small disturbances on the initial state. By combining the results of each single situation, we infer the locations of each property of the detected neutrons between pre- and post-selection.

The relevant matrices for the spin and energy flips in the DC and RF cases are given by

$$\hat{\sigma}_x^{\text{DC}} = |\uparrow\rangle\langle\downarrow| + |\downarrow\rangle\langle\uparrow| = \begin{pmatrix} 0 & 1 \\ 1 & 0 \end{pmatrix}_{\text{spin}} \quad (4.3)$$

and

$$\hat{\sigma}_x^{\text{RF}} = \hat{\sigma}_x^{\text{DC}} \otimes \left( |E'\rangle\langle E_0| + |E_0\rangle\langle E'| \right) = \begin{pmatrix} 0 & 1 \\ 1 & 0 \end{pmatrix}_{\text{spin}} \otimes \begin{pmatrix} 0 & 1 \\ 1 & 0 \end{pmatrix}_{\text{energy}}, \quad (4.4)$$

respectively. The path projectors  $\hat{\Pi}_j = |j\rangle\langle j|$  indicate in which path an operation or manipulation is conducted. Then the unitary operators for spin and energy rotations  $\hat{U}_j^{\text{DC}}$  and  $\hat{U}_j^{\text{RF}}$ , with the rotation angle  $\alpha_{\text{rot}}$  around the  $x$ -axis in path  $j$ , while leaving the states in the other paths unchanged, can be expressed as (detailed calculation in Sec. A.1)

$$\begin{aligned} \hat{U}_j^{\text{DC}}(\alpha_{\text{rot}}) &= \exp\left(-i\frac{\alpha_{\text{rot}}}{2}\hat{\sigma}_x^{\text{DC}}\hat{\Pi}_j\right) \\ &= \mathbb{1} - \left(1 - \cos\left(\frac{\alpha_{\text{rot}}}{2}\right)\right)\hat{\Pi}_j - i\sin\left(\frac{\alpha_{\text{rot}}}{2}\right)\hat{\sigma}_x^{\text{DC}}\hat{\Pi}_j \quad \text{and} \\ \hat{U}_j^{\text{RF}}(\alpha_{\text{rot}}) &= \exp\left(-i\frac{\alpha_{\text{rot}}}{2}\hat{\sigma}_x^{\text{RF}}\hat{\Pi}_j\right) \\ &= \mathbb{1} - \left(1 - \cos\left(\frac{\alpha_{\text{rot}}}{2}\right)\right)\hat{\Pi}_j - i\sin\left(\frac{\alpha_{\text{rot}}}{2}\right)\hat{\sigma}_x^{\text{RF}}\hat{\Pi}_j. \end{aligned} \quad (4.5)$$

The  $x$ -direction is always defined by the beam direction in the respective section of the setup (see Sec. 4.3 for further explanation). Equation (4.5) indicates that the DC (RF) spin rotation reduces the amplitude of the original spin component (spin/energy component) in the corresponding path  $j$  from 1 to  $\cos(\alpha_{\text{rot}}/2)$  and creates a spin-flipped (spin/energy-flipped) component of amplitude  $-i\sin(\alpha_{\text{rot}}/2)$ . In the limit of small  $\alpha_{\text{rot}}$ ,  $\sin(\alpha_{\text{rot}}/2)$  is linear in  $\alpha_{\text{rot}}/2$ , while the change of the original component,  $1 - \cos(\alpha_{\text{rot}}/2)$ , is smaller, proportional to  $\alpha_{\text{rot}}^2/8$ .

The operator  $\hat{A}_j^{\text{Abs}}(\mathcal{A})$  for a weak absorption is written as

$$\hat{A}_j^{\text{Abs}}(\mathcal{A}) = \mathbb{1} - (1 - \sqrt{1 - \mathcal{A}})\hat{\Pi}_j. \quad (4.6)$$

It simply describes an attenuation in path  $j$  while all other paths are undisturbed.

To define post-selected states which are discriminated in their energy degrees of freedom, we introduce two ancillary states

$$|f_0\rangle = |f\rangle|E_0\rangle \quad \text{and} \quad |f'\rangle = |f\rangle|E'\rangle \quad (4.7)$$

and define the weak value [24, 51, 52, 138, 139] for the hypothetical energy selection of  $|E_0\rangle$  as

$$\langle\hat{O}\rangle_w^{E_0} = \frac{\langle f_0|\hat{O}|i\rangle}{\langle f_0|i\rangle}. \quad (4.8)$$

As we will see shortly, the weak values of the operators  $\hat{\sigma}_x^{\text{DC}}\hat{\Pi}_j$ ,  $\hat{\Pi}_j$  and  $\hat{\sigma}_x^{\text{RF}}\hat{\Pi}_j$ , where  $j$  denotes the path, describe our results. The operator  $\hat{\sigma}_x^{\text{DC}}\hat{\Pi}_j$  represents the

## 4.2 Schematic and Theory

$x$ -component of the spin in path  $j$ , while the operator  $\hat{\sigma}_x^{\text{RF}} \hat{\Pi}_j$  is the  $x$ -component of the energy observable in path  $j$  which is associated with flipping in the energy system. The calculation of their weak values is straightforward for the initial and final states given in Eqs. (4.1) and (4.2) and yields

$$\begin{aligned}\langle \hat{\sigma}_x^{\text{DC}} \hat{\Pi}_j \rangle_w^{E_0} &= \delta_{j,\text{I}} e^{2i\chi_1}, \\ \langle \hat{\Pi}_j \rangle_w^{E_0} &= \delta_{j,\text{II}}, \quad \text{and} \\ \langle \hat{\sigma}_x^{\text{RF}} \hat{\Pi}_j \rangle_w^{E_0} &= \delta_{j,\text{III}} e^{2i\chi_2}.\end{aligned}\tag{4.9}$$

The Kronecker delta  $\delta_{i,j}$  yields the modulus of the respective weak value. Quantifying the location of properties through the weak values, a modulus of an operator's weak value of 1, which is one of the operator's eigenvalues, is attributed to finding the corresponding property in the considered path. A modulus of the weak value of zero excludes finding the property in that path.

With these expressions, the time-averaged intensity  $I$  in the post-selected output port of the interferometer, with a weak DC spin rotation applied (DC case) in path  $j$ , is written as (details in Sec. A.1)

$$\begin{aligned}I_j^{\text{DC}}(\chi_1) &= \left| \langle f | \hat{U}_j^{\text{DC}}(\alpha_{\text{rot}}) | i \rangle \right|^2 \\ &= |\langle f | i \rangle|^2 \left[ 1 + \alpha_{\text{rot}} \text{Im} \left\{ \langle \hat{\sigma}_x^{\text{DC}} \hat{\Pi}_j \rangle_w^{E_0} \right\} + \frac{\alpha_{\text{rot}}^2}{4} \left( \frac{|\langle f_0 | \hat{\sigma}_x^{\text{DC}} \hat{\Pi}_j | i \rangle|^2}{|\langle f | i \rangle|^2} + \frac{|\langle f' | \hat{\sigma}_x^{\text{DC}} \hat{\Pi}_j | i \rangle|^2}{|\langle f | i \rangle|^2} \right) \right. \\ &\quad \left. - \frac{\alpha_{\text{rot}}^2}{4} \text{Re} \left\{ \langle \hat{\Pi}_j \rangle_w^{E_0} \right\} + \mathcal{O}(\alpha_{\text{rot}}^3) \right] \\ &= \frac{1}{9} \left[ 1 + \alpha_{\text{rot}} \delta_{j,\text{I}} \sin(2\chi_1) + \frac{\alpha_{\text{rot}}^2}{4} (\delta_{j,\text{I}} - \delta_{j,\text{II}} + \delta_{j,\text{III}}) \right] + \mathcal{O}(\alpha_{\text{rot}}^3).\end{aligned}\tag{4.10}$$

The second and third lines describe the intensity in terms of weak values and terms closely resembling them. The last line gives the expected intensity in terms of phase shifter orientation and chosen path number. An intensity oscillation with an amplitude of order  $\alpha_{\text{rot}}$  emerges under the condition of the Kronecker delta  $\delta_{j,\text{I}}$ , which still gives the modulus of the respective weak value. This condition is met when the weak DC spin rotation is applied in path I. Then, part of the prepared down spin state, which is orthogonal to the reference state, is inverted to the up spin state, which is parallel to the reference state. The down-component is filtered out by the supermirror of the post-selection and the up-component is transmitted to the detector. Simultaneous to the emergence of the intensity oscillation, the mean intensity is increased by the additional parallel component with order  $\alpha_{\text{rot}}^2$  as also pointed out in [123]. The same mean intensity increase is expected from a weak DC spin rotation in the RF-flipped path III because the same up spin component is created which is transmitted through the supermirror. No intensity oscillation due to the differing energies is observable, though, in our time-integrating detection mode. In contrast, by applying the weak DC spin rotation in path II, the portion of the reference beam accepted by the supermirror is decreased with order  $\alpha_{\text{rot}}^2$ . For

small  $\alpha_{\text{rot}}$ , the first order term is dominant and the reactions to a weak DC spin rotation on the intensity in path I are conspicuous.

A similar result can be derived assuming a weak RF spin rotation (RF case) applied in path  $j$ :

$$\begin{aligned}
 I_j^{\text{RF}}(\chi_2) &= \left| \langle f | \hat{U}_j^{\text{RF}}(\alpha_{\text{rot}}) | i \rangle \right|^2 \\
 &= |\langle f | i \rangle|^2 \left[ 1 + \alpha_{\text{rot}} \text{Im} \left\{ \langle \hat{\sigma}_x^{\text{RF}} \hat{\Pi}_j \rangle_w^{E_0} \right\} + \frac{\alpha_{\text{rot}}^2}{4} \left( \frac{|\langle f_0 | \hat{\sigma}_x^{\text{RF}} \hat{\Pi}_j | i \rangle|^2}{|\langle f | i \rangle|^2} + \frac{|\langle f' | \hat{\sigma}_x^{\text{RF}} \hat{\Pi}_j | i \rangle|^2}{|\langle f | i \rangle|^2} \right) \right. \\
 &\quad \left. - \frac{\alpha_{\text{rot}}^2}{4} \text{Re} \left\{ \langle \hat{\Pi}_j \rangle_w^{E_0} \right\} + \mathcal{O}(\alpha_{\text{rot}}^3) \right] \\
 &= \frac{1}{9} \left[ 1 + \alpha_{\text{rot}} \delta_{j,\text{III}} \sin(2\chi_2) + \frac{\alpha_{\text{rot}}^2}{4} (\delta_{j,\text{I}} - \delta_{j,\text{II}} + \delta_{j,\text{III}}) \right] + \mathcal{O}(\alpha_{\text{rot}}^3).
 \end{aligned} \tag{4.11}$$

The results in the DC and RF cases are similar up to the exchange of  $\delta_{j,\text{I}}$ ,  $\delta_{j,\text{III}}$ , and  $\chi_1$  in the DC case, respectively, for  $\delta_{j,\text{III}}$ ,  $\delta_{j,\text{I}}$ , and  $\chi_2$  in the RF case.

In the third case of an added weak absorber (absorber case), the intensity  $I$  is described as (details in Sec. A.1)

$$\begin{aligned}
 I_j^{\text{Abs}} &= \left| \langle f | \hat{A}_j^{\text{Abs}}(\mathcal{A}) | i \rangle \right|^2 \\
 &= |\langle f | i \rangle|^2 \left[ 1 - \mathcal{A} \langle \hat{\Pi}_j \rangle_w^{E_0} \right] \\
 &= \frac{1}{9} [1 - \mathcal{A} \delta_{j,\text{II}}].
 \end{aligned} \tag{4.12}$$

As a result, only an attenuation of the sub-beam in path II with its prepared up spin state will be registered after the post-selection at the detector in the O-beam.

## 4.3 Experimental Data

### 4.3.1 Orienting the interferometer

The interferometer crystal depicted in Fig. 4.3 is oriented relative to the incident beam coming from the monochromator such that a maximum number of neutrons traverse the interferometer on the theoretically predicted paths. The orientation of the interferometer is defined through two angles which are both changed through rotation stages controlled through linear stages. The axes in the linear stages are adjusted roughly with stepper motors and fine tuned with Piezo crystals. The azimuthal angle  $\theta$  is changed in a so-called rocking scan. The polar angle  $\rho$  is changed through the so-called  $\rho$  axis. The adjustment of these angles is relative to the incident direction of the neutrons and therefore relative to the upstream monochromator. The orientation of the interferometer crystal determines which wavelength satisfies the Bragg condition of Eq. (3.9). If the lattice orientations differ between monochromator and interferometer, the neutrons selected by the monochromator do

### 4.3 Experimental Data



Figure 4.3: Photograph of the four-plate single crystal neutron interferometer used for the experiment presented in this section. The length is about 10 cm. At each interferometer plate, a beam splitting is produced in Laue configuration. This leads to three separated beam paths interfering at the last interferometer plate as depicted schematically in Fig. 4.2.

not precisely fulfil the Bragg condition at the interferometer crystal and the diffraction peak of the interferometer is broadened; the maximum intensity is reduced at the output ports. The broadening is equivalent to an increased divergence. With proper adjustment of the  $\rho$  axis, the neutrons impinge in a plane perpendicular to the crystal planes of the interferometer. This is supposed to be true when the basis for the interferometer is horizontal. However, there are deviations in the orientation of the monochromator crystal and manufacturing process of the interferometer. Consequently, the best alignment of the crystal basis is in general not horizontal.

When correctly orienting the crystal, the intensity in the O-beam is maximal. Dynamical theory of diffraction as introduced in Sec. 3.3.3 causes the diffracted H-beam of the interferometer to have a higher peak in intensity than the O-beam. Maximum intensity in O- and H-beam are coupled to each other.

Adjustment of the orientation starts by choosing which paths in the interferometer to keep open. The intensity in specific output beams changes with the phase relation between the paths. In the case of the present four-plate interferometer experiment, all paths are opened and the sum of all three output intensities is used in this section. (A different method is described for the second experiment presented in Sec. 5.4.2.) The outputs are O- and H-beam as well as the output from the first interferometer loop, as seen in Fig. 4.2. Using the sum renders the phase relation between the paths inconsequential for the total intensity. However, the intensity distribution over the three output ports is phase dependent. Each beam is characterised as a series of reflections and transmissions which determine properties such as the sharpness of the beam. In consequence, the sum of intensities may be distributed more sharply or broader dependent on the phase relations. The phase relation is assumed as constant for adjustment of the  $\rho$  axis.

A value for the  $\rho$  axis is chosen and a rocking scan is started. The resulting intensity is characterised by a Gaussian peak. By repeating the rocking scan for

different  $\rho$  axis values, , the rocking scans depicted in Fig. 4.4 were recorded. The sharpest rocking scan with highest intensity determines the value of the  $\rho$  axis for the remainder of the experiment.

To extract the broadness and height of the peaks, the intensities are fit. The fit function for the Gaussian peaks is chosen as

$$I(\theta) = I_0 \exp\left(-\frac{(\theta - \theta_0)^2}{2\sigma^2}\right), \quad (4.13)$$

with the maximum intensity  $I_0$ , the position of the maximum at  $\theta_0$  and the standard deviation  $\sigma$ . The intensity of each of the three output ports is close to a Gaussian distribution, centred at about the same position of the rocking angle with different standard deviations. Their sum is not a Gaussian function. Fitting the sum with a single Gaussian, either well characterises the peak or its tails. Since the purpose of this adjustment is to maximise the peak height, only the data between and close to the inclination points is used, as can be seen in Fig. 4.4. Even with cutting off the tails, the maxima of the fit are systematically lower than the data points, while the tails of the fit are systematically higher than the data points. This demonstrates that a Gaussian is suited but not the ideal to model the sum of different output intensities in a rocking curve. (A farther reaching argument is given by means of the rocking scans during the other presented experiment in Sec. 5.4.1.)

The resulting FWHMs from the fits are depicted in Fig. 4.5. The results of the re-evaluation, using all depicted data points in Fig. 4.4, are plotted in Fig. 4.5 in yellow. The blue data and fit refer to the ad hoc analysis. A function of the software used ad hoc during data acquisition is to drop data points below a certain threshold relative to the maximum intensity recorded. The threshold is typically at 70%. With this value, the tails of the peak are cut off even closer to the maximum than the inclination points are. This reduces effects from, e.g. background. The ad hoc results for the FWHMs are lower than their counter-parts in the re-evaluation, since the ad hoc analysis elevates the influence of the sharpest output peak. Due to statistical effects, the difference between the data sets is not amended by a single factor. Both analyses agree closely, however, on the value for  $\rho$  where the sharpest maximum emerges.

### 4.3.2 Interferograms with Empty Interferometer

Temperature stability in the environment of the interferometer is crucial to observe the interference effect. As stated in Secs. 3.3.3 and 4.3.1, an adjustment between the monochromator and interferometer crystal is necessary. In addition, when the spin-rotators are inserted in the interferometer, temperature adjustment of these devices is also essential to get high contrast of the interference fringes. A temperature scan of the water cooling circuit for the RF coils is depicted in Fig. 4.6 as yellow curve. As can be seen, the temperature was changed in steps of 0.2 °C. (Some systematic effects are explained in the caption of Fig. 4.6.) During the time for a step, three interferograms were recorded which resulted in interferometric contrasts depicted in Fig. 4.7. The contrast rises and falls again with changing temperature. When reducing the temperature, the first interferogram in each step exhibits a slightly lower contrast than the consecutive two interferograms. This can be attributed

### 4.3 Experimental Data

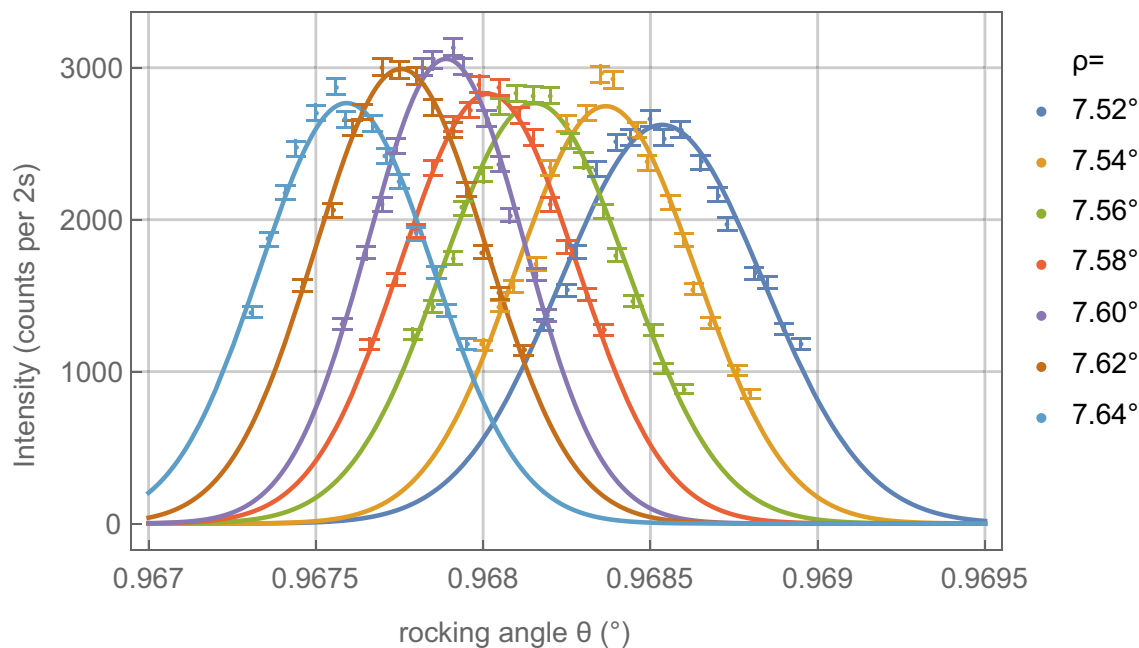


Figure 4.4: Counts of rocking curves for different  $\rho$  axis positions as indicated to the right. Error bars indicate one standard deviation. Fits of the form of Eq. (4.13) are plotted as solid curves. The counts of each rocking scan is the sum of the three output ports. Each output is modelled as a Gaussian function with different standard deviations. Therefore, the sum is not fitted well for both the peak and its tails. For the presented fits, only the data between the inclination points is used to fit the peak well.

to the high instability in temperature directly after each step. Nevertheless, it is curious why this effect is not as pronounced when increasing the temperature. The temperature interval, in which interference fringes are observed, stretches over  $\approx 1^\circ\text{C}$ . This concerns the mean temperature. Recurring disturbances in temperature of this order of magnitude have to be avoided to observe interference fringes at all. The necessary temperature stability to reach a saturation in contrast is estimated to be of the order  $0.1^\circ\text{C}$ - $0.01^\circ\text{C}$ .

The contrasts are plotted in Fig. 4.8 dependent on the water temperature for the RF coils. A fit indicates the temperature for the highest contrast. The fit gave a temperature different from the temperature measured at the monochromator. We questioned this discrepancy at first. However, there is a systematic difference of about  $0.2^\circ\text{C}$  in the temperature sent to the water cooling control system on the one hand and the temperature measured at the housing of the coils in the interferometer on the other hand. Therefore, the ideal water temperature for the water cooler is effectively the same as the temperature at the monochromator.

Each pair of sub-beams constitutes an interference loop. They are referred to as front, rear and outer loop which are composed, respectively, of beams I and II, beams II and III, and beams I and III. To confirm the initial coherence of the sub-beams in the interferometer, interferograms (IFGs) of the interferometer empty of any local fields or absorbers were recorded which are depicted in Fig. 4.9. In the left case of Fig. 4.9, only phase shifter 1 (PS1) was rotated and phase shifter 2 (PS2) was oriented such that the rear loop passes on a maximum intensity in

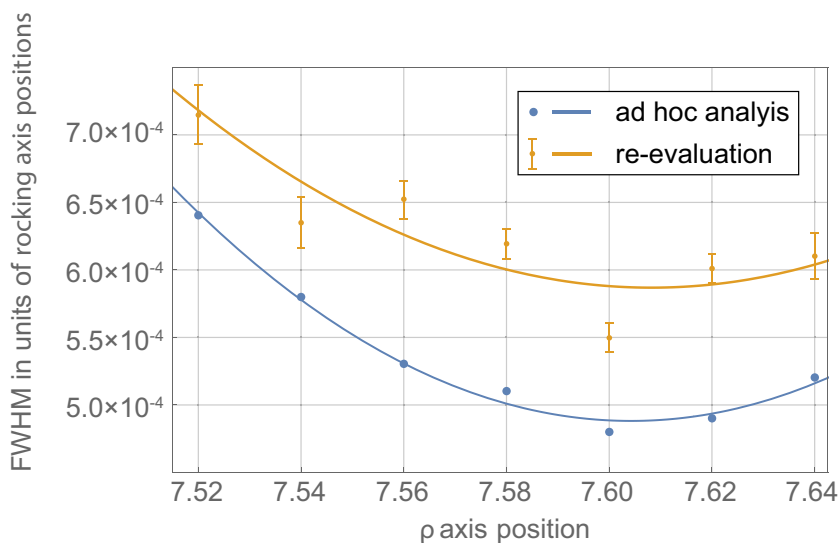


Figure 4.5: Full widths at half maxima (FWHM) plotted over  $\rho$  axis position. Blue data refers to the ad hoc analysis. Yellow data is the re-evaluation after the measurement campaign. Error bars indicate one standard deviation. Polynomial fits to the second order in  $\rho$  are plotted as solid curves.

O-direction (see Fig. 4.2). Likewise, in the right case only PS2 was rotated and PS1 was oriented such that the front loop passes on a maximum intensity towards the last interferometer plate. In the middle case, both PS1 and PS2 are initially oriented such that a maximum intensity is acquired in O-direction. The IFG is then recorded by simultaneously rotating both PS1 and PS2 to induce a relative phase between the reference beam II and the other two sub-beams. Contrasts  $\geq 50\%$  were reached which indicate the moderate level of coherence achievable with our interferometer in the respective loops. The specific values, given in the caption of Fig. 4.9, are used in the data analysis of Sec. 4.3.6 to compare the observed contrasts when applying weak interactions.

### 4.3 Experimental Data

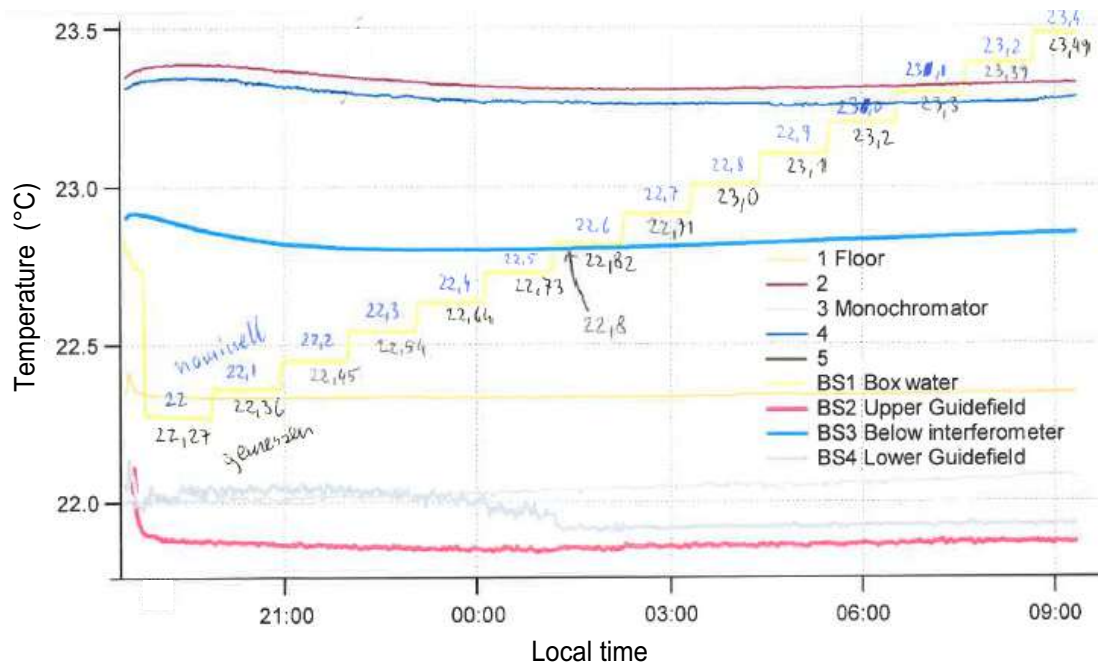


Figure 4.6: Temperatures at different sensor positions of the setup plotted dependent on the local time. The temperature of the two guide field coils are plotted in red and gray. The water in the same cooling circuit flows through the upper coil first. The lower coil is therefore warmer. The unstepped yellow temperature is recorded at a sensor on the floor. It has a sharp peak with a width of several minutes at the beginning of the graph at about 8 p.m. This can be attributed to opening the doors to the instrument a last time to check on the setup before the end of the shift. The top blue and red temperatures (sensors 2 and 4) at higher positions are more inert to this disturbance and stabilise only after multiple hours. The blue curve indicates the temperature recorded by a sensor below the interferometer. This temperature can be compared to the temperature of the water which cools the coils inside the interferometer, plotted in yellow with multiple steps. This yellow temperature is regulated by a water cooling system in the outer room of the instrument S18, cf. Sec. 3.3.6. The yellow water temperature is changed in steps of 0.2°C. The temperature is indicated with two values. The nominal temperature which is sent to the water cooling system is written on top. The temperature measured with a sensor positioned on the housing of the cooled coils is written below. During each step, interferograms are recorded. The contrasts of these interferograms is depicted in Fig. 4.7.

## 4 Three-Path Quantum Cheshire Cat

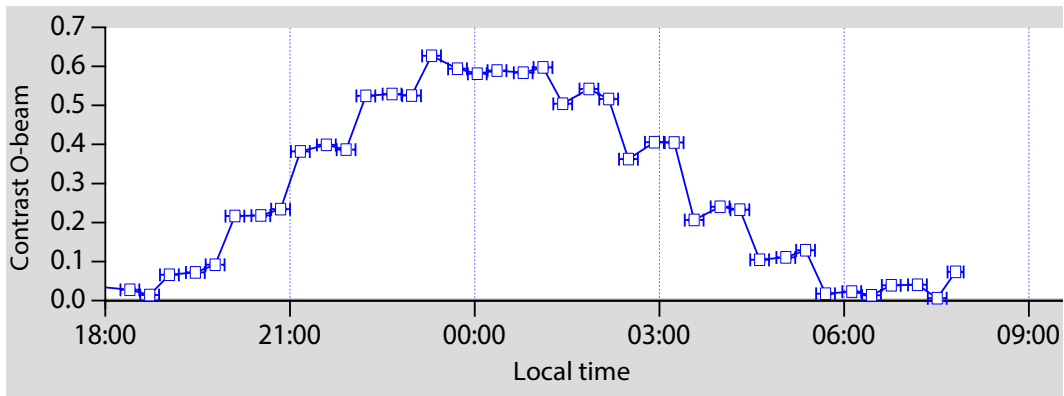


Figure 4.7: Contrasts of interferograms plotted dependent on the local time. The temperature in the water cooling circuits of the coils in the interferometer was scanned as depicted in Fig. 4.6. At each step of the temperature, three interferogram loops were recorded by inducing a relative phase shift in each of the three interference loops. The contrasts are extracted from sinusoidal fits. The contrast increases to a maximum before falling again. These contrast values are plotted dependent on the regulated water temperature in Fig. 4.8.

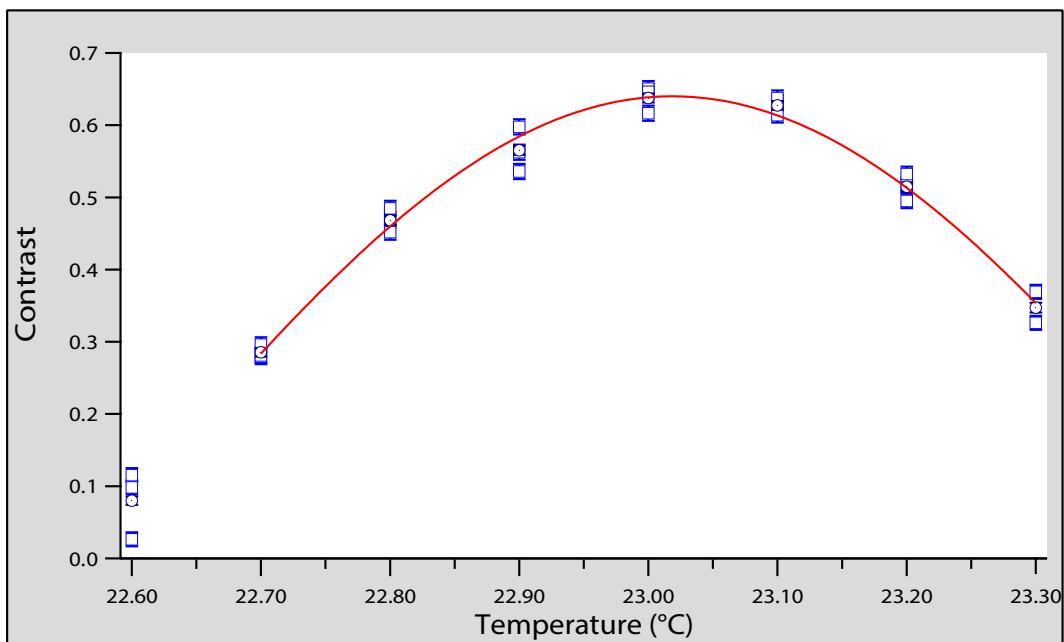


Figure 4.8: Contrasts of interferograms plotted dependent on the water temperature for the coiling circuit running through the magnetic coils in the interferometer. Error bars indicate one standard deviation. The temperature scan and the contrasts of interferograms recorded during this time are depicted in Figs. 4.6 and 4.7. A parabolic fit function is chosen to determine the temperature at which the highest interferometric contrast is achieved.

### 4.3 Experimental Data

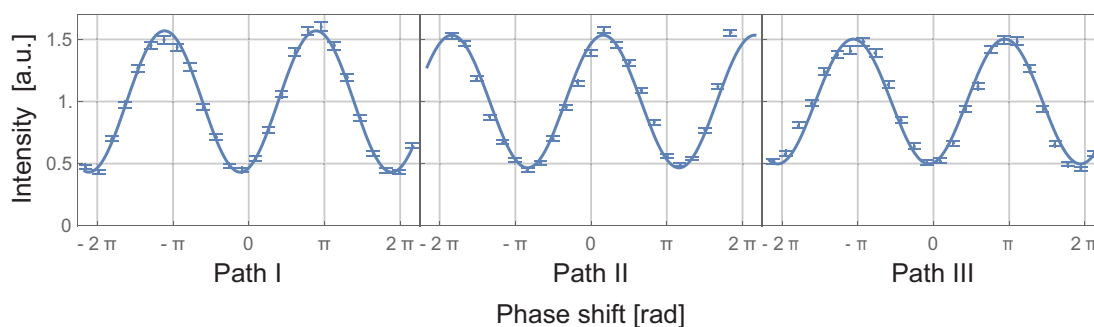


Figure 4.9: **Interferograms and their fits for the empty interferometer.** Intensity detected in the O-beam normalised by mean intensity plotted against phase shift induced in the path specified at the bottom. The integration time per point is 30 s with a mean count rate of about 50/s. The statistical error bars indicate one standard deviation. Contrasts are extracted from the respective sinusoidal fits plotted as solid lines. The contrasts from left to right of 57(1)%, 53(3)%, and 50(2)% indicate the achievable level of coherence.

### 4.3.3 Coil Adjustment

We define the  $z$ -axis vertically and the  $x$ -axis by the local beam direction in each section of the interferometer. Alternatively, one could differentiate between the orientations of the coils by explicitly defining global  $x$ - and  $y$ -axes. This would add a phase shift to certain spin components. Since the analysis of the data will not require a detailed justification of the phase shift between different IFGs, a local definition suffices.

For both DC and RF coils, the currents for a spin flip have to be adjusted. These currents regulate the magnetic fields in  $x$ - and  $z$ -direction of each coil. The frequency for the RF coils is chosen as 60 kHz. This corresponds to a resonant field of about 20 G=2 mT local guide field strength. A global guide field of about 10 G is applied to allow for both RF and DC spin rotations: while this field is compensated to a net zero  $z$ -field in coils when applying DC rotations, it is approximately doubled to meet the flip condition for RF rotations. This combination minimises inhomogeneities in the fields of the miniature spin rotators [140, 141]. To roughly adjust and determine the flip currents in both the DC as well as RF coils, only the respective sub-beam is used, while all others are blocked by beam stoppers. This composes a polarimetric setup and the intensity is measured with varied  $z$ -field and rotation currents. Estimates for guide field compensation (DC case) and amplification (RF case) are determined as well as for the currents/amplitudes  $I_{\text{flip}}$  for the  $x$ -fields of DC and RF flips. After that an interferometric method is used to ensure low initial contrasts: as spin flips produce an orthogonal state compared to the reference beam of path II, interferograms have minimal contrast at the flip conditions. When recording several interferograms with slightly varied currents  $I$  applied as described in the polarimetric case above, the resulting contrasts should have a sharper minimum due to the behaviour proportional to  $|\sin(I - I_{\text{flip}})|$  which is locally proportional to  $I - I_{\text{flip}}$ . This has to be compared to the direct polarimetric approach with its cosine behaviour of the intensity which is locally proportional to  $(I - I_{\text{flip}})^2$  at its differentiable minimum.

A typical adjustment scan is depicted in Fig. 4.10 where the contrast is found the lowest at 1.5 A. To both sides of that value, the contrast is increasing at lowest order linearly. A residual contrast of about 3% remains which is dominant in a small current interval at the minimum and which quantifies the overall spin manipulation efficiency of the setup.

A principal source for reduced spin manipulation efficiencies  $\epsilon_I$ ,  $\epsilon_{III}$  in paths I and III are the field inhomogeneities over the beam cross-section. The systematic errors of the preparational contrast are estimated in Tab. 4.5. The efficiencies can be estimated by assuming a pure state but with components unaffected by the preparing DC and RF flippers. The component  $\epsilon_I$  is spin flipped by the DC flipper in path I, while the remaining component stays in the reference state. Similarly, the component  $\epsilon_{III}$  is spin-energy flipped by the RF flipper in path III while the remaining component stays in the reference state. The unaffected components are still coherent and interfere at recombination with the reference state from path II; a residual final contrast is observed. This reasoning can be extended to the weak measurement IFGs where the weak interactions modify the spin manipulation efficiencies to the values  $\epsilon'_I$ ,  $\epsilon'_{III}$  and according contrast values for the off-diagonal elements of Fig. 4.12.

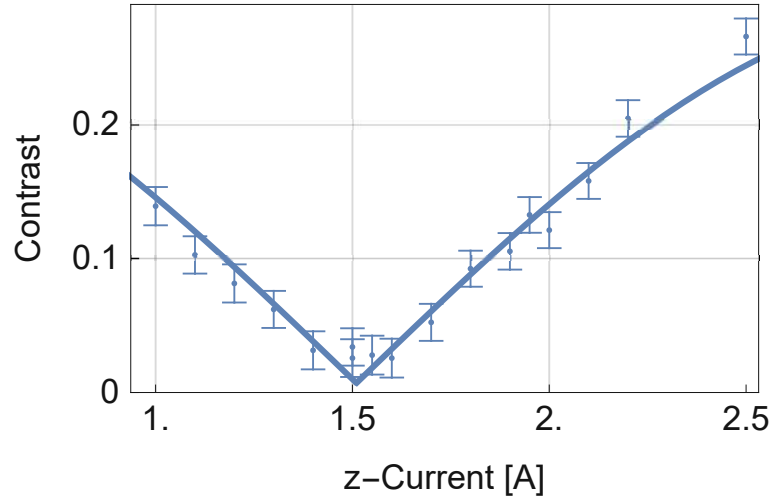


Figure 4.10: **Coil adjustment through contrast measurements.** The blue dots indicate the contrasts recorded with a radio-frequency (RF) spin flipper in operation and the current  $I$  for its local guide field amplification varied. The blue statistical error bars indicate one standard deviation, solid blue curve is the fit. Around the minimum at  $I_{\text{flip}}$ , the contrast has a local behaviour proportional to  $|I - I_{\text{flip}}|$  and therefore a sharper minimum than with a polarimetric approach via the intensity.

#### 4.3.4 Interferograms with Applied Preparation

The preparation of the initial state, given in Eq. (4.1), is implemented by a DC flip in path I and an RF flip in path III. Let us call the measured IFGs, depicted in Fig. 4.11, preparational IFGs. Phase shifts are implemented in all three paths, resulting in the three columns of Fig. 4.11. The fit function for the time-averaged intensity of all IFGs is of the form

$$I(\chi) = I_0 + B \sin(\omega\chi + \varphi), \quad (4.14)$$

with the mean intensity offset  $I_0$  and an intensity oscillation with amplitude  $B$ , angular velocity  $\omega$ , the phase shifter orientation  $\chi$ , and the phase offset  $\varphi$ . Contrasts extracted from the fits are given in Tab. 4.1. The preparational IFGs characterise the orthogonality of the initial sub-states and are a reference for the quantitative data analysis. The obtained contrast values quantify the quality of the preparation. We will refer to the following  $3 \times 3$  arrays of IFGs or numbers as matrices and to their diagonal, off-diagonal, and anti-diagonal elements as in a normal square matrix.

As stated in Sec. [Coil Adjustment](#), to meet the resonance condition for spin rotations, the external guide field is locally suppressed by a compensation field for the weak DC rotations, while it is locally increased for the weak RF rotations. All local fields create stray fields and switching them on and off induces field offsets and inhomogeneities in the adjacent coils which lower the efficiency of their spin manipulations. The offsets can be compensated with our devices but the inhomogeneities cannot.

When the preparation is applied in anticipation of the weak RF measurements, we chose to leave the local guide field amplification permanently turned on and compensate the field offset in the adjacent coils. Then only the RF-field is turned

on and off rather than both the RF and  $z$ -fields. This technique lowers the efficiency of the manipulations through the inhomogeneities in the preparational cases but increases the overall efficiency when the weak interactions are applied later on. The technique cannot be applied in the DC case because it would create a zero-field region which induces depolarisation. When the preparation is applied anticipating measurements with weak absorptions, the global guide field is remained as in the DC case. The experimental parameters slightly shifted in time, however, between absorption and DC case. Consequently, there are different preparational adjustments applied which ought to produce the same pre-selected state. This is the reason why there are multiple rows of preparational IFGs and their contrasts in Fig. 4.11 and Tab. 4.1.

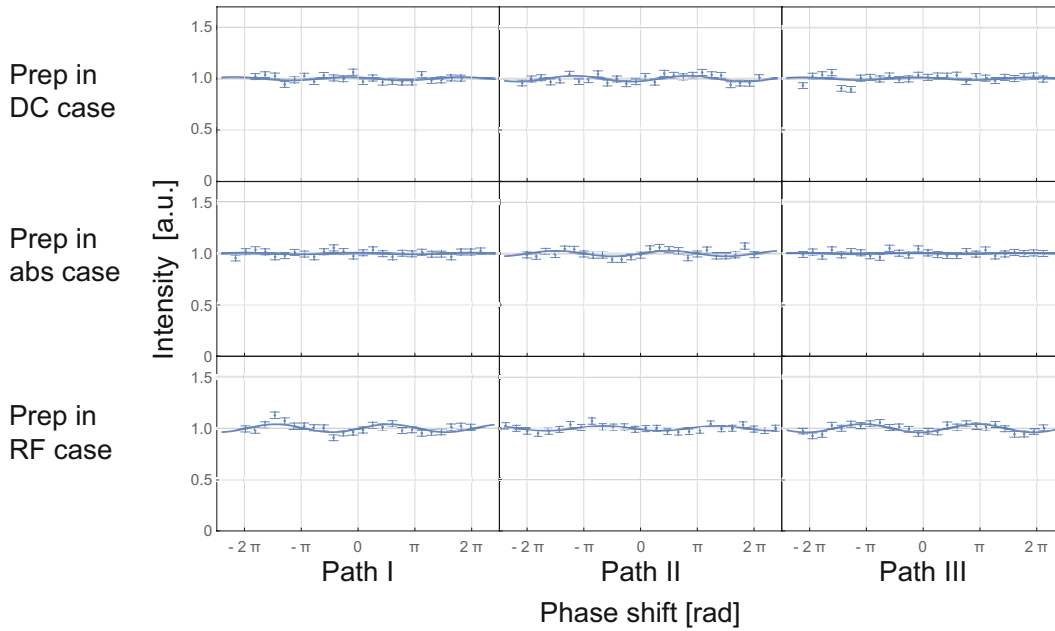


Figure 4.11: **Interferograms and their fits with preparation applied.** The blue data points indicate the intensities detected in the O-beam normalised by mean intensities plotted against phase shifts induced in the path specified at the bottom. The integration time per point is 90 s with a mean count rate of about 15/s. The blue statistical error bars indicate one standard deviation. The three rows of interferograms in the figure are obtained with different configurations for the preparation (prep) for the direct-current (DC), absorber (abs), and radio-frequency (RF) case as written to the left, which are used for different further reference measurements (see Sec. 4.3 for further explanation). Contrasts are extracted from sinusoidal fits plotted as solid blue lines. The low contrasts  $\leq 4\%$ , given in Tab. 4.1, imply a good preparational quality, i.e. a high degree of orthogonality between the sub-beams.

### 4.3.5 Interferograms with Applied Preparation and Weak Interaction

The preparation is assumed to be applied from now on. Finally, when separately applying one of the three weak interactions in one of the three sub-beams, the nine IFGs presented in Fig. 4.12 were recorded, which will be called weak-interaction

<b>Contrasts with preparation</b>			
<b>preparation for weak interaction</b>	<b>phase shift in path</b>		
	I	II	III
DC	$1.7\%_{\pm 4\% \text{ sys}}^{\pm 0.9\% \text{ stat}}$	$2.8\%_{\pm 4\% \text{ sys}}^{\pm 0.9\% \text{ stat}}$	$1.3\%_{\pm 4\% \text{ sys}}^{\pm 1.1\% \text{ stat}}$
Abs	$0.8\%_{\pm 4\% \text{ sys}}^{\pm 0.7\% \text{ stat}}$	$2.7\%_{\pm 4\% \text{ sys}}^{\pm 0.9\% \text{ stat}}$	$0.3\%_{\pm 4\% \text{ sys}}^{\pm 0.6\% \text{ stat}}$
RF	$3.8\%_{\pm 4\% \text{ sys}}^{\pm 1.1\% \text{ stat}}$	$2.3\%_{\pm 4\% \text{ sys}}^{\pm 0.6\% \text{ stat}}$	$4.0\%_{\pm 4\% \text{ sys}}^{\pm 0.6\% \text{ stat}}$

Table 4.1: Contrasts of fitted interferograms in Fig. 4.11 with preparations applied for the three different weak interactions but without the weak interactions themselves. The statistical errors (stat) given indicate one standard deviation. The systematic errors (sys) are estimated in the Tab. 4.5. The three rows are obtained with different configurations for the preparation as written to the left which are used for different further reference measurements (see Sec. 4.3.3). The values in contrast quantify the quality of the preparation.

IFGs. When comparing the weak-interaction IFGs of Fig. 4.12 with the preparational IFGs of Fig. 4.11, conspicuous reactions appear in the coloured diagonal elements of Fig. 4.12 where either significant intensity oscillations or a significant drop in count rate is produced.

The weak interaction IFGs were recorded in combination with the preparational IFGs in an alternating “on”/“off” scheme, i.e. by turning the weak interaction on and off, before moving the phase shifter to the next orientation. This measurement protocol ensures the comparability of phase and contrast of the “on” and “off” IFGs which is needed in the data analysis. The IFGs with absorbers were not recorded in an ‘on’/‘off’ scheme but right after each other while ensuring stable phase relations via the thermal control system.

### 4.3.6 Extraction of Weak Values

Weak values are extracted for all nine situations, where the term situation now refers to a combination of a specific weak interaction applied in a specific path. Weak values are given by comparing the measured IFGs of Figs. 4.11 and 4.12 with the predictions from Eqs. (4.10), (4.11), and (4.12) in the limit of small interaction strengths. One may be inclined to directly extract the weak values as ratio of contrast divided by the maximum contrast for the absolute values of the spin weak values and the energy weak values; and as the reduction in mean count divided by the mean counts in the preparation interferograms for the path weak values (as will be given in Eq. (4.26)). This procedure results in the raw weak values given in Tab. 4.2. One can differentiate between two deviations from the expectation of an identity matrix: the deviations of the single weak values and the deviations of the sum of all weak values over all paths for a specific interaction (as indicated to the right) or over all interactions for a specific path. The single weak values are all consistent with a unity matrix when considering the statistical errors and the efficiencies in our setup. Yet, the weak values summed over all paths or interactions differ substantially from the prediction of 1. This implies a systematic over-estimation of the weak values.

#### 4 Three-Path Quantum Cheshire Cat

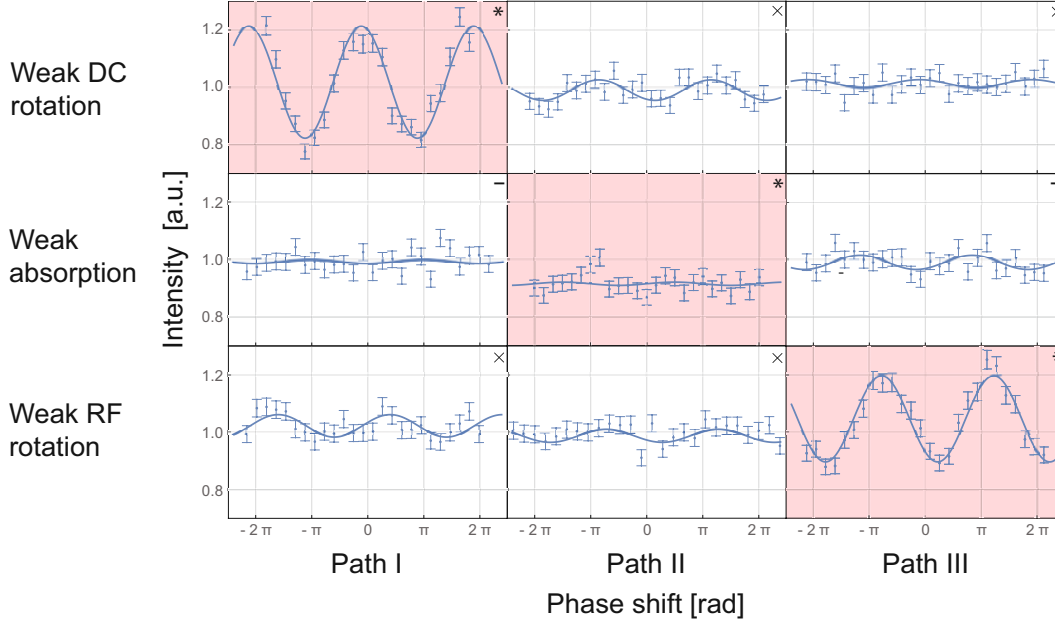


Figure 4.12: **Interferograms and their fits with preparation and weak interactions applied.** In each row, a different weak interactions is applied, i.e. the direct-current (DC), absorber, and radio-frequency (RF) cases as labelled to the left. The blue data points indicate the intensities recorded in the O-beam, normalised by mean intensities of corresponding preparational interferograms of Fig. 4.11, plotted against phase shifts induced in the path specified at the bottom. The blue statistical error bars indicate one standard deviation, solid blue curves are fits. The most noticeable reactions compared to the preparational interferograms of Fig. 4.11 are found in the coloured diagonal elements, coloured in light red. The off-diagonal elements (shown with white background) exhibit only inconspicuous reactions. The symbols in the upper right corners indicate different kinds of situations described in the Sec. 4.4.3.

The above “naive” method to extract the weak values ignores, however, the phase shifts between the preparational IFGs and the weak measurement IFGs. The detailed data correction is given in the following. Parameters in this section with indices “empty”, “prep” and “weak” correspond to the three types of interferograms recorded, respectively, with either no elements in the interferometer, with the preparational DC and RF flip applied, and an additional weak interaction applied. To read out the signal generated by the weak interaction, we assume that, in the case of the weak interaction IFGs, the time-independent intensity oscillation of Eq. (4.14) is the sum of two independent oscillations:

$$\begin{aligned}
 I_{\text{weak}}(\chi) &= I_{0,\text{weak}} + B_{\text{weak}} \cos(\omega_{\text{empty}}\chi + \varphi_{\text{weak}}) \\
 &= I_{0,\text{weak}} + B_{\text{prep}} \cos(\omega_{\text{empty}}\chi + \varphi_{\text{prep}}) + B_{\text{signal}} \cos(\omega_{\text{empty}}\chi + \varphi_{\text{signal}}).
 \end{aligned}
 \tag{4.15}$$

Therein, the “signal” refers to the changes in the IFGs from the preparational case to the weak interaction case. The amplitude and phase of the signal can be retrieved by comparing interferograms of the sets consisting of an interferogram with only the preparation applied and an interferogram with an additional weak interaction

### 4.3 Experimental Data

Raw weak values				
weak value	path			$\sum_{I,II,III}$
	I	II	III	
$ \langle \hat{\sigma}_x^{\text{DC}} \hat{\Pi}_j \rangle_w^{E_0} $	$0.96 \pm 0.09$	$0.19 \pm 0.04$	$0.08 \pm 0.04$	$1.23 \pm 0.11$
$\langle \hat{\Pi}_j \rangle_w^{E_0}$	$0.07 \pm 0.08$	$0.85 \pm 0.12$	$0.09 \pm 0.07$	$1.01 \pm 0.16$
$ \langle \hat{\sigma}_x^{\text{RF}} \hat{\Pi}_j \rangle_w^{E_0} $	$0.19 \pm 0.04$	$0.12 \pm 0.04$	$0.82 \pm 0.07$	$1.13 \pm 0.11$
$\sum_{\text{DC,Abs,RF}}$	$1.22 \pm 0.13$	$1.16 \pm 0.13$	$0.99 \pm 0.11$	-

Table 4.2: Numerical presentation of the raw weak values of the  $x$  spin component, path operator, and energy transition operator of each path without data correction. The statistical errors given indicate one standard deviation. While the modulus of the weak values is extracted for the spin and energy observables, the path weak values are extracted directly. The sums of the weak values in each row and column are given at the bottom and right, respectively. An additional data correction leads to the

applied. The signal amplitude  $B_{\text{signal}}$  and its statistical error  $\Delta B_{\text{signal}}$  follow from Eq. (4.15) as

$$B_{\text{signal}} = \sqrt{B_{\text{weak}}^2 + B_{\text{prep}}^2 - 2B_{\text{weak}}B_{\text{prep}} \cos(\varphi_{\text{weak}} - \varphi_{\text{prep}})} \quad (4.16)$$

and

$$\Delta B_{\text{signal}} = \frac{1}{B_{\text{signal}}} \left[ [(B_{\text{weak}} - B_{\text{prep}} \cos(\varphi_{\text{weak}} - \varphi_{\text{prep}})) \Delta B_{\text{weak}}]^2 + [(B_{\text{prep}} - B_{\text{weak}} \cos(\varphi_{\text{weak}} - \varphi_{\text{prep}})) \Delta B_{\text{prep}}]^2 + (B_{\text{weak}}B_{\text{prep}} \sin(\varphi_{\text{weak}} - \varphi_{\text{prep}}))^2 (\Delta\varphi_{\text{weak}}^2 + \Delta\varphi_{\text{prep}}^2) \right]^{1/2}. \quad (4.17)$$

We compare the experimental data with the theoretical prediction. By substituting the second last equality in Eq. (A.3) into Eq. (4.15) and neglecting terms of order higher than  $\alpha_{\text{rot}}$  we obtain

$$|\langle f|i \rangle|^2 \left[ 1 + C_{\text{empty}} \alpha_{\text{rot}} \text{Im} \left\{ \langle \hat{\sigma}_x^{\text{DC}} \hat{\Pi} \rangle_w^{E_0} \right\} \right] = I_{0,\text{weak}} + B_{\text{prep}} \cos(\omega_{\text{empty}} \chi + \varphi_{\text{prep}}) + B_{\text{signal}} \cos(\omega_{\text{empty}} \chi + \varphi_{\text{signal}}). \quad (4.18)$$

This includes the correction considering the maximum experimental contrast  $C_{\text{empty}}$  of the empty interferometer given through the fits in Fig. 4.9. The index  $j$  of the path where the rotation is implemented is omitted here. We can drop the oscillation proportional to  $B_{\text{prep}}$  already present in the preparational IFGs as it is an experimental imperfection and does not represent the behaviour described by weak

values. It is however included through the error propagation of Eq. (4.17). Furthermore, we can insert  $|\langle f|i \rangle|^2 = I_{0,\text{prep}} \approx I_{0,\text{weak}}$ . In this context, it is important to discern between the phase  $\chi'$  of the wave function and the phase shifter position  $\chi$  that are related via  $\chi' = \omega_{\text{empty}}\chi + \text{const.}$  such that  $\omega_{\text{empty}}\chi + \varphi_{\text{signal}} = \chi' + \varphi'_{\text{signal}}$ . It follows that

$$\begin{aligned}
 I_{0,\text{prep}} \left[ 1 + C_{\text{empty}}\alpha_{\text{rot}} \text{Im} \left\{ \langle \hat{\sigma}_x^{\text{DC}} \hat{\Pi} \rangle_w^{E_0} \right\} \right] &= I_{0,\text{weak}} + B_{\text{signal}} \cos(\chi' + \varphi'_{\text{signal}}), \\
 1 + C_{\text{empty}}\alpha_{\text{rot}} \text{Im} \left\{ \langle \hat{\sigma}_x^{\text{DC}} \hat{\Pi} \rangle_w^{E_0} \right\} &= \frac{I_{0,\text{weak}}}{I_{0,\text{prep}}} + \frac{B_{\text{signal}}}{I_{0,\text{prep}}} \cos(\chi' + \varphi'_{\text{signal}}), \\
 C_{\text{empty}}\alpha_{\text{rot}} \text{Im} \left\{ \langle \hat{\sigma}_x^{\text{DC}} \hat{\Pi} \rangle_w^{E_0} \right\} &\approx \frac{B_{\text{signal}}}{I_{0,\text{prep}}} \cos(\chi' + \varphi'_{\text{signal}}), \\
 \frac{\text{Im} \left\{ \langle \hat{\sigma}_x^{\text{DC}} \hat{\Pi} \rangle_w^{E_0} \right\}}{\cos(\chi' + \varphi'_{\text{signal}})} &\approx \frac{B_{\text{signal}}}{C_{\text{empty}}\alpha_{\text{rot}}}, \quad \forall \chi' \in \mathbb{R}.
 \end{aligned} \tag{4.19}$$

Since this relation must hold for all  $\chi'$ , the imaginary part of the weak value must be sinusoidal as obtained in Eq. (4.9). Furthermore, the cosine function and the imaginary part of the weak value must have the same frequency and be in phase. The weak values of Eq. (4.9) all have constant moduli and we also assume this to hold for all extracted weak values. Thus we finally obtain in first order of  $\alpha_{\text{rot}}$  the measured modulus of the weak value

$$\left| \langle \hat{\sigma}_x^{\text{DC}} \hat{\Pi} \rangle_w^{E_0} \right| = \frac{B_{\text{signal}}}{C_{\text{empty}}\alpha_{\text{rot}}}, \tag{4.20}$$

and its statistical error

$$\begin{aligned}
 \Delta \left| \langle \hat{\sigma}_x^{\text{DC}} \hat{\Pi} \rangle_w^{E_0} \right| &= \frac{B_{\text{signal}}}{I_{0,\text{prep}} C_{\text{empty}} \alpha_{\text{rot}}} \times \\
 &\times \sqrt{\left( \frac{\Delta B_{\text{signal}}}{B_{\text{signal}}} \right)^2 + \left( \frac{\Delta I_{0,\text{prep}}}{I_{0,\text{prep}}} \right)^2 + \left( \frac{\Delta C_{\text{empty}}}{C_{\text{empty}}} \right)^2 + \left( \frac{\Delta \alpha_{\text{rot}}}{\alpha_{\text{rot}}} \right)^2}.
 \end{aligned} \tag{4.21}$$

The same steps lead to a similar result for the RF case. For the case of weak absorption, we measured the absorption coefficient of the indium foil with a single interferometer path as

$$\mathcal{A} = 1 - 0.90(1) = 0.10(1). \tag{4.22}$$

We substitute the second last line in Eq. (A.4) into Eq. (4.15) such that

$$\begin{aligned}
 |\langle f|i \rangle|^2 \left[ 1 - \langle \hat{\Pi} \rangle_w^{E_0} \mathcal{A} \right] &= I_{0,\text{weak}} + A_{\text{prep}} \cos(\omega_{\text{empty}}\chi + \varphi_{\text{prep}}) \\
 &+ A_{\text{signal}} \cos(\omega_{\text{empty}}\chi + \varphi_{\text{signal}}).
 \end{aligned} \tag{4.23}$$

The index  $j$  of the path where the absorption is implemented is omitted again. Both oscillations can be neglected as they neither describe a reaction to the weak absorption nor change the mean intensity. With similar steps as for the DC case we

### 4.3 Experimental Data

calculate

$$\begin{aligned}
 |\langle f|i \rangle|^2 \left[ 1 - \langle \hat{\Pi} \rangle_w^{E_0} \mathcal{A} \right] &= I_{0,\text{weak}} \\
 I_{0,\text{prep}} \left[ 1 - \langle \hat{\Pi} \rangle_w^{E_0} \mathcal{A} \right] &= I_{0,\text{weak}} \\
 1 - \langle \hat{\Pi} \rangle_w^{E_0} \mathcal{A} &= \frac{I_{0,\text{weak}}}{I_{0,\text{prep}}} \\
 \langle \hat{\Pi} \rangle_w^{E_0} \mathcal{A} &= 1 - \frac{I_{0,\text{weak}}}{I_{0,\text{prep}}} \\
 \langle \hat{\Pi} \rangle_w^{E_0} &= \frac{\mathcal{A}_w}{\mathcal{A}},
 \end{aligned} \tag{4.24}$$

with the effective absorption coefficient  $\mathcal{A}_w$  in the path of the interferometer written as

$$\mathcal{A}_w = 1 - \frac{I_{0,\text{weak}}}{I_{0,\text{prep}}}. \tag{4.25}$$

The propagated statistical error of the path weak value is given by

$$\Delta \langle \hat{\Pi} \rangle_w^{E_0} = \frac{1}{\mathcal{A}} \sqrt{\left[ \left( 1 - \frac{I_{0,\text{weak}}}{I_{0,\text{prep}}} \right) \frac{\Delta \mathcal{A}}{\mathcal{A}} \right]^2 + \left( I_{0,\text{weak}} \frac{\Delta I_{0,\text{prep}}}{I_{0,\text{prep}}^2} \right)^2 + \left( \frac{\Delta I_{0,\text{weak}}}{I_{0,\text{prep}}} \right)^2}. \tag{4.26}$$

The respective final results for the corrected weak values are presented in Fig. 4.13 and Tab. 4.3 and approximate the ideal identity matrix given by Eq. (4.9). The raw path weak values are not corrected and the raw values from Tab. 4.2 are displayed again. In contrast to the raw results, the corrected weak values summed up over all paths or over all interactions are more consistent with the expected value of 1. The data correction considering the phase shifts between preparational and weak measurement interferograms can be considered to eliminate the systematic over-estimation of the weak values.

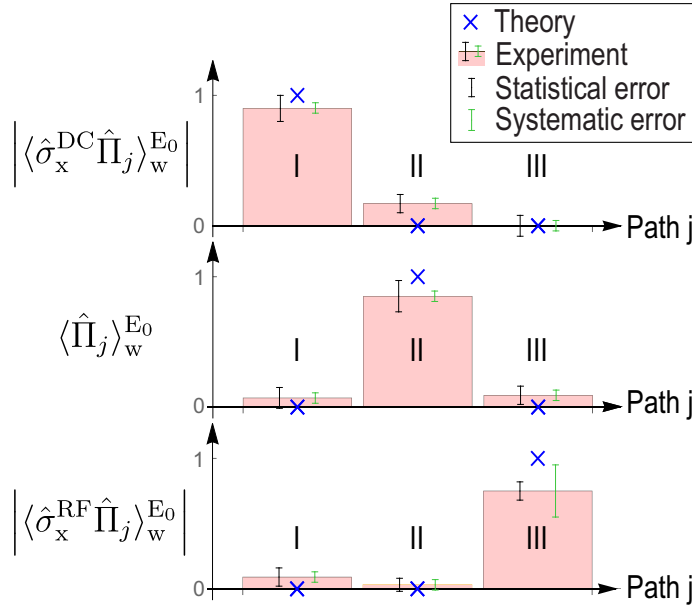


Figure 4.13: **Weak values presented graphically.** Graphical presentation of the weak values of the  $x$  spin component, path operator, and energy transition operator of each path as presented numerically in Tab. 4.3. The light red bars give the moduli of the relevant weak values extracted from interferograms in Figs. 4.11 and 4.12 for each path  $j$ . The black statistical error bars indicate one standard deviation. The green systematic error bars are estimated in Tab. 4.5. For the path weak values  $\langle \hat{\Pi}_j \rangle_w^{E_0}$  of the absorber measurements, not the modulus but the weak value itself is given. Blue crosses indicate the ideal theoretical moduli of weak values which compose an identity matrix.

Weak values				
weak value	path			$\sum_{\text{I,II,III}}$
	I	II	III	
$ \langle \hat{\sigma}_x^{\text{DC}} \hat{\Pi}_j \rangle_w^{E_0} $	$0.90^{\pm 0.10}_{\pm 0.04}$ stat sys	$0.17^{\pm 0.07}_{\pm 0.04}$ stat sys	$0.00^{\pm 0.08}_{\pm 0.04}$ stat sys	$1.07^{\pm 0.15}_{\pm 0.07}$ stat sys
$\langle \hat{\Pi}_j \rangle_w^{E_0}$	$0.07^{\pm 0.08}_{\pm 0.04}$ stat sys	$0.85^{\pm 0.12}_{\pm 0.04}$ stat sys	$0.09^{\pm 0.07}_{\pm 0.04}$ stat sys	$1.01^{\pm 0.16}_{\pm 0.07}$ stat sys
$ \langle \hat{\sigma}_x^{\text{RF}} \hat{\Pi}_j \rangle_w^{E_0} $	$0.09^{\pm 0.07}_{\pm 0.04}$ stat sys	$0.03^{\pm 0.05}_{\pm 0.04}$ stat sys	$0.75^{\pm 0.07}_{\pm 0.20}$ stat sys	$0.87^{\pm 0.11}_{\pm 0.20}$ stat sys
$\sum_{\text{DC,Abs,RF}}$	$1.06^{\pm 0.15}_{\pm 0.04}$ stat sys	$1.05^{\pm 0.15}_{\pm 0.07}$ stat sys	$0.84^{\pm 0.13}_{\pm 0.20}$ stat sys	-

Table 4.3: Numerical presentation of the weak values of the  $x$  spin component, path operator, and energy transition operator of each path as presented graphically in Fig. 4.13. The statistical errors (stat) given indicate one standard deviation. The systematic errors (sys) are estimated in Tab. 4.5. While the modulus of the weak values is extracted for the spin and energy observables, the path weak values are extracted directly. The sums of the weak values in each row and column are given at the bottom and right, respectively.

### 4.3.7 Second Order Behaviour

When applying the weak interactions in our experiment, changes in the mean intensities compared to the preparational IFGs are expected in seven of the nine situations. For the weak beam attenuations, the intensity changes directly give the path weak values of Eqs. (4.9) and (4.12), Fig. 4.13, and Tab. 4.3. For the unitary spin/energy manipulations, the mean intensity changes correspond to the terms proportional to  $\pm\alpha_{\text{rot}}^2$  in Eqs. (4.10) and (4.11). (In the exact calculation of Eq. (4.32), the mean intensity changes are represented by the terms proportional to  $\pm\sin^2(\alpha/2)$ .) In our experiment, the intensities are expected to increase by  $\alpha_{\text{rot}}^2/4 \approx 3\%$  when inducing weak unitary rotations in paths I or III, while a decrease of the same amount is expected for weak unitary rotations induced in path II. The measured intensity changes between the IFGs of Figs. 4.11 and 4.12 are given in Fig. 4.14 and Tab. 4.4. The theoretical prediction and the experimental results show reasonable agreement. Their comparison suffices to establish higher order reactions which demonstrate that the intensity changes in all three paths through the unitary weak interactions as described in [23, 123]. But a higher statistical precision will be necessary to quantitatively confirm the theoretically predicted intensity changes.

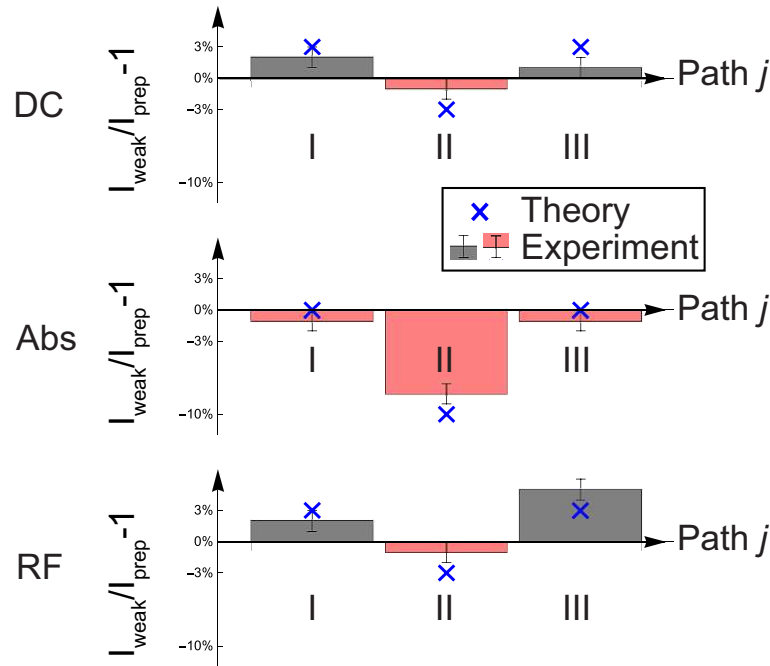


Figure 4.14: **Changes of the mean intensities presented graphically.** Graphical presentation of relative changes between mean intensities  $I_{\text{weak}}$  of weak measurement IFGs in Fig. 4.12 normalised with mean intensities  $I_{\text{prep}}$  of preparational IFGs in Fig. 4.11 for each combination of weak interaction and path. Gray bars refer to an increase in intensity, pink ones to a decrease. The statistical error bars indicate one standard deviation. Blue crosses indicate the values expected from theory. The normalised intensities are directly given in Tab. 4.4. In the absorber cases described by Eq. (4.12), an intensity drop proportional to  $\mathcal{A}$  of 10% is expected in path II. In the DC and RF cases described by Eqs. (4.10) and (4.11), intensity changes proportional to  $\alpha_{\text{rot}}^2$  of approximately  $\pm 3\%$  are expected.

weak interaction	Relative intensities		
	path		
	I	II	III
DC	1.02(1)	0.99(1)	1.01(1)
Abs	0.99(1)	0.92(1)	0.99(1)
RF	1.02(1)	0.99(1)	1.05(1)

Table 4.4: Numerical mean intensities of weak measurement IFGs in Figs. 4.12 normalised with mean intensities of preparational IFGs in Fig. 4.11 for each combination of weak interaction and path as presented graphically through relative intensity changes in Fig. 4.14. The statistical errors given indicate one standard deviation. In the case of a weak absorber, solely a 10% decrease is expected in path II, while the other paths are expected to be unaffected. In the DC and RF cases, reactions proportional to  $\alpha_{\text{rot}}^2$  are expected to change the mean intensities according to Eqs. (4.10) and (4.11) by approximately  $\pm 3\%$ .

## 4.4 Discussion

### 4.4.1 Experimental Resources

For the given pre- and post-selection of Eqs. (4.1) and (4.2), the contrast of IFGs is ideally zero. As can be seen from Fig. 4.11 and Tab. 4.1, lower contrasts were achieved in the DC and absorber cases compared to the RF case. This is expected when implementing the technique for locally modifying the guide field for the coil adjustments described in Sec. 4.3. On the other hand, the technique should increase the quality of the weak RF spin rotations. However, the weak value deviating the most from the theory is in the case of a weak RF interaction in path III where it is obtained as 0.7 compared to the prediction of 1, cf. Fig. 4.13, Tab. 4.3, and Eq. (4.9). As the coil for the preparational RF spin flip in path III is close to the coil inducing the weak RF rotation (see Fig. 4.2), their interaction in terms of electrical oscillating circuits could have induced unintended additional spin manipulations. An estimation of the upper boundaries of systematic errors is given in Tab. 4.5.

Again, the weak value for the RF case in path III deviates from the theory. The deviations of all the other weak values from their expectations are of the magnitude of their statistical errors. The errors are of the same magnitude for all elements as the decreased error of the amplitude for IFGs with low contrast is partly compensated by the increased error of the phase, see Eq. (4.17) in the data analysis below. Furthermore, we extract only the modulus of the weak values for spin and energy observables. Thus, these off-diagonal weak values cannot be distributed symmetrically around zero.

The energy changes produced with the RF coils are coupled with spin flips in our experiment. This is in principle avoidable when using a combination of an RF and a DC spin flipper instead. The first one flips the energy and spin vector, while the second one flips the spin vector back to the initial orientation. This effectively produces an energy change without spin manipulation.

Since both spin and energy in our experiment are treated as two-level systems, four possible combinations exist which are orthogonal to each other. The keen reader might have noticed that one of them, the state  $|\uparrow, E'\rangle$ , was not mentioned, yet. This fourth state could only be produced by a combination of both a DC spin flip and an RF spin flip as described in the previous paragraph. This state has a particular character as it is expected to exhibit no conspicuous reaction to any single weak interaction – neither of DC nor RF spin rotations.

Estimation of systematic errors

origin of systematic	expressed as		systematic error on	
	measure	quantity	prep. contrast	weak value
thermal stability	contrast	$\Delta C \leq \pm 0.02$	$< 0.01$	$< 0.01$
	phase stability	$\Delta\varphi \leq \pm 1^\circ/\text{hour}$	–	$< 0.01$
current adjustment	spin rotation angle	$\Delta\alpha \leq \pm 0.5^\circ$	$< 0.01$	$\leq 0.025$
eddy currents in Indium foil (weak Abs)	spin rotation angle	$\Delta\alpha \leq \pm 0.5^\circ$	–	$\leq 0.025$
mutual current induction between coils (weak RF path III)	spin rotation angle	$\Delta\alpha \leq \pm 4^\circ$	–	$\leq 0.20$
monochromaticity	wavelength distribution	$\delta\lambda/\lambda_0 \leq 0.02$ $\Downarrow$ $\epsilon \geq 0.98$	$\leq 0.02$	$< 0.01$ (corrected for)
field inhomogeneity	spin manipulation efficiency	$\epsilon \geq 0.9$	$\leq 0.03$	$< 0.01$ (corrected for)
spin polarisation	degree of polarisation	$P > 99\%$	$< 0.01$	$< 0.01$ (corrected for)
<b>total systematic error</b>			$\leq 0.04$	$\leq 0.20$ (weak RF path III) $\leq 0.04$ (other cases)

Table 4.5: Origins of systematic errors and their estimated consequences on the preparational contrast of Fig. 3/Tab. I and weak values of Fig. 5 and Tab. II. The highest systematic error is expected when applying a weak RF spin rotation in path III where an RF spin flip is conducted for preparation. The interaction between these coils produces unintended consequences as described in Sec. 4.3.7.

### 4.4.2 Comparison with Standard Weak Measurements

The standard weak measurements introduced in Sec. 2.1.2 use a meter system to measure the observable. For the experiment in the present chapter, this condition is eased. While an entanglement between different observables is introduced as in Eq. (2.20), the entanglement is already there in the initial state of Eq. (4.1). The weak interactions to infer the locations of spin and energy DOF further manipulate the combined Hilbert space of path, spin, and energy. Concerning the aspect that the weak interaction is not the cause of entanglement, the interaction performed is described by a single operator without separation between observable and meter. Therefore, the procedure rather resembles the case of Eq. (2.22) of a unitary rotation by means of the observable. Furthermore, not two but three DOF are necessary to perform the presented experiment. The weak exponential beam attenuation with indium foils fulfils the criteria of a standard weak measurement to a reduced extent. However, a main motivation for weak measurements is their minimal disturbance on the intermediate state between pre- and post-selection which simplifies characterising the respective quantum state. This criterion is fulfilled for the presented procedure. Therefore, the presented experiment shares some but not all features of standard weak measurements such that one can regard it as a generalised weak measurement.

### 4.4.3 Comparison with Proposal by Pan

To analyse the emergence of the qCC mathematically, we compare our experiment with the generalized N-path qCC described by Pan [130]. The generalised case considers N paths (indexed as  $j$ ) and  $N - 1$  properties of two level systems (indexed as  $p$ ). The two basis vectors in each Hilbert space of a property will be denoted as 1 and 0. The state vector entering the interferometer is assumed as  $|1, 1, 1, \dots\rangle$ . The sub-states in each path are prepared to be mutually orthogonal by flipping the respective state vector of property  $p$  in path  $j = p + 1$ . (Roman numerals indicating paths will henceforth appear in equations together with Arabic numerals indicating properties.) The according pre-selection  $|i_N\rangle$  is denoted as

$$|i_N\rangle = \frac{1}{\sqrt{N}} \left[ |I\rangle |1, 1, 1, \dots\rangle + |II\rangle |0, 1, 1, \dots\rangle + \dots + |N\rangle |1, \dots, 1, 0\rangle \right]. \quad (4.27)$$

The according post-selected state  $|f_N\rangle$  which is dependent on the phases  $\chi_j$  of the phase shifters in path  $j$  is chosen as

$$|f_N\rangle = \frac{1}{\sqrt{N}} \left( e^{i\chi_1} |I\rangle + e^{i\chi_2} |II\rangle + \dots + e^{i\chi_N} |N\rangle \right) |1, 1, 1, \dots\rangle. \quad (4.28)$$

Please note that there is an analysis in the post-selection for each property  $p$  realised with a respective projection on the post-selected state  $|f_N\rangle$ . Similarly to the previous three-path consideration, the post-selected intensity  $|\langle f_N | i_N \rangle|^2$  between pre- and post-selection has only a single non-zero contribution, coming from the component of path I, while the components from the other paths in the initial state  $|i_N\rangle$  are orthogonal to  $|f_N\rangle$  such that their contributions to the post-selected intensity are zero. This means that, given the pre-selection, only the component of the sub-beam

through path I is post-selected. We will therefore refer to path I as the reference beam and all others as non-reference beams in the generalised case. The operator for a manipulation of property  $p$  in path  $j$ , while leaving the states in all other sub-beams unchanged, is given by

$$\begin{aligned}\hat{O}_j^p(\alpha) &= \exp\left(-i\frac{\alpha}{2}\hat{\sigma}_x^p\hat{\Pi}_j\right) \\ &= \mathbf{1} - \left(1 - \cos\frac{\alpha}{2}\right)\hat{\Pi}_j - i\sin\left(\frac{\alpha}{2}\right)\hat{\sigma}_x^p\hat{\Pi}_j.\end{aligned}\quad (4.29)$$

The weak values of the operators  $\hat{\sigma}_x^p\hat{\Pi}_j$  are written as

$$\langle\hat{\sigma}_x^p\hat{\Pi}_j\rangle_w = \delta_{j,p+1}e^{i(\chi_1-\chi_j)},\quad (4.30)$$

and the path weak values are written as

$$\langle\hat{\Pi}_j\rangle_w = \delta_{j,1}.\quad (4.31)$$

In addition to the  $N - 1$  properties indexed as  $p$ , the “zeroth” property of the generalised case would be the particle behaviour in path I such that a beam attenuation only causes a linear reaction of the mean intensity in path I. This is analogous to Eq. (4.12) of the three-path consideration.

It follows in an exact calculation (details in Sec. A.1), without regarding the limit of small  $\alpha$ , that the time-independent intensity behaves as

$$\begin{aligned}I_j^p(\alpha) &= \left|\langle f_N | \hat{O}_j^p(\alpha) | i_N \rangle\right|^2 \\ &= |\langle f_N | i_N \rangle|^2 \left[ 1 + 2\sin\left(\frac{\alpha}{2}\right) \operatorname{Im} \left\{ \langle \hat{\sigma}_x^p \hat{\Pi}_j \rangle_w \right\} + \sin^2\left(\frac{\alpha}{2}\right) \left| \langle \hat{\sigma}_x^p \hat{\Pi}_j \rangle_w \right|^2 - \sin^2\left(\frac{\alpha}{2}\right) \langle \hat{\Pi}_j \rangle_w \right] \\ &= \left[ \underbrace{\frac{1}{N} e^{-i\chi_1}}_{\text{term 1}} - \underbrace{\left(1 - \cos\frac{\alpha}{2}\right) \frac{1}{N} e^{-i\chi_1} \delta_{j,1}}_{\text{term 2}} - i \underbrace{\sin\left(\frac{\alpha}{2}\right) \frac{1}{N} e^{-i\chi_j} \delta_{j,p+1}}_{\text{term 3}} \right]^2 \\ &= \frac{1}{N^2} \left[ 1 + 2\delta_{j,p+1} \sin\left(\frac{\alpha}{2}\right) \sin(\chi_1 - \chi_j) + \delta_{j,p+1} \sin^2\left(\frac{\alpha}{2}\right) - \delta_{j,1} \sin^2\left(\frac{\alpha}{2}\right) \right].\end{aligned}\quad (4.32)$$

This expresses the intensity through the related measures of weak values, amplitudes, and experimental parameters. The first line states that the intensity is determined by the projection between the post-selected state  $|f_N\rangle$  and the state unitarily rotated by  $\hat{O}_j^p(\alpha)$  from the initial state  $|i_N\rangle$ . The second line gives the intensity in terms of weak values for given interaction strength  $\alpha$ . The weak values are multiplied with sine functions which depend on  $\alpha$ . It follows by expanding the intensity for small  $\alpha$  that the weak values appear in every order of  $\alpha$ . Even though weak values were introduced as low order approximations [24], they are the expansion coefficients in the Taylor series [142, 143] and describe the intensity for arbitrary interaction strengths  $\alpha$ . In the third line, the intensity is expressed as the absolute squared of amplitudes from different paths; term 1 is the amplitude from the reference state in path I which is reduced by term 2 if the condition  $\delta_{j,1} = 1$ , or  $j = 1$ ,

is met. This means any weak interaction implemented in the reference beam will reduce its post-selected component through the projection in the first line. Term 3 is the amplitude of a non-reference beam in path  $j$  which is produced if  $\delta_{j,p+1} = 1$ , or  $j = p + 1$ . The last line gives the intensity dependent on the experimental parameters of the interaction strength  $\alpha$  and the phases  $\chi_1, \chi_j$ . The intensity oscillation proportional to  $\sin(\chi_1 - \chi_j)$  is the cross-term between the amplitudes of terms 1 and 3 in the third line. The third and fourth terms in the last line are mean intensity changes which are conditioned through the Kronecker deltas  $\delta_{j,p+1}$  and  $\delta_{j,1}$ . The data is analysed for second-order intensity changes in Sec. 4.3.7.

We will go into detail now regarding the first line of Eq. (4.32) where the intensity is obtained by considering a rotation of the initial state  $|i_N\rangle$  and a projection on the final state  $|f_N\rangle$ . Therefore, the projection in Hilbert space between the vectors of the post-selected state and the intermediate state before post-selection is essential. Any changes in the intensity compared to the preparational IFGs are a reaction to a weak interaction. As the weak interactions are unitary and the calculated intensity involves the projection to  $|f_N\rangle$ , the reactions are expressed by sinusoidal functions in the last line of Eq. (4.32). By regarding the parallel and orthogonal components to the post-selected state, we can identify three different kinds of situations:

The first kind of situation arises when a weak interaction is applied to a non-reference beam. Let us consider a perturbation rotating the sub-state of a non-reference beam and thereby generating a state component that is parallel to the post-selected state. This is equivalent to inverting a fraction of the sub-state from the orthogonal to the parallel component. Due to the behaviour given in Eqs. (4.5) and (4.29), in the limits of  $\alpha_{\text{rot}}$  and  $\alpha$  becoming zero, the magnitude of the following reaction of the intensity is linear in the interaction strength  $\alpha$ . The large reaction is identified with the behaviour proportional to  $2\sin(\alpha/2)$  given in Eq. (4.32) for the exact calculation and, in the limit of  $\alpha_{\text{rot}}$  becoming zero, with the term proportional to  $\alpha_{\text{rot}}$  in Eqs. (4.10) and (4.11). In these situations, the detected intensity is sensitive to the weak interaction applied. At the same time, the parallel component causes an increased intensity proportional to  $+\sin^2(\alpha/2)$  in Eq. (4.32) and proportional to  $+\alpha_{\text{rot}}^2$  in Eqs. (4.10) and (4.11).

The second kind of situation arises if any rotation is applied to the reference beam. Then the amplitude of the post-selected component is reduced. However, in comparison to the first kind of situation, it is only a small reaction proportional to  $-\sin^2(\alpha/2)$  in Eq. (4.32) and proportional to  $-\alpha_{\text{rot}}^2$  in Eqs. (4.10) and (4.11). The intensity in these situations is robust with respect to the weak interaction.

The third kind of situation concerns the states of the non-reference beams again, now in combination with unitary rotations which do not produce a post-selected component. Any reaction of the intensity is excluded by the Kronecker deltas and we conclude that in these situations the intensity is indifferent to the respective unitary rotations.

To first order, the intensity dependencies on the weak interaction strengths are the same in the generalised and our experimental case. The large first order reactions are seen in the diagonal elements in the weak-interaction IFGs of Fig. 4.12, which are marked with asterisks (\*) in the upper right corners of the graphs. In the same figure, second order reductions in the mean intensities compared to the preparational IFGs are expected to appear in the upper and lower IFGs of the mid-

dle column. The small reactions are due to the robustness of the reference beam with respect to rotations which is indicated with crosses ( $\times$ ). The differences between the general and our three-path case can be seen in the corner elements of the anti-diagonal in Fig. 4.12: in the generalised case, these elements should behave indifferently. However, without energy projection in our post-selection, we expect an increase in intensity proportional to  $+\alpha_{\text{rot}}^2$ . This is caused by the up spin components created by the weak interactions that produce additional counts without time-independent interference (explained in second paragraph of Sec. 4.2). Additionally, the left and right IFGs in the absorber case in Fig. 4.12 are indifferent in accordance with Eq. (4.12), as indicated with dashes ( $-$ ). These situations do not involve rotations, however, and concern the location of the particle which is not explicitly regarded as a property by Pan.

Finally, we consider the weak values again. According to the considerations on the projection between the state vectors, if the modulus of a weak value is zero, the intensity does not have a linear dependence on the interaction strength  $\alpha$ . Then, the intensity is either robust or indifferent to the weak interaction in the considered path. If the modulus of a weak value is 1, it identifies a combination of path and weak interaction in which the intensity is sensitive to the weak interaction.

The sensitive behaviour is an interference effect emerging through the cross-term of amplitudes between the sub-beams I and  $j$  proportional to  $\sin(\chi_1 - \chi_j)$ , cf. Eqs. (4.32) and (A.6). The magnitude of the cross-term is linear in  $\alpha$  for small interaction strengths. Therefore, the cross-term describes the conspicuous reactions of the intensity. Because the cross-term involves two paths, it offers an interpretation of delocalisation of properties in the interferometer [144].

#### 4.4.4 Comparison with Realistic Interpretation

An alternative interpretation proposed by Aharonov *et al.* [22] is inspired by realism and quantifies the location of a property in a path through the weak values. A weak value of 1 is attributed to finding the property in that path; a value of zero excludes finding the property in that path. We identify these values with the modulus of the weak values in the present experiment which is equivalent for phase shifter positions  $\chi_1 = \chi_2 = 0$ . According to the latter interpretation, with the present results of Fig. 4.13 and Tab. 4.3, the neutron's  $x$  spin component is in path I, the particle in path II, and its  $x$  component of the energy q-bit in path III; a spatial separation of the neutron's properties inside the interferometer is observed.

But how is the interpretation of separated properties compatible with the pre-selected state  $|i\rangle$  of Eq. (4.1) where a specific value for spin and energy is attributed to each sub-state? Initially, the state of the neutron is distributed equally over all three paths, indicated by the expectation value  $\langle i | \hat{\Pi}_j | i \rangle = 1/3$  for all paths. While we have so far considered only one particular final state, one could in principle also monitor all possible final states denoted by  $|f_m\rangle$ , where  $m$  is an index over all combinations of exit beam, spin state and energy state. This set of states is orthonormal and complete and we can express any expectation value as a weighted average over the weak values [145, 146]. The expectation value of the path projector

then reads

$$\begin{aligned}
\langle i | \hat{\Pi}_j | i \rangle &= \sum_m \langle i | f_m \rangle \langle f_m | \hat{\Pi}_j | i \rangle \\
&= \sum_m p_m \langle f_m | \hat{\Pi}_j | i \rangle / \langle f_m | i \rangle \\
&= \sum_m p_m \langle \hat{\Pi}_j \rangle_{w,m}
\end{aligned} \tag{4.33}$$

where  $p_m$  denotes the probability for a given  $|i\rangle$  of reaching the final state  $|f_m\rangle$ . Therefore, if we do not observe any intensity change when applying a weak beam attenuation in path I, it doesn't exclude a non-zero component to the state vector in that path. But it means that the component only contributes to intensities in other exit channels. However, for all neutrons that did reach our final state we can retrospectively say that these neutrons never were in path I.

As for the spin degree of freedom (likewise for the energy), the expectation value of the joint operator  $\hat{\sigma}_x^{\text{DC}} \hat{\Pi}_j$  yields the  $x$ -component of the spin in path  $j$ . For our initial state, this value becomes zero in all paths,  $\langle i | \hat{\sigma}_x^{\text{DC}} \hat{\Pi}_j | i \rangle = 0$ , because the spin in each path is prepared in the  $\pm z$  directions and therefore has equal probabilities  $\pm x$  directions [123]. Nevertheless, the weak value associated with our post-selected final state  $\langle \hat{\sigma}_x^{\text{DC}} \hat{\Pi}_j \rangle_w = e^{2i\chi_1}$  does not become zero, cf. Eq. (4.9). The expectation value of zero results from the compensation by a similar weak value with opposite sign in another output port of the interferometer, which is in our setup the down spin component of the side exit of the front loop. The opposite sign results from the phase shift of  $\pi$  which always appears between the two output ports of an interferometer loop.

Only for weak beam attenuations, both considered interpretations agree that the weak values give the locations in the interferometer of the neutrons found in our output port  $|f\rangle$ . For the weak interactions with spin and energy, the interference effect allows for the conservative interpretation of a delocalisation of properties.

All weak interactions applied in our experiment cause similar reactions locally – in the respective path. But it is the inner product of the weakly manipulated state with the post-selected state which can generate a post-selected amplitude. In turn, this amplitude constitutes a cross-term in the intensity linear to the interaction strength. Only for distinct pairs of paths and weak interactions, the reactions are conspicuous for a particular final state. We suggest to regard the conspicuous reactions to give the effective locations. In context of the qCC, where each property is effectively located in a different path we suggest the term effective separation of properties. The further reaching interpretation of a physical separation of properties is not required to describe all observed phenomena. While we cannot decide between effective and physical separation with the present experiment, the realistically inspired interpretation of physically separated properties would need extraordinary evidence as verification. Therefore, at the present moment, physical reality of separated properties is unproven, both for an ensemble of and for single neutrons themselves.

### 4.4.5 Subjective Remarks

The presented experiment is a follow-up to the first experiment on the Cheshire Cat of Denkmayr *et al.* [23] with two paths and a single phase shifter inducing the phase shift  $\chi$ . In response to that first experiment, Stuckey *et al.* [123] pointed out that the extraction of spin weak value by Denkmayr *et al.* was dependent on the path weak values. This is caused by the extraction of the weak values at a phase shifter position  $\chi = 0$  which causes the weak values to be real. As can also be seen in the three-path equivalent of Eq. (4.9) by means of Eq. (4.10), the linear contribution to the intensity in  $\alpha$  vanishes at  $\chi_1 = 0$ . Only the quadratic dependencies in  $\alpha$  remain which couple different weak values.

The critics' conclusion is that the separation of properties should not be claimed. Stuckey *et al.* [123] postulated the criterion that the weak values should be extracted from the linear dependencies such that the weak values are independent from each other. While the initial experiment certainly is mind-boggling and worthy on its own, the criticism is valid. The experimental data of Denkmayr *et al.* even could have been evaluated in the demanded manner if the spin weak values were extracted through the amplitude of the sinusoidal intensity oscillation. Notwithstanding the final extraction of weak values in the previous experiment at  $\chi = 0$ , the extraction was performed after a fit over a full oscillation period of the interferograms. Therefore, the value of the fitted neutron counts at  $\chi = 0$  was already equally influenced by the counts at all recorded phase shifter positions. This circumstance might incline one to say that the criticism is superficial and petty. Or it stimulates an advancement.

In the presented three-path version, we amended the extraction procedure such that the weak values are extracted from the linear dependence in  $\alpha$  and the postulated criterion by Stuckey is fulfilled. The disadvantage of the extraction through the amplitude of the intensity oscillations is that only the absolute value of the weak values is extractable. I consider stating the absolute values as more transparent. In this way, the further development of the data analysis led to results with less information due to the missing phase information.

However, we encountered similar, further developed criticism concerning the separation of properties in the three-path version, too. The argument is that there are no three independent degrees of freedom, since spin and energy are coupled for the supposed third property. This does not concern the mathematical extraction as above but the physical properties themselves. This weak point should be taken serious and is disclosed in this thesis and the related publication [112]. At the same time, it is even more intriguing how the weak interactions induce three independent reactions in this particular setup. (As discussed, the answer lies in the missing time-resolution.) Both positive and negative criticism are essential for any progress. If the work is appreciated, criticism challenges further advancements. It is my hope that with improved techniques in neutron optics an amended version of the three-path quantum Cheshire Cat will be realised.

Determining the locations of properties is performed in several consecutive steps. The initial proposal [22] suggests to induce spatial deviations through the weak interactions, such that two independent translations can be performed simultaneously. A step in the direction of simultaneous measurements was done by W. Kersten in his diploma thesis [60]. He performed all measurements at the same time. However,

he turned off the weak interactions one at a time with the outcome of as many measurements to extract the weak values. Instead of using a data set with no weak interaction applied, Kersten uses a data set with all weak interactions applied; instead of a data set each for every weak interaction turned on, Kersten uses a data set each for every weak interaction turned on. I consider this interesting concept to be a symmetric case to the sequence in previous works and this thesis.

The three-path quantum Cheshire Cat reminds me of the quark model. The results of scattering experiments demanded the quark model and I know of no alternative. It is accepted theory that any quark can only be observed in a pair of quarks. However, the characteristics of the pairs led to the description based on individual quarks. Therefore, the separation of properties for the quantum Cheshire Cat should not be rejected out of hand.

In contrast to the quark model for scattering experiments, there are alternative explanations for the quantum Cheshire Cat and quantum physics in general. My perception of the quantum Cheshire Cat is based on the Copenhagen interpretation, i.e. there is no paradox since the counting events are statistically distributed based on the interference between partial waves. I was faced with the realistic interpretation distribution of many times. To merge these perspectives into an agnostic view seems now beneficial to me. This allows on an individual level what I suppose that the community should do: understand all perspectives and being open to research in all directions.

Weak values extend the concept of expectation values beyond the eigenvalue range. The expectation values can be regarded to be equivalent with the concept of balance points for scales. Any attempt of their generalisation is welcome in a field with prevalent disputes. Because we know of the quantum measurement problem, any new reasonable approach could be the basis for surprising developments and insights. The change between expectation and weak values, and between weak values for different post-selections (and pre-selections) resembles the change between coordinate systems. Different observers might measure different results, but these results follow the same laws of physics and all observers can agree to disagree. No one doubts that the procedure of a (generalised) weak measurement results in weak values. The question is simply of how much meaning one can or should give them. It is often in the extreme cases that one can learn the most about the core structure. Besides the counter-intuitive, the extreme includes anomalous weak values.

In several demanding discussions with my colleagues, I learned to acknowledge the different possible perspectives deviating from my point of view, specifically relative to the quantum Cheshire Cat. In turn, it is remarkable how some members of the community with much more experience are captivated to an extent by their viewpoint that they claim it to be the only true one. Also extensions to their own extensions are not accepted. The Copenhagen interpretation of its underlying mechanism is probably most common in the community. The rather fantastic view inspired by realism of the quantum Cheshire Cat proposing separation of properties is as valid in the sense that it cannot be refuted. The fantastic view raises the question whether an observation of a response is equivalent to the manifestation of the object which we seek after with the interaction. Do weak values give an equivalent or even more fundamental insight into quantum systems? Or are they a sheer projection disguising the more fundamental expectation value? The answer to these

## 4.5 Conclusion

ontological and epistemological questions eludes the findings of this thesis. Even if weak values turn out to be a mere projection, they are often times an intriguing means to expand our understanding of quantum mechanics. Bearing in mind Plato's cave allegory, the shadows on the cave's wall are our sole stimulus to free ourselves from long lasting misconceptions.

The concept of weak values and weak measurements is based on a time-symmetric formulation of quantum mechanics [50–52]. It is surprising that in some specific aspects, crucial differences in assumptions lead to identical experimental predictions. I was exposed a few times to categorisations of quantum theories, their overlap in one or the other aspect. These categorisations could contribute to the field as a periodic tables did in the past or as the standard model of particle physics does now.

That being said, let me state my disagreement with the realistic interpretation of the quantum Cheshire Cat; that different properties are separated from each other in these kind of experiments. I base my criticism on the term of interference. While semantically any two entities can interfere on some level with each other, to my knowledge in physics the term was always referring to an effect considering two entities which are similar or identical. To me it is an unjustifiably large step to invoke both the terms interference for the intensity oscillations and separation of properties for the quantum Cheshire Cat at the same time. One would expect interference also in any pair of coherent systems where a phase information can be inferred due a strong coupling between them beforehand. E.g. an atom and a photon emitted by it or an electron-positron pair emerging from a photon field.

While it is possible that a spatial separation of some kind occurs, an interpretation of that kind could hint at a different underlying level of physical entities such as quarks were at the time of their discovery. With these assumptions, the properties of the neutron distinguished in our experiments could be composite systems themselves. Different compositions would be located in some form in specific paths of an interferometer while the more fundamental entities interfere after recombination. An insight like this would be astounding. At the same time, the paradox would vanish again with the same argument as brought forward in the present thesis concerning the cross-term between probability amplitudes from different interferometer paths—only one or two levels deeper.

## 4.5 Conclusion

A three-path quantum Cheshire Cat is demonstrated in neutron interferometry; the neutron, its spin and its energy appear to be in different paths of the interferometer. In the experiment, a state preparation (pre-selection) as well as a state filtration (post-selection) are implemented. Even though the post-selection is without energy discrimination, the quantum Cheshire Cat in the three-path interferometer emerges as predicted by the theory. The conspicuous reactions to the local weak interactions are used to infer the locations of the properties of the neutron. Intensity oscillations emerge when a weak spin or energy manipulation is applied, while the intensity is reduced for the weak beam attenuation applied. These reactions are observed only for a particular interaction for each path. Taking a realistic viewpoint, one may conclude that the neutrons propagate through the interferometer, with the particle,

## 4 Three-Path Quantum Cheshire Cat

energy, and the spin's  $x$ -component taking different paths.

However, the intensity is calculated through the inner product of the weakly manipulated state with the post-selected state and its absolute value squared. Only for distinct pairs of weak interactions and paths they are applied in, a certain component parallel to the reference state, i.e. the component originally remaining through the post-selection, is generated. The respective generated amplitude constitutes a cross-term between the amplitude of the weakly evolved sub-beam and the reference state. The cross-term gives rise to a conspicuous interference effect which in turn suggests the delocalisation of properties. This suggests the possible explanation of the effect not as physical but as effective separation of properties in the interferometer.

# Chapter 5

## Simultaneous Path Weak-Measurements

This chapter is based on publication [147] which is reproduced with permission from Springer Nature.

The statistical properties of the detection events constituting the interference fringes at the output of an interferometer are well-known. Nevertheless, there is still no unified view of what is happening to a quantum system inside an interferometer. Strong measurements of path operators destroy the interference effect. In weak measurements, an observable is weakly coupled to a pointer system and the resulting weak values quantify the observable by minimally disturbing the system. Previous which-way experiments with weak measurements could extract either the real or imaginary part of a single weak value with each ensemble. Here, a simultaneous full complex quantification of two path weak values with a single ensemble in a Mach-Zehnder neutron interferometer is presented. Magnetic fields, oscillating with different frequencies, change the energy state in each interferometer path. The time-dependent phase between the energy states distinctly marks each path. The resulting beating intensity modulation at the interferometer output gives both path weak values. For the present experiment, the weak values' absolute value and phase directly describe the observed amplitude and phase of the intensity modulation.

### 5.1 Introduction

The double-slit experiment and interferometry as a whole are corner-stones of quantum physics. Any coherent system, e.g. light, electrons or the neutrons regarded in this letter, may exhibit interference fringes at the detector behind an interferometer. This is accurately described as a wave phenomenon [4]. While the first interference experiments with light [1] and electrons [5] worked with high-flux sources, the same effects also emerge with single photons [148], electrons [149], and neutrons [9]. The latter self-interference defies any classical analysis.

Notwithstanding the accurate description through delocalised waves [144], one may attempt to find out which path the system went. One may, e.g. block a particular path of the interferometer—only to see the interference fringes disappear completely. Such a strong measurement with a beam blocker destroys the investigated interference phenomenon. The behaviour of the interference fringes was

investigated with deterministic and probabilistic absorbers for neutrons [150]. This characterised the coherence of the quantum state dependent on the kind of absorption and different interaction strengths.

A tool to quantify the system inside an interferometer while preserving interference are weak measurements [24] where the interaction between the quantum system to be measured and the measurement instrument is so weak that the back-action of the measurement is practically negligible. Weak measurements are defined for a pre- and post-selection procedure as introduced in Sec. 2.1. A specific state is prepared (pre-selected) and another state is accepted (post-selected) towards the detector. A degree of freedom (DOF) of the system is investigated. A pointer system, i.e. auxiliary DOF, is manipulated through a weak interaction implemented midway between pre- and post-selection. Through entanglement between the two DOF, the interaction marks the investigated DOF. Comparing the detected intensities with and without applying the weak interaction quantifies the investigated DOF through weak values. Usually, the real and imaginary parts of a weak value are measured separately. In the interpretation of their physical significance, this separation is maintained: the real part gives the best estimate of an observable [33, 38] and the imaginary part is a measure of the intrinsic measurement disturbance on the system [32, 38].

A realisation of a weak measurement with photons [25] was implemented early after the theoretical introduction. With neutrons, the path DOF was used as a pointer system to retrieve spin weak values [26] and, vice versa, the spin degree of freedom to retrieve path weak values [27, 28]. A photonic proposal [151] suggested multiple simultaneous path markings through the energy DOF via mirrors with different vibration frequencies. The proposal was realised with photons [152] and in an adopted version with neutrons [153]. The experimental intensity at the output of the interferometer was time-resolved and exhibited oscillations in time with the applied frequencies. A path marking through the energy DOF as a pointer was demonstrated. However, weak values were not retrieved. In photonic setups, successive measurements of weak values were reported [154–157]. For atoms, the weak measurements of the polarisation and spin were reported [29, 30].

In this chapter, we want to find out which path the neutrons went in a two-path neutron interferometer [131, 132, 158, 159]. Therefore, the path DOF is investigated with the goal of retrieving both path weak values simultaneously. Each previously determined real and imaginary part of a path weak value was extracted separately with a different ensemble. In the case of weak measurements, it was regularly stressed that the weakness of the interaction minimises the disturbance on the system [160, 161]. Thus, each weak value describes the intermediate quantum system between pre- and postselection as best as possible. But it is not clear if multiple weak values extracted with different ensembles are valid for each ensemble.

In the present experiment, we exploit the minimal disturbance of the measurement to accomplish a simultaneous weak measurement of two path observables. The energy DOF, i.e. the system of different energy levels, is used as pointer system for the path DOF. In each path, the energy is manipulated differently to trace each path individually with a characteristic time-dependent phase. Detecting the resulting time-dependent intensity makes both path weak values accessible simultaneously. The validity of the retrieved weak values for the whole ensemble is hence assured.

The measurements are carried out in parallel in the interferometer in contrast to the reported successive measurements.

## 5.2 Theory and Schematic

The pre-selected (initial) state  $|i\rangle$  of a neutron in the interferometer is written as

$$|i\rangle = \frac{1}{\sqrt{2}} (|I\rangle + e^{-i\chi} |II\rangle) |\uparrow_z\rangle, \quad (5.1)$$

where  $\chi$  is the relative phase between paths I and II. The spin state is written with up and down arrows with the index of the basis used  $(x, y, z)$ . The post-selected (final) state  $|f\rangle$  is written as

$$|f\rangle = \frac{1}{\sqrt{2}} (|I\rangle + |II\rangle) |\uparrow_x\rangle. \quad (5.2)$$

The path weak values [24]  $\langle \hat{\Pi}_j \rangle_w = \langle f | \hat{\Pi}_j | i \rangle / \langle f | i \rangle$  of the path operators  $\hat{\Pi}_j = |j\rangle \langle j|$ ,  $j \in \{I, II\}$ , are calculated as

$$\langle \hat{\Pi}_I \rangle_w = \frac{1}{1 + e^{-i\chi}}, \quad \langle \hat{\Pi}_{II} \rangle_w = \frac{1}{1 + e^{i\chi}}. \quad (5.3)$$

Note that these weak values are the same as for the initial and final states  $|i'\rangle = (|I\rangle + \exp(-i\chi) |II\rangle) / \sqrt{2}$  and  $|f'\rangle = (|I\rangle + |II\rangle) / \sqrt{2}$ , without the spin component, since  $|i\rangle$  and  $|f\rangle$  are spin-path separable. Thus, the results are valid for the weak-value extraction of both sets of initial and final states. In the polar representation

$$\langle \hat{\Pi}_j \rangle_w = A_j e^{i\varphi_j}, \quad (5.4)$$

the absolute value  $A_j$  and the phase  $\varphi_j$  are calculated as

$$A_j = \frac{1}{2 \cos(\chi/2)}, \quad \varphi_j = \pm \frac{\chi}{2}, \quad (5.5)$$

where the plus sign refers to  $j = I$  and the minus sign to  $j = II$ . The absolute value diverges at phase shifter positions  $\chi = \pm\pi$  due to the orthogonality between pre- and post-selection for this case. The phase  $\varphi$  of the weak value is linear to the phase  $\chi$  induced by the phase shifter. Real and imaginary part of the weak values are calculated as

$$\text{Re} \left\{ \langle \hat{\Pi}_j \rangle_w \right\} = \frac{1}{2}, \quad \text{Im} \left\{ \langle \hat{\Pi}_j \rangle_w \right\} = \pm \frac{1}{2} \tan\left(\frac{\chi}{2}\right), \quad (5.6)$$

with the same convention for the  $\pm$  sign as above.

Consider the time-dependent oscillating external magnetic field of a radio-frequency (RF) spin-rotator coil (see also Sec. 3.3.6)

$$\vec{B}(t) = (B_1 \cos(2\pi ft + \delta), 0, B_0)^T, \quad (5.7)$$

with time  $t$ , the frequency  $f$  in resonance to the field strength  $B_0$  [105] and the phase offset  $\delta$  of the magnetic field in the coil at  $t = 0$ . A neutron's spin is manipulated by

this external magnetic field which is described in the rotating wave approximation [162] by the operator [105]

$$\begin{aligned}\hat{U}_{\text{RF}}(t, \alpha, f, \delta) &= \begin{pmatrix} \cos \frac{\alpha}{2} & \text{i}e^{\text{i}(2\pi ft + \delta)} \sin \frac{\alpha}{2} \\ \text{i}e^{-\text{i}(2\pi ft + \delta)} \sin \frac{\alpha}{2} & \cos \frac{\alpha}{2} \end{pmatrix} \\ &= \begin{pmatrix} 1 & \text{i}e^{\text{i}(2\pi ft + \delta)} \frac{\alpha}{2} \\ \text{i}e^{-\text{i}(2\pi ft + \delta)} \frac{\alpha}{2} & 1 \end{pmatrix} + \mathcal{O}(\alpha^2),\end{aligned}\quad (5.8)$$

in the  $z$  spin basis with the spin rotation angle  $\alpha$ . Each spin-flipped component is phase shifted by the phase  $\delta$  of the magnetic field. The last step assumes the limit of weak interaction strengths, i.e. small rotation angles  $\alpha \ll 1$ .

The spin flip in an RF coil is coupled to an energy shift  $\Delta E = hf$ , with the Planck constant  $h$ , which manifests itself in a time-dependent relative phase  $\pm 2\pi ft$  compared to the initial spin state. The interaction between the neutron and the magnetic field can be regarded in second quantisation of the magnetic field as a photon exchange [47, 163] with conserved energy and angular momentum. A neutron has a spin quantum number  $S = 1/2$ . The spin flip of a neutron, described by a change  $\pm \hbar = \pm h/(2\pi)$  in spin angular momentum, is compensated by the absorption or emission of a photon with the same angular momentum.

From now on, one RF spin-rotator is considered in each path  $j \in \{\text{I}, \text{II}\}$  of the interferometer. We will distinguish the different frequencies of the coils  $f_j$  and their different phase offsets  $\delta_j$ . We will use spin rotation angles  $\alpha_{\text{I}} = \alpha_{\text{II}} = \alpha$ . The path operators  $\hat{\Pi}_j$  will indicate in which path an operation is conducted. In the ideal case, the intensity  $I$  after post-selection results as (detailed calculation in Sec. A.2.1)

$$\begin{aligned}I_{\text{ideal}}(t) &= \left| \langle f | \left( \hat{U}_{\text{RF}}(t, \alpha, f_{\text{I}}, \delta_{\text{I}}) \hat{\Pi}_{\text{I}} + \hat{U}_{\text{RF}}(t, \alpha, f_{\text{II}}, \delta_{\text{II}}) \hat{\Pi}_{\text{II}} \right) | i \rangle \right|^2 \\ &= |\langle f | i \rangle|^2 \left[ 1 - \alpha \text{Im} \left\{ \langle \hat{\Pi}_{\text{I}} \rangle_{\text{w}} e^{-\text{i}(2\pi f_{\text{I}} t + \delta_{\text{I}})} + \langle \hat{\Pi}_{\text{II}} \rangle_{\text{w}} e^{-\text{i}(2\pi f_{\text{II}} t + \delta_{\text{II}})} \right\} + \mathcal{O}(\alpha^2) \right] \\ &= |\langle f | i \rangle|^2 \left( 1 - \alpha \left[ A_{\text{I}} \sin(\varphi_{\text{I}} - 2\pi f_{\text{I}} t - \delta_{\text{I}}) + A_{\text{II}} \sin(\varphi_{\text{II}} - 2\pi f_{\text{II}} t - \delta_{\text{II}}) \right] \right. \\ &\quad \left. + \mathcal{O}(\alpha^2) \right),\end{aligned}\quad (5.9)$$

where Eq. (5.4) is inserted for the last step. In the linear approximation for  $\alpha \ll 1$  and with  $(f_{\text{I}} - f_{\text{II}})/(f_{\text{I}} + f_{\text{II}}) \ll 1$ , this constitutes a temporal beating of the intensity. With a double-sine fit function for the time-resolved measurements, the absolute values  $A_j$  will be directly extracted from the amplitudes of the intensity oscillations and the phases  $\varphi_j$  of the weak values from the phases of the intensity oscillations (see Sec. 5.4.4). Real and imaginary components of the weak value are equivalent but secondary measures.

### 5.3 Setup

The experiment was conducted at the neutron interferometer station S18 at the Institut Laue-Langevin (ILL). All neutron optical elements used are described in

### 5.3 Setup

Sec. 3. The setup is depicted in Fig. 5.1. A neutron beam is monochromatised to a wavelength  $\lambda = 1.92 \text{ \AA}$ ,  $\delta\lambda/\lambda \approx 0.02$ , and polarised with a total degree of polarisation  $P > 0.99$  in the vertical  $+z$ -direction, which defines the quantisation axis. The beam is split by the first plate of the single-crystal silicon neutron interferometer into two paths, denoted as  $j \in \{\text{I, II}\}$ . In both paths of the interferometer, a phase shifter is placed which is rotated to align the relative phase  $\chi$  between the paths. After recombination of the two paths at the third plate of the interferometer crystal, two exiting beams emerge: the H-beam detected in diffracted direction and the O-beam detected in incident direction. In the present experiment, the O-beam exhibits a maximum count rate  $N_{\text{max}}$  of the order of 10 counts/s and an experimental contrast  $C_{\text{exp}} = 0.64 \pm 0.03$ . The intensity  $I = N/N_{\text{max}}$  in the O-beam with the neutron optical elements described so far is given as [158]

$$I_{\text{O}} = \frac{1}{2}(1 + C_{\text{exp}} \cos \chi). \quad (5.10)$$

In the interferometer, an RF spin manipulating coil is operated in each path which realises the weak interactions of two path weak measurements simultaneously. The axes of the coils coincide with the local beam directions. Alternating currents are applied with radio-frequencies  $f_{\text{I}} = 62.5 \text{ kHz}$  in path I and  $f_{\text{II}} = 55.5 \text{ kHz}$  in path II. The amplitudes are adjusted to realise spin rotation angles  $\alpha = \pi/9 \pm \pi/720 \hat{=} (20 \pm 0.5) \text{ degree}$  [112] with a spin manipulation efficiency  $\epsilon_{\text{exp}} = 0.92 \pm 0.02$ . The vertical fields  $B_{0,j}$  in the RF coils are generated by a large Helmholtz coil, which surrounds the interferometer and the O-beam, and a small Helmholtz coil at each RF coil for fine tuning of the resonance [164]. In the O-beam, a direct-current (DC) coil is positioned which applies a  $\pi/2$  rotation of the polarisation vector around the local  $x$ -direction. Further downstream, a polarising CoTi multilayer array (see Sec. 3.3.2), referred to as supermirror, transmits the spin-up component. The sequence of DC coil and supermirror allows the  $+x$  spin analysis assumed in Eq. (5.2). With the  $+x$  spin analysis, the initial spin up component and spin down component produced by the weak interaction interfere [165, 166]. The RF signals are reset every  $304 \mu\text{s}$  by the trigger of a function generator. In the O-beam, a mean count rate of up to 2 neutron counts per interval is expected. The detector in the O-beam registers the arrival time of the neutrons with a time-resolution of  $1 \mu\text{s}$ . Each binning time corresponds to a neutron which interacted with a magnetic field induced by the RF coils of a specific phase. To improve the counting statistics, the time-dependent measurements are repeated for 1 hour. Due to the low intensity given by Eq. (5.10) in the vicinity of  $\chi = \pm\pi$ , the measurements are extended to 2 hours at the closest points of  $\chi = \pm 35/36 \pi$ . The sum of all time-dependent measurements at the same phase shifter position  $\chi$  is called a time spectrum.

The choice of the RF-frequencies and the time intervals before resetting the RF-signals is influenced by multiple circumstances. First, the resonant frequency of the electrical circuits inducing the magnetic fields need to be reasonably close to the frequency induced by the signal generator. Secondly, the frequencies were often chosen in the 10s of kHz to reduce the influence of the Bloch-Siegert shift as introduced in Sec. 3.3.6. In a previous reactor cycle, Richard Wagner used the frequencies  $55.5 \text{ kHz}$  and  $60 \text{ kHz}$  [61] which were chosen in the early calibrations for the presented results. Furthermore, the acquisition interval needs to be in some relation to the frequencies. The time interval should be at least cover one envelope

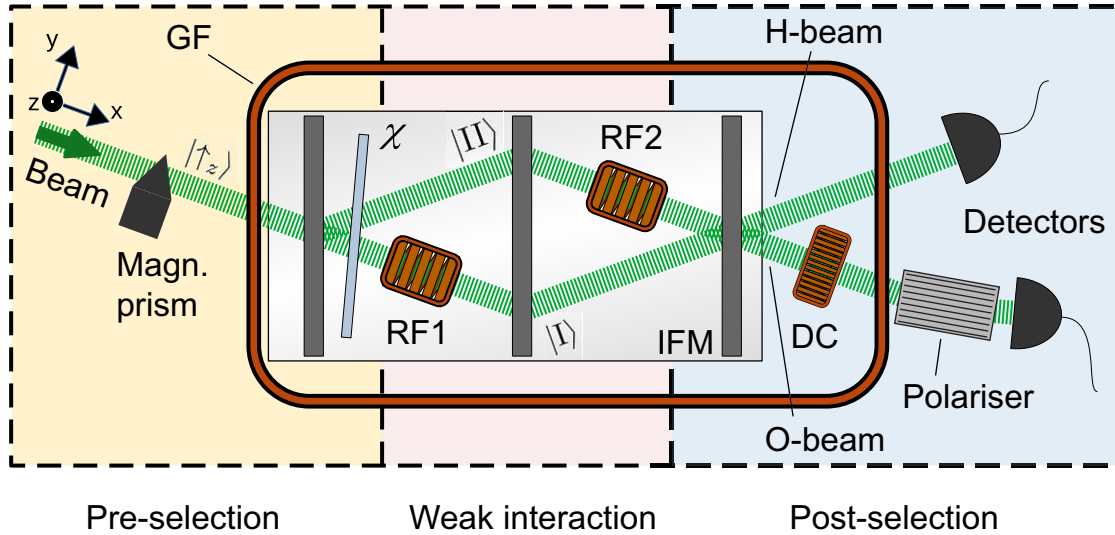


Figure 5.1: Setup of the neutron interferometer experiment. A monochromatised neutron beam is polarised in  $+z$ -direction by a magnetic prism. The interferometer crystal (IFM) splits the beam into the paths I and II. The sub-beams are recombined and the neutrons in the outgoing O-beam are detected with time resolution of  $1 \mu\text{s}$ . A guide field (GF) coil surrounds the experiment between prism and the polariser in the O-beam. The experiment consists of three stages: first, the pre-selection or preparation stage (light yellow) where the phase shifter determines the phase  $\chi$ , cf. Eq. (5.1). Second, the weak interaction stage (light red) where the spin is rotated by a rotation angle  $\alpha = \pi/9$  in both radio-frequency (RF) spin manipulation coils RF1 and RF2. The coils are operated at frequencies  $f_I = 62.5 \text{ kHz}$  and  $f_{II} = 55.5 \text{ kHz}$ . Finally, the analysis or post-selection (light blue), cf. Eq. (5.2). At the recombination of the sub-beams, the incoming state is projected onto a specific phase relation between the sub-beams in the O-beam. There, the direct-current (DC) coil rotates the polarisation vector  $\vec{P} = \langle \vec{\sigma} \rangle$  by  $\pi/2$  around the  $x$ -direction. The polariser projects onto the  $+z$  spin state. The combination of DC coil and polariser acts as a spin analysis in  $+x$ -direction.

of the intensity oscillation. In our case, the goal was to record a full period of the envelope of the intensity beating, i.e. two times the distance between two knots of the oscillation. The envelope has a frequency  $f_{\text{env}} = |f_1 - f_2|/2$ . The time interval, before the signal exhibits deviations in its phase, is about  $300 \mu\text{s}$ . The signal has to be reset after such a time interval. The period of the envelope for the frequencies  $55.5 \text{ kHz}$  and  $60 \text{ kHz}$  was too long, i.e.  $444 \mu\text{s}$ , to fulfil this condition. By increasing the frequency  $f_1$  to  $62.5 \text{ kHz}$ , the frequency for the envelope of the beating is  $3.5 \text{ kHz}$  which corresponds to a period of about  $286 \mu\text{s}$ . Furthermore, one period equals  $1/62500 \text{ s} = 16 \mu\text{s}$  and 19 periods equal  $304 \mu\text{s}$  which was finally chosen as the time interval before resetting the signal. It follows that the time spectra are also  $304 \mu\text{s}$  long with a time bin for each  $\mu\text{s}$ . In a Fourier transform of the time-resolved signal, the calculated frequency resolution  $\Delta f \approx 3.29 \text{ kHz}$  for this case can separate the two peaks expected at the chosen RF frequencies.

Thermal disturbances to the interferometer limit its contrast and phase sensitivity. To improve the quality of the results, a thermal control system stabilises the temperature through insulation and air conditioning. The coils close to the interferometer crystal are water cooled to stabilise their temperature [164, 167]. In effect, the phase drift of interferograms is restricted to 1 degree/hour. Additionally, the distance between the RF coils is maximised by installing them in different sections of the interferometer as depicted in Fig. 5.1 to reduce the mutual influences between the weak interactions.

## 5.4 Experimental Data

### 5.4.1 Orienting the Interferometer

The  $\rho$  axis, rocking scans, ad hoc analysis, and re-evaluation procedure were introduced for the first presented experiment in Sec. 4.3.1. For the present experiment, the interferometer crystal depicted in Fig. 5.2 is oriented. Rocking scans of the H-beam, depicted in Fig. 5.3, were recorded for different positions of the  $\rho$  axis. These were recorded with only one of the two paths in the interferometer opened, which reduces the total intensity. On the other hand, the output intensities are therefore independent from any phase relation between the paths. The order of rocking scans was from  $\rho = 4.06^\circ$  to  $\rho = 4.00^\circ$  and only then a rocking for  $\rho = 4.03^\circ$  was recorded. However, the positions of the peaks are not monotonous according to the value for  $\rho$ . The rocking curve for  $\rho = 4.03^\circ$  is the lefternmost. This indicates some hysteresis in the regulation of the piezo crystal.

The rocking scans recorded with multiple open paths in Sec. 4.3.1 were the sum of multiple output ports. In contrast, the counts in Fig. 5.3 are detected only in the H-beam. A single Gaussian function is expected to fit both peak and tails of these rocking curves. Ad hoc analysis of the rocking scans gave the full widths at half maximum (FWHM) plotted in Fig. 5.4 as blue points. The results indicate a minimum in FWHM at  $\rho \approx 4.02^\circ$ . The experiment was advanced with this value for  $\rho$ .

However, re-evaluation after the measurement campaign reveals some peculiarities in the data. Contrary to the fits in Fig. 4.4, the maxima in Fig. 5.3 are systematically underestimated, the most pronounced for  $\rho = 4.00^\circ$ . The resulting fit

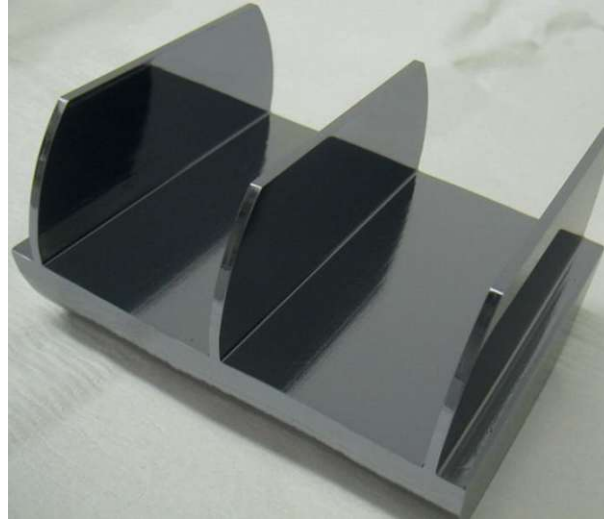


Figure 5.2: Photograph of the three-plate single crystal neutron interferometer used for the experiment presented in this section. The length is about 10 cm. At each interferometer plate, a beam splitting is produced in Laue configuration. This leads to two separated beam paths interfering at the last interferometer plate as depicted schematically in Fig. 5.1.

parameters with a Gaussian fit function are plotted in Fig. 5.4 as yellow data. These results indicate a strict monotonous change in FWHM in the scanned interval of  $\rho$  and a minimum outside the scanned interval at  $\rho \approx 3.98^\circ$ . The ad hoc analysis relies on the data points close to the maximum and led to systematically higher values for the FWHMs. This suggests a deviation in the characteristics of the intensity from the Gaussian behaviour also for a single recorded output port. With these observations, to focus the the ad hoc analysis on the highest data points to maximise the intensity is validated. Despite these peculiarities, it can be concluded that the experiment was proceeded at position  $\rho = 4.03$  with sufficient intensity.

## 5.4 Experimental Data

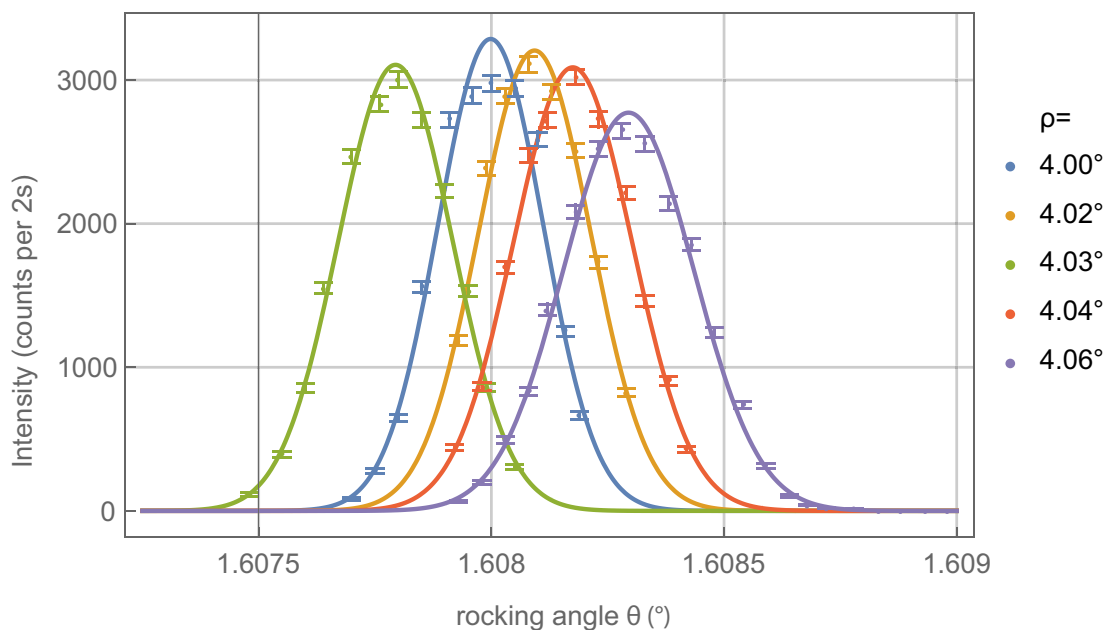


Figure 5.3: Counts of rocking curves in the H-beam for different  $\rho$  axis angles as indicated to the right. Error bars indicate one standard deviation. Fits of the form of Eq. (4.13) are plotted as solid curves.

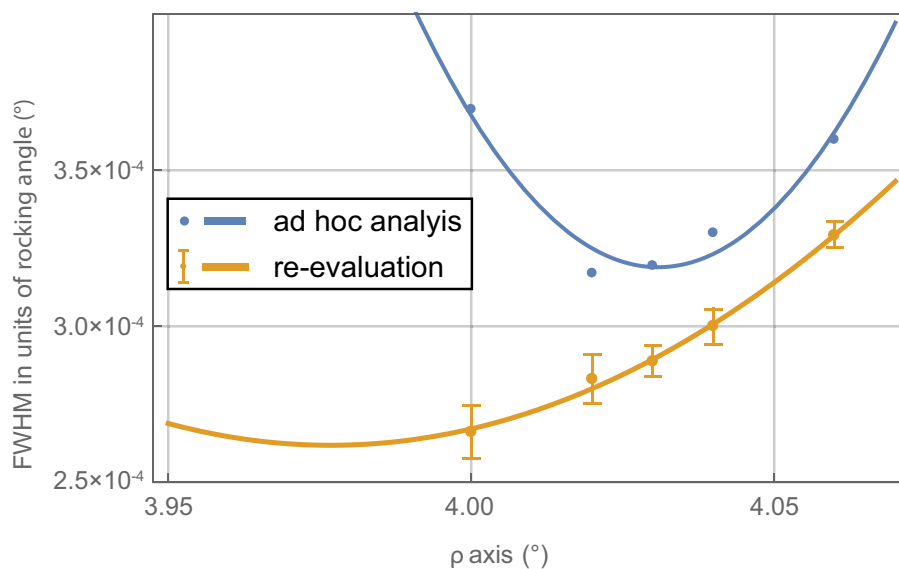


Figure 5.4: Full widths at half maxima (FWHM) plotted over  $\rho$  axis angle. Blue data refers to the ad hoc analysis. Yellow data is the re-evaluation after the measurement campaign. Error bars indicate one standard deviation. Polynomial fits to the second order in  $\rho$  are plotted as solid curves. The two evaluations indicate different values for the minimal FWHM and, therefore, the sharpest peaks.

## 5.4.2 Time-Resolved Measurements

### Pre-Measurements

Before the case of two simultaneous weak spin rotations was performed, the intensities with only one RF coil operating were recorded. Also, strong interaction strengths in the form of large spin rotation angles  $\alpha = \pi/2$  were applied. Exemplary time spectra for single RF coil operation with large spin rotation angles are depicted in Fig. 5.5 for RF1 and Fig. 5.6 for RF2.

An exemplary time spectrum with both RF coils operating and large rotation angles is depicted in Fig. 5.7. In the latter figure, the intensity oscillation does not fit to a beating with a sinusoidal envelop. This indicates that the second order terms in  $\alpha$  are non-negligible as is confirmed by a discrete Fourier transform depicted in Fig. 5.8. In the depiction of the Fourier transform the offset is equivalent to the high peak at frequency 0 kHz. The oscillation with a frequency of 7 kHz is dominant over the frequencies of the RF coils. The Fourier transformation resolves the two peaks at the coil frequencies separately. If the frequencies were chosen closer together, as initially done, a merged broader single peak is expected. The difference between the RF coil frequencies is 7 kHz which appears in second order terms in  $\alpha$ . Although not written explicitly, this behaviour can easily be derived from Eq. A.9. Because Fig. 5.7 is only a pre-measurement with high values for  $\alpha$ , the stated characteristics in intensity and the Fourier transform are expected. However, some mismatch between the amplitudes of the RF frequencies is noticeable in the Fourier transform. The depicted time-resolved measurement was followed by a re-adjustment of the coil RF1 with its frequency of 62.5 kHz to match the amplitude of the oscillation with frequency 55.5 kHz.

### Final Results

The time-resolved count rates in the O-beam were recorded for several phase shifter settings  $\chi$ . The example with the most pronounced oscillations of such a recording is depicted in Fig. 5.9. All other time spectra contributing to the final results are depicted in Fig. 5.10. A beating modulation of the count rate is observed as predicted per Eq. (5.9). The mean counts and the amplitude of the oscillations are highest for  $\chi = 0$  and decrease towards  $\chi = \pm\pi$ .

The count rates are normalised into intensities and fitted with a corresponding double-sine fit function,

$$I_{\text{fit}}(t) = I_{0,\text{fit}} + D_{\text{I}} \sin(2\pi f_{\text{I}} t + \phi_{\text{I}}) + D_{\text{II}} \sin(2\pi f_{\text{II}} t + \phi_{\text{II}}) \quad (5.11)$$

with the mean intensity  $I_{0,\text{fit}}$  and oscillations with amplitudes  $D_j$  and phases  $\phi_j$ ,  $j \in \{\text{I}, \text{II}\}$ . The raw resulting fit parameters are depicted in Fig. 5.11 in terms of amplitudes of the two oscillations over the mean intensity,  $D_j/I_{0,\text{fit}}$ , and the phase  $\phi_j$  of the oscillations. The offset of the phase  $\phi_j$  is chosen such that the mean over each set  $\phi_j$  is zero. The argument for this offset is found in Sec. 5.4.4 where it is motivated in context of Eq. (5.13). The theoretical prediction for the ratio of amplitude over mean counts is symmetric in the interferometric phase  $\chi$  with two maxima. The extracted amplitudes are also roughly symmetric but lower than expected and exhibit two maxima. The phase of the intensity oscillations is

## 5.4 Experimental Data

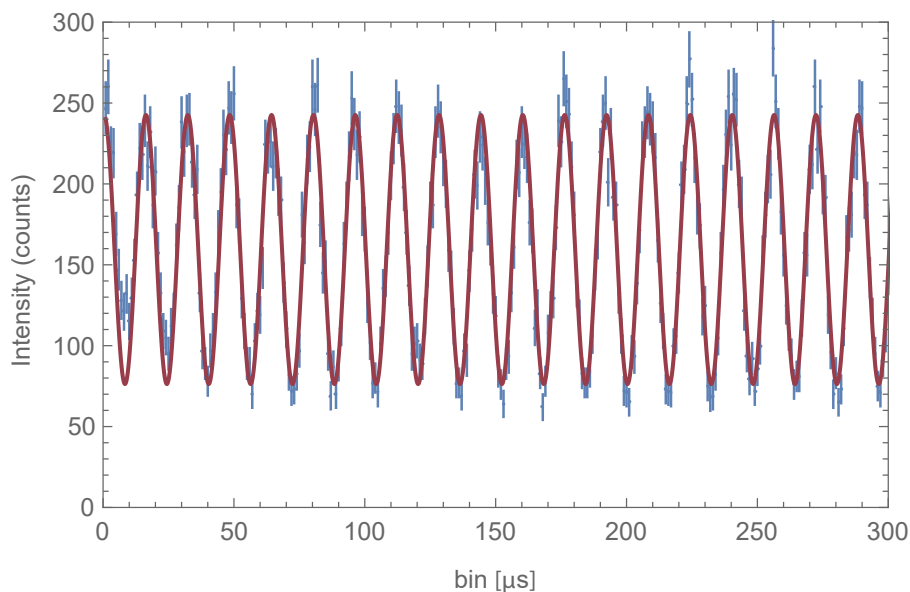


Figure 5.5: Time spectrum at phase shifter position  $\chi = 0$  while coil RF1 is operating with a large spin rotation angle  $\alpha = \pi/2$ . The coil RF2 is turned off for this measurement. Error bars indicate one standard deviation. The sinusoidal fit is plotted as solid red curve.

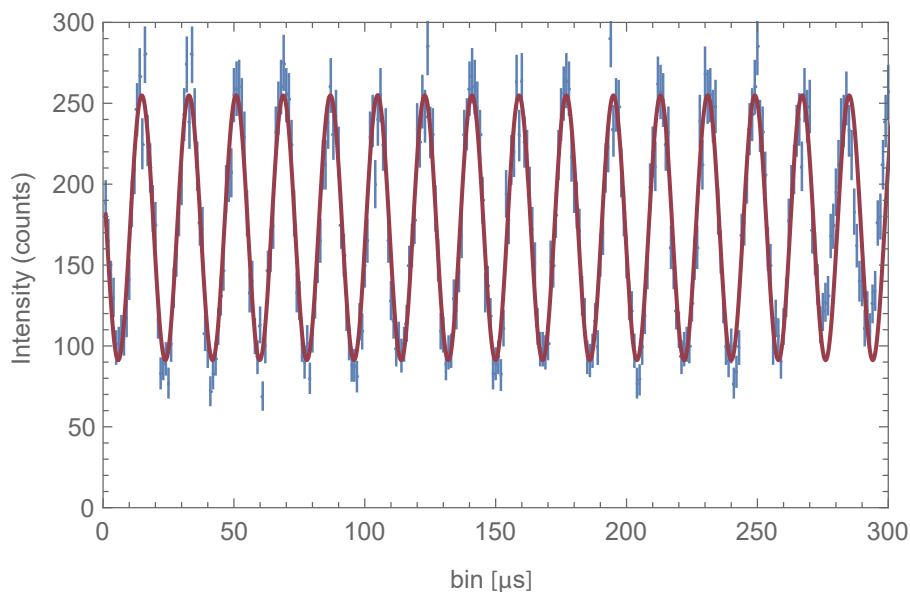


Figure 5.6: Time spectrum at phase shifter position  $\chi = 0$  while coil RF2 is operating with a large spin rotation angle  $\alpha = \pi/2$ . The coil RF1 is turned off for this measurement. Error bars indicate one standard deviation. The sinusoidal fit is plotted as solid red curve.

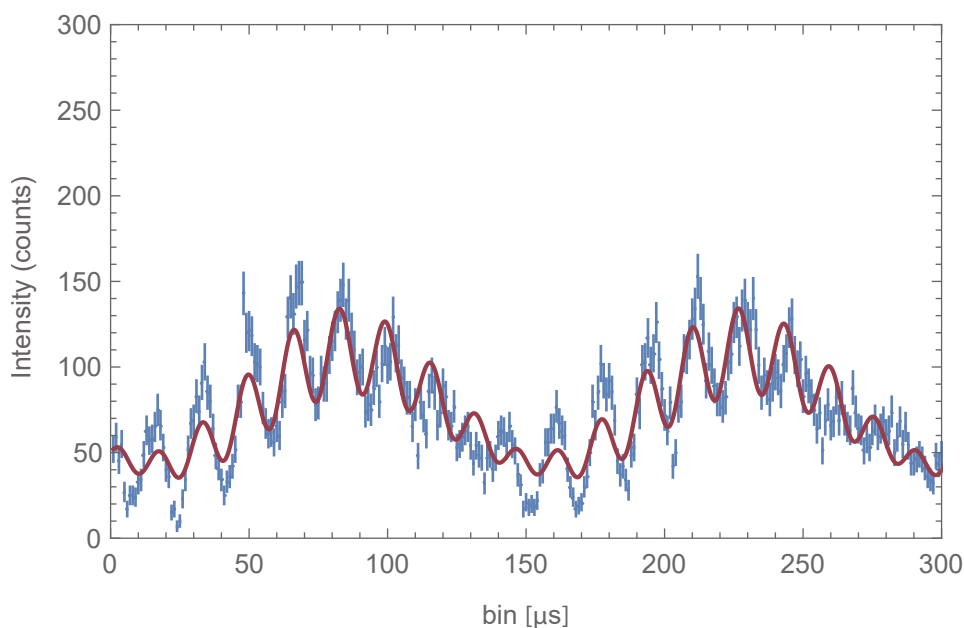


Figure 5.7: Exemplary time spectrum with high spin rotation angles  $\alpha \approx \pi/2$  at  $\chi = 8\pi/9$  with scales of counts and time bin to the left and bottom, respectively. Error bars indicate one standard deviation. The intensity modulation is not a beating which indicates that the spin rotation angles are too high to neglect second-order terms in  $\alpha$ . To include the second-order terms, a triple-sine fit with the frequencies 7 kHz, 55.5 kHz, and 62.5 kHz is plotted as solid red curve. Furthermore, the results form a discrete Fourier analysis depicted in Fig. 5.8 indicates a misalignment between the two spin rotation angles. Re-adjustment of the amplitudes of the magnetic fields is necessary.

## 5.4 Experimental Data

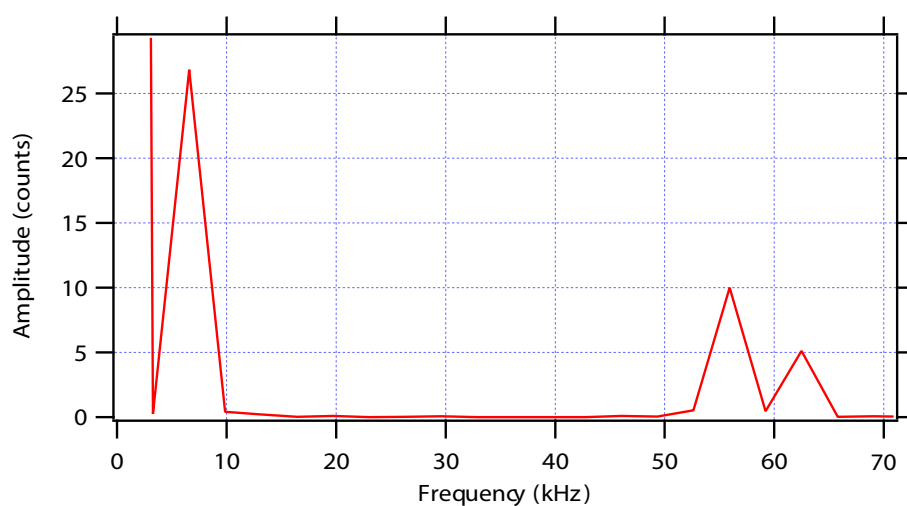


Figure 5.8: Fourier transform of the time-resolved measurement depicted in Fig. 5.5 with both coils RF1 and RF2 operated with a spin rotation angle  $\alpha = \pi/2$ . The large, cut-off peak at 0 kHz represents the main neutron count. Three additional peaks are present: at 7 kHz, 55.5 kHz, and 62.5 kHz, the latter two being chosen for the RF coils. The difference in frequencies of 7 kHz were chosen such that one can distinguish between the two RF frequencies with the frequency resolution of about 3.5 kHz. The goal is a neutron count with only the two higher frequencies. The oscillation with 7 kHz is dominant as also conspicuous in the time-resolved measurement. However, for the large spin rotation angle, contributions to the intensity of the second order in  $\alpha$  become dominant. Therefore, the large peak at 7 kHz, the difference between the two RF frequencies, is to be expected. The peaks at the RF frequencies are of different height which makes a re-adjustment of coil RF1 necessary.

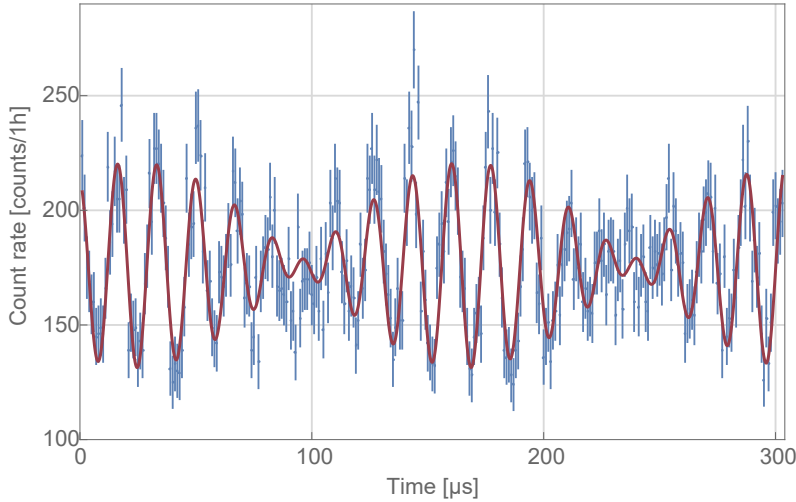


Figure 5.9: Example of a time spectrum of the count rate at relative phase  $\chi = 0$ . Data points in blue. Error bars indicate one statistical standard deviation. The time axis is with regards to the trigger for the reset of the signals to both radio-frequency coils every  $304 \mu\text{s}$  (see Sec. 5.3). Time-resolved measurements are repeated over 1 hour and summed up to the depicted time spectrum. The count rate is beating in time following the theoretical prediction of Eq. (5.9). Solid red line is a fit according to Eq. (5.11).

predicted as anti-symmetric towards themselves and symmetric with each other as they are mirrored counterparts. The phases mostly follow the prediction within the measurement error. Some phase deviations are observed for frequency  $f_{\text{II}} = 55.5 \text{ kHz}$  when approaching the phase shifter position  $\chi = \pm\pi$ .

### 5.4.3 Data Correction

Some deviations of the measured results from the theoretical predictions originate in the experimental contrast  $C_{\text{exp}} = 0.64 \pm 0.02$  of the interferometer and the spin manipulation efficiency  $\epsilon = 0.92 \pm 0.02$  of the magnetic coils. The data correction considering these parameters is described in Sec. A.2.2. Applying the correction results in the data depicted in Fig. 5.12. For the phase of the intensity oscillations, the ambiguity of the arctangent in the correction procedure is used to move the outermost phases by  $\pm\pi/2$ . In this way, the agreement between data and prediction is conspicuous. The maxima in the ratios of amplitude over mean move outward compared to Fig. 5.11. The gradient dependent on  $\chi$  in all predictions of Fig. 5.11 is the highest close to  $\chi = \pm\pi$ . Therefore, the correction procedure most strongly influences the position of the respective data points. This entails drastically increased error bars when approaching  $\chi = \pm\pi$ . The high relative errors are to be expected with the low count rates there. In contrast to the phase at  $\chi = 0$ , the data correction becomes crucial when considering the phases close to  $\chi = \pm\pi$ . All three phases  $\phi_j$  at  $\chi \in -\pi, 0, +\pi$  are predicted to be zero. The data correction enlarges absolute value of the phases but preserves the sign of the initial phases. Therefore, the agreement between data and prediction after correction depends on the accuracy in the raw data.

## 5.4 Experimental Data

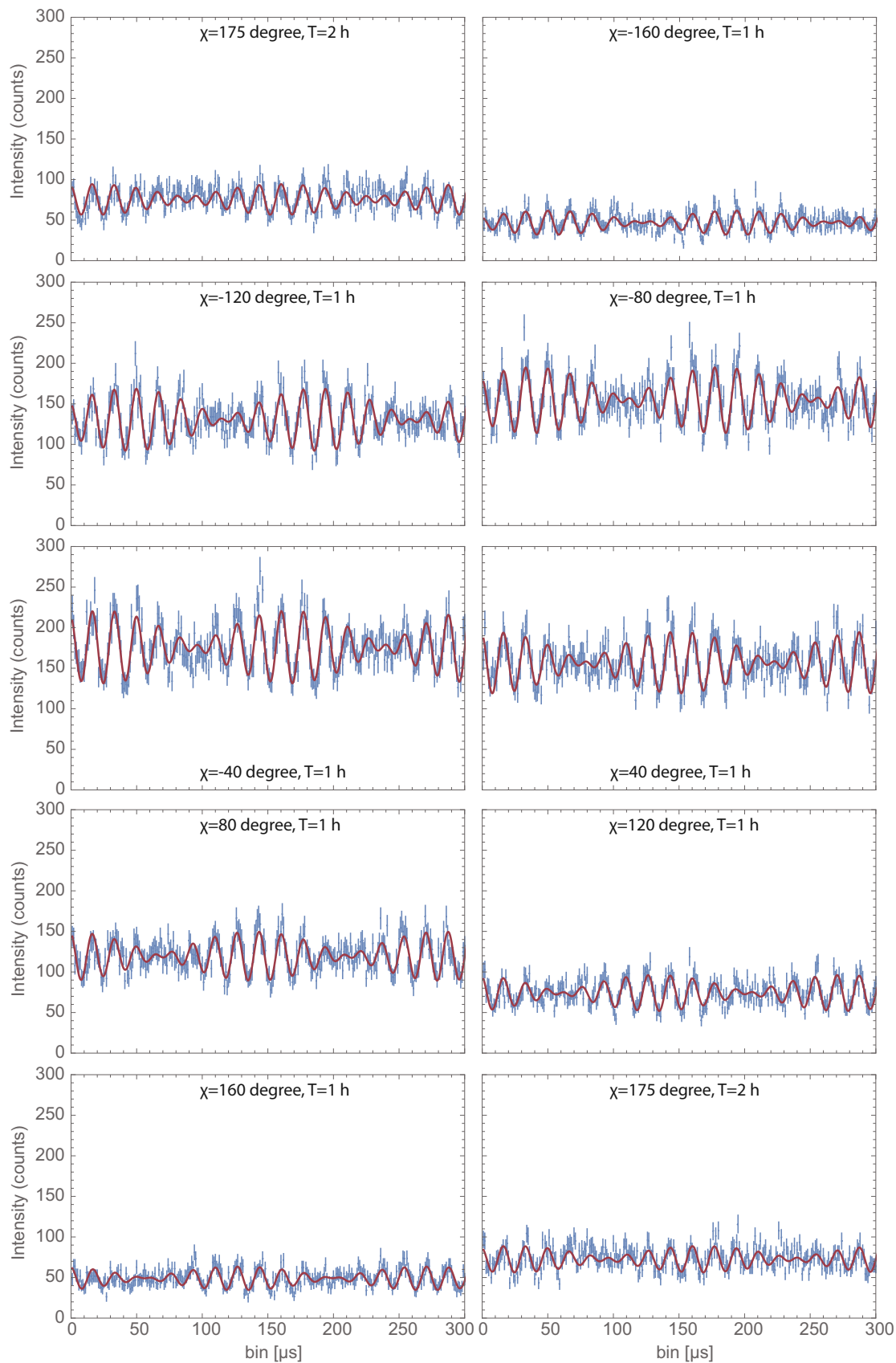


Figure 5.10: Time spectra in addition to Fig. 5.9 with scales of counts and time bin to the left and bottom, respectively. Phase shifter position  $\chi$  and integration time  $T$  indicated in each panel. See caption of Fig. 5.9 for further information.

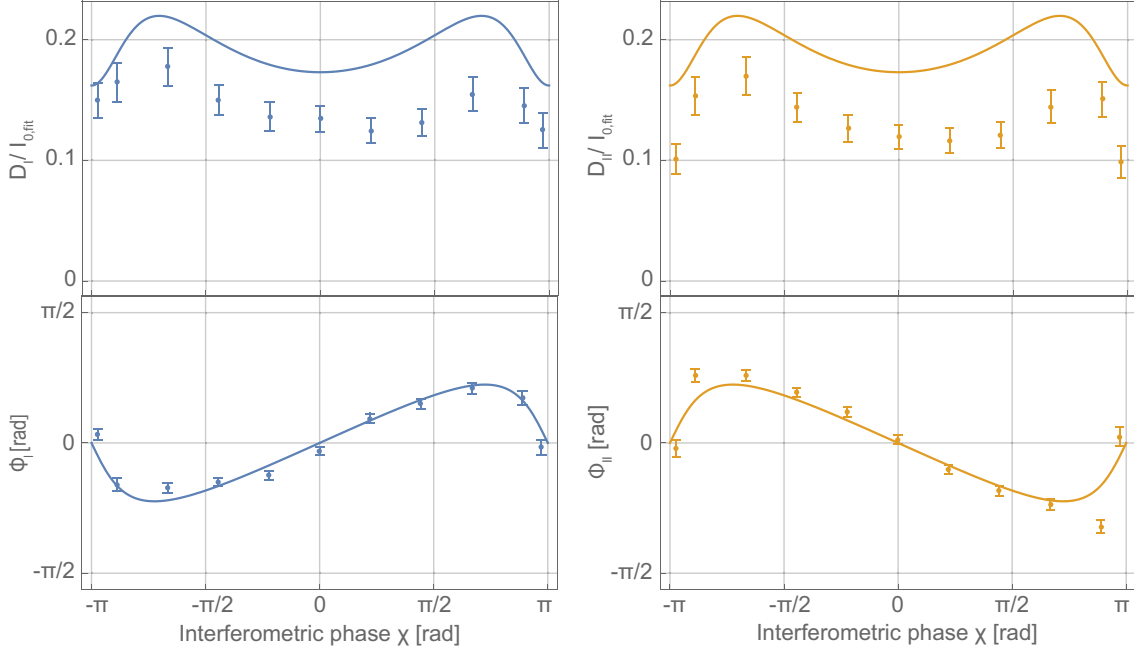


Figure 5.11: Characteristics of the raw time spectra of Figs. 5.9 and 5.10 plotted over the phase shifter position  $\chi$  as indicated on the bottom. The relation of the amplitude of the oscillation with frequency  $f_j$  over the mean intensity is depicted on top, the phase of the respective oscillation below. Error bars indicate one standard deviation. The solid curves are the theoretical prediction according to Eq. (5.9).

#### 5.4.4 Conversion to Weak Values

The amplitudes  $D_j$  and phases  $\phi_j$  of the oscillations naturally offer the direct extraction of the complex weak values  $\langle \hat{\Pi}_j \rangle_w = A_j e^{i\varphi}$  in polar coordinates. To extract the weak values from the measured intensities, we equate the linear approximation in  $\alpha$  of Eq. (5.9) for the ideal case from theory with the fit function of Eq. (5.11). Quantities with index “exp” refer to the experimentally retrieved values in contrast to the theoretical prediction, “corr” to the corrected values. Due to spatial reasons, the correction is implied for the measures  $D_j$ ,  $\phi_j$ , and  $I_0$ .

$$\begin{aligned}
 I_{\text{ideal}}(t) &= I_{\text{fit,corr}}(t) \\
 \Rightarrow |\langle f|i \rangle|^2 &\left( 1 - \alpha \left[ A_{\text{I,exp}} \sin(\varphi_{\text{I,exp}} - 2\pi f_{\text{I}}t - \delta_{\text{I,exp}}) + A_{\text{II,exp}} \sin(\varphi_{\text{II,exp}} - 2\pi f_{\text{II}}t - \delta_{\text{II,exp}}) \right] \right) \\
 &= I_0 + D_{\text{I}} \sin(2\pi f_{\text{I}}t + \phi_{\text{I}}) + D_{\text{II}} \sin(2\pi f_{\text{II}}t + \phi_{\text{II}}).
 \end{aligned} \tag{5.12}$$

By comparing the coefficients to the left and right, we obtain

$$\begin{aligned}
 |\langle f|i \rangle|^2 &= I_0, \\
 |\langle f|i \rangle|^2 \alpha A_{\text{I,exp}} \sin(2\pi f_{\text{I}}t + \delta_{\text{I,exp}} - \varphi_{\text{I,exp}}) &= D_{\text{I}} \sin(2\pi f_{\text{I}}t + \phi_{\text{I}}), \\
 |\langle f|i \rangle|^2 \alpha A_{\text{II,exp}} \sin(2\pi f_{\text{II}}t + \delta_{\text{II,exp}} - \varphi_{\text{II,exp}}) &= D_{\text{II}} \sin(2\pi f_{\text{II}}t + \phi_{\text{II}}), \\
 \Rightarrow A_{\text{I,exp}} &= \frac{D_{\text{I}}}{\alpha I_0}, \quad A_{\text{II,exp}} = \frac{D_{\text{II}}}{\alpha I_0}, \\
 \varphi_{\text{I,exp}} &= \delta_{\text{I,exp}} - \phi_{\text{I}}, \quad \varphi_{\text{II,exp}} = \delta_{\text{II,exp}} - \phi_{\text{II}}.
 \end{aligned} \tag{5.13}$$

## 5.4 Experimental Data

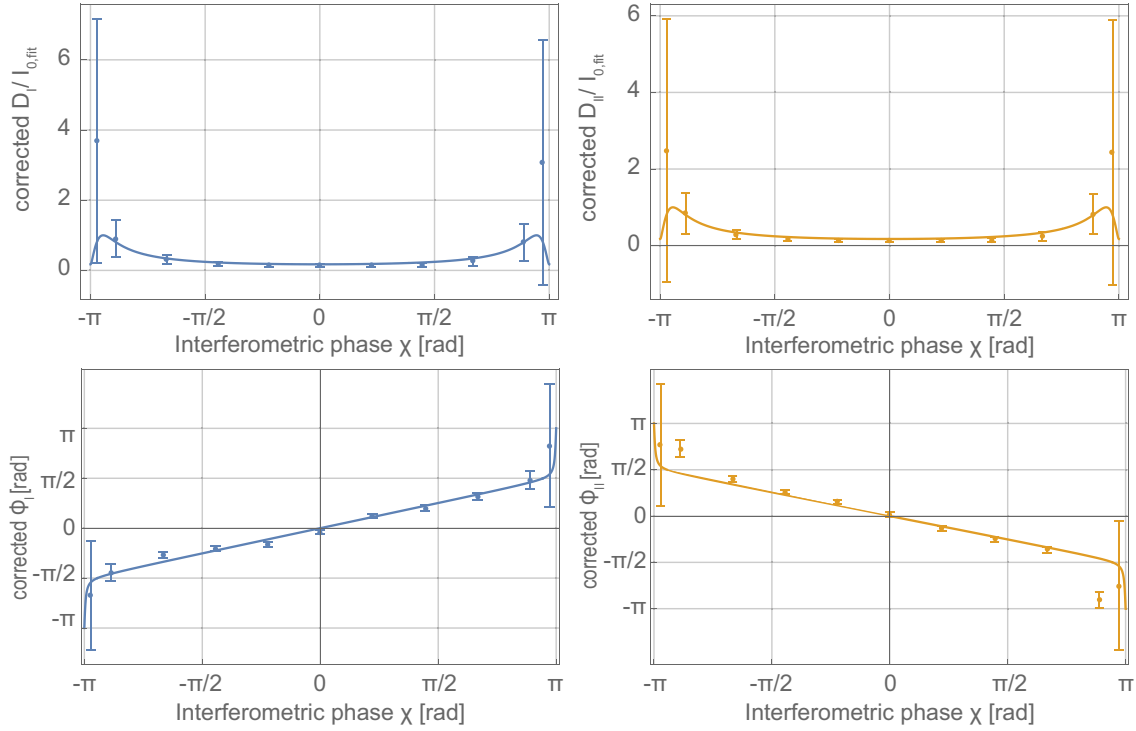


Figure 5.12: The corrected fit parameters of the time spectra of Figs. 5.9 and 5.10 plotted over the phase shifter position  $\chi$ . The corrected amplitudes of the oscillation with frequency  $f_j$  over the corrected mean intensities is depicted on top, the corrected phase of the respective oscillation below. Error bars indicate one standard deviation. The solid curves are the theoretical prediction according to Eq. (5.9) The correction procedure described in Sec. A.2.2 considers the experimental contrast of the interferometer  $C_{\text{exp}} = 0.64 \pm 0.02$  and the spin manipulation efficiency  $\epsilon = 0.92 \pm 0.02$  of the magnetic coils.

The absolute phase between the paths of the interferometer is unknown and only the relative phase  $\chi$  is controlled. Therefore, the phase offsets  $\delta_j$  are also undetermined albeit predictable. However, according to Eq. (5.5), the phases  $\varphi_j$  of the weak value are anti-symmetric in  $\chi$  and their mean is zero. So we chose the phase offsets  $\delta_{j,\text{exp}}$  such that both means of the phases  $\varphi_j$  of the time-dependent oscillation are zero,  $\bar{\varphi}_j = 0$ .

The quantities at the end of Eq. (5.13) are closely related to the quantities depicted in Figs. 5.11 and 5.12. For the absolute value of the weak values, the corrected data from Sec. 5.4.3 is normalised with the spin rotation angle  $\alpha = \pi/9$ . This only concerns the amplitudes over phases, while the corrected phases are identical with the phases of the weak values. The absolute values and phases of the path weak values are plotted in Fig. 5.13 dependent on the interferometer phase  $\chi$  between the two paths. The absolute value diverges at interferometer phases  $\chi = \pm\pi$  as predicted by Eq. (5.5). The phases of the weak values are linear in  $\chi$  as predicted by Eq. (5.5). This directly represents the phase of the intensity modulation in time. By changing the basis to real and imaginary coordinates, the data in Fig. 5.14 arise. Theory predicts that the real part is constant for all  $\chi$ . The imaginary parts are anti-symmetric functions which also diverge for  $\chi = \pm\pi$ . Note that the polar coordinates are ex-

## 5 Simultaneous Path Weak-Measurements

tracted directly from fitting a double-sine curve as in Eqs. (5.9) and (5.11), while the real and imaginary components are equivalent but secondary measures. It is clearly seen that the extracted data agree with the theoretical predictions. Simultaneous weak-measurements are accomplished.

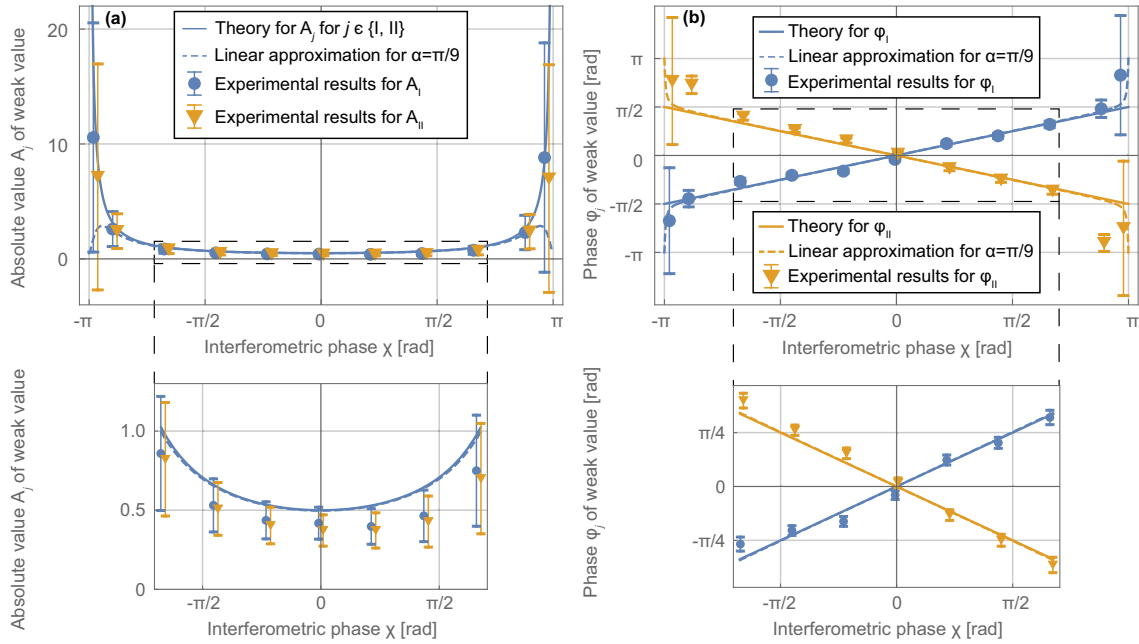


Figure 5.13: The complex weak values in polar coordinates  $\langle \hat{\Pi}_j \rangle_w = A_j e^{i\varphi_j}$ . They are given through (a) the absolute value  $A_j$  and (b) the phase  $\varphi_j$  dependent on the interferometric phase shift  $\chi$  with theoretical predictions. In (a) and (b), the dashed frame is magnified on the bottom. Error bars indicate one standard deviation and include the systematic errors. Solid curves are the theoretical predictions in the limit of the spin rotation angle  $\alpha \ll 1$ . Dashed curves indicate the expected behaviour of the linear data analysis used with the applied finite spin rotation angle  $\alpha = \pi/9$ . Where the solid and dashed lines separate, the linear approximation in  $\alpha$  of Eq. (5.9) does not hold any more.

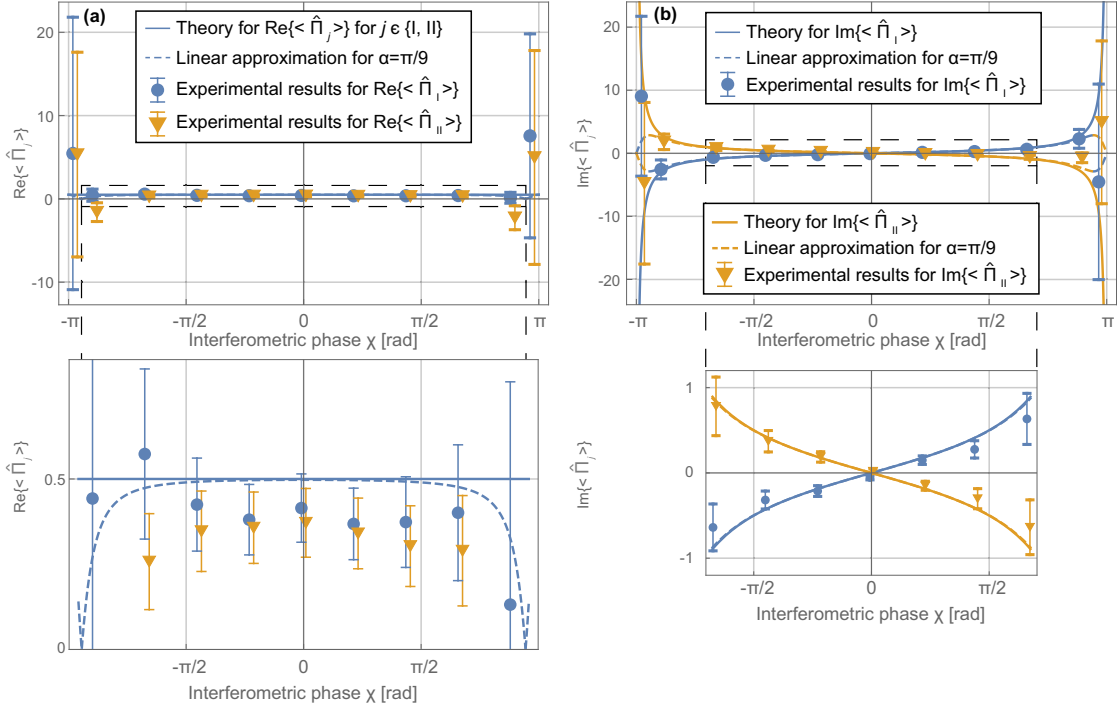


Figure 5.14: The complex weak values  $\langle \hat{\Pi}_j \rangle_w$  given through (a) the real and (b) the imaginary part dependent on the interferometric phase shift  $\chi$  with theoretical predictions. In (a) and (b), the dashed frame is magnified on the bottom. Error bars indicate one standard deviation and include the systematic errors. Solid curves are the theoretical prediction in the limit of the spin rotation angle  $\alpha \ll 1$ . Dashed curves indicate the expected behaviour of the linear data analysis used with the applied finite spin rotation angle  $\alpha = \pi/9$ . Where the solid and dashed lines separate, the linear approximation in  $\alpha$  of Eq. (5.9) does not hold any more.

The results are also plotted in the complex plane as depicted in Fig. 5.15. Most corrected data points agree with the theoretical prediction in red. In the complex representation, all information on the weak values but for the interferometer phase  $\chi$  is displayed at once. However, the data is also more difficult to understand. Note a detail in the data: the imaginary part is predicted to monotonously increase (decrease) with  $\chi$  for  $\langle \hat{\Pi}_I \rangle_w$  ( $\langle \hat{\Pi}_{II} \rangle_w$ ). As can be seen in Fig. 5.14(b), the outermost points at  $\chi = \pm 35/36\pi$  change the sign of their imaginary parts in both data sets. Therefore the position in the complex plane is inverted or mirrored around the real axis. This is in contrast to the theory prediction in the limit of  $\alpha \rightarrow 0$ . However, this inversion is predicted for the case  $\alpha = \pm 35\pi/36$ .

## 5.5 Discussion

### 5.5.1 Comparison with Standard Weak Measurements

The standard weak measurements introduced in Sec. 2.1.2 use a meter system to gain information about the observable. For simultaneous measurements, it would be most convenient to use a different meter system for each observable as in the Arthurs-Kelly protocol [161, 168, 169]. Articles [161, 168] assume non-commuting

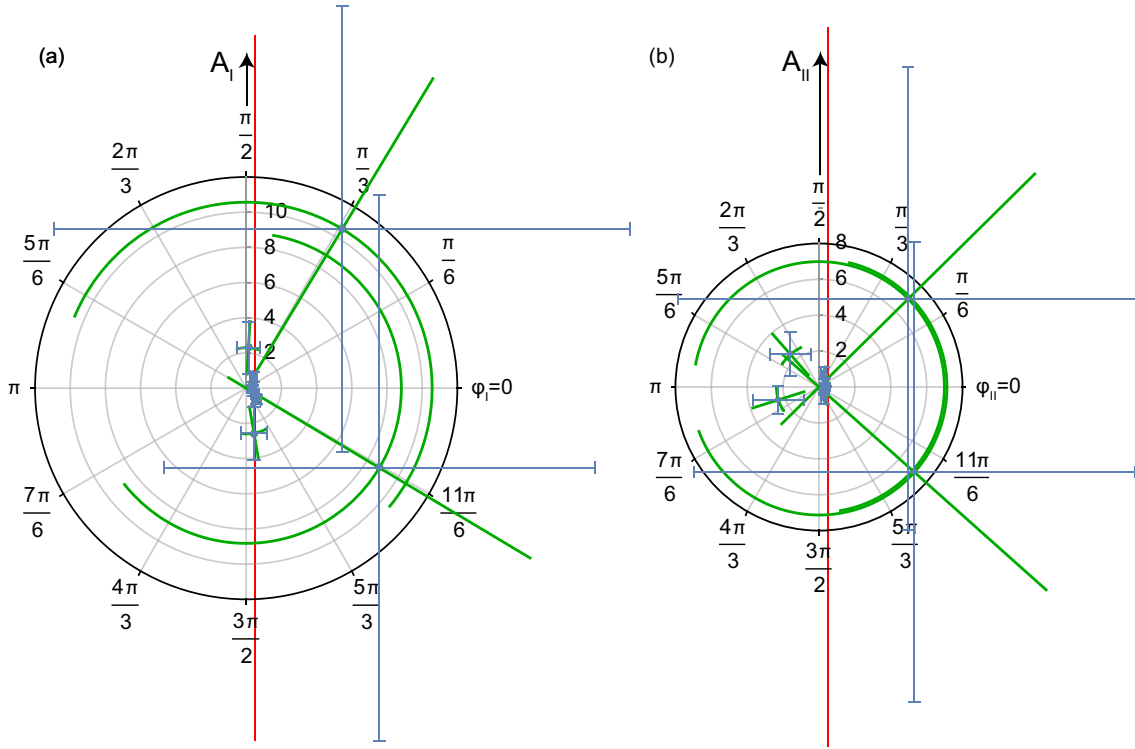


Figure 5.15: The corrected complex weak values  $\langle \hat{\Pi}_j \rangle_w$  given in the complex plane. The left graph (a) depicts the weak values  $\langle \hat{\Pi}_I \rangle_w = A_I \exp(i\varphi_I) = \text{Re}\{\langle \hat{\Pi}_I \rangle_w\} + i \text{Im}\{\langle \hat{\Pi}_I \rangle_w\}$  and the right graph (b) the weak values  $\langle \hat{\Pi}_{II} \rangle_w = A_{II} \exp(i\varphi_{II}) = \text{Re}\{\langle \hat{\Pi}_{II} \rangle_w\} + i \text{Im}\{\langle \hat{\Pi}_{II} \rangle_w\}$ . Blue data sets are the Cartesian coordinates, green sets the polar coordinates. While the positions of the data points match, the difference between the coordinate systems becomes apparent with the error bars which indicate one standard deviation, including the systematic errors. The theoretical predictions are on the red lines defined through  $\text{Re}\{\langle \hat{\Pi}_j \rangle_w\} = 1/2$ .

observables, while the observables in the presented experiment are commuting path operators. For a standard weak measurement, the meter is the expectation value of the operator entangled with the observable, e.g. the meter gives a value of momentum. For the simultaneous measurements of this chapter, the energy system is used as a meter system. Not the energy itself gives the path information but the occupation of each energy level. A situation described by Eq. (2.20) is the case. For each energy shift, a different operator is coupled with the path observable. This is why the energy system can in principle be used as the sole meter for an arbitrary number of simultaneous weak path measurements. In contrast, if any combination of the three weak interactions for the three-path quantum Cheshire Cat were applied simultaneously, the resulting intensity were difficult to interpret. As stated in Sec. 4.4, a main motivation for weak measurements is their minimal disturbance on the intermediate state between pre- and post-selection which simplifies characterising the respective quantum state. This criterion is fulfilled for the presented simultaneous weak path measurements. Therefore, the experiment shares some but not all features with standard weak measurements such that one can regard it as a generalised weak measurement.

### 5.5.2 Emergence and Properties of the Results

A simultaneous one-shot measurement of two weak values is conducted by implementing sinusoidal oscillations of the magnetic fields with different frequencies in each path. Time-resolved measurements of the intensity are used to directly extract the weak values in polar coordinates from the fitting parameters of a double-sine fit. The absolute values and phases of the weak values are furthermore converted to the real and imaginary components. For the present experiment, this indicates that the absolute value and phase are the measures with direct physical significance rather than the secondary real and imaginary components.

While it is not any more necessary in the presented procedure to turn the devices for the weak interactions on and off, a time-dependent measurement is necessary to retrieve multiple weak values. This can be regarded as trading in one experimental requirement with another. However, the presented results are extracted with a single ensemble at each phase shifter setting  $\chi$ . The simultaneous validity of the two weak values is therefore guaranteed while preserving the studied interference effect. We should emphasise that the simultaneously extracted weak values agree with the predictions for single weak values.

We will now discuss the connection between the neutron optical elements and the measured intensity. The mean intensity  $\bar{I}_O$  in the O-beam of Fig. 5.9 for  $\alpha \ll 1$  is given by  $I_O$  of Eq. (5.10), multiplied by another factor of 1/2 due to the spin analysis in  $+x$ -direction of the initial  $+z$  spin state. The time-dependence of the weak interaction makes the intensity time-dependent. The beating intensity modulation of Fig. 5.9 originates in the sinusoidal RF signal. Let us first consider only a single applied RF signal. The time of entry into the RF field determines the relative phase at the end of the coil between the flipped spin down component and the initial spin up component. The relative phase between spin up and down component regulates the  $+x$ -component of the spin state and in effect the transmission probability at the spin analysis. This relative phase is time-dependent after exiting the coil, due to the energy shift. Therefore, the polarisation vector  $\vec{P} = \langle \vec{\sigma} \rangle$ , with the Pauli matrices  $\hat{\sigma}_i$ , rotates [105]. With the spin analysis in  $+x$ -direction, an oscillating intensity is observed with one coil. With two coils operated at different frequencies, two such oscillations can be directly added in the limit  $\alpha \ll 1$  such that a beating emerges if  $(f_I - f_{II})/(f_I + f_{II}) \ll 1$ . The weak values are directly given by the amplitude and phase of the oscillations via Eq. (5.9). For a fixed  $\alpha$ , the amplitude is connected to the probability amplitude in the respective path and in turn to the path operator. The phase of the magnetic field determines the phase of the detected intensity modulation. Therefore, the magnetic fields of the RF coils encode the weak values into the intensity. (The spin rotation angle  $\alpha$  scales the amplitude of the time-dependent signal with the absolute value of the weak value.)

The extracted weak values of Figs. 5.13 and 5.14 conform mostly with the theoretical prediction. When the interferometer phase  $\chi$  approaches  $\pm\pi$ , the absolute value and the imaginary part of the weak values diverge according to Eqs. (5.5) and (5.6). Consequently, the error bars drastically increase at these phase shifter positions in both the polar and Cartesian representation.

The absolute values of Fig. 5.13 are systematically too small. This is caused in the time-resolved measurements (cf. Fig. 5.9) by amplitudes of the oscillations which are lower than predicted. We attribute this to a systematically too small

spin rotation angle  $\alpha$  which we estimate to be too low by a factor of  $\approx 0.8$ . For  $\alpha = \pi/9 \hat{=} 20$  degree, this is an order of magnitude more than the uncertainty of  $\pm 0.5$  degree as estimated in Sec. 5.3. The phase  $\varphi_{\text{II}}$  also exhibits a systematic deviation from theory. The slope of the data points for  $\varphi_{\text{II}}$  is steeper than expected. We attribute this to the reset of the field every  $304 \mu\text{s}$ : while this is a multiple of the oscillation period for  $f_{\text{I}}$ , the oscillation with  $f_{\text{II}}$  is cut off at the reset. The magnetic field inside the coil and its driving stimulus are then off-phase which can explain some phase deviations.

The data extraction uses the double-sine fit which assumes small rotation angles  $\alpha \ll 1$ . However, we apply a finite rotation angle  $\alpha = \pi/9$ . For finite rotation angles, deviations from the linear approximation in  $\alpha$  of the extracted values due to higher order terms are expected. These deviations are depicted in the graphs as dashed lines. (They assume single weak value extraction and omit the cross-term between the spin down components of both paths. Equation (A.11) in Sec. A.2.2 explicitly states this cross-term  $\sim \sin^2(\alpha/2)$  just before the approximation.) The extracted data comply with both the first order approximation and the expected deviations due to the size of the error bars. Therefore, the chosen spin rotation angle is suitable for the chosen combination of setup and measurement time and the linear approximation in  $\alpha$  is reasonable.

The systematic effects described for the polar coordinates are also visible in Fig. 5.14 in the equivalent terms of real and imaginary part of the weak values. For large interferometer phases  $\chi$ , the errors are increased. The systematically reduced absolute values compared to prediction translate in the systematically reduced real and imaginary parts. The real part is usually interpreted as the best estimate for the path operators [33, 38]. One can interpret the estimates in terms of detection probabilities. For our symmetric beam splitter, a real part of  $1/2$  is predicted. In the comparison of the two sets of real parts, the deviations between both sets are comparable with the error bars. This is consistent with both paths being equally probable and visibility of the interference fringes is maintained. The second and second-last real parts of the yellow data set  $\text{Re}\{\hat{\Pi}_{\text{II}}\}$  are incompatible with the prediction. This is linked to the similarly incompatible phases  $\varphi_{\text{II}}$  of the weak value in Fig. 5.13.

The absolute values of the imaginary part are also systematically too small. The phase inaccuracy is visible here, too. The imaginary parts are often interpreted as intrinsic measurement disturbance [32, 38]. The divergences of the imaginary parts at  $\chi = \pm\pi$  are connected to the vanishing intensity at the detector such that no information can be gained. The change in sign for the left and right-most points is consistent with the theory prediction for the finite angle of  $\alpha$ . The sum of the imaginary parts is expected to be zero because the sum of the path weak values is supposed to be  $1 \in \mathbb{R}$ .

Although the presented weak values are valid for the same ensemble, they do not necessarily characterise individual neutrons. Yet, a recent experimental report [170] characterises individual neutrons with weak values. This assumes the theoretically vanishing Ozawa-uncertainty [171] for a specific phase shifter position  $\chi$ . The authors argue that without a variance in the weak values, they must be valid for every neutron. With their asymmetric beam splitter, real weak values are extracted which are interpreted as fractions of single neutrons in each path. With the pre-

sented data, a Leggett-Garg relation can be investigated [172] testing the combined presence in nature of both macro-realism and non-invasive measurements.

The extraction method through time-resolved measurements can be extended to an arbitrary number of paths with as many different frequencies, since the number of energy levels used is, in principle, not limited. In case of neutron interferometer experiments, three simultaneous weak path measurements can be the next target. In comparison, implementing spatial shifts as a path marking with a detector with a 2-dimensional spatial resolution is limited to the extraction of two weak values. Further experiments will involve simultaneous measurements of weak values in the case of a magnetic field along a single axis [173] and asymmetric beam splitters.

### 5.5.3 Complementarity Principle

Wave and particle are complementary properties [174]. The visibility of interference fringes and distinguishability between paths are related through a trade-off [175–177]. A spin flip of probability 1 in one path of an interferometer makes the paths distinguishable through a spin analysis while the visibility vanishes due to the orthogonality between the spin states. A so-called quantum eraser makes the paths indistinguishable again which can be implemented by projecting the orthogonal states onto a different basis. This was done in neutron interferometer experiments [47] and in versions with entangled photons [178–180].

In the present experiment, the spin analysis in  $+x$ -direction resembles the quantum eraser. Some minimal path marking is memorised in the spin system given through the spin rotation angle  $\alpha$ . As the same rotation angle  $\alpha$  from the initial  $+z$  spin state is applied in both paths, the paths cannot be distinguished by projecting on a  $z$  spin state. However, the two polarisation vectors are rotating with different frequencies in an  $x$ - $y$  plane of the Bloch sphere. The  $x$ - $y$  spin components are periodically in parallel and anti-parallel. For the anti-parallel orientation, the corresponding spin states are orthogonal. If all parameters of the experiment were determined, the detection of a neutron at specific moments would infer different probabilities for either path taken. In contrast to a quantum eraser, some minimal path distinguishability could be inferred with the combination of  $+x$  spin analysis and time-resolved detection. Since both flipped components are involved for this argument, the reduced visibility emerges in the intensity with the second order in  $\alpha$ . Due to the small size of  $\alpha$ , the present experiment is adequately described by the linear dependence on  $\alpha$ . The minimal distinguishability between the paths does not lower the visibility noticeably.

### 5.5.4 Subjective Remarks

The meaning of weak values is not entirely clear to me. One interpretation of the imaginary part is that it quantifies disturbance on the system. In the experiment of this chapter, the imaginary part diverges in the vicinity of phase shifter position  $\chi = \pm\pi$ . At this point, pre- and post-selection are orthogonal to each other. If one interprets disturbance as loss of information, disturbance is maximal at this point, since all information is lost when only regarding the intensity at the O-beam. Also the interpretation of weak values as best estimate of the respective operator is

reasonable. The real part agrees with the theoretically predicted absolute value of the probability amplitudes in the two paths.

Another argument concerns the number of systems (or neutrons here) which weak values characterise. It is evident that weak measurements can only be performed for ensembles of systems. However, this does in general not distinguish weak measurements from ordinary projective measurements. For the latter, even one-shot measurements entail a rigid preparation. The preparation can be considered as an initial measurement such that one cannot reduce the entire procedure to a single measurement.

The difference between weak and strong (projective) measurements is not equivalent to the interaction strength, as a weak measurement involves two projections. A weak measurement involves, however, first of all a third interaction in between those two. Only then regarding the strength of interaction itself becomes relevant. It is then a dynamical feature of the specific pre- and post-selection that the response of the system to an interaction is strong, i.e. with a linear dependence. The weak values are easier to extract from a mathematical viewpoint if the interaction is weak because only one contribution is relevant. From this viewpoint, it is far fetched to me to read a fundamental meaning into weak values. It is therefore a weak but still notable argument for me to criticise an interaction strength as too high. Should the threshold for a small enough interaction strength be dependent on current technology? One should always choose an interaction strength as low as possible. For the presented experiments, the interaction strength might be able to be reduced a notch as has already been realised in follow-up experiments. To argue about factors  $< 2$  in the interaction strength for realisations of concepts previously assumed to be Gedankenexperiments might overdo it.

In extension to the interaction strength, a similar thing happens from my perspective when devaluing a study because it does not involve “genuine” weak measurements since the procedure does not follow the initially introduced formalism to the letter. If the meaning of weak values stays to debate in the community after some time and effort, it is necessary to reframe weak measurements by either generalising or specifying them.

## 5.6 Conclusion

Simultaneous measurements of two path weak values in neutron interferometry are presented. The path degree of freedom of the neutron is coupled to the energy degree of freedom through weak interactions with oscillating magnetic fields. By use of two different frequencies, two different energy eigenstates are occupied which act as two probe states. Since the choice of the frequencies has no limitation, the potential number of probe states and extracted path weak values in the experiment is unlimited. By recording the time-dependent intensity, two path weak values are simultaneously extracted as full complex numbers at each phase shifter position. This simplified measurement protocol guarantees the validity of multiple weak values for the same ensemble.

In contrast to strong measurements, e.g. with beam blockers or  $\pi$  spin rotations in the interferometer arms, weak measurements preserve the investigated interference effect. In the present experiment, the principal physical significance of the weak

## 5.6 Conclusion

values lies in their polar coordinates of absolute value and phase which directly characterise the amplitude and phase of the observed intensity modulation. Further experiments will involve the extension to simultaneous measurements of three or more weak values and the use of asymmetric beam splitters.



## Chapter 6

# Conclusion and outlook

Two neutron interferometer experiments are performed in generalised weak measurements with pre- and post-selection. The first experiment concerns a quantum Cheshire Cat and the second one the simultaneous measurements of two path weak values. Weak values describe the changes in intensity recorded at the output of the interferometer when weak interactions are applied. The meaning of weak values beyond the mathematical description stays to debate.

For the quantum Cheshire Cat, weak values describe the conspicuous responses to weak interactions. A realistic interpretation of weak values as quantification of the location of properties is possible but not necessary. The emergence of the quantum Cheshire Cat can be regarded in a more conventional way as an interference phenomenon.

In the Cheshire Cat experiment, an energy manipulation is always coupled to a spin manipulation. At the moment, Ismaele Masiello is implementing RF magnetic fields parallel to the polarisation vector in generalised weak measurements. This prevents the entanglement between spin and energy. While energy manipulations are frequently described as two-level systems with its own Hilbert space, an equivalent description is given through time-dependent phases between quantum states. The recently investigated orbital angular momentum of neutrons could be used instead of energy as the third degree of freedom. The rigid restrictions for devices in a perfect crystal neutron interferometer have to be overcome. A stricter realisation of the proposal by Pan could be achieved. Also the measurements could be performed simultaneously such that all measurements to infer the locations of properties are performed at the same time.

In the simultaneous weak-path measurements, a coupling between the path state in the interferometer and the energy level is performed. Besides its presented results, the data can be evaluated to test a Leggett-Garg inequality which constrain the presence of macro-realism and non-invasive measurements in nature. The technique can also contribute to improvements of experiments such as above quantum Cheshire Cat.

Neutron interferometry developed a reputation since its introduction in 1974. Experiments are performed to this day. Neutron interferometry faces potent competition, specifically by atom interferometry. Reactor technology is criticised due to security reasons related to possible incidents and nuclear waste. Spallation sources as the International Spallation Source (ISIS) in England and the newly founded Eu-

## 6 Conclusion and outlook

ropean Spallation Source (ESS) in Sweden will become more important for neutron optics.

The neutron interferometry station S18 at ILL in Grenoble, France, undergoes continuous improvements carried out primarily by its instrument responsible Hartmut Lemmel. A split crystal interferometer is introduced recently which allows for loop areas increased by an order of magnitude. The increased phase sensitivity can be used to probe for smaller effects depending on the area such as the Sagnac effect. Additionally, the whole instrument S18 is currently rebuilt. The prospected end state will result in better spin polarisation and reduced alignment times. The latter is because entire tables filled with devices such as coils and the interferometer will be placed on stages moveable with air pressure. The many degrees of freedom in aligning the devices will be reduced significantly for each new experiment. In this way, the rationed beam time will be used more efficiently. Another ongoing development are polarising supermirrors which do not absorb one spin-component but allow the detection of both spin-components individually and simultaneously.

# Appendix A

## Detailed Calculations

### A.1 Three-Path Quantum Cheshire Cat

The Euler representation of the unitary operators in Eq. (4.29) is derived in the following.

$$\begin{aligned}
 \hat{O}_j^p(\alpha) &= e^{-i\frac{\alpha}{2}\hat{\sigma}_x^p\hat{\Pi}_j} \\
 &= \mathbb{1} - i\frac{\alpha}{2}\hat{\sigma}_x^p\hat{\Pi}_j + \frac{1}{2!}\left(i\frac{\alpha}{2}\hat{\sigma}_x^p\hat{\Pi}_j\right)^2 - \frac{1}{3!}\left(i\frac{\alpha}{2}\hat{\sigma}_x^p\hat{\Pi}_j\right)^3 + \frac{1}{4!}\left(i\frac{\alpha}{2}\hat{\sigma}_x^p\hat{\Pi}_j\right)^4 - \dots \\
 &= \mathbb{1} + \sum_{n=1}^{\infty} \frac{1}{(2n)!} \left(i\frac{\alpha}{2}\hat{\sigma}_x^p\hat{\Pi}_j\right)^{2n} - \sum_{n=0}^{\infty} \frac{1}{(2n+1)!} \left(i\frac{\alpha}{2}\hat{\sigma}_x^p\hat{\Pi}_j\right)^{2n+1} \\
 &= \mathbb{1} + \sum_{n=1}^{\infty} \frac{(-1)^n}{(2n)!} \left(\frac{\alpha}{2}\right)^{2n} \hat{\Pi}_j - i \sum_{n=0}^{\infty} \frac{(-1)^n}{(2n+1)!} \left(\frac{\alpha}{2}\right)^{2n+1} \hat{\sigma}_x^p\hat{\Pi}_j \\
 &= \mathbb{1} - \left(1 - \cos\frac{\alpha}{2}\right) \hat{\Pi}_j - i \sin\left(\frac{\alpha}{2}\right) \hat{\sigma}_x^p\hat{\Pi}_j.
 \end{aligned} \tag{A.1}$$

Equation (4.5) is reached by substituting  $\hat{\sigma}_x^p$  with  $\hat{\sigma}_x^{\text{DC}}$  and  $\hat{\sigma}_x^p$  with  $\hat{\sigma}_x^{\text{RF}}$ , respectively. When a weak DC spin rotation is applied in path  $j$ , the measured intensity is given by Eq. (4.10). Here we present the detailed derivation. We use the completeness relation

$$\mathbb{1} = |E_0\rangle\langle E_0| + |E'\rangle\langle E'|, \tag{A.2}$$

such that the time-averaged intensity  $I$  is written as

$$\begin{aligned}
& I_j^{\text{DC}}(\chi_1) \\
&= \left| \langle f | \hat{U}_j^{\text{DC}} | i \rangle \right|^2 = \left| \langle f | \exp \left( -i \frac{\alpha_{\text{rot}}}{2} \hat{\sigma}_x^{\text{DC}} \hat{\Pi}_j \right) | i \rangle \right|^2 \\
&= \left| \langle f | \left[ \mathbb{1} - i \frac{\alpha_{\text{rot}}}{2} \hat{\sigma}_x^{\text{DC}} \hat{\Pi}_j - \frac{\alpha_{\text{rot}}^2}{8} \hat{\Pi}_j + \mathcal{O}(\alpha_{\text{rot}}^3) \right] | i \rangle \right|^2 \\
&= \left| \langle f | i \rangle - i \frac{\alpha_{\text{rot}}}{2} \langle f | \hat{\sigma}_x^{\text{DC}} \hat{\Pi}_j | i \rangle - \frac{\alpha_{\text{rot}}^2}{8} \langle f | \hat{\Pi}_j | i \rangle + \mathcal{O}(\alpha_{\text{rot}}^3) \right|^2 \\
&= |\langle f | i \rangle|^2 + \alpha_{\text{rot}} \text{Im} \left\{ \langle i | f \rangle \langle f | \hat{\sigma}_x^{\text{DC}} \hat{\Pi}_j | i \rangle \right\} + \frac{\alpha_{\text{rot}}^2}{4} \left| \langle f | \hat{\sigma}_x \hat{\Pi}_j | i \rangle \right|^2 \\
&\quad - \frac{\alpha_{\text{rot}}^2}{4} \text{Re} \left\{ \langle i | f \rangle \langle f | \hat{\Pi}_j | i \rangle \right\} + \mathcal{O}(\alpha_{\text{rot}}^3) \\
&= |\langle f | i \rangle|^2 + \alpha_{\text{rot}} \text{Im} \left\{ \langle i | f \rangle (|E_0\rangle \langle E_0| + |E'\rangle \langle E'|) \langle f | \hat{\sigma}_x^{\text{DC}} \hat{\Pi}_j | i \rangle \right\} \\
&\quad + \frac{\alpha_{\text{rot}}^2}{4} \langle i | \hat{\sigma}_x^{\text{DC}} \hat{\Pi}_j | f \rangle \langle f | \hat{\sigma}_x^{\text{DC}} \hat{\Pi}_j | i \rangle - \frac{\alpha_{\text{rot}}^2}{4} \text{Re} \left\{ \langle i | f \rangle (|E_0\rangle \langle E_0| + |E'\rangle \langle E'|) \langle f | \hat{\Pi}_j | i \rangle \right\} \\
&\quad + \mathcal{O}(\alpha_{\text{rot}}^3) \\
&= |\langle f | i \rangle|^2 + \alpha_{\text{rot}} \text{Im} \left\{ \langle i | f_0 \rangle \langle f_0 | \hat{\sigma}_x^{\text{DC}} \hat{\Pi}_j | i \rangle + \langle i | f' \rangle \langle f' | \hat{\sigma}_x^{\text{DC}} \hat{\Pi}_j | i \rangle \right\} \\
&\quad + \frac{\alpha_{\text{rot}}^2}{4} \langle i | \hat{\sigma}_x^{\text{DC}} \hat{\Pi}_j | f \rangle (|E_0\rangle \langle E_0| + |E'\rangle \langle E'|) \langle f | \hat{\sigma}_x^{\text{DC}} \hat{\Pi}_j | i \rangle \\
&\quad - \frac{\alpha_{\text{rot}}^2}{4} \text{Re} \left\{ \langle i | f_0 \rangle \langle f_0 | \hat{\Pi}_j | i \rangle + \langle i | f' \rangle \langle f' | \hat{\Pi}_j | i \rangle \right\} + \mathcal{O}(\alpha_{\text{rot}}^3) \\
&= |\langle f | i \rangle|^2 + \alpha_{\text{rot}} \text{Im} \left\{ \langle i | f_0 \rangle \langle f_0 | \hat{\sigma}_x^{\text{DC}} \hat{\Pi}_j | i \rangle \right\} + \frac{\alpha_{\text{rot}}^2}{4} \left( \left| \langle f_0 | \hat{\sigma}_x^{\text{DC}} \hat{\Pi}_j | i \rangle \right|^2 + \left| \langle f' | \hat{\sigma}_x^{\text{DC}} \hat{\Pi}_j | i \rangle \right|^2 \right) \\
&\quad - \frac{\alpha_{\text{rot}}^2}{4} \text{Re} \left\{ \langle i | f_0 \rangle \langle f_0 | \hat{\Pi}_j | i \rangle \right\} + \mathcal{O}(\alpha_{\text{rot}}^3) \\
&= |\langle f | i \rangle|^2 + \alpha_{\text{rot}} \text{Im} \left\{ \left| \langle f_0 | i \rangle \right|^2 \frac{\langle f_0 | \hat{\sigma}_x^{\text{DC}} \hat{\Pi}_j | i \rangle}{\langle f_0 | i \rangle} \right\} - \frac{\alpha_{\text{rot}}^2}{4} \text{Re} \left\{ \left| \langle f_0 | i \rangle \right|^2 \frac{\langle f_0 | \hat{\Pi}_j | i \rangle}{\langle f_0 | i \rangle} \right\} \\
&\quad + \frac{\alpha_{\text{rot}}^2}{4} |\langle f | i \rangle|^2 \left( \frac{\left| \langle f_0 | \hat{\sigma}_x^{\text{DC}} \hat{\Pi}_j | i \rangle \right|^2}{|\langle f | i \rangle|^2} + \frac{\left| \langle f' | \hat{\sigma}_x^{\text{DC}} \hat{\Pi}_j | i \rangle \right|^2}{|\langle f | i \rangle|^2} \right) + \mathcal{O}(\alpha_{\text{rot}}^3) \\
&= |\langle f | i \rangle|^2 \left[ 1 + \alpha_{\text{rot}} \text{Im} \left\{ \langle \hat{\sigma}_x^{\text{DC}} \hat{\Pi}_j \rangle_w^{E_0} \right\} + \frac{\alpha_{\text{rot}}^2}{4} \left( \frac{\left| \langle f_0 | \hat{\sigma}_x^{\text{DC}} \hat{\Pi}_j | i \rangle \right|^2}{|\langle f | i \rangle|^2} + \frac{\left| \langle f' | \hat{\sigma}_x^{\text{DC}} \hat{\Pi}_j | i \rangle \right|^2}{|\langle f | i \rangle|^2} \right) \right. \\
&\quad \left. - \frac{\alpha_{\text{rot}}^2}{4} \text{Re} \left\{ \langle \hat{\Pi}_j \rangle_w^{E_0} \right\} + \mathcal{O}(\alpha_{\text{rot}}^3) \right] \\
&= \frac{1}{9} \left[ 1 + \alpha_{\text{rot}} \delta_{j,\text{I}} \sin(2\chi_1) + \frac{\alpha_{\text{rot}}^2}{4} (\delta_{j,\text{I}} - \delta_{j,\text{II}} + \delta_{j,\text{III}}) \right] + \mathcal{O}(\alpha_{\text{rot}}^3),
\end{aligned} \tag{A.3}$$

with the Kronecker delta  $\delta_{i,j}$ . Similar steps lead to Eq. (4.11).

The step-by-step calculation of the intensity in the absorber case of Eq. (4.12) is

written as

$$\begin{aligned}
 I_j^{\text{Abs}} &= \left| \langle f | \hat{A}_j^{\text{Abs}} | i \rangle \right|^2 \\
 &= \left| \langle f | \left[ \mathbf{1} - \hat{\Pi}_j (1 - \sqrt{1 - \mathcal{A}}) \right] | i \rangle \right|^2 \\
 &= \left| \langle f | i \rangle - (1 - \sqrt{1 - \mathcal{A}}) \langle f | \hat{\Pi}_j | i \rangle \right|^2 \\
 &= |\langle f | i \rangle|^2 - (1 - \sqrt{1 - \mathcal{A}}) \left( \langle f | i \rangle \langle i | \hat{\Pi}_j | f \rangle + \langle i | f \rangle \langle f | \hat{\Pi}_j | i \rangle \right) \\
 &\quad + (1 - \sqrt{1 - \mathcal{A}})^2 \langle i | \hat{\Pi}_j | f \rangle \langle f | \hat{\Pi}_j | i \rangle \\
 &= |\langle f | i \rangle|^2 - 2(1 - \sqrt{1 - \mathcal{A}}) \text{Re} \left\{ \langle i | f \rangle \langle f | \hat{\Pi}_j | i \rangle \right\} + (1 - \sqrt{1 - \mathcal{A}})^2 \langle i | \hat{\Pi}_j | f \rangle \langle f | \hat{\Pi}_j | i \rangle \\
 &= |\langle f | i \rangle|^2 - 2(1 - \sqrt{1 - \mathcal{A}}) \text{Re} \left\{ \langle i | f \rangle (|E_0\rangle \langle E_0| + |E'\rangle \langle E'|) \langle f | \hat{\Pi}_j | i \rangle \right\} \\
 &\quad + (1 - \sqrt{1 - \mathcal{A}})^2 \langle i | \hat{\Pi}_j | f \rangle (|E_0\rangle \langle E_0| + |E'\rangle \langle E'|) \langle f | \hat{\Pi}_j | i \rangle \\
 &= |\langle f | i \rangle|^2 - 2(1 - \sqrt{1 - \mathcal{A}}) \text{Re} \left\{ \langle i | f_0 \rangle \langle f_0 | \hat{\Pi}_j | i \rangle \right\} + (1 - \sqrt{1 - \mathcal{A}})^2 \langle i | \hat{\Pi}_j | f_0 \rangle \langle f_0 | \hat{\Pi}_j | i \rangle \\
 &= |\langle f | i \rangle|^2 - 2(1 - \sqrt{1 - \mathcal{A}}) \text{Re} \left\{ |\langle f_0 | i \rangle|^2 \frac{\langle f_0 | \hat{\Pi}_j | i \rangle}{\langle f_0 | i \rangle} \right\} \\
 &\quad + (1 - \sqrt{1 - \mathcal{A}})^2 |\langle f_0 | i \rangle|^2 \left| \frac{\langle f_0 | \hat{\Pi}_j | i \rangle}{\langle f_0 | i \rangle} \right|^2 \\
 &= |\langle f | i \rangle|^2 \left[ 1 - 2(1 - \sqrt{1 - \mathcal{A}}) \text{Re} \left\{ \langle \hat{\Pi}_j \rangle_w^{E_0} \right\} + (1 - \sqrt{1 - \mathcal{A}})^2 \left| \langle \hat{\Pi}_j \rangle_w^{E_0} \right|^2 \right] \\
 &= |\langle f | i \rangle|^2 \left[ 1 - 2(1 - \sqrt{1 - \mathcal{A}}) \langle \hat{\Pi}_j \rangle_w^{E_0} + (1 - \sqrt{1 - \mathcal{A}})^2 \langle \hat{\Pi}_j \rangle_w^{E_0} \right] \\
 &= |\langle f | i \rangle|^2 \left[ 1 - \left( 2(1 - \sqrt{1 - \mathcal{A}}) - (1 - \sqrt{1 - \mathcal{A}})^2 \right) \langle \hat{\Pi}_j \rangle_w^{E_0} \right] \\
 &= |\langle f | i \rangle|^2 \left[ 1 - \mathcal{A} \langle \hat{\Pi}_j \rangle_w^{E_0} \right] \\
 &= \frac{1}{9} [1 - \mathcal{A} \delta_{j,\text{II}}],
 \end{aligned} \tag{A.4}$$

where, according to Eq. (4.9),

$$\langle \hat{\Pi}_j \rangle_w^{E_0} = \delta_{j,\text{II}} = \text{Re} \left\{ \langle \hat{\Pi}_j \rangle_w^{E_0} \right\} = \left| \langle \hat{\Pi}_j \rangle_w^{E_0} \right|^2. \tag{A.5}$$

The detailed calculation of the exact result with N paths and N – 1 properties

of Eq. (4.32) is given here:

$$\begin{aligned}
I_j^p(\alpha) &= \left| \langle f_N | \hat{O}_j^p(\alpha) | i_N \rangle \right|^2 \\
&= \left| \langle f_N | \left[ \mathbf{1} - \left( 1 - \cos \frac{\alpha}{2} \right) \hat{\Pi}_j - i \sin \left( \frac{\alpha}{2} \right) \hat{\sigma}_x^p \hat{\Pi}_j \right] | i_N \rangle \right|^2 \\
&= \left| \langle f_N | i_N \rangle - \left( 1 - \cos \frac{\alpha}{2} \right) \langle f_N | \hat{\Pi}_j | i_N \rangle - i \sin \left( \frac{\alpha}{2} \right) \langle f_N | \hat{\sigma}_x^p \hat{\Pi}_j | i_N \rangle \right|^2 \\
&= |\langle f_N | i_N \rangle|^2 + \left( 1 - \cos \frac{\alpha}{2} \right)^2 \left| \langle f_N | \hat{\Pi}_j | i_N \rangle \right|^2 + \sin^2 \left( \frac{\alpha}{2} \right) \left| \langle f_N | \hat{\sigma}_x^p \hat{\Pi}_j | i_N \rangle \right|^2 \\
&\quad - \langle i_N | f_N \rangle \left( 1 - \cos \frac{\alpha}{2} \right) \langle f_N | \hat{\Pi}_j | i_N \rangle - \langle f_N | i_N \rangle \left( 1 - \cos \frac{\alpha}{2} \right) \langle i_N | \hat{\Pi}_j | f_N \rangle \\
&\quad - \langle i_N | f_N \rangle i \sin \left( \frac{\alpha}{2} \right) \langle f_N | \hat{\sigma}_x^p \hat{\Pi}_j | i_N \rangle + \langle f_N | i_N \rangle i \sin \left( \frac{\alpha}{2} \right) \langle i_N | \hat{\sigma}_x^p \hat{\Pi}_j | f_N \rangle \\
&\quad + \left( 1 - \cos \frac{\alpha}{2} \right) \langle i_N | \hat{\Pi}_j | f_N \rangle i \sin \left( \frac{\alpha}{2} \right) \langle f_N | \hat{\sigma}_x^p \hat{\Pi}_j | i_N \rangle \\
&\quad - \left( 1 - \cos \frac{\alpha}{2} \right) \langle f_N | \hat{\Pi}_j | i_N \rangle i \sin \left( \frac{\alpha}{2} \right) \langle i_N | \hat{\sigma}_x^p \hat{\Pi}_j | f_N \rangle,
\end{aligned} \tag{A.6}$$

where the last two summands are zero because at least one of the two brackets in each term is zero. This is in close relation to the calculation of the weak values in Eq. (4.9) but not exemplified here. Continuing the derivation,

$$\begin{aligned}
I_j^p(\alpha) &= |\langle f_N | i_N \rangle|^2 \left[ 1 + \left( 1 - \cos \frac{\alpha}{2} \right)^2 \left| \frac{\langle f_N | \hat{\Pi}_j | i_N \rangle}{\langle f_N | i_N \rangle} \right|^2 + \sin^2 \left( \frac{\alpha}{2} \right) \left| \frac{\langle f_N | \hat{\sigma}_x^p \hat{\Pi}_j | i_N \rangle}{\langle f_N | i_N \rangle} \right|^2 \right. \\
&\quad - \left( 1 - \cos \frac{\alpha}{2} \right) \frac{\langle f_N | \hat{\Pi}_j | i_N \rangle}{\langle f_N | i_N \rangle} - \left( 1 - \cos \frac{\alpha}{2} \right) \frac{\langle i_N | \hat{\Pi}_j | f_N \rangle}{\langle i_N | f_N \rangle} \\
&\quad \left. - i \sin \left( \frac{\alpha}{2} \right) \frac{\langle f_N | \hat{\sigma}_x^p \hat{\Pi}_j | i_N \rangle}{\langle f_N | i_N \rangle} + i \sin \left( \frac{\alpha}{2} \right) \frac{\langle i_N | \hat{\sigma}_x^p \hat{\Pi}_j | f_N \rangle}{\langle i_N | f_N \rangle} \right] \\
&= |\langle f_N | i_N \rangle|^2 \left[ 1 + \left( 1 - \cos \frac{\alpha}{2} \right)^2 \left| \langle \hat{\Pi}_j \rangle_w \right|^2 + \sin^2 \left( \frac{\alpha}{2} \right) \left| \langle \hat{\sigma}_x^p \hat{\Pi}_j \rangle_w \right|^2 \right. \\
&\quad \left. - \left( 1 - \cos \frac{\alpha}{2} \right) \left( \langle \hat{\Pi}_j \rangle_w + \langle \hat{\Pi}_j \rangle_w^* \right) - i \sin \left( \frac{\alpha}{2} \right) \left( \langle \hat{\sigma}_x^p \hat{\Pi}_j \rangle_w - \langle \hat{\sigma}_x^p \hat{\Pi}_j \rangle_w^* \right) \right] \\
&= |\langle f_N | i_N \rangle|^2 \left[ 1 + \left( 1 - \cos \frac{\alpha}{2} \right)^2 \left| \langle \hat{\Pi}_j \rangle_w \right|^2 + \sin^2 \left( \frac{\alpha}{2} \right) \left| \langle \hat{\sigma}_x^p \hat{\Pi}_j \rangle_w \right|^2 \right. \\
&\quad \left. - 2 \left( 1 - \cos \frac{\alpha}{2} \right) \operatorname{Re} \left\{ \langle \hat{\Pi}_j \rangle_w \right\} - 2i^2 \sin \left( \frac{\alpha}{2} \right) \operatorname{Im} \left\{ \langle \hat{\sigma}_x^p \hat{\Pi}_j \rangle_w \right\} \right] \\
&= |\langle f_N | i_N \rangle|^2 \left[ 1 + 2 \sin \left( \frac{\alpha}{2} \right) \operatorname{Im} \left\{ \langle \hat{\sigma}_x^p \hat{\Pi}_j \rangle_w \right\} + \sin^2 \left( \frac{\alpha}{2} \right) \left| \langle \hat{\sigma}_x^p \hat{\Pi}_j \rangle_w \right|^2 \right. \\
&\quad \left. + \left( \left( 1 - \cos \frac{\alpha}{2} \right)^2 - 2 \left( 1 - \cos \frac{\alpha}{2} \right) \right) \langle \hat{\Pi}_j \rangle_w \right] \\
&= |\langle f_N | i_N \rangle|^2 \left[ 1 + 2 \sin \left( \frac{\alpha}{2} \right) \operatorname{Im} \left\{ \langle \hat{\sigma}_x^p \hat{\Pi}_j \rangle_w \right\} + \sin^2 \left( \frac{\alpha}{2} \right) \left| \langle \hat{\sigma}_x^p \hat{\Pi}_j \rangle_w \right|^2 - \sin^2 \left( \frac{\alpha}{2} \right) \langle \hat{\Pi}_j \rangle_w \right],
\end{aligned} \tag{A.7}$$

where we also use Eq. (A.5). This concludes the derivation of the second line in Eq. (4.32). The derivation of lines three and four of Eq. (4.32) takes a different way.

By explicitly writing the brackets, given by Eqs. (4.27) and (4.28), in the third line of Eq. (A.6), we obtain

$$\begin{aligned}
 & I_j^p(\alpha) \\
 &= \left| \langle f_N | i_N \rangle - \left( 1 - \cos \frac{\alpha}{2} \right) \left[ \frac{1}{\sqrt{N}} \left( e^{-i\chi_1} \langle I | + e^{-i\chi_2} \langle II | + \dots + e^{-i\chi_N} \langle N | \right) \langle 1, 1, \dots, 1, 1 | \right] \right. \\
 &\quad \times \hat{\Pi}_j \left[ \frac{1}{\sqrt{N}} \left( |I\rangle |1, 1, \dots, 1, 1\rangle + |II\rangle |0, 1, \dots, 1, 1\rangle + \dots + |N\rangle |1, 1, \dots, 1, 0\rangle \right) \right] \\
 &\quad - i \sin \frac{\alpha}{2} \left[ \frac{1}{\sqrt{N}} \left( e^{-i\chi_1} \langle I | + e^{-i\chi_2} \langle II | + \dots + e^{-i\chi_N} \langle N | \right) \langle 1, 1, \dots, 1, 1 | \right] \hat{\sigma}_x^p \hat{\Pi}_j \times \\
 &\quad \times \left[ \frac{1}{\sqrt{N}} \left( |I\rangle |1, 1, \dots, 1, 1\rangle + |II\rangle |0, 1, \dots, 1, 1\rangle + \dots + |N\rangle |1, 1, \dots, 1, 0\rangle \right) \right] \left. \right|^2 \\
 &= \left| \frac{1}{N} e^{-i\chi_1} - \left( 1 - \cos \frac{\alpha}{2} \right) \frac{1}{N} e^{-i\chi_1} \delta_{j,1} - i \sin \left( \frac{\alpha}{2} \right) \frac{1}{N} e^{-i\chi_j} \delta_{j,p+1} \right|^2 \\
 &= \frac{1}{N^2} \left[ 1 + \left( 1 - \cos \frac{\alpha}{2} \right)^2 \delta_{j,1} + \sin^2 \left( \frac{\alpha}{2} \right) \delta_{j,p+1} \right. \\
 &\quad - \left( 1 - \cos \frac{\alpha}{2} \right) e^{-i\chi_1} \delta_{j,1} e^{i\chi_1} - \left( 1 - \cos \frac{\alpha}{2} \right) e^{i\chi_1} \delta_{j,1} e^{-i\chi_1} \\
 &\quad - i \sin \left( \frac{\alpha}{2} \right) e^{i(\chi_1 - \chi_j)} \delta_{j,p+1} + i \sin \left( \frac{\alpha}{2} \right) e^{-i(\chi_1 - \chi_j)} \delta_{j,p+1} \\
 &\quad - \left( 1 - \cos \frac{\alpha}{2} \right) e^{-i\chi_1} \delta_{j,1} i \sin \left( \frac{\alpha}{2} \right) e^{i\chi_j} \delta_{j,p+1} \\
 &\quad \left. - \left( 1 - \cos \frac{\alpha}{2} \right) \delta_{j,1} (-i) \sin \left( \frac{\alpha}{2} \right) e^{-i(\chi_j - \chi_1)} \delta_{j,p+1} \right] \\
 &= \frac{1}{N^2} \left[ 1 - \delta_{j,p+1} i \sin \left( \frac{\alpha}{2} \right) \left( e^{i(\chi_1 - \chi_j)} - e^{-i(\chi_1 - \chi_j)} \right) + \delta_{j,p+1} \sin^2 \left( \frac{\alpha}{2} \right) \right. \\
 &\quad \left. + \delta_{j,1} \left( \left( 1 - \cos \frac{\alpha}{2} \right)^2 - 2 \left( 1 - \cos \frac{\alpha}{2} \right) \right) \right] \\
 &= \frac{1}{N^2} \left[ 1 - \delta_{j,p+1} i \sin \left( \frac{\alpha}{2} \right) \frac{2i}{2i} \left( e^{i(\chi_1 - \chi_j)} - e^{-i(\chi_1 - \chi_j)} \right) + \delta_{j,p+1} \sin^2 \left( \frac{\alpha}{2} \right) \right. \\
 &\quad \left. + \delta_{j,1} \left( \cos^2 \left( \frac{\alpha}{2} \right) - 1 \right) \right] \\
 &= \frac{1}{N^2} \left[ 1 + 2\delta_{j,p+1} \sin \left( \frac{\alpha}{2} \right) \sin(\chi_1 - \chi_j) + \delta_{j,p+1} \sin^2 \left( \frac{\alpha}{2} \right) - \delta_{j,1} \sin^2 \left( \frac{\alpha}{2} \right) \right], \tag{A.8}
 \end{aligned}$$

which concludes the derivation of Eq. (4.32).

## A.2 Simultaneous Weak-Path Measurements

### A.2.1 Calculation of Intensity

Equation (5.9) is derived as

## A Detailed Calculations

$$\begin{aligned}
I_{\text{ideal}}(t) &= \left| \langle f | \left( \hat{U}_{\text{RF}}(t, \alpha, \omega_{\text{I}}, \delta_{\text{I}}) \hat{\Pi}_{\text{I}} + \hat{U}_{\text{RF}}(t, \alpha, \omega_{\text{II}}, \delta_{\text{II}}) \hat{\Pi}_{\text{II}} \right) |i\rangle \right|^2 \\
&\approx \left| \frac{1}{\sqrt{2}} (\langle \text{I} | + \langle \text{II} |) \langle \uparrow_x | \left[ \begin{pmatrix} 1 & i\frac{\alpha}{2} e^{i(\omega_{\text{I}t+\delta_{\text{I}})}} \\ i\frac{\alpha}{2} e^{-i(\omega_{\text{I}t+\delta_{\text{I}})}} & 1 \end{pmatrix} \hat{\Pi}_{\text{I}} \right. \right. \\
&\quad \left. \left. + \begin{pmatrix} 1 & i\frac{\alpha}{2} e^{i(\omega_{\text{II}t+\delta_{\text{II}})}} \\ i\frac{\alpha}{2} e^{-i(\omega_{\text{II}t+\delta_{\text{II}})}} & 1 \end{pmatrix} \hat{\Pi}_{\text{II}} \right] \frac{1}{\sqrt{2}} (|\text{I}\rangle + e^{-i\chi} |\text{II}\rangle) |\uparrow_z\rangle \right|^2 \\
&= \left| \frac{1}{2} (\langle \text{I} | + \langle \text{II} |) \langle \uparrow_x | \left[ |\text{I}\rangle (|\uparrow_z\rangle + i\frac{\alpha}{2} e^{-i(\omega_{\text{I}t+\delta_{\text{I}})}} |\downarrow_z\rangle) + e^{-i\chi} |\text{II}\rangle (|\uparrow_z\rangle + i\frac{\alpha}{2} e^{-i(\omega_{\text{II}t+\delta_{\text{II}})}} |\downarrow_z\rangle) \right] \right|^2 \\
&= \left| \frac{1}{2} (\langle \text{I} | + \langle \text{II} |) \frac{1}{\sqrt{2}} (\langle \uparrow_z | + \langle \downarrow_z |) \left[ |\text{I}\rangle (|\uparrow_z\rangle + i\frac{\alpha}{2} e^{-i(\omega_{\text{I}t+\delta_{\text{I}})}} |\downarrow_z\rangle) \right. \right. \\
&\quad \left. \left. + e^{-i\chi} |\text{II}\rangle (|\uparrow_z\rangle + i\frac{\alpha}{2} e^{-i(\omega_{\text{II}t+\delta_{\text{II}})}} |\downarrow_z\rangle) \right] \right|^2 \\
&= \left| \frac{1}{2\sqrt{2}} \left[ \left( 1 + i\frac{\alpha}{2} e^{-i(\omega_{\text{I}t+\delta_{\text{I}})}} \right) + e^{-i\chi} \left( 1 + i\frac{\alpha}{2} e^{-i(\omega_{\text{II}t+\delta_{\text{II}})}} \right) \right] \right|^2 \\
&= \left| \frac{1}{2\sqrt{2}} \left[ 1 + e^{-i\chi} + i\frac{\alpha}{2} e^{-i(\omega_{\text{I}t+\delta_{\text{I}})}} + i\frac{\alpha}{2} e^{-i(\omega_{\text{II}t+\delta_{\text{II}})}} e^{-i\chi} \right] \right|^2 \\
&\approx \frac{1}{8} \left[ 1 + 1 + e^{-i\chi} + e^{i\chi} + i\frac{\alpha}{2} e^{-i(\omega_{\text{I}t+\delta_{\text{I}})}} - i\frac{\alpha}{2} e^{i(\omega_{\text{I}t+\delta_{\text{I}})}} + i\frac{\alpha}{2} e^{-i(\omega_{\text{I}t+\delta_{\text{I}})}} e^{i\chi} - i\frac{\alpha}{2} e^{i(\omega_{\text{I}t+\delta_{\text{I}})}} e^{i\chi} \right. \\
&\quad \left. + i\frac{\alpha}{2} e^{-i(\omega_{\text{II}t+\delta_{\text{II}})}} e^{-i\chi} - i\frac{\alpha}{2} e^{i(\omega_{\text{II}t+\delta_{\text{II}})}} e^{-i\chi} + i\frac{\alpha}{2} e^{-i(\omega_{\text{II}t+\delta_{\text{II}})}} - i\frac{\alpha}{2} e^{i(\omega_{\text{II}t+\delta_{\text{II}})}} \right] \\
&= \frac{1}{8} \left[ 2 [1 + \cos(\chi)] + 2\text{Re} \left\{ i\frac{\alpha}{2} e^{-i(\omega_{\text{I}t+\delta_{\text{I}})}} \right\} + 2\text{Re} \left\{ i\frac{\alpha}{2} e^{-i(\omega_{\text{I}t+\delta_{\text{I}})}} e^{i\chi} \right\} + 2\text{Re} \left\{ i\frac{\alpha}{2} e^{-i(\omega_{\text{II}t+\delta_{\text{II}})}} e^{-i\chi} \right\} \right. \\
&\quad \left. + 2\text{Re} \left\{ i\frac{\alpha}{2} e^{-i(\omega_{\text{II}t+\delta_{\text{II}})}} \right\} \right] \\
&= \frac{1}{8} \left[ 2 [1 + \cos(\chi)] + 2\text{Re} \left\{ i\frac{\alpha}{2} e^{-i(\omega_{\text{I}t+\delta_{\text{I}})}} + i\frac{\alpha}{2} e^{-i(\omega_{\text{I}t+\delta_{\text{I}})}} e^{i\chi} + i\frac{\alpha}{2} e^{-i(\omega_{\text{II}t+\delta_{\text{II}})}} e^{-i\chi} + i\frac{\alpha}{2} e^{-i(\omega_{\text{II}t+\delta_{\text{II}})}} \right\} \right] \\
&= \frac{1}{8} \left[ 2 [1 + \cos(\chi)] - 2\text{Im} \left\{ \frac{\alpha}{2} e^{-i(\omega_{\text{I}t+\delta_{\text{I}})}} + \frac{\alpha}{2} e^{-i(\omega_{\text{I}t+\delta_{\text{I}})}} e^{i\chi} + \frac{\alpha}{2} e^{-i(\omega_{\text{II}t+\delta_{\text{II}})}} e^{-i\chi} + \frac{\alpha}{2} e^{-i(\omega_{\text{II}t+\delta_{\text{II}})}} \right\} \right] \\
&= \frac{1}{8} \left[ 2 [1 + \cos(\chi)] - \alpha \text{Im} \left\{ e^{-i(\omega_{\text{I}t+\delta_{\text{I}})}} + e^{-i(\omega_{\text{I}t+\delta_{\text{I}})}} e^{i\chi} + e^{-i(\omega_{\text{II}t+\delta_{\text{II}})}} e^{-i\chi} + e^{-i(\omega_{\text{II}t+\delta_{\text{II}})}} \right\} \right] \\
&= \frac{1}{8} \left[ 2 [1 + \cos(\chi)] - \alpha \text{Im} \left\{ (1 + e^{i\chi}) e^{-i(\omega_{\text{I}t+\delta_{\text{I}})}} + (1 + e^{-i\chi}) e^{-i(\omega_{\text{II}t+\delta_{\text{II}})}} \right\} \right] \\
&= \frac{1 + \cos(\chi)}{4} - \frac{\alpha}{8} \text{Im} \left\{ (1 + e^{i\chi}) \frac{(1 + e^{i\chi}) (1 + e^{-i\chi})}{(1 + e^{i\chi}) (1 + e^{-i\chi})} e^{-i(\omega_{\text{I}t+\delta_{\text{I}})}} \right. \\
&\quad \left. + (1 + e^{-i\chi}) \frac{(1 + e^{i\chi}) (1 + e^{-i\chi})}{(1 + e^{i\chi}) (1 + e^{-i\chi})} e^{-i(\omega_{\text{II}t+\delta_{\text{II}})}} \right\} \\
&= |\langle f | i \rangle|^2 - \frac{\alpha}{8} (1 + e^{i\chi}) (1 + e^{-i\chi}) \text{Im} \left\{ e^{-i(\omega_{\text{I}t+\delta_{\text{I}})}} \frac{1}{(1 + e^{-i\chi})} + e^{-i(\omega_{\text{II}t+\delta_{\text{II}})}} \frac{1}{(1 + e^{i\chi})} \right\} \\
&= |\langle f | i \rangle|^2 \left[ 1 - \alpha \text{Im} \left\{ \langle \hat{\Pi}_{\text{I}} \rangle_{\text{w}} e^{-i(\omega_{\text{I}t+\delta_{\text{I}})}} + \langle \hat{\Pi}_{\text{II}} \rangle_{\text{w}} e^{-i(\omega_{\text{II}t+\delta_{\text{II}})}} \right\} \right] \\
&= |\langle f | i \rangle|^2 \left( 1 - \alpha \left[ A_{\text{I}} \sin(\varphi_{\text{I}} - \omega_{\text{I}t} - \delta_{\text{I}}) + A_{\text{II}} \sin(\varphi_{\text{II}} - \omega_{\text{II}t} - \delta_{\text{II}}) \right] \right).
\end{aligned}$$

(A.9)

### A.2.2 Data Correction

In the ideal case, the weak values are extracted in polar coordinates through Eq. (5.13). The dominant experimental imperfections are given by the interferometer contrast  $C$  and the coil efficiency  $\epsilon$ . The experimentally retrieved parameters are  $C_{\text{exp}} = 0.64 \pm 0.03$  and  $\epsilon_{\text{exp}} = 0.92 \pm 0.02$ . The predicted experimental intensity  $I_{\text{pred}}$  dependent on the adjustable parameters  $\alpha_j$  and  $\chi$  is derived as

$$\begin{aligned}
I_{\text{pred}}(t) &= \left| \langle f | \left( \hat{U}_{\text{RF}}(t, \alpha_{\text{I}}, f_{\text{I}}, \delta_{\text{I}}) \hat{\Pi}_{\text{I}} + \hat{U}_{\text{RF}}(t, \alpha_{\text{II}}, f_{\text{II}}, \delta_{\text{II}}) \hat{\Pi}_{\text{II}} \right) |i\rangle \right|^2 \\
&= \left| \frac{1}{\sqrt{2}} (\langle \text{I} | + \langle \text{II} |) \langle \uparrow_x | \frac{1}{\sqrt{2}} \left[ |\text{I}\rangle \left( \cos\left(\frac{\alpha_{\text{I}}}{2}\right) |\uparrow_z\rangle + i \sin\left(\frac{\alpha_{\text{I}}}{2}\right) e^{-i(2\pi f_{\text{I}} t + \delta_{\text{I}})} |\downarrow_z\rangle \right) \right. \right. \\
&\quad \left. \left. + e^{-i\chi} |\text{II}\rangle \left( \cos\left(\frac{\alpha_{\text{II}}}{2}\right) |\uparrow_z\rangle + i \sin\left(\frac{\alpha_{\text{II}}}{2}\right) e^{-i(2\pi f_{\text{II}} t + \delta_{\text{II}})} |\downarrow_z\rangle \right) \right] \right|^2 \\
&= \left| \frac{1}{\sqrt{2}} (\langle \text{I} | + \langle \text{II} |) \frac{1}{\sqrt{2}} (\langle \uparrow_z | + \langle \downarrow_z |) \right. \\
&\quad \times \frac{1}{\sqrt{2}} \left[ |\text{I}\rangle \left( \cos\left(\frac{\alpha_{\text{I}}}{2}\right) |\uparrow_z\rangle + i \sin\left(\frac{\alpha_{\text{I}}}{2}\right) e^{-i(2\pi f_{\text{I}} t + \delta_{\text{I}})} |\downarrow_z\rangle \right) \right. \\
&\quad \left. \left. + e^{-i\chi} |\text{II}\rangle \left( \cos\left(\frac{\alpha_{\text{II}}}{2}\right) |\uparrow_z\rangle + i \sin\left(\frac{\alpha_{\text{II}}}{2}\right) e^{-i(2\pi f_{\text{II}} t + \delta_{\text{II}})} |\downarrow_z\rangle \right) \right] \right|^2 \\
&= \left| \frac{1}{2\sqrt{2}} \left[ \left( \cos\left(\frac{\alpha_{\text{I}}}{2}\right) + i \sin\left(\frac{\alpha_{\text{I}}}{2}\right) e^{-i(2\pi f_{\text{I}} t + \delta_{\text{I}})} \right) \right. \right. \\
&\quad \left. \left. + e^{-i\chi} \left( \cos\left(\frac{\alpha_{\text{II}}}{2}\right) + i \sin\left(\frac{\alpha_{\text{II}}}{2}\right) e^{-i(2\pi f_{\text{II}} t + \delta_{\text{II}})} \right) \right] \right|^2 \\
&= \frac{1}{8} \left[ \cos^2\left(\frac{\alpha_{\text{I}}}{2}\right) + \sin^2\left(\frac{\alpha_{\text{I}}}{2}\right) \right. \\
&\quad + e^{i\chi} \left( \cos\left(\frac{\alpha_{\text{II}}}{2}\right) - i \sin\left(\frac{\alpha_{\text{II}}}{2}\right) e^{+i(2\pi f_{\text{II}} t + \delta_{\text{II}})} \right) \times \\
&\quad \times e^{-i\chi} \left( \cos\left(\frac{\alpha_{\text{II}}}{2}\right) + i \sin\left(\frac{\alpha_{\text{II}}}{2}\right) e^{-i(2\pi f_{\text{II}} t + \delta_{\text{II}})} \right) \\
&\quad - i \sin\left(\frac{\alpha_{\text{I}}}{2}\right) e^{+i(2\pi f_{\text{I}} t + \delta_{\text{I}})} \cos\left(\frac{\alpha_{\text{I}}}{2}\right) + \cos\left(\frac{\alpha_{\text{I}}}{2}\right) i \sin\left(\frac{\alpha_{\text{I}}}{2}\right) e^{-i(2\pi f_{\text{I}} t + \delta_{\text{I}})} \\
&\quad + \cos\left(\frac{\alpha_{\text{I}}}{2}\right) \left[ e^{-i\chi} \left( \cos\left(\frac{\alpha_{\text{II}}}{2}\right) + i \sin\left(\frac{\alpha_{\text{II}}}{2}\right) e^{-i(2\pi f_{\text{II}} t + \delta_{\text{II}})} \right) \right. \\
&\quad \left. + e^{i\chi} \left( \cos\left(\frac{\alpha_{\text{II}}}{2}\right) - i \sin\left(\frac{\alpha_{\text{II}}}{2}\right) e^{+i(2\pi f_{\text{II}} t + \delta_{\text{II}})} \right) \right] \\
&\quad + e^{i\chi} \left( \cos\left(\frac{\alpha_{\text{II}}}{2}\right) - i \sin\left(\frac{\alpha_{\text{II}}}{2}\right) e^{+i(2\pi f_{\text{II}} t + \delta_{\text{II}})} \right) i \sin\left(\frac{\alpha_{\text{I}}}{2}\right) e^{-i(2\pi f_{\text{I}} t + \delta_{\text{I}})} \\
&\quad \left. - i \sin\left(\frac{\alpha_{\text{I}}}{2}\right) e^{+i(2\pi f_{\text{I}} t + \delta_{\text{I}})} e^{-i\chi} \left( \cos\left(\frac{\alpha_{\text{II}}}{2}\right) + i \sin\left(\frac{\alpha_{\text{II}}}{2}\right) e^{-i(2\pi f_{\text{II}} t + \delta_{\text{II}})} \right) \right].
\end{aligned} \tag{A.10}$$

Here, we insert the experimental parameters of interferometer contrast  $C$  and the spin manipulation efficiency  $\epsilon$  of the coils. The contrast is added in summands

## A Detailed Calculations

with factors attributed to both paths, which is equivalent to the dependence on both  $\alpha_I$  and  $\alpha_{II}$ . From here on, we set  $\alpha_I = \alpha_{II} = \alpha$ . The spin manipulation efficiency is added in summands with factors attributed to different spin components. The latter is equivalent to adding the factor  $\epsilon$  in summands with factors  $\sin(\alpha/2) \cos(\alpha/2)$ , where the cosine quantifies the component remaining in the initial  $+z$  spin state and the sine quantifies the component flipped into the  $-z$  spin state.

$$\begin{aligned}
 I_{\text{pred}}(t) &= \frac{1}{8} \left[ 1 + \cos^2 \left( \frac{\alpha}{2} \right) + \sin^2 \left( \frac{\alpha}{2} \right) - \epsilon i \sin \left( \frac{\alpha}{2} \right) e^{+i(2\pi f_{II}t + \delta_{II})} \cos \left( \frac{\alpha}{2} \right) \right. \\
 &\quad + \epsilon \cos \left( \frac{\alpha}{2} \right) i \sin \left( \frac{\alpha}{2} \right) e^{-i(2\pi f_{II}t + \delta_{II})} + 2\epsilon \sin(2\pi f_I t + \delta_I) \sin \left( \frac{\alpha}{2} \right) \cos \left( \frac{\alpha}{2} \right) \\
 &\quad + 2C \cos(\chi) \cos \left( \frac{\alpha}{2} \right) \cos \left( \frac{\alpha}{2} \right) + 2\epsilon C \sin(2\pi f_{II}t + \delta_{II} + \chi) \cos \left( \frac{\alpha}{2} \right) \sin \left( \frac{\alpha}{2} \right) \\
 &\quad + 2\epsilon C \sin(2\pi f_I t + \delta_I - \chi) \sin \left( \frac{\alpha}{2} \right) \cos \left( \frac{\alpha}{2} \right) \\
 &\quad \left. + 2C \cos((2\pi f_I - 2\pi f_{II})t + \delta_I - \delta_{II} - \chi) \sin^2 \left( \frac{\alpha}{2} \right) \right] \\
 &= \frac{1}{4} \left[ 1 + C \cos(\chi) \cos^2 \left( \frac{\alpha}{2} \right) \right. \\
 &\quad + \epsilon \left( \sin(2\pi f_I t + \delta_I) \sin \left( \frac{\alpha}{2} \right) \cos \left( \frac{\alpha}{2} \right) + \sin(2\pi f_{II}t + \delta_{II}) \sin \left( \frac{\alpha}{2} \right) \cos \left( \frac{\alpha}{2} \right) \right. \\
 &\quad \quad + C \sin(2\pi f_{II}t + \delta_{II} + \chi) \cos \left( \frac{\alpha}{2} \right) \sin \left( \frac{\alpha}{2} \right) \\
 &\quad \quad \left. \left. + C \sin(2\pi f_I t + \delta_I - \chi) \sin \left( \frac{\alpha}{2} \right) \cos \left( \frac{\alpha}{2} \right) \right) \right. \\
 &\quad \left. + C \cos((2\pi f_I - 2\pi f_{II})t + \delta_I - \delta_{II} - \chi) \sin^2 \left( \frac{\alpha}{2} \right) \right] \\
 &\approx \frac{1}{4} \left[ 1 + C \cos(\chi) + \frac{\epsilon\alpha}{2} \left( \sin(2\pi f_I t + \delta_I) + \sin(2\pi f_{II}t + \delta_{II}) \right. \right. \\
 &\quad \quad \left. \left. + C(\sin(2\pi f_I t + \delta_I - \chi)) + \sin(2\pi f_{II}t + \delta_{II} + \chi) \right) \right] \\
 &=: I_0 + I(t) \\
 &= I_0 + \frac{\epsilon\alpha}{8} \left[ \sin(2\pi f_I t + \delta_I) + \sin(2\pi f_{II}t + \delta_{II}) \right. \\
 &\quad + C \left( \sin(2\pi f_I t + \delta_I) \cos(\chi) - \cos(2\pi f_I t + \delta_I) \sin(\chi) \right. \\
 &\quad \quad \left. \left. + \sin(2\pi f_{II}t + \delta_{II}) \cos(\chi) + \cos(2\pi f_{II}t + \delta_{II}) \sin(\chi) \right) \right] \\
 &= I_0 + \frac{\epsilon\alpha}{8} \left[ \sin(2\pi f_I t + \delta_I) (1 - C \cos(\chi)) + \cos(2\pi f_I t + \delta_I) C \sin(\chi) \right. \\
 &\quad \left. + \sin(2\pi f_{II}t + \delta_{II}) (1 + C \cos(\chi)) + \cos(2\pi f_{II}t + \delta_{II}) C \sin(\chi) \right], \tag{A.11}
 \end{aligned}$$

## A.2 Simultaneous Weak-Path Measurements

with  $I_0 = [1 + C \cos(\chi)]/4$ . There is a sine and a cosine summand for each applied frequency. We combine each pair by defining new amplitudes  $R_j$  and phases  $\beta_j$ .

$$\begin{aligned} I_{\text{exp}}(t) &=: I_0 - \alpha \left( R_{\text{I}} \sin(\beta_{\text{I}} - 2\pi f_{\text{I}} t - \delta_{\text{I}}) + R_{\text{II}} \sin(\beta_{\text{II}} - 2\pi f_{\text{II}} t - \delta_{\text{II}}) \right) \\ &= I_0 - \alpha \left( R_{\text{I}} \left( \sin(2\pi f_{\text{I}} t + \delta_{\text{I}}) \cos(\beta_{\text{I}}) + \cos(2\pi f_{\text{I}} t + \delta_{\text{I}}) \sin(\beta_{\text{I}}) \right) \right. \\ &\quad \left. + R_{\text{II}} \left( \sin(2\pi f_{\text{II}} t + \delta_{\text{II}}) \cos(\beta_{\text{II}}) + \cos(2\pi f_{\text{II}} t + \delta_{\text{II}}) \sin(\beta_{\text{II}}) \right) \right). \end{aligned} \quad (\text{A.12})$$

By comparing the coefficients of Eqs. (A.11) and (A.12), we obtain

$$\begin{aligned} R_{\text{I}} \sin(\beta_{\text{I}}) &= \frac{\epsilon}{8} C \sin(\chi), & R_{\text{I}} \cos(\beta_{\text{I}}) &= \frac{\epsilon}{8} [1 + C \cos(\chi)] \\ R_{\text{II}} \sin(\beta_{\text{II}}) &= -\frac{\epsilon}{8} C \sin(\chi), & R_{\text{II}} \cos(\beta_{\text{II}}) &= \frac{\epsilon}{8} [1 + C \cos(\chi)] \\ \Rightarrow R_{\text{I}}^2 &= R_{\text{II}}^2 = R^2(C, \epsilon) = \frac{\epsilon^2}{8^2} [C^2 \sin^2(\chi) + (1 + C \cos(\chi))^2] \\ R_{\text{I}}(C, \epsilon) &= R_{\text{II}}(C, \epsilon) = R(C, \epsilon) = \frac{\epsilon}{8} \sqrt{1 + 2C \cos(\chi) + C^2} \\ \frac{R_j(C=1, \epsilon=1)}{I_0(C=1)} &= A_{j,\text{corr}}, \\ \tan(\beta_{\text{I}}) &= -\tan(\beta_{\text{II}}) = \frac{C \sin(\chi)}{1 + C \cos(\chi)} \\ \beta_j(C, \epsilon) &= \pm \arctan\left(\frac{C \sin(\chi)}{1 + C \cos(\chi)}\right) \\ \beta_j(C=1, \epsilon=1) &= \varphi_j, \end{aligned} \quad (\text{A.13})$$

by substituting Eq. (5.5). The data is corrected accordingly by scaling the extracted values as

$$A_{j,\text{corr}} = \frac{\frac{R_j(C=1, \epsilon=1)}{I_0(C=1)}}{\frac{R_j(C=C_{\text{exp}}, \epsilon=\epsilon_{\text{exp}})}{I_0(C=C_{\text{exp}})}} A_{j,\text{exp}} \quad (\text{A.14})$$

$$\varphi_{j,\text{corr}} = \frac{\beta_j(C=1, \epsilon=1)}{\beta_j(C=C_{\text{exp}}, \epsilon=\epsilon_{\text{exp}})} \varphi_{j,\text{exp}}. \quad (\text{A.15})$$



# Bibliography

- [1] T. Young, “I. The Bakerian Lecture. Experiments and calculations relative to physical optics,” *Philos. Trans. R. Soc.* **94**, 1 (1804), <https://royalsocietypublishing.org/doi/pdf/10.1098/rstl.1804.0001> .
- [2] M. Planck, “Über das Gesetz der Energieverteilung im Normalspectrum,” *Ann. Phys. (Berl.)* **309**, 553 (1901), <https://onlinelibrary.wiley.com/doi/pdf/10.1002/andp.19013090310> .
- [3] A. Einstein, “Über einen die Erzeugung und Verwandlung des Lichtes betreffenden heuristischen Gesichtspunkt,” *Ann. Phys. (Berl.)* **322**, 132 (1905).
- [4] De Broglie, Louis, “Recherches sur la théorie des quanta,” *Ann. Phys.* **10**, 22 (1925), (French).
- [5] G. P. Thomson and A. Reid, “Diffraction of cathode rays by a thin film,” *Nature* **119**, 890 (1927).
- [6] C. Davisson and L. H. Germer, “The scattering of electrons by a single crystal of nickel,” *Nature* **119**, 558 (1927).
- [7] D. P. Mitchell and P. N. Powers, “Bragg Reflection of Slow Neutrons,” *Phys. Rev.* **50**, 486 (1936).
- [8] P. Preiswerk and H. von Halban, “Preuve expérimental de la diffraction des neutrons,” *CR Acad. Sci* **203**, 73 (1936).
- [9] H. Rauch, W. Treimer, and U. Bonse, “Test of a single crystal neutron interferometer,” *Phys. Lett. A* **47**, 369 (1974).
- [10] M. Rekveldt, “Novel SANS instrument using Neutron Spin Echo,” *Nucl. Instrum. Methods Phys. Res. B* **114**, 366 (1996).
- [11] I. Estermann and O. Stern, “Beugung von Molekularstrahlen,” *Z. Phys.* **61**, 95 (1930).
- [12] O. Carnal and J. Mlynek, “Young’s double-slit experiment with atoms: A simple atom interferometer,” *Phys. Rev. Lett.* **66**, 2689 (1991).
- [13] D. Leibfried, R. Blatt, C. Monroe, and D. Wineland, “Quantum dynamics of single trapped ions,” *Rev. Mod. Phys.* **75**, 281 (2003).

## A Bibliography

- [14] M. Arndt, O. Nairz, J. Vos-Andreae, C. Keller, G. van der Zouw, and A. Zeilinger, “Wave–particle duality of C60 molecules,” *Nature* **401**, 680 (1999).
- [15] S. Sala, A. Ariga, A. Ereditato, R. Ferragut, M. Giammarchi, M. Leone, C. Pistillo, and P. Scampoli, “First demonstration of antimatter wave interferometry,” *Sci. Adv.* **5** (2019), 10.1126/sciadv.aav7610.
- [16] E. Schrödinger, “An Undulatory Theory of the Mechanics of Atoms and Molecules,” *Phys. Rev.* **28**, 1049 (1926).
- [17] A. Einstein, B. Podolsky, and N. Rosen, “Can quantum-mechanical description of physical reality be considered complete?” *Phys. Rev.* **47**, 777 (1935).
- [18] J. S. Bell, “On the Einstein-Podolsky-Rosen paradox,” *Physics (Long Island City, N.Y.)* **1**, 195 (1964).
- [19] E. Schrödinger, “Die gegenwärtige Situation in der Quantenmechanik,” *Sci. Nat.* **23**, 807 (1935).
- [20] W. Heisenberg, “Über den anschaulichen inhalt der quantentheoretischen kinematik und mechanik,” *Z. Phys.* **43**, 172 (1927).
- [21] H. Rauch, “Quantum Zeno-effect with polarized neutrons,” *Physica B* **297**, 299 (2001).
- [22] Y. Aharonov, S. Popescu, D. Rohrlich, and P. Skrzypczyk, “Quantum Cheshire Cats,” *New J. Phys.* **15**, 113015 (2013).
- [23] T. Denkmayr, H. Geppert, S. Sponar, H. Lemmel, A. Matzkin, J. Tollaksen, and Y. Hasegawa, “Experimental observation of a quantum Cheshire Cat in matter-wave interferometry,” *Nat. Commun.* **5**, 4492 (2014).
- [24] Y. Aharonov, D. Z. Albert, and L. Vaidman, “How the result of a measurement of a component of the spin of a spin-1/2 particle can turn out to be 100,” *Phys. Rev. Lett.* **60**, 1351 (1988).
- [25] N. W. M. Ritchie, J. G. Story, and R. G. Hulet, “Realization of a measurement of a “weak value”,” *Phys. Rev. Lett.* **66**, 1107 (1991).
- [26] S. Sponar, T. Denkmayr, H. Geppert, H. Lemmel, A. Matzkin, J. Tollaksen, and Y. Hasegawa, “Weak values obtained in matter-wave interferometry,” *Phys. Rev. A* **92**, 062121 (2015).
- [27] T. Denkmayr, H. Geppert, H. Lemmel, M. Waegell, J. Dressel, Y. Hasegawa, and S. Sponar, “Experimental demonstration of direct path state characterization by strongly measuring weak values in a matter-wave interferometer,” *Phys. Rev. Lett.* **118**, 010402 (2017).
- [28] T. Denkmayr, J. Dressel, H. Geppert-Kleinrath, Y. Hasegawa, and S. Sponar, “Weak values from strong interactions in neutron interferometry,” *Physica B* **551**, 339 (2018), the 11th International Conference on Neutron Scattering (ICNS 2017).

- [29] I. Shomroni, O. Bechler, S. Rosenblum, and B. Dayan, “Demonstration of Weak Measurement Based on Atomic Spontaneous Emission,” *Phys. Rev. Lett.* **111**, 023604 (2013).
- [30] V. Monachello and R. Flack, “The weak value of spin for atomic systems,” *J. Phys. Conf. Ser.* **701**, 012028 (2016).
- [31] J. Dressel, S. Agarwal, and A. N. Jordan, “Contextual Values of Observables in Quantum Measurements,” *Phys. Rev. Lett.* **104**, 240401 (2010).
- [32] J. Dressel and A. N. Jordan, “Significance of the imaginary part of the weak value,” *Phys. Rev. A* **85**, 012107 (2012).
- [33] M. J. W. Hall, “Prior information: How to circumvent the standard joint-measurement uncertainty relation,” *Phys. Rev. A* **69**, 052113 (2004).
- [34] R. Wagner, W. Kersten, A. Danner, H. Lemmel, A. K. Pan, and S. Sponar, “Direct experimental test of commutation relation via imaginary weak value,” *Phys. Rev. Res.* **3**, 023243 (2021).
- [35] Y. Aharonov, A. Botero, S. Popescu, B. Reznik, and J. Tollaksen, “Revisiting Hardy’s paradox: counterfactual statements, real measurements, entanglement and weak values,” *Phys. Lett. A* **301**, 130 (2002).
- [36] J. S. Lundeen and A. M. Steinberg, “Experimental Joint Weak Measurement on a Photon Pair as a Probe of Hardy’s Paradox,” *Phys. Rev. Lett.* **102**, 020404 (2009).
- [37] M. Ozawa, T. Ralph, and P. K. Lam, “Universal Uncertainty Principle, Simultaneous Measurability, and Weak Values,” in *AIP Conf. Proc.* (AIP, 2011) pp. 53–62.
- [38] J. Dressel, “Weak values as interference phenomena,” *Phys. Rev. A* **91**, 032116 (2015).
- [39] O. Hosten and P. Kwiat, “Observation of the Spin Hall Effect of Light via Weak Measurements,” *Science* **319**, 787 (2008).
- [40] M. Song, J. Steinmetz, Y. Zhang, J. Nauriyal, K. Lyons, A. N. Jordan, and J. Cardenas, “Enhanced on-chip phase measurement by inverse weak value amplification,” *Nat. Commun.* **12**, 6247 (2021).
- [41] J. Dressel, M. Malik, F. M. Miatto, A. N. Jordan, and R. W. Boyd, “Colloquium: Understanding quantum weak values: Basics and applications,” *Rev. Mod. Phys.* **86**, 307 (2014).
- [42] M. Tsang, “Time-Symmetric Quantum Theory of Smoothing,” *Phys. Rev. Lett.* **102**, 250403 (2009).
- [43] M. Tsang, “Continuous Quantum Hypothesis Testing,” *Phys. Rev. Lett.* **108**, 170502 (2012).

## A Bibliography

- [44] T. Kovachy, P. Asenbaum, C. Overstreet, C. A. Donnelly, S. M. Dickerson, A. Sugarbaker, J. M. Hogan, and M. A. Kasevich, “Quantum superposition at the half-metre scale,” *Nature* **528**, 530 (2015).
- [45] H. Rauch, A. Zeilinger, G. Badurek, A. Wilfing, W. Bauspiess, and U. Bonse, “Verification of coherent spinor rotation of fermions,” *Phys. Lett. A* **54**, 425 (1975).
- [46] R. Colella, A. W. Overhauser, and S. A. Werner, “Observation of gravitationally induced quantum interference,” *Phys. Rev. Lett.* **34**, 1472 (1975).
- [47] J. Summhammer, G. Badurek, H. Rauch, U. Kischko, and A. Zeilinger, “Direct observation of fermion spin superposition by neutron interferometry,” *Phys. Rev. A* **27**, 2523 (1983).
- [48] Y. Hasegawa, R. Loidl, G. Badurek, M. Baron, and H. Rauch, “Violation of a Bell-like inequality in single-neutron interferometry,” *Nature* **425**, 45 (2003).
- [49] Y. Hasegawa, R. Loidl, G. Badurek, K. Durstberger-Rennhofer, S. Sponar, and H. Rauch, “Engineering of triply entangled states in a single-neutron system,” *Phys. Rev. A* **81**, 032121 (2010).
- [50] W. Schottky, “Das Kausalproblem der Quantentheorie als eine Grundfrage der modernen Naturforschung überhaupt,” *Sci. Nat.* **9**, 506 (1921).
- [51] S. Watanabe, “Symmetry of Physical Laws. Part III. Prediction and Retrodiction,” *Rev. Mod. Phys.* **27**, 179 (1955).
- [52] Y. Aharonov, P. G. Bergmann, and J. L. Lebowitz, “Time Symmetry in the Quantum Process of Measurement,” *Phys. Rev.* **134**, B1410 (1964).
- [53] M. F. Pusey, “Anomalous weak values are proofs of contextuality,” *Phys. Rev. Lett.* **113**, 200401 (2014).
- [54] R. Kunjwal, M. Lostaglio, and M. F. Pusey, “Anomalous weak values and contextuality: Robustness, tightness, and imaginary parts,” *Phys. Rev. A* **100**, 042116 (2019).
- [55] M. Yang, Q. Li, Z.-H. Liu, Z.-Y. Hao, C.-L. Ren, J.-S. Xu, C.-F. Li, and G.-C. Guo, “Experimental observation of an anomalous weak value without post-selection,” *Photonics Res.* **8**, 1468 (2020).
- [56] E. Rebufello, F. Piacentini, A. Avella, M. A. d. Souza, M. Gramegna, J. Dziewior, E. Cohen, L. Vaidman, I. P. Degiovanni, and M. Genovese, “Anomalous weak values via a single photon detection,” *Light Sci. Appl.* **10** (2021), 10.1038/s41377-021-00539-0.
- [57] A. C. Ipsen, “Anomalous Weak Values are Caused by Disturbance,” *Found. Phys.* **52** (2022), 10.1007/s10701-021-00534-w.
- [58] R. Wagner and E. F. Galvão, “Simple proof that anomalous weak values require coherence,” *Phys. Rev. A* **108**, 1040202 (2023).

- [59] L. Vaidman, “Symposium for Daniel Greenberger’s 80th Birthday,” (2023).
- [60] W. Kersten, *Simultaneous Measurement of a Quantum Cheshire Cat*, [Master’s thesis](#), TU Wien (2017).
- [61] R. Wagner, *Quantum causality and macrorealism studied with the neutron interferometer*, [Ph.D. thesis](#), TU Wien (2021).
- [62] J. Von Neumann, *Mathematische Grundlagen der Quantenmechanik*, Die Grundlehren der mathematischen Wissenschaften: in Einzeldarstellungen mit besonderer Berücksichtigung der Anwendungsgebiete (Julius Springer, 1932).
- [63] Y. Aharonov and D. Rohrlich, “Weak Values,” in *Quantum Paradoxes* (John Wiley & Sons, Ltd, 2005) Chap. 16, p. 237, <https://onlinelibrary.wiley.com/doi/pdf/10.1002/9783527619115.ch16> .
- [64] R. Jozsa, “Complex weak values in quantum measurement,” *Phys. Rev. A* **76**, 044103 (2007).
- [65] J. Chadwick, “The existence of a neutron,” *Proc. R. Soc. B* **136**, 692 (1932).
- [66] V. F. Sears, “Neutron scattering lengths and cross sections,” *Neutron News* **3**, 26 (1992).
- [67] A. Mikhailovskaya, L. Zhang, F. Cousin, F. Boué, P. Yazhgur, F. Muller, C. Gay, and A. Salonen, “Probing foam with neutrons,” *Adv. Colloid Interface Sci.* **247**, 444 (2017).
- [68] E. Jericha, “Vorlesungsskriptum Neutronen und Kernphysik,” (2018), unpublished lecture notes (German).
- [69] A. Danner, *Spin-rotation coupling in a neutron polarimeter experiment*, [Master’s thesis](#), TU Wien (2019).
- [70] J. T. Cremer, H. Filter, J. Klepp, P. Geltenbort, C. Dewhurst, T. Oda, and R. H. Pantell, “Focusing and imaging of cold neutrons with a permanent magnetic lens,” *Rev. Sci. Instrum.* **91** (2020), 10.1063/1.5116759.
- [71] R. Wagner, J. Barrow, C. Bohm, G. Brooijmans, H. Calen, J. Cederkäll, J. Collin, K. Dunne, L. Eklund, P. Fierlinger, U. Friman-Gayer, M. Frost, M. Holl, T. Johansson, Y. Kamyshkov, E. Klinkby, A. Kupsc, B. Meirose, D. Milstead, A. Nepomuceno, T. Nilsson, A. Oskarsson, H. Perrey, B. Rataj, N. Rizzi, V. Santoro, S. Silverstein, A. Takibayev, M. Wolke, S. Yiu, A. Young, L. Zanini, and O. Zimmer, “Design of an optimized nested-mirror neutron reflector for a nbar experiment,” *Nucl. Instrum. Methods Phys. Res. A* **1051**, 168235 (2023).
- [72] B. Demirel, *Spin-rotation-coupling in neutron polarimetry*, [Master’s thesis](#), TU Wien (2013).
- [73] M. Villa, *Reactor Physics* (2000) unpublished lecture notes.

## A Bibliography

- [74] W. Demtröder, “Experimentalphysik 1,” (Springer-Verlag Berlin Heidelberg, 2006) Chap. Systeme von Massenpunkten, Stöße.
- [75] Z. Wang, F. Liu, Z. Guo, J. Zhang, L. Wang, and G. Yan, “Advance in and prospect of moderator materials for space nuclear reactors,” *Int. J. Energy Res.* **45**, 11493 (2021).
- [76] “ILL technical characteristics,” Accessed 15 July 2024.
- [77] “TRIGA reactor Atominstitut technical data,” Accessed 15 July 2024.
- [78] “Treaty on the Non-Proliferation of Nuclear Weapons,” Retrieved September 9, 2024.
- [79] “Stahlschutzgesetz § 36b (3),” (2020), „Betreiber von Forschungsreaktoren haben sicherzustellen, dass keine abgebrannten Brennelemente zur Entsorgung in Österreich anfallen.“.
- [80] “Stahlschutzgesetz § 36c (1),” (2020), „Der Bundesminister für Land- und Forstwirtschaft, Umwelt und Wasserwirtschaft wird [...] weiters ermächtigt als Auftraggeber mit der Austrian Research Centers Ges.m.b.H. – ARC oder anderen geeigneten Institutionen [...] als Auftragnehmer Leistungsverträge über die dem Stand der Technik entsprechende Entsorgung radioaktiver Abfälle, beginnend mit deren Sammlung, abzuschließen.“.
- [81] “Outline History of Nuclear Energy,” Retrieved September 9, 2024.
- [82] P. Klein, “Aktuelle Flüssigsalzreaktorprojekte,” (2021), unpublished project thesis.
- [83] D. Deutsch, *The beginning of infinity*, 1st ed. (Lane, London, 2011).
- [84] W. Mach, *Installation of a neutron beam instrument at the TRIGA reactor in Vienna*, Ph.D. thesis, TU Wien (2018).
- [85] R. D. Deslattes and A. Henins, “X-Ray to Visible Wavelength Ratios,” *Phys. Rev. Lett.* **31**, 972 (1973).
- [86] P. Becker, K. Dorenwendt, G. Ebeling, R. Lauer, W. Lucas, R. Probst, H.-J. Rademacher, G. Reim, P. Seyfried, and H. Siegert, “Absolute Measurement of the (220) Lattice Plane Spacing in a Silicon Crystal,” *Phys. Rev. Lett.* **46**, 1540 (1981).
- [87] F. Otálora, B. Capelle, A. Ducruix, and J. M. García-Ruiz, “Mosaic spread characterization of microgravity-grown tetragonal lysozyme single crystals,” *Acta Crystallogr. D* **55**, 644 (1999).
- [88] J. G. Barker, C. J. Glinka, J. J. Moyer, M. H. Kim, A. R. Drews, and M. Agamalian, “Design and performance of a thermal-neutron double-crystal diffractometer for USANS at NIST,” *J. Appl. Crystallogr.* **38**, 1004 (2005).

- [89] G. Badurek, R. Buchelt, G. Kroupa, M. Baron, and M. Villa, “Permanent magnetic field-prism polarizer for perfect crystal neutron interferometers,” *Physica B* **283**, 389 (2000).
- [90] H. Maier-Leibnitz and T. Springer, “The use of neutron optical devices on beam-hole experiments on beam-hole experiments,” *Ann. Nucl. Energy A/B* **17**, 217 (1963).
- [91] B. P. Schoenborn, D. L. D. Caspar, and O. F. Kammerer, “A novel neutron monochromator,” *J. Appl. Crystallogr.* **7**, 508 (1974).
- [92] F. Mezei, “Novel polarized neutron devices: supermirror and spin component amplifier,” *Communications on Physics* **1** (1976).
- [93] R. Golub, *Ultra cold neutrons*, edited by D. J. Richardson and S. K. Lamoreaux (Adam Hilger, Bristol [u.a.], 1991) Literaturverz. S. 277 - 286.
- [94] R. Cubitt and G. Fragneto, “Neutron Reflection: Principles and Examples of Applications,” in *Scattering* (Elsevier, 2002) pp. 1198–1208.
- [95] I. S. Anderson, O. Schärpf, P. Høghøj, and P. Ageron, “Multilayers for neutron optics,” *J. Neutron Res.* **5**, 51 (1996).
- [96] P. Böni, “Polarizing supermirrors,” *J. Neutron Res.* **5**, 63 (1996).
- [97] T. Habersohn, *Erste experimentelle Versuche zur magnetischen Spintomographie mit Neutronen (German)*, Master’s thesis, TU Wien (2006).
- [98] M. Fally, J. Klepp, Y. Tomita, T. Nakamura, C. Pruner, M. A. Ellabban, R. A. Rupp, M. Bichler, I. D. Olenik, J. Kohlbrecher, H. Eckerlebe, H. Lemmel, and H. Rauch, “Neutron Optical Beam Splitter from Holographically Structured Nanoparticle-Polymer Composites,” *Phys. Rev. Lett.* **105**, 123904 (2010).
- [99] F. Mezei, “The principles of neutron spin echo,” in *Neutron Spin Echo* (Springer Berlin Heidelberg, 1980) pp. 1–26.
- [100] H. Rauch and S. A. Werner, *Neutron Interferometry* (Oxford University Press, 2000).
- [101] E. S. Kreuzgruber, *Time-resolved postselection and the violation of a Leggett–Garg inequality in thermal neutron interferometry*, Master’s thesis, TU Wien (2022).
- [102] M. Suda, “The dynamical theory of diffraction,” in *Quantum Interferometry in Phase Space: Theory and Applications* (Springer Berlin Heidelberg, Berlin, Heidelberg, 2006) pp. 75–89.
- [103] B. Demirel, S. Sponar, A. A. Abbott, C. Branciard, and Y. Hasegawa, “Experimental test of an entropic measurement uncertainty relation for arbitrary qubit observables,” *New J. Phys.* **21**, 013038 (2019).

## A Bibliography

- [104] H. Geppert-Kleinrath, *Experimental studies of Bell-like inequality and a which-way measurement in neutron interferometry*, Ph.D. thesis, TU Wien (2017).
- [105] M. Suda, “Zero-field spin-echo,” in *Quantum Interferometry in Phase Space: Theory and Applications* (Springer Berlin Heidelberg, Berlin, Heidelberg, 2006) pp. 157–174.
- [106] F. Bloch and A. Siegert, “Magnetic resonance for nonrotating fields,” *Phys. Rev.* **57**, 522 (1940).
- [107] J. Baumann, R. Gähler, J. Kalus, and W. Mampe, “Experimental limit for the charge of the free neutron,” *Phys. Rev. D* **37**, 3107 (1988).
- [108] J. Bosina, H. Filter, J. Micko, T. Jenke, M. Pitschmann, S. Roccia, R. I. P. Sedmik, and H. Abele, “qBounce: First Measurement of the Neutron Electric Charge with a Ramsey-type GRS Experiment,” (2023), [arXiv:2301.05984 \[hep-ex\]](https://arxiv.org/abs/2301.05984) .
- [109] T. Jenke, G. Cronenberg, H. Filter, P. Geltenbort, M. Klein, T. Lauer, K. Mitsch, H. Saul, D. Seiler, D. Stadler, M. Thalhammer, and H. Abele, “Ultracold neutron detectors based on 10B converters used in the qBounce experiments,” *Nucl. Instrum. Methods Phys. Res. A* **732**, 1 (2013).
- [110] N. Naganawa, T. Ariga, S. Awano, M. Hino, K. Hirota, H. Kawahara, M. Kitaguchi, K. Mishima, H. M. Shimizu, S. Tada, S. Tasaki, and A. Umemoto, “A cold/ultracold neutron detector using fine-grained nuclear emulsion with spatial resolution less than 100 nm,” *Eur. Phys. J. C* **78** (2018), [10.1140/epjc/s10052-018-6395-7](https://doi.org/10.1140/epjc/s10052-018-6395-7).
- [111] H. Karttunen, P. Kröger, H. Oja, M. Poutanen, and K. J. Donner, eds., *Fundamental Astronomy*, 5th ed. (Springer Berlin Heidelberg, Berlin, Heidelberg, 2007).
- [112] A. Danner, N. Geerits, H. Lemmel, R. Wagner, S. Sponar, and Y. Hasegawa, “Three-path quantum Cheshire cat observed in neutron interferometry,” *Commun. Phys.* **7** (2024), [10.1038/s42005-023-01494-5](https://doi.org/10.1038/s42005-023-01494-5).
- [113] E. Schrödinger, “Die gegenwärtige Situation in der Quantenmechanik,” *Sci. Nat.* **23**, 807 (1935).
- [114] E. Schrödinger, “Die gegenwärtige Situation in der Quantenmechanik,” *Sci. Nat.* **23**, 823 (1935).
- [115] A. K. Ekert, “Quantum cryptography based on Bell’s theorem,” *Phys. Rev. Lett.* **67**, 661 (1991).
- [116] A. Ourjoumtsev, R. Tualle-Brouri, J. Laurat, and P. Grangier, “Generating Optical Schrödinger Kittens for Quantum Information Processing,” *Science* **312**, 83 (2006), <https://www.science.org/doi/pdf/10.1126/science.1122858> .

- [117] M. A. Nielsen and I. L. Chuang, *Quantum Computation and Quantum Information: 10th Anniversary Edition* (Cambridge University Press, 2010).
- [118] D. Neamen, “Semiconductor Physics and Devices: Basic Principles,” (McGraw-Hill, 2012) pp. 25–57.
- [119] L. Carroll, *Alice’s Adventures in Wonderland* (MacMillan & Co., London, 1866) pp. 89–94.
- [120] D. P. Atherton, G. Ranjit, A. A. Geraci, and J. D. Weinstein, “Observation of a classical Cheshire cat in an optical interferometer,” *Opt. Lett.* **40**, 879 (2015).
- [121] J. M. Ashby, P. D. Schwarz, and M. Schlosshauer, “Observation of the quantum paradox of separation of a single photon from one of its properties,” *Phys. Rev. A* **94**, 012102 (2016).
- [122] R. Corrêa, M. F. Santos, C. H. Monken, and P. L. Saldanha, “‘Quantum Cheshire Cat’ as simple quantum interference,” *New J. Phys.* **17**, 053042 (2015).
- [123] W. Stuckey, M. Silberstein, and T. McDevitt, “Concerning Quadratic Interaction in the Quantum Cheshire Cat Experiment,” *Int. J. Quantum Found.* **2**, 17 (2016).
- [124] Q. Duprey, S. Kanjilal, U. Sinha, D. Home, and A. Matzkin, “The Quantum Cheshire Cat effect: Theoretical basis and observational implications,” *Ann. Phys. (N. Y.)* **391**, 1 (2018).
- [125] D. Das and A. K. Pati, “Teleporting Grin of a Quantum Cheshire Cat without cat,” (2019).
- [126] Z.-H. Liu, W.-W. Pan, X.-Y. Xu, M. Yang, J. Zhou, Z.-Y. Luo, K. Sun, J.-L. Chen, J.-S. Xu, C.-F. Li, and G.-C. Guo, “Experimental exchange of grins between quantum Cheshire cats,” *Nat. Commun.* **11**, 3006 (2020).
- [127] Y. Kim, D.-G. Im, Y.-S. Kim, S.-W. Han, S. Moon, Y.-H. Kim, and Y.-W. Cho, “Observing the quantum Cheshire cat effect with noninvasive weak measurement,” *npj Quantum Inf.* **7**, 13 (2021).
- [128] A. Ghoshal, S. Sau, D. Das, and U. Sen, “Isolating noise and amplifying the signal using weak quantum measurement and postselection,” *Phys. Rev. A* **107**, 052214 (2023).
- [129] J.-K. Li, K. Sun, Y. Wang, Z.-Y. Hao, Z.-H. Liu, J. Zhou, X.-Y. Fan, J.-L. Chen, J.-S. Xu, C.-F. Li, and G.-C. Guo, “Experimental demonstration of separating the wave–particle duality of a single photon with the quantum Cheshire cat,” *Light Sci. Appl.* **12**, 18 (2023).
- [130] A. K. Pan, “Disembodiment of arbitrary number of properties in quantum Cheshire cat experiment,” *Eur. Phys. J. D* **74**, 151 (2020).

## A Bibliography

- [131] J. Klepp, S. Sponar, and Y. Hasegawa, “Fundamental phenomena of quantum mechanics explored with neutron interferometers,” *Prog. Theor. Exp. Phys.* **2014** (2014).
- [132] S. Sponar, R. I. P. Sedmik, M. Pitschmann, H. Abele, and Y. Hasegawa, “Tests of fundamental quantum mechanics and dark interactions with low-energy neutrons,” *Nat. Rev. Phys.* **3**, 309 (2021).
- [133] G. Badurek, R. J. Buchelt, G. Kroupa, M. Baron, and M. Villa, “Permanent magnetic field-prism polarizer for perfect crystal neutron interferometers,” *Physica B* **283**, 389 (2000).
- [134] G. Badurek, H. Rauch, and D. Tuppinger, “Neutron interferometric double-resonance experiment,” *Phys. Rev. A* **34**, 2600 (1986).
- [135] S. Sponar, J. Klepp, R. Loidl, S. Filipp, G. Badurek, Y. Hasegawa, and H. Rauch, “Coherent energy manipulation in single-neutron interferometry,” *Phys. Rev. A* **78**, 061604 (2008).
- [136] J. Shen, S. J. Kuhn, R. M. Dalglish, V. O. de Haan, N. Geerits, A. A. M. Irfan, F. Li, S. Lu, S. R. Parnell, J. Plomp, A. A. van Well, A. Washington, D. V. Baxter, G. Ortiz, W. M. Snow, and R. Pynn, “Unveiling contextual realities by microscopically entangling a neutron,” *Nat. Commun.* **11**, 930 (2020).
- [137] S. Lu, A. A. M. Irfan, J. Shen, S. J. Kuhn, W. M. Snow, D. V. Baxter, R. Pynn, and G. Ortiz, “Operator analysis of contextuality-witness measurements for multimode-entangled single-neutron interferometry,” *Phys. Rev. A* **101**, 042318 (2020).
- [138] I. M. Duck, P. M. Stevenson, and E. C. G. Sudarshan, “The sense in which a ”weak measurement” of a spin-1/2 particle’s spin component yields a value 100,” *Phys. Rev. D* **40**, 2112 (1989).
- [139] Y. Aharonov and L. Vaidman, “The two-state vector formalism of quantum mechanics: an updated review,” (2007), [arXiv:quant-ph/0105101](https://arxiv.org/abs/quant-ph/0105101) [quant-ph].
- [140] H. Geppert, T. Denkmayr, S. Sponar, H. Lemmel, and Y. Hasegawa, “Improvement of the polarized neutron interferometer setup demonstrating violation of a Bell-like inequality,” *Nucl. Instrum. Methods Phys. Res. A* **763**, 417 (2014).
- [141] A. Danner, B. Demirel, S. Sponar, and Y. Hasegawa, “Development and performance of a miniaturised spin rotator suitable for neutron interferometer experiments,” *J. Phys. Commun.* **3**, 035001 (2019).
- [142] T. Cheon and S. Poghosyan, “Weak value expansion of quantum operators and its application in stochastic matrices,” (2013).
- [143] J. Dziewior, “Weak measurements,” in *The Concept of Weak Values* (Ludwig-Maximilians-Universität München, 2016) pp. 44–52.

- [144] S. E. Canton, E. Plésiat, J. D. Bozek, B. S. Rude, P. Decleva, and F. Martín, “Direct observation of young’s double-slit interferences in vibrationally resolved photoionization of diatomic molecules,” *Proc. Natl. Acad. Sci. U.S.A.* **108**, 7302 (2011), <https://www.pnas.org/doi/pdf/10.1073/pnas.1018534108> .
- [145] A. Hosoya and Y. Shikano, “Strange weak values,” *J. Phys. A* **43**, 385307 (2010).
- [146] M. J. W. Hall, A. K. Pati, and J. Wu, “Products of weak values: Uncertainty relations, complementarity, and incompatibility,” *Phys. Rev. A* **93**, 052118 (2016).
- [147] A. Danner, I. V. Masiello, A. Dvorak, W. Kersten, H. Lemmel, R. Wagner, and Y. Hasegawa, “Simultaneous path weak-measurements in neutron interferometry,” *Sci. Rep.* **14**, 25994 (2024).
- [148] G. I. Taylor, “Interference fringes with feeble light,” in *Proceedings of the Cambridge Philosophical Society*, Vol. 15 (1909) pp. 114–115.
- [149] P. G. Merli, G. F. Missiroli, and G. Pozzi, “On the statistical aspect of electron interference phenomena,” *Am. J. Phys.* **44**, 306 (1976), [https://pubs.aip.org/aapt/ajp/article-pdf/44/3/306/11843743/306\\_1\\_online.pdf](https://pubs.aip.org/aapt/ajp/article-pdf/44/3/306/11843743/306_1_online.pdf) .
- [150] J. Summhammer, H. Rauch, and D. Tuppinger, “Stochastic and deterministic absorption in neutron-interference experiments,” *Phys. Rev. A* **36**, 4447 (1987).
- [151] L. Vaidman, “Past of a quantum particle,” *Phys. Rev. A* **87**, 052104 (2013).
- [152] A. Danan, D. Farfurnik, S. Bar-Ad, and L. Vaidman, “Asking photons where they have been,” *Phys. Rev. Lett.* **111**, 240402 (2013).
- [153] H. Geppert-Kleinrath, T. Denkmayr, S. Sponar, H. Lemmel, T. Jenke, and Y. Hasegawa, “Multifold paths of neutrons in the three-beam interferometer detected by a tiny energy kick,” *Phys. Rev. A* **97**, 052111 (2018).
- [154] G. Mitchison, R. Jozsa, and S. Popescu, “Sequential weak measurement,” *Phys. Rev. A* **76**, 062105 (2007).
- [155] Y. Kim, Y.-S. Kim, S.-Y. Lee, S.-W. Han, S. Moon, Y.-H. Kim, and Y.-W. Cho, “Direct quantum process tomography via measuring sequential weak values of incompatible observables,” *Nat. Commun.* **9** (2018), 10.1038/s41467-017-02511-2.
- [156] J.-S. Chen, M.-J. Hu, X.-M. Hu, B.-H. Liu, Y.-F. Huang, C.-F. Li, C.-G. Guo, and Y.-S. Zhang, “Experimental realization of sequential weak measurements of non-commuting Pauli observables,” *Opt. Express* **27**, 6089 (2019).
- [157] G. Foletto, M. Padovan, M. Avesani, H. Tebyanian, P. Villoresi, and G. Vallone, “Experimental test of sequential weak measurements for certified quantum randomness extraction,” *Phys. Rev. A* **103**, 062206 (2021).

## A Bibliography

- [158] H. Rauch and S. A. Werner, *Neutron Interferometry 2nd Edn: Lessons in Experimental Quantum Mechanics, Wave-Particle Duality, and Entanglement* (Oxford University Press, 2015).
- [159] A. Danner, H. Lemmel, R. Wagner, S. Sponar, and Y. Hasegawa, “Neutron interferometer experiments studying fundamental features of quantum mechanics,” *Atoms* **11** (2023), 10.3390/atoms11060098.
- [160] A. C. Ipsen, “Disturbance in weak measurements and the difference between quantum and classical weak values,” *Phys. Rev. A* **91**, 062120 (2015).
- [161] M. A. Ochoa, W. Belzig, and A. Nitzan, “Simultaneous weak measurement of non-commuting observables: a generalized Arthurs-Kelly protocol,” *Sci. Rep.* **8** (2018), 10.1038/s41598-018-33562-0.
- [162] F. Bloch and A. Siegert, “Magnetic Resonance for Nonrotating Fields,” *Phys. Rev.* **57**, 522 (1940).
- [163] G. Sulyok, K. Durstberger-Rennhofer, and J. Summhammer, “Photon exchange and entanglement formation during transmission through a rectangular quantum barrier,” *Phys. Lett. A* **379**, 1699 (2015).
- [164] H. Geppert, T. Denkmayr, S. Sponar, H. Lemmel, and Y. Hasegawa, “Improvement of the polarized neutron interferometer setup demonstrating violation of a Bell-like inequality,” *Nucl. Instrum. Methods Phys. Res. A* **763**, 417 (2014).
- [165] G. Badurek, H. Rauch, and J. Summhammer, “Time-Dependent Superposition of Spinors,” *Phys. Rev. Lett.* **51**, 1015 (1983).
- [166] G. Badurek, H. Rauch, and D. Tuppinger, “Neutron interferometric double-resonance experiment,” *Phys. Rev. A* **34**, 2600 (1986).
- [167] A. Danner, B. Demirel, S. Sponar, and Y. Hasegawa, “Development and performance of a miniaturised spin rotator suitable for neutron interferometer experiments,” *J. Phys. Commun.* **3**, 035001 (2019).
- [168] E. Arthurs and J. L. Kelly, “On the Simultaneous Measurement of a Pair of Conjugate Observables,” *Bell Labs Tech. J.* **44**, 725 (1965).
- [169] A. Hariri, D. Curic, L. Giner, and J. S. Lundeen, “Experimental simultaneous readout of the real and imaginary parts of the weak value,” *Phys. Rev. A* **100**, 032119 (2019).
- [170] H. Lemmel, N. Geerits, A. Danner, H. F. Hofmann, and S. Sponar, “Quantifying the presence of a neutron in the paths of an interferometer,” *Phys. Rev. Res.* **4**, 023075 (2022).
- [171] M. Ozawa, “Universally valid reformulation of the Heisenberg uncertainty principle on noise and disturbance in measurement,” *Phys. Rev. A* **67**, 042105 (2003).

- [172] A. J. Leggett and A. Garg, “Quantum mechanics versus macroscopic realism: Is the flux there when nobody looks?” *Phys. Rev. Lett.* **54**, 857 (1985).
- [173] J. Summhammer, K. A. Hamacher, H. Kaiser, H. Weinfurter, D. L. Jacobson, and S. A. Werner, “Multiphoton exchange amplitudes observed by neutron interferometry,” *Phys. Rev. Lett.* **75**, 3206 (1995).
- [174] N. BOHR, “The Quantum Postulate and the Recent Development of Atomic Theory1,” *Nature* **121**, 580 (1928).
- [175] D. M. Greenberger and A. Yasin, “Simultaneous wave and particle knowledge in a neutron interferometer,” *Phys. Lett. A* **128**, 391 (1988).
- [176] G. Jaeger, A. Shimony, and L. Vaidman, “Two interferometric complementarities,” *Phys. Rev. A* **51**, 54 (1995).
- [177] B.-G. Englert, “Fringe visibility and which-way information: An inequality,” *Phys. Rev. Lett.* **77**, 2154 (1996).
- [178] M. O. Scully, B.-G. Englert, and H. Walther, “Quantum optical tests of complementarity,” *Nature* **351**, 111 (1991).
- [179] S. P. Walborn, M. O. Terra Cunha, S. Pádua, and C. H. Monken, “Double-slit quantum eraser,” *Phys. Rev. A* **65**, 033818 (2002).
- [180] T. Qureshi, “The Delayed-Choice Quantum Eraser Leaves No Choice,” *Int. J. Theor. Phys.* **60**, 3076 (2021).